Optical Trapping and Evaporative Cooling of Fermionic Atoms

by

Kenneth Martin O'Hara

Department of Physics
Duke University

Date: _____
Approved:

_____
Dr. John E. Thomas, Supervisor

_____
Dr. Daniel J. Gauthier

_____
Dr. Konstantin Matveev

_____
Dr. David D. Skatrud

_____
Dr. Stephen W. Teitsworth

Dissertation submitted in partial fulfillment of the
requirements for the degree of Doctor of Philosophy
in the Department of Physics
in the Graduate School of
Duke University

2000

ABSTRACT

(Physics)

Optical Trapping and Evaporative Cooling of Fermionic Atoms

by

Kenneth Martin O'Hara

Department of Physics
Duke University

Date:_____
Approved:

_____
Dr. John E. Thomas, Supervisor

_____
Dr. Daniel J. Gauthier

_____
Dr. Konstantin Matveev

_____
Dr. David D. Skatrud

_____
Dr. Stephen W. Teitsworth

An abstract of a dissertation submitted in partial fulfillment of
the requirements for the degree of Doctor of Philosophy
in the Department of Physics
in the Graduate School of
Duke University

2000

Abstract

This dissertation describes the development of the first stable optical trap for neutral atoms and its application to studies of interactions between and evaporative cooling of a gas of fermionic atoms. This work lays the foundation for future investigations of quantum statistical effects in a dilute, ultracold gas of fermionic atoms in which the temperature, density and interaction strength can be independently controlled. Such studies may include the observation of superfluidity via Cooper pair formation at a high critical temperature. In addition, the development of a stable optical trap impacts a wide variety of applications including fundamental precision measurements, quantum computing, improved frequency standards and the precise manipulation of atoms and molecules.

Optical traps are ideally suited for studies of interacting Fermi gases since they are able to confine stable two-state mixtures of fermionic atoms. The ability to trap multiple states enables ultracold collisions, which would otherwise be forbidden by the exclusion principle in a single-state fermionic vapor. However, optical traps have previously suffered from residual heating and loss mechanisms, which have limited trap lifetimes to several seconds. Using an ultrastable carbon dioxide laser to confine atoms in an ultrahigh vacuum environment, we minimize all known sources of residual heating including those due to fluctuations in the laser intensity and position. By this method we obtain trap lifetimes of 370 seconds, limited by the background gas pressure of $< 10^{-11}$ Torr, with residual heating rates of < 50 nanoKelvin/sec.

The construction of a stable optical trap has enabled the first experimental studies of evaporative cooling of a two-state mixture of lithium fermions. By monitoring the rate of evaporation of atoms from the trap we directly measure a large low-energy cross section predicted to exist for ^{6}Li. Based on the existence of this large interaction strength, an optically trapped gas of lithium atoms is expected to be a promising candidate for the observation of superfluidity in a dilute, ultracold, interacting Fermi gas.

Ultracold temperatures and high phase space densities can be achieved in this system through forced evaporative cooling. In this process, the highest energy atoms are selectively removed from the trap by adiabatically lowering the well depth. Using this technique, a temperature of 2.4 μK with a corresponding phase space density of 1.6×10^{-3} is achieved. Based on a theoretical model of evaporative cooling we describe in this dissertation, we expect that modest improvements to this system should enable cooling to temperatures below the Fermi temperature and possibly below the critical temperature for Cooper pair formation.

Acknowledgments

The completion of this dissertation would not have been possible had it not been for the encouragement and support of a number of people whom I have had the fortunate to know over the years. I feel truly blessed to have had all of these people in my life. I sincerely appreciate their support and guidance over the years and wish to acknowledge their efforts here.

I owe a great debt of gratitude to my parents Martin and Mary. They provided my brother and me with a good home and nurtured our intellectual pursuits. Parenting is often a very difficult and thankless job. I am not sure that I made their job any less difficult, but I would hate to miss this opportunity to express my heartfelt appreciation for all that they have done for me.

I am indebted to my brother Keith for inspiring in me an interest and love for physics. I feel very lucky to have had such a patient and brilliant older brother always willing to answer his younger brother's questions. I have treasured the enumerable conversations about physics and life we have had over the years and look forward to many more in the future.

While in college I had the fortune of working with Dr. Don Blankenship at Ohio State University and Dr. Ani Aprahamian at the University of Notre Dame. Both Don and Ani developed my confidence as an experimentalist and gave me the courage to pursue a graduate degree in physics. I appreciate the time they took to encourage me and wish them both the best.

At Duke University, I have had the privilege of having Dr. John Thomas as

my advisor. John approaches physics with an excitement, intensity and sheer joy that is unparalleled. One cannot help but be inspired by him. I have learned a great deal under John's supervision. Probably the most enduring lesson is that "nothing is magic." Unexpected or mysterious results can often be explained upon carefully reexamination of the problem at hand. I have also learned a great deal from John about how to manage a research group. John has been a very fair and judicious advisor. His perpetual optimism and unbridled enthusiasm helps to uplift the morale of the group and inspires his students to work hard to reach their goals. I have enjoyed the daily spirited discussions I have had with John about the research project. I am sure that I will look back on this time in my life with fond memories and that is in no small part due to how much I have enjoyed working with such a great advisor.

I have had the opportunity to work with a number of bright and talented graduate students while at Duke. I enjoyed working with Hongzhi Zhao, Tom Savard, Adam Wax and Chris Baird when I first joined the group. I especially appreciate the patient and thoughtful training that Tom Savard supplied. Tom is an excellent experimentalist and I feel fortunate to have had the opportunity to work with him. I am particularly indebted to Mike Gehm and Stephen Granade who provided invaluable assistance on this project. This dissertation work could not have been completed without Stephen and Mike's contributions. They were quick to generate new ideas of how to move our research forward and always willing to build whatever new piece of equipment was required for the experiment. I really appreciate all of their hard work and I hope that I can return the favor in the near future. I am thankful for the assistance of our post-doc Dr. Samir Bali. Having worked on cooling and trapping research at the University of Wisconsin, Samir provided

numerous ideas for the experiment from a fresh perspective. Samir was an excellent sounding board for new ideas and was a master at writing papers. I wish him well in his career at Miami University. I am also indebted to Zehuang Lu for selflessly offering both his dye laser and his expertise when we needed an additional laser in order to align the CO_2 laser trap. I am glad that he didn't get too mad at me on the day I turned his laser into a dye fountain. I have also enjoyed working with the newer students in our group: Frank Reil, Kim Fook Lee, Ming-Shien Chang, Anand Priyadarshee and Staci Hemmer.

The development of the ultrastable carbon dioxide laser on which this dissertation work is based was made possible through the assistance of Dr. Charles Freed at Lincoln Laboratory in Massachusetts. Dr. Freed is an expert at building ultrastable carbon dioxide lasers and provided many invaluable suggestions on the design and construction of the laser that we built. I am grateful that Dr. Freed was willing to take the time not only to collaborate on the design of the carbon dioxide laser but also to provide us with high voltage power supplies on loan from Lincoln Laboratory.

I have also had the fortune of working with some very capable people in the construction of various pieces of the experiment. We are fortunate to have a skilled group of machinists in the instrument shop in the physics department at Duke University. I enjoyed working with Robert Timberlake and his crew as they built most of the parts for the carbon dioxide laser. I also appreciate the patient assistance provided by Richard Poole in the student instrument shop. I hope he is enjoying his retirement. I am also grateful to Larry Stone at University Research Glass who constructed the glass discharge tube for the carbon dioxide laser. I really appreciate that Larry took some of the design considerations for the laser tube off of our hands allowing us to concentrate on other things.

I would also like to acknowledge the contributions of my dissertation committee which included Dr. Daniel Gauthier, Dr. Konstantin Matveev, Dr. David Skatrud and Dr. Stephen Teitsworth. I appreciate the many helpful comments that they have made regarding this thesis.

Finally, I am thankful to have had my wife Jessica by my side throughout my graduate career. I could not have made it through graduate school without her. She is my best friend and has been incredibly supportive of me in our life together. I'm very proud of Jessica for pursuing a doctoral degree in English. I hope I can be as supportive of her as she has been of me. I'm also thankful for the wonderful family that Jessica has brought into my life. I appreciate the thoughtful words of encouragement from Jessica's parents Debbie and Jim Shoup, Jessica's step-mother Gloria, Annie and Casey Shoup, Jane Mastro, Cindy, Nick and Andy Orbison, and Joe and Cynthia Mastro.

For Jessica

Contents

List of Figures

List of Tables

Chapter 1

Introduction

In 1995, three research groups unambiguously observed Bose-Einstein condensation (BEC) in a dilute gas of weakly interacting alkali atoms cooled to ultralow temperatures [1–3]. With the realization of BEC in a dilute atomic vapor, a new epoch in the study of low-temperature physics began. While BEC is understood to play a principle role in the superfluid properties of degenerate liquid ^{4}He, the realization of BEC in a dilute atomic vapor now permits the study of BEC in the low density regime. Trapped, ultracold atomic vapors offer exciting new opportunities for fundamental studies of interacting quantum gases in which the temperature, density and interaction strength can be independently controlled. Due to the dilute nature of the vapors, the interactions are weak and well understood making these systems amenable to quantitative comparison with theoretical prediction. In addition, a wide variety of techniques have been developed for the precise manipulation and observation of the condensate. The achievement of BEC is also viewed as an enabling technology as it provides a source of coherent matter waves [4–6] for investigations of matter wave optics and provides ultimate control over the external degrees of freedom of an atom which is of importance to precision measurements and neutral atom lithography.

Although the study of Bose-Einstein condensation is far from exhausted, an obvious direction for future investigation is the realization of a quantum degener-

ate Fermi gas in a dilute atomic vapor. As for dilute, degenerate Bose gases, the attainment of a dilute, degenerate Fermi gas would permit the quantitative investigation of quantum statistical effects in a Fermi gas over a wide range of physical conditions. The observation of BEC in a dilute vapor has inspired a number of theoretical investigations of the properties of a degenerate, trapped Fermi gas. These have included studies of the thermodynamic properties of the gas [7–10], many-body dynamics [11,12] and the interaction of light with the degenerate Fermi gas [13,14].

For a Fermi gas with an attractive interaction, a particularly exciting possibility is the existence of a superfluid transition due to the formation of Cooper pairs similar to the superconducting transition in metals. This would enable quantitative investigation of the Bardeen-Cooper-Schrieffer (BCS) theory of superconductivity over a wide range of physical conditions. Previously, it was concluded that the superfluid transition would occur at an experimentally unattainable temperature for a dilute gas due to the weakness of the interatomic interactions [15]. However, based on a prediction that ultracold ^{6}Li atoms exhibit an anomalously large and attractive interaction [16], this conclusion has recently been revised [17]. In fact, the interaction strength between ^{6}Li atoms is expected to be so large that, measured relative to the Fermi temperature of the gas, the critical temperature T_c for the superfluid transition is expected to be the highest of all known BCS superfluids [18]. Thus, a dilute gas of ultracold ^{6}Li atoms is considered a particularly interesting candidate for investigations of quantum statistical effects in an interacting Fermi gas.

However, in order for interactions to exist in an ultracold Fermi gas, one must confine a *two component* Fermi gas—a collection of atoms where each atom is in one of two different internal states. This is due to the fact that at the ultracold

temperatures being considered, only head on (*i.e.* *s*-wave) collisions occur. Such collisions are forbidden by the Pauli Exclusion principle in a single component Fermi gas. The attainment of interactions in a Fermi gas is not only important to studies of an interacting Fermi gas; interactions are also critical to the success of evaporative cooling, the final cooling stage used in the production of BEC and the only technique which has proven successful in generating quantum degenerate gases. However, confining a two component Fermi gas can lead to complications. For example, a magnetically trapped two component ^{6}Li gas is highly unstable due to exothermic inelastic collisions which makes the achievement of evaporative cooling and superfluidity in this system impossible [19].

Optical traps, in contrast to magnetic traps, are well suited for studies of interacting Fermi gases since they can confine stable two-state mixtures of fermionic atoms. Unfortunately, optical traps have previously been plagued by unexplained heating and trap loss rates that have limited their usefulness in studies of ultracold, dilute gases. In this dissertation we describe the construction of the first stable optical trap for neutral atoms and its application to studies of interactions in a two-component gas of ^{6}Li atoms [20]. We report on the first direct verification of the large interaction strength predicted to exist for ^{6}Li and describe initial experimental and theoretical investigations of evaporative cooling in this system [21]. Modest improvements to this system should enable cooling to temperatures below the Fermi temperature and possibly below the critical temperature for Cooper pair formation. This work lays the foundation for future investigations of quantum statistical effects in a dilute, ultracold gas of fermionic atoms which may include the observation of a superfluid transition.

1.1 Dilute, Degenerate Gases

There has recently been a great deal of scientific interest in the study of dilute, ultracold gases of identical neutral atoms due to the extraordinary quantum effects one observes in such systems. As a gas of identical, non-interacting particles are cooled, the wave-like nature of matter eventually becomes important and gives rise to fascinating phenomena. Consider a gas of identical particles at density n and temperature T. In quantum mechanics, particles of mass M and temperature T are described by a wavepacket with a characteristic wavelength given by $\lambda_{dB} = \sqrt{2\pi\hbar^2/Mk_BT}$, the thermal de Broglie wavelength. Thus, at high temperature and low density, the de Broglie wavelength is short, the wavepackets of adjacent particles do not overlap and a classical description of the gas as consisting of distinguishable particles is appropriate. However, as the gas is cooled to lower and lower temperatures, the de Broglie wavelength increases. Eventually, when the thermal de Broglie wavelength is comparable to the average interparticle spacing, the wavepackets of adjacent particles begin to overlap and the indistinguishability of the particles becomes important. This occurs when the *phase space* density defined as $n\lambda_{dB}^3$ is of order unity. In this quantum degenerate regime, a classical description of the gas is no longer possible.

The quantum degenerate gas is properly described by a many-body wavefunction that is either symmetric or antisymmetric under the exchange of particle labels depending on whether the gas constituents are bosons (particles with integer spin) or fermions (particles with half-integer spin) respectively. In terms of statistical mechanics the appropriate symmetry of the wavefunction imposes either Bose or Fermi statistics on the occupancy number of the quantum states of the system. In the case of fermions this yields the celebrated Pauli exclusion principle which states

that the occupancy number of a quantum state must be zero or one for a gas of fermions. For bosons, the occupancy number has no restriction whatsoever.

The macroscopic behavior exhibited by degenerate Bose and Fermi gases can be striking. For example, quantum statistical mechanics predicts that as the temperature of a non-interacting gas of bosons is cooled below a critical temperature which satisfies $n\lambda_{dB}^3 = 2.612$, a macroscopic number of particles will suddenly condense into the ground state of the system. This quantum phase transition is known as Bose-Einstein condensation. The existence of a coherent macroscopic number of particles occupying the same quantum state gives rise to remarkable phenomena such as superfluidity in liquid ^{4}He. For an ideal Fermi gas, a corresponding phase transition does not exist. However, if a weak attractive interaction between the fermions is present a superfluid phase transition is possible due to the formation and condensation of Cooper pairs as was first realized by Bardeen, Cooper and Schrieffer (BCS) in 1952. Cooper pair formation of electrons in metals is believed to be the microscopic explanation of the superconducting properties of metals first observed in 1911. BCS theory also provides the explanation of the superfluid properties of liquid ^{3}He.

The majority of low temperature, many-body physics research is focused on studying the extraordinary properties of matter in the quantum degenerate regime. In order to satisfy the condition for degeneracy, $n\lambda_{dB}^3 > 1$, the de Broglie wavelength must exceed the average interparticle spacing. For denser matter, this condition is satisfied at a higher temperature. Thus, most investigations of quantum degenerate matter have concentrated on studying dense systems such as liquid ^{4}He, liquid ^{3}He or the electron gas in metals. However, the strong interactions present in these systems can somewhat obscure the quantum effects and complicates the analysis

of the system. Alternatively, one could study a dilute gas of particles in which the interactions are weak due to the dilute nature of the gas. However, in order to satisfy the condition for degeneracy in a dilute gas where n is small, the dilute gas must be cooled to extremely low temperatures so that $n\lambda_{dB}^3 > 1$.

Over the past several decades, a number of techniques have been developed which use electromagnetic fields to confine dilute atomic vapors and cool them to extremely low temperatures. These techniques include the laser cooling and trapping techniques for which the Nobel prize was awarded in 1997 and magnetic trapping and evaporative cooling techniques developed to confine and cool atomic hydrogen. These techniques have proven successful in achieving BEC in a dilute vapor of alkali atoms

In these experiments, alkali atoms are pre-cooled in a magneto-optical trap (MOT) which combines laser and magnetic fields to confine and cool the atoms. The MOT yields atoms at temperatures between $10 - 100$ μK and spatial densities $\sim 10^{11}\,\mathrm{atoms/cm}^3$ with a typical phase space density $\sim 10^{-6}$. The alkali atoms are then transferred to a magnetic trap which confines alkali atoms through an interaction with the permanent magnetic dipole moment of the atom (alkali atoms have a sizeable magnetic dipole moment due to the presence of an unpaired valance electron). To increase the phase space density by 10^6 as required for degeneracy, the atoms are evaporatively cooled in the magnetic trap. Evaporative cooling consists of the selective removal of the highest energy atoms from the trap. The atoms that remain rethermalize via elastic collisions to a lower temperature. The resulting degenerate gas typically consists of atoms cooled to between $0.1 - 1\mu$K at densities $\sim 10^{13}\,\mathrm{atoms/cm}^3$.

By virtue of the low densities and energies present in a dilute, degenerate gas of

neutral atoms, a simple but rigorous description of the interatomic interactions is possible. First of all, the vapors considered are in the dilute limit $nr_0^3 << 1$ where r_0 is the range of the interatomic potential. Thus, the average interparticle spacing is much greater than the range of the interatomic potential and the interaction between particles is weak. In this limit, three-body collisions are rare and only two-body collisions need to be considered. The low energies present in the gas yield a second small parameter $r_0/\lambda_{dB} << 1$. This condition implies that if two atoms collide, their relative angular momentum $l = 0$. Thus, we need only consider two-body, s-wave ($l = 0$) collisions. The situation is simplified further by the fact that in the low energy limit, the two-body s-wave collision cross section is specified by a single parameter a known as the scattering length. In 1^{st} order perturbation theory, one can model the interaction as an effective contact potential $\mathrm{V}(\boldsymbol{r} - \boldsymbol{r}') = \mathrm{U}_0\delta(\boldsymbol{r} - \boldsymbol{r}')$ where $\boldsymbol{r}$ and $\boldsymbol{r}'$ specify the location of the two atoms. As shown in Chapter 2, this potential gives the exact low-energy scattering amplitude if $\mathrm{U}_0 \equiv 4\pi\hbar^2 a/m$, where m is the mass of the atom. Note that for attractive interactions $a < 0$ whereas for repulsive interactions $a > 0$.

The attainment of quantum degeneracy in dilute gases has captured a great deal of attention from the scientific community for a number of reasons. Dilute gases have properties markedly different from their high density counterparts. The atoms in the vapor exhibit macroscopic quantum features which are easily observed and manipulated in the laboratory. Since the dilute gases are weakly interacting, the coherence properties of the dilute vapors are much more prominent. The density, temperature and interaction strength of the atoms can be independently adjusted permitting systematic investigation over a wide range of physical parameters. In addition, since the interactions are weak and well understood, these systems are well

suited to comparison with theoretical investigations. A number of optical techniques exist for probing the spatial and momentum distributions of dilute, degenerate gases. There also exist a wide variety of methods for perturbing the gas in order to study collective effects.

Following the achievement of BEC a flurry of theoretical and experimental investigations into the properties of condensates has occurred. Studies of the frequency and dissipation of collective oscillations of the gas in the zero-temperature-limit permitted the verification of predictions made by Nikolai Bogoliubov 50 years earlier concerning the excitation frequencies of a dilute, weakly interacting Bose condensate [22–24]. Conversely, for finite temperatures, disagreement between theory and experiment has led theorists to reexamine their understanding of this simple quantum system [25].

The first-order coherence of the condensate was verified in a striking experiment in which two condensates were allowed to overlap [26]. The resulting density distribution exhibited fringes expected for the interference between two coherent matter waves. By measuring the mean-field energy, the second-order coherence of the condensate has also been observed [27–29]. In addition, the third-order coherence of the condensate has been determined by a measurement of three-body recombination rates [30]. All of these experiments are consistent with the assumption that a Bose condensate is coherent to first and higher order.

Resonant scattering features known as Feshbach resonances allow the interaction strength to be widely tuned with a bias magnetic field which may enable the systematic study of properties of the condensate for different interaction strengths [31,32]. Recently, the superfluid properties of the condensate have been confirmed in experiments which study vortex formation [33] and the existence of a critical velocity [34].

As an enabling technology, the achievement of BEC promises to revolutionize the field of matter wave optics. Matter wave amplification has been observed [35] and nonlinear matter wave effects such as four-wave mixing [36] and soliton formation has been demonstrated [37]. By providing an output coupler for the trapped condensate, a propagating coherent matter wave or "atom laser" has been constructed [4–6]. The construction of practical, high power, continuous wave atom lasers is being vigorously pursued.

The remarkable success with which dilute, degenerate Bose gases have been generated and studied has created an interest in the study of dilute, degenerate Fermi gases. Initial theoretical investigations focused on the thermodynamic properties of a trapped, non-interacting gas of fermions [7, 8] and later were extended to include interactions [11]. In addition to exhibiting familiar properties of a degenerate Fermi gas such as the existence of a filled "Fermi sea" or the linear dependence of the heat capacity on the temperature, novel shell structure features arising from the trapping potential might also be observable [8, 11]. The light scattering properties of a degenerate Fermi gas have also been investigated [10, 13, 14]. These authors find that the presence of a degenerate Fermi gas is expected to inhibit spontaneous emission since the filled "Fermi sea" reduces the available recoil momentum phase space. Collective oscillations excited in the degenerate Fermi gas have also been theoretically explored and are expected to give a rich structure [11, 12, 38].

The exciting possibility of observing a BCS superfluid transition in a dilute Fermi gas has recently been explored [17–19, 39–42]. This phase transition requires an attractive interaction in order to occur. In addition, the interaction strength needs to be large in order for the transition temperature to be experimentally attainable. Fortunately, the fermionic isotope of lithium, ^{6}Li, is predicted to exhibit a very

large and negative scattering length (*i.e.*, a large and attractive interaction). In the case of ultracold ^{6}Li, the transition temperature for Cooper pair formation is expected to be comparable to conditions attained in BEC experiments. In fact, as Ref. [18] points out, the critical temperature for Cooper pair formation in an ultracold ^{6}Li gas is the highest of all known BCS superfluids measured relative to the Fermi temperature. Since the interaction strength is large, density fluctuations may have a sizeable effect on the superfluid transition temperature. Systematic investigations of the effect of density fluctuations on the critical temperature may be of relevance to similar effects believed to occur in High-T_C superconductors and liquid ^{3}He [18]. Techniques for observing the superfluid transition have been examined. These include changes in the light scattering properties of the gas [43] or changes in the collective oscillation spectrum [11, 12].

Despite the successful use of evaporative cooling to produce Bose-Einstein condensates, the attainment of a degenerate Fermi gas by similar means has proven challenging. This is evidenced by the fact that, while over twenty groups worldwide have observed BEC in five different atomic species, only recently has the first degenerate gas of fermionic atoms been observed [44] by a group at the University of Colorado in an ultracold gas of ^{40}K. Unfortunately, the degenerate ^{40}K gas produced offers only a fixed repulsive interaction. Thus, a number of phenomena described above, most notably a superfluid phase transition, cannot be observed in this system. It remains of current interest to obtain a degenerate interacting Fermi gas in which the interaction strength is widely tunable and, in particular, offers a large and attractive interatomic interaction for the observation of superfluidity. In this respect, an optically trapped mixture of ^{6}Li provides a particularly attractive system for study.

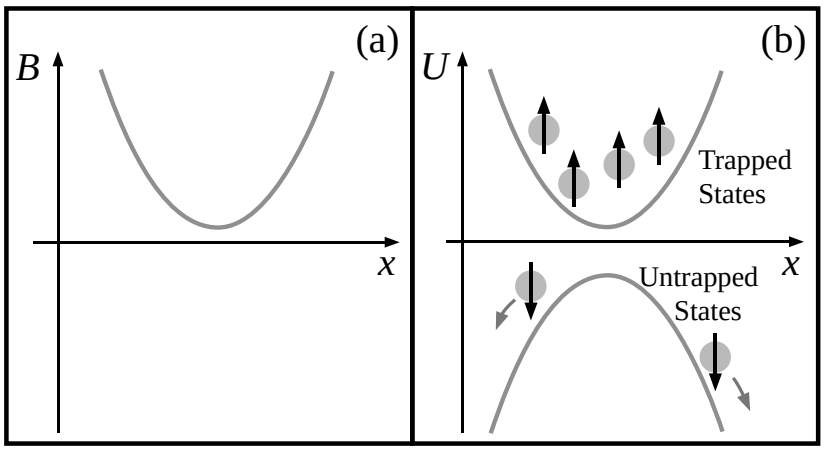

Figure 1.1: Magnetic trap for neutral atoms. (a) A magnetic field with a local minimum in $|\mathbf{B}|$ can be used (b) to confine atoms with a permanent magnetic dipole moment. The arrows represent the magnetic dipole moment of the atom. Only those atoms which have a dipole moment anti-parallel to the local B-field are confined.

1.2 The Quest for a Degenerate Fermi Gas

1.2.1 Interactions and Evaporative Cooling in a Magnetically Confined Fermi Gas

Evaporative cooling from a magnetic trap remains the only successful means by which degenerate atomic vapors have been produced. In BEC experiments, alkali atoms are loaded into a magnetic trap in which they are evaporatively cooled. The magnetic trap consists of a magnetic field $\mathbf{B}$ with a nonzero local minimum in $|\mathbf{B}|$. This is shown in Figure 1.1(a) for one-dimension. Alkali atoms are confined in this magnetic bowl since they have a sizeable permanent magnetic dipole moment $\boldsymbol{\mu}$ primarily arising from the single unpaired valance electron. See Figure 1.1(b). Since the interaction potential is given by $-\boldsymbol{\mu}\cdot\mathbf{B}$, atoms for which $\boldsymbol{\mu}$ is anti-parallel to the local field $\mathbf{B}$ are confined. However, atoms for which $\boldsymbol{\mu}$ is parallel to the local field $\mathbf{B}$ are expelled from the trap. Thus, magnetic traps are susceptible to spin

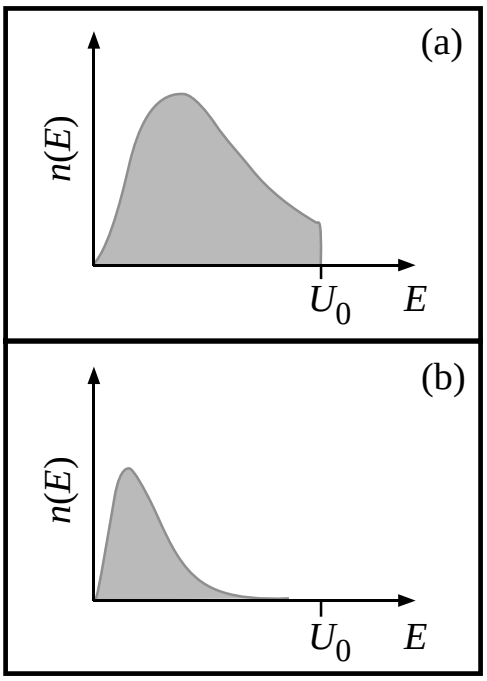

Figure 1.2: Evaporative cooling of trapped atoms. (a) Evaporative cooling consists of the selective removal of the high energy atoms yielding a truncated thermal energy distribution $n(E)$. (b) Following rethermalization via elastic collisions, the energy distribution is characterized by a thermal distribution with a lower temperature.

flip transitions to untrapped states. Such transitions can occur during a two-body collision. However, these transitions can be strongly suppressed in a Bose gas by confining only those atoms in which both the electron and nuclear spins are parallel to the local **B** field [1].

To reach degeneracy, the atoms are evaporatively cooled in the magnetic trap. Evaporative cooling consists of the selective removal of the highest energy atoms from the trap. This yields a thermal distribution $n(E)$ truncated at the well depth U_0 as shown in Figure 1.2(a). Here $n(E)\,dE$ gives the number of atoms between

[1]The suppression arises from the fact that the dominant interaction which causes spin flip processes conserves angular momentum and the state is chosen such that no other two-particle spin states have the same angular momentum. Thus, conservation of angular momentum precludes transitions to different two-particle states.

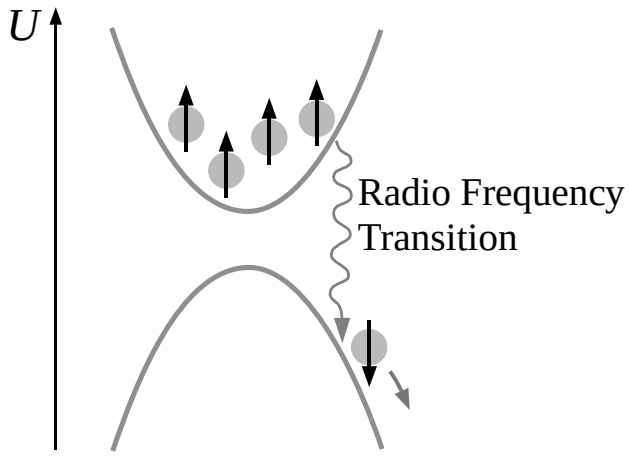

Figure 1.3: Forced evaporative cooling from a magnetic trap. A radio frequency transition can be excited to selectively transfer high energy atoms into an untrapped state which is expelled from the trap.

an energy E and $E + dE$. The atoms that remain in the trap rethermalize to a lower temperature via elastic collisions (see Figure 1.2(b)). The selective removal of high energy atoms is accomplished by inducing a radio frequency (rf) transition from a confined state to an expelled state for high energy atoms which reach the outskirts of the magnetic bowl. This process is shown schematically in Figure 1.3. Note that the process of rethermalization is critical to the the success of evaporative cooling. Without rethermalization the selective removal of high energy atoms would merely create a truncated thermal distribution. Elastic collisions permit this non-equilibrium truncated distribution to rethermalize to a lower temperature. For suitable starting conditions, a bosonic gas of atoms can be cooled into the degenerate regime by this method.

Evaporative cooling of an ultracold Fermi vapor becomes somewhat more complicated. This is due to the fact that, for a gas of fermions in which all of the atoms are in the same internal state, elastic collisions between the particles are suppressed

at low temperature. Thus, the rethermalization process cannot proceed. If all of the fermions are in the same internal spin state, the total *spin* wave function for a pair of colliding atoms is *symmetric* under exchange of particle labels. In order for the total wave function of the colliding atoms to be *antisymmetric*, the two-particle *spatial* wave function must be *antisymmetric*. Thus, the fermions must collide with a relative orbital angular momentum $l = 1, 3, 5, \ldots$. However, at the low temperatures being considered $r_0/\lambda_{dB} << 1$ and only $l = 0$ (s-wave) collisions can occur. In other words, two fermions in the same spin state cannot occupy the same region of space (*i.e.* within a volume λ_{dB}^3) without disobeying the Pauli exclusion principle. However, at the ultracold temperatures considered $\lambda_{dB} >> r_0$. Therefore, the atoms will not interact. This situation is depicted in Figure 1.4(a). Thus, elastic collisions are forbidden by the Pauli exclusion principle for a gas of spin-polarized, ultracold fermions. This means that an ultracold, gas of spin-polarized fermions is essentially non-interacting and the rethermalizing collisions required for evaporative cooling will not proceed.

Several solutions to the problem of evaporative cooling of fermions have been explored. One solution is to simultaneously confine a mixture of bosonic and fermionic atoms in the magnetic trap. The evaporative cooling of the bosonic atoms proceeds as usual. Since the fermionic and bosonic atoms are not identical particles, the two-particle wave function describing the collision does not need to be symmetrized. In this case, two-body s-wave collisions involving a bosonic atom and a fermionic atom are allowed. Thus, the fermionic atoms will come into thermal equilibrium with the evaporatively cooled bosonic atoms. While this technique is a viable method for cooling a Fermi gas into the degenerate regime, the resulting degenerate Fermi gas is non-interacting. Thus, while the properties of a non-interacting, degenerate Fermi

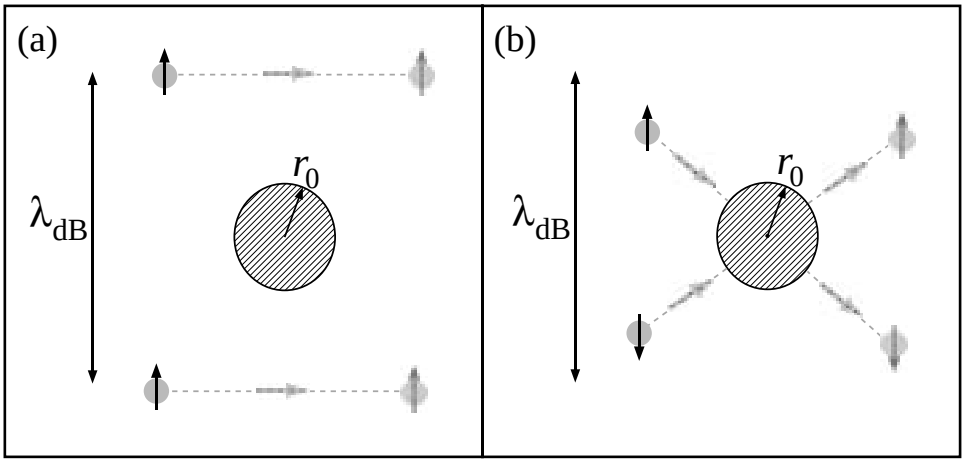

Figure 1.4: Ultracold collisions between fermions. (a) Two fermions in the same spin state are forbidden by the exclusion principle to occupy the same spatial region within a volume $\sim \lambda_{dB}^3$. For ultracold temperatures λ_{dB} greatly exceeds r_0 the range of the potential and the fermions do not interact. (b) Two fermions in different spin states can occupy the same region of space. Therefore, fermions in different spin state can interact with one another even when $\lambda_{dB} >> r_0$.

gas may be explored, the study of an interacting Fermi gas and the formation of Cooper pairs is not possible in this system.

To attain interactions in an ultracold Fermi gas one must confine, at the very least, a two-state mixture of fermionic atoms. For two fermions in different spin states, the exclusion principle allows for the possibility that the atoms occupy the same region of space even within a volume λ_{dB}^3. Therefore, the fermions can interact as depicted in Figure 1.4(b).

If two colliding fermions are in different internal spin states, an *antisymmetric* two-particle *spin* wave function is possible. In this case, a *symmetric* two-particle *spatial* wave function is required implying that s-wave collisions are allowed. Thus, elastic collisions are permitted in an ultracold gas containing fermions in more than one spin state. Since the total spin of an alkali atom arises from the coupling of the unpaired valance electron to the nuclear spin there are, in general, a number of

internal spin states which the atom can occupy.

For a magnetically confined two-state mixture, it is necessary to trap two states which have magnetic dipole moments with the same sign. However, as is the case with magnetically confined Bose gases, spin-flip collisions can occur in which one or both atoms make a transition to an untrapped state. The presence of two atomic species makes matters worse in that it is much more difficult to find mixtures for which spin-flip collisions are suppressed. For ^{40}K, certain two-state mixtures exist that can be magnetically trapped which are stable against the dominant spin-flip process. Evaporative cooling of one of these meta-stable two-state mixtures led to the recent success in attaining a dilute, degenerate gas of fermions. Unfortunately, the mixtures of ^{40}K that are stable in the magnetic trap only exhibit a repulsive interatomic interaction which cannot be adjusted. In the case of ^{6}Li, there are a number of two-state mixtures which provide widely tunable interaction strengths including large and attractive interactions suitable for the observation of Cooper pairing. Regrettably, all of the two-state ^{6}Li mixtures that can be confined in a magnetic trap suffer from extremely large spin-exchange collision rates. In Chapter 2, we calculate the spin-flip collision rate for a magnetically confined two-state mixture of ^{6}Li and find that it is prohibitively large.

1.2.2 Optical Dipole Force Traps to the Rescue

An alternative approach to magnetic confinement is to confine atoms in an optical dipole force trap. A simple implementation of an optical dipole force trap consists of a single Gaussian laser beam focused to a tight spot. If the laser beam is tuned below the atomic resonance frequency, atoms are attracted to the region of highest intensity. The attractive potential arises from an induced dipole force. The oscillat-

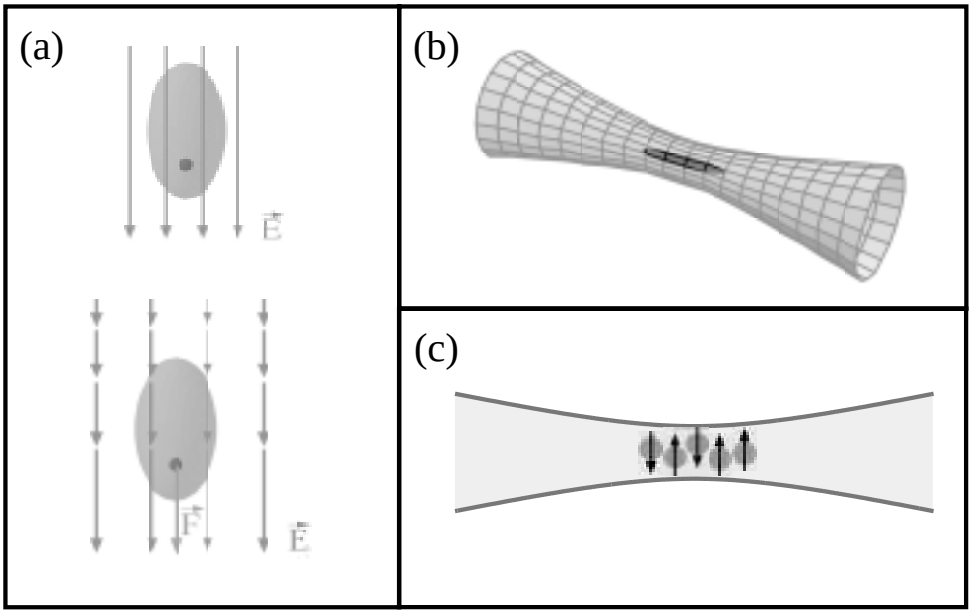

Figure 1.5: Optical Dipole Force Trap. (a) A neutral atom in an electic field gradient experiences a net force in the direction of increasing field strength. (b) A focussed Gaussian laser beam can be used to confine atoms which are attracted to the region of highest field strength. (c) The optical trap confines ground state atoms in any spin state.

ing electric field of the laser induces an electric dipole moment in the atom. Due to the induced dipole moment, the atom experiences a force in the direction of increasing field strength (see Figure 1.5(a)). Thus, the atoms are attracted to the region of highest intensity which occurs at the laser beam focus as shown in Figure 1.5(b). In order to suppress heating of the atoms from optical excitation, the trap laser beam is tuned far from resonance with the atomic transition frequency.

In Chapter 3, we show that the potential experienced by the atoms is independent of the spin state of the atom if the laser is linearly polarized and tuned far from resonance. Thus, all internal spin states experience the same potential and can be confined at the focus of the laser as depicted in Figure 1.5(c). The fact that the optical dipole force trap provides a state independent potential has important ramifications for studies of interactions in ultracold Fermi gases. Since any internal spin state can be trapped, a two-component interacting Fermi gas can be confined in which the two states are chosen to be the lowest energy states. In this case, exothermic inelastic collisions are precluded since there are no lower lying energy states. The ability to confine a stable two-state mixture of fermionic atoms makes optical traps well suited for the evaporative cooling and study of an interacting Fermi gas.

Forced evaporative cooling in an optical trap can be achieved by adiabatically reducing the trap laser beam power which reduces the trap well depth. This allows the more energetic atoms to escape the confining potential as shown in Figure 1.6.

Unfortunately, optical traps have historically suffered from unexplained heating and trap loss rates which have compromised the usefulness of optical traps for studies of ultracold gases. In this dissertation we describe the construction of the first stable optical trap. Using an ultrastable CO_2 laser to confine atoms in an

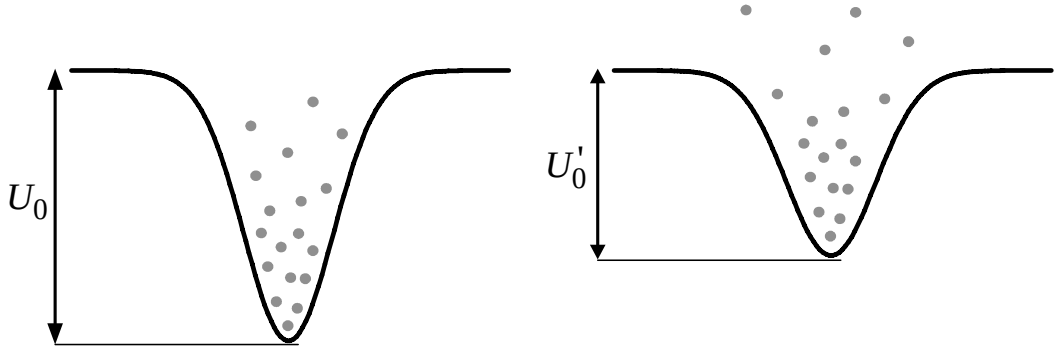

Figure 1.6: Evaporative cooling of atoms in an optical trap. The laser power can be reduced to lower the well depth allowing the more energetic atoms to leave the trap. The atoms which remain in the trap rethermalize via elastic collisions to a new lower temperature.

ultrahigh vacuum environment, we minimized all known sources of residual heating. By using a CO_2 laser which produces radiation at an infrared wavelength of 10.6 μm, we have virtually eliminated heating due to optical scatter. In addition, our group has identified fluctuations in the laser intensity and position as a possible source of heating which has limited the lifetime of previous optical traps [45, 46]. A properly designed CO_2 laser can be made extremely quiet in both intensity and position noise. By employing an ultrastable CO_2 laser, we have obtained trap lifetimes of 370 seconds, limited by the background gas pressure of $< 10^{-11}$ Torr with residual heating rates of < 50 nanoKelvin/sec.

By constructing a stable optical trap, we have been able to perform the first experimental studies of interactions and evaporative cooling in a two-state mixture of lithium fermions. We confirm for the first time the existence of a large collision cross section predicted to exist for ultracold ^{6}Li collisions by measuring the evaporation rate of atoms from the optical trap. Evaporative cooling of ^{6}Li atoms from the optical trap increases the phase space density of the ^{6}Li gas by two orders of magnitude over that which is produced by the magneto-optical trap. This work lays

the foundation for future investigations of quantum statistical effects in a dilute, ultracold gas of fermionic atoms

1.2.3 Scales of Interest in a Degenerate Fermi Gas

At zero temperature, a non-interacting Fermi gas behaves very differently from a Bose gas. In contrast to the Bose gas only one fermion can occupy a given state. Thus, at zero temperature, an N-particle Fermi gas is in a state in which the particles occupy the N lowest quantum states of the system. The energy of the highest occupied state is known as the Fermi energy E_F. The Fermi energy is the natural scale of energy in a degenerate Fermi gas.

If we consider a spin-polarized gas of fermions (a gas in which all particles are in the same spin state) the Fermi energy satisfies

$$N = \int_0^{E_F} \mathcal{D}(\epsilon)\, d\epsilon, \tag{1.1}$$

where $\mathcal{D}(\epsilon)$ is the density of states for the confining potential. The dilute atomic vapors we will consider are usually confined in a harmonic oscillator potential. In general, the potential may be anisotropic with oscillation frequencies ω_x, ω_y and ω_z in which case $\mathcal{D}(\epsilon) = \epsilon^2/2\hbar^3\omega_x\omega_y\omega_z$. The Fermi energy for a harmonic potential is given using (1.1) by

$$E_F = \hbar\omega \left[6N\right]^{1/3}, \tag{1.2}$$

where $\omega \equiv \left[\omega_x\omega_y\omega_z\right]^{1/3}$. For a trap with $\omega = 2\pi \times 1$ kHz and containing 10^5 atoms, the Fermi temperature $T_F = E_F/k_B = 4\mu$K. For temperatures $T < T_F$ the gas is in the degenerate regime.

An estimate of the radius R_F of the spatial distribution at $T = 0$ is given by the classical turning point R_F for a particle of energy E_F in the harmonic potential. For an isotropic harmonic potential

$$R_F = \sqrt{\frac{2E_F}{M\omega^2}} = (48\,N)^{1/6}\sigma_{ho}, \tag{1.3}$$

where $\sigma_{ho} = \sqrt{\hbar/m\omega}$ is the natural length scale of a quantum harmonic oscillator, which is radius of a Bose gas at $T = 0$ since all of the atoms are in the ground state. The radius of the cloud is $\simeq 17\,\mu$m for ^{6}Li atoms confined in an isotropic harmonic oscillator potential with $\omega = 2\pi \times 1$kHz at $T = 0$. This corresponds to a density $n \sim N/R_F^3 = 2 \times 10^{13}\,\text{atoms/cm}^3$.

It is also useful to define the Fermi wave number k_F, which is the wave number for a particle with energy E_F. In terms of R_F, $k_F = \sqrt{2mE_F}/\hbar = (48N)^{1/3}/R_F$. Thus, k_F is the order of the reciprocal of the typical interparticle spacing. For the parameters described above $k_F \simeq 10^5$ cm^{-1}.

In contrast to an ideal Bose gas, a non-interacting Fermi gas does not exhibit a phase transition as the atoms are cooled below $T = T_F$. However, if an attractive interaction between the atoms exists, a superfluid transition will occur due to the formation of Cooper pairs below a critical temperature T_C. Loosely speaking, the transition can be thought of as a Bose condensation of Cooper pairs. The transition is described by the theory of Bardeen, Cooper, and Scrieffer (BCS) that was originally developed to explain superconductivity in metals. Recently, BCS theory has been applied to predict the transition temperature for a trapped ultracold gas

of fermionic atoms [17,39]. The transition temperature T_C is found to be

$$T_C \simeq 0.61\, T_F \exp\left[-\frac{\pi}{2\, k_F\, |a|}\right], \tag{1.4}$$

where a is the s-wave scattering length parameterizing the interaction between the fermions. Since the formation of Cooper pairs requires an effective attractive interaction, the sign of the scattering length must be negative. Also, note that T_C depends exponentially on the quantity $-1/k_F|a|$. Since k_F is nominally the reciprocal of the typical interparticle spacing, the quantity $k_F|a|$ is normally much less than one for a dilute gas since the scattering length a is usually on the order of the range of the molecular interaction. For this reason, it was previously concluded that the BCS transition temperature is experimentally unattainable in a dilute Fermi gas. However, following the prediction that ^{6}Li exhibits a very large and negative scattering length due to a resonant scattering process this conclusion has since been revised.

Collisions between two ultracold ^{6}Li atoms are predicted to exhibit a "zero energy resonance" at low energy. ^{6}Li atoms interact primarily via an electrostatic molecular potential. Depending on whether the valance electron from each atom are coupled into a spin singlet or a spin triplet state, the atoms approach one another along either a singlet or a triplet molecular potential. The ^{6}Li triplet molecular potential has an unbound virtual state near zero energy as shown in Figure 1.7. If the ^{6}Li triplet potential were slightly deeper, this state would become bound. The presence of this virtual state near zero energy causes a resonant behaviour in the low energy scattering properties of ^{6}Li. This resonant behaviour gives rise to a large and negative triplet scattering length predicted to be $a = -2160\, a_0$ ($a_0 = 1\,\text{bohr} = 0.529\ \mathring{\text{A}}$).

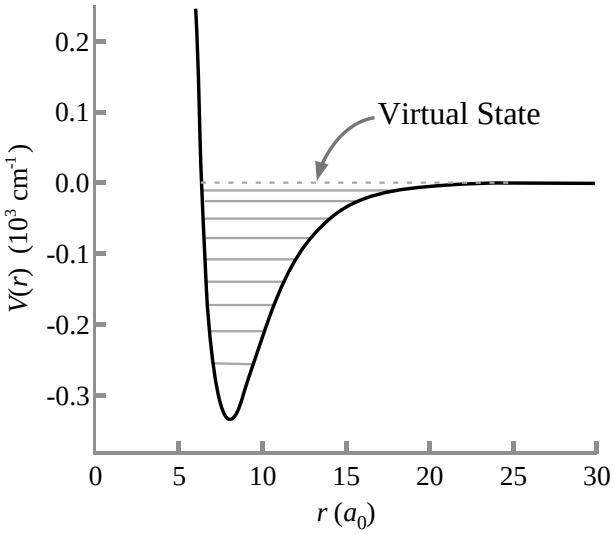

Figure 1.7: Zero energy resonance in the ^{6}Li-^{6}Li triplet molecular potential. The resonant behavior arises from the presence of an unbound virtual state at zero energy (dashed line).

Due to the existence of this large and negative triplet scattering length predicted to exist for ^{6}Li collisions, the superfluid phase transition temperature is expected to be experimentally attainable in dilute ^{6}Li gas. Consider a two-state mixture of ^{6}Li atoms which exhibits the triplet scattering length confined in an optical trap where the trap oscillation frequencies satisfy $\omega = (\omega_x \omega_y \omega_z)^{1/3} = 1$ kHz. If 10^5 atoms are in each state, we can use the parameters given above for the Fermi wave number and Fermi temperature. In this case $k_F|a| = 1.1$ and the critical temperature for the superfluid temperature T_C is found using (1.4) to be $T_C \simeq 0.6\,\mu$K. These parameters are comparable to the temperatures and densities achieved in BEC experiments and thus appear experimentally feasible.

1.3 Significance of Current Work

1.3.1 Stable Optical Trap for Neutral Atoms

Optical dipole force traps are useful for studies of ultracold atomic vapors since, in contrast to magnetic traps, they can provide a potential that is independent of the internal spin state of the atom. As discussed below, this feature makes optical traps particularly useful in a wide range of applications from studies of dilute quantum degenerate gases to precision measurements. In addition, optical potentials are extremely versatile and can be used to form novel trap designs such as lattice potentials. This dissertation describes the development of the first stable optical trap for neutral atoms in which the residual heating and loss rates are minimized. Previous optical traps have suffered from residual heating and loss rates that compromised the usefulness of these traps. While the ultrastable CO_2 laser trap described in this dissertation was developed for the purpose of confining and studying two-state mixtures of lithium fermions, the construction of a stable optical trap for neutral atoms is of broad interest for the wide range of applications described below.

That optical traps can confine atoms in arbitrary spin states adds a great deal of flexibility to the study of ultracold Bose gases with different collisional properties. Atoms in different spin states exhibit different elastic and inelastic collision properties. Optical traps provide the flexibility to choose states with the most appealing properties. For example, despite the importance of cesium as a frequency standard and as an optimal candidate for precision measurements, Bose Einstein condensation of cesium has eluded realization in a magnetic trap due to abnormally large inelastic spin-flip collision rates. These inelastic collisions can be avoided by

trapping the lowest energy state in an optical trap. As another example, the ability to trap atoms in an arbitrary uniform magnetic field has allowed for the exploration of Feshbach resonances in cold atomic collisions [31, 32]. These resonances permit wide tunability of the interatomic interaction strength enabling systematic studies of collective phenomena of the gas. Recently, mixtures of Bose condensates in different internal states have been confined and studied using an optical trap [47]. Such systems are of interest since the order parameter of the condensate is no longer a scalar but a vector quantity giving rise to rich phenomena [48, 49].

The magnetic state independence of the potential also makes optical traps compatible with certain optical cooling techniques [50, 51]. These techniques rely on making high-resolution velocity-selective two-photon Raman transitions between the internal ground states of the atom and are rendered useless if the energy splitting between the ground states is spatially dependent. Thus, these optical cooling techniques cannot be applied to magnetically confined atoms for which the energy splitting between different spin states has a strong spatial dependence. The application of these techniques may potentialy produce degenerate atomic vapors by all optical means. However, the success of previous attempts have been comprimised by residual heating rates in the optical trap (see for example Ref. [52]. Cooling bosonic atoms to degeneracy by all-optical means remains a long sought after goal. All-optical cooling to degeneracy may permit the construction of continuous wave atom lasers and the condensation of bosonic cesium.

Since the internal ground states of the trapped atoms all experience a nearly identical potential, long internal state coherence lifetimes should be obtainable in such traps. Long coherence lifetimes are important for applications such as atomic clock standards and quantum computing. Precision measurements such as searches

for the electric dipole moment of an atom, beta-decay asymmetries and atomic parity violation greatly benefit from long coherence times.

The versatility of the optical dipole force has also generated a great deal of interest in the variety of ways matter can be manipulated. By steering the focused laser beam, atoms can be moved around inside the vacuum system. This will facilitate studies of ultracold atoms inside microwave and optical cavities or near surfaces. In addition to the simple focused beam trap described above, a wide range of novel trap designs can be conceived. By using multiple trapping beams, interference patterns can be formed. For red detuned traps, atoms are confined to the maxima in the interference patterns. Using this technique, one-, two- and three-dimensional lattice potentials can be constructed. This enables the study of lattice potential effects in a controlled environment. By using blue detuned sheets of light from which atoms are repelled, box potentials can be constructed that confine atoms in a virtually interaction free environment. In addition, dipole forces can be used to study ultracold gases in a two-dimensional system. Finally, hybrid traps that combine both magnetic and optical dipole forces have been instrumental in studying the properties of Bose condensed gases. Collective oscillations have been excited using moving, repulsive dipole forces [53]. The critical velocity in a superfluid was found by moving a repulsive optical potential through a condensate at various speeds [34]. Recently, the first observations of both a superfluid vortex [54] and a soliton wave [37] in a dilute condensate were made possible by using an optical dipole potential to imprint a phase pattern on the condensate wavefunction.

As discussed earlier, optical traps are particularly well suited to studies of interacting Fermi gases since they can confine stable two-state mixtures of fermions—a prerequisite to attaining interactions in an ultracold Fermi gas. In ^{6}Li this is of

critical importance since the magnetically trapable two-state mixtures of ^{6}Li are inherently unstable [39, 55]. Optical traps, on the other hand, can confine stable two-state mixtures of ^{6}Li which exhibit a large and tunable interaction strength. Optical traps may also greatly benefit the study of degenerate ^{40}K gases. Although a meta-stable two-state mixture of ^{40}K can be confined in a magnetic trap [44], this mixtures does not have suitable collisional properties for observing certain collective effects such as superfluidity [56]. However, an optically trapped two-state mixture of ^{40}K is expected to exhibit a Feshbach resonance which would allow the interatomic interaction strength to be adjusted by an external magnetic field [57]. Thus, an optically trapped two-state mixture of fermionic atoms appears at this point to be the only system in which a superfluid transition in a dilute Fermi gas can be observed.

1.3.2 Optically Trapped, Ultracold Fermi Vapor

In addition to investigations of condensed matter physics in a dilute Fermi gas, an optically trapped, ultracold Fermi vapor may also be useful in making precision measurements of atomic properties. While the absence of interactions in a spin-polarized Fermi gas is a detriment to achieving evaporative cooling or investigating interactions in a dilute Fermi gas, the absence of interactions is a blessing for many precision measurement applications. In a recent article [58] reviewing the possibility of using an optically trapped gas of atoms in a search for the electric dipole moment of an atom, the authors note that

> Spin-polarized fermionic atoms held in a conservative trap would give the closest approximation yet to an interaction-free sample of atoms.

Collisions between atoms can reduce the accuracy of precision measurements by causing collision induced frequency shifts, inelastic collisions and limiting the coherence lifetime of the sample.

1.3.3 Evaporative Cooling of Fermionic Atoms in an Optical Trap

In this dissertation, we present both theoretical and experimental studies of evaporative cooling of lithium fermions from an optical trap. One primary result of these invesitgations is the confirmation that ^{6}Li exhibits a very large scattering length arising from the zero energy resonance in the triplet scattering potential. The existence of this large scattering length has been the basis for the prediction that a dilute gas of ^{6}Li should undergo a superfluid phase transition at an experimentally attainable critical temperature. The prediction that ^{6}Li should exhibit this large elastic scattering cross section relies on a combination of *ab initio* calculations and experimental molecular spectroscopy to determine the shape of the ^{6}Li-^{6}Li molecular potentials. From these constructed potentials, the scattering properties of ultracold ^{6}Li atoms are calculated. The existence of a zero energy resonance in the triplet molecular potential is extremely sensitive to the dissociation energy of the triplet potential. In this dissertation we describe a measurement of the evaporation of ^{6}Li atoms from a time-independent optical potential. The evaporation rate is directly sensitive to the elastic collision cross section. By measuring the rate of evaporation of ^{6}Li atoms from the optical trap we confirm that ^{6}Li atoms exhibit a large collision cross section in agreement with theoretical predictions.

For the experimental studies of interactions and evaporative cooling described in this dissertation, we use a meta-stable two-state mixture of ^{6}Li atoms confined

in an optical trap. Most two-state mixtures of ^{6}Li only exhibit a large and negative scattering length in a magnetic field $\geq$ 1 kG. In contrast, the mixture used in the experiments described here, exhibits a scattering length equal to 2/3 that of the triplet scattering length at zero field. Thus, this mixture provides a large and negative scattering length at low field. The mixture, which has never been discussed before in the literature, exhibits only a small inelastic decay rate when a small bias field is applied and exhibits a widely tunable interaction strength when the magnetic bias field is adjusted between 0 and 10 Gauss. Also, we demonstrate that interactions can be turned on and off in this system by suddenly transferring atoms from this two-state mixture to a non-interacting two-state mixture. This mixture may be useful for studies of a strongly interacting Fermi gas in a low field and for investigations of many-body quantum dynamics in which the interactions can be turned on and off rapidly.

A primary concern is the study of evaporative cooling as a means of obtaining a dilute, degenerate gas of ^{6}Li atoms in an optical trap. This dissertation includes theoretical and experimental investigations of forced evaporative cooling of fermions in an optical trap. Forced evaporative cooling is accomplished by selectively removing the high energy atoms from the optical trap which in turn is achieved by adiabatically lowering the optical potential well depth. The high energy atoms become unbound from the optical potential as the well depth is lowered and the atoms that remain rethermalize to a lower temperature. While the primary interest here is the study of evaporative cooling of fermions from an optical potential, the majority of the results can be applied directly to the evaporative cooling of bosons from an optical potential. The evaporative cooling of bosonic cesium atoms from an optical potential is of current interest since, as described above, Bose-Einstein condensation

of cesium cannot be achieved by evaporative cooling in a magnetic trap due to the presence of anomalously large spin-flip collisions.

1.4 Organization

The organization of this dissertation follows the progression of logic that has led us to the study of interacting ^{6}Li fermions in a stable optical trap. We begin the main body of the dissertation in Chapter 2 with a theoretical discussion of ultracold collisions in a ^{6}Li gas. This chapter is intended to relate the exceptional promise ^{6}Li presents as a candidate for investigations of an interacting Fermi gas based on its extraordinary collisional properties. Ultracold ^{6}Li interactions exhibit two resonant scattering processes, a zero energy resonance and a Feshbach resonance, which give rise to an interatomic interaction that is widely tunable. The origin and calculation of these scattering properties are presented. Chapter 2 also motivates the need for confining ^{6}Li fermions in an optical trap in that we show that large exothermic inelastic collision rates are expected for a magnetically trapped two-component ^{6}Li gas. These large inelastic rates make the magnetic storage of ^{6}Li unfeasible. However, they can be avoided in an optical trap by trapping the lowest energy states. The chapter concludes with a suggestion of two stable mixtures, that exhibit promising collisional properties, that can be confined in an optical trap.

The results of Chapter 2 lead naturally to a discussion of the operation of optical traps in Chapter 3. In reviewing the experimental literature, however, we find that unexplained heating and trap loss rates have limited the usefulness of optical traps. We present a description of two possible sources of heating due to fluctuations in the intensity and position of the trap laser beam and suggest that an optical trap based on an ultrastable CO_2 laser provides the best option for optical storage of neutral

atoms with minimal heating. Chapter 4 presents the experimental realization of the first stable trap for neutral atoms. A two-state mixture of ^{6}Li atoms is confined at the focus of an ultrastable CO_2 laser for hundreds of seconds. This chapter describes the experimental apparatus required for obtaining this result which includes an ultrahigh vacuum system and a ^{6}Li magneto-optical trap (MOT), which provides a cold source of atoms to load the CO_2 laser trap. In Chapter 5 we examine the loading dynamics of a CO_2 laser trap loaded from a MOT and report on an increase in loading efficiency over our initial experiments.

The next section of the dissertation turns its attention toward the study of interactions and evaporative cooling of ^{6}Li in an optical trap. In Chapter 6, we present the theory of evaporative cooling from an optical trap that is based on the evolution of a kinetic Boltzmann equation. Effects of Fermi statistics and the energy dependence of the ^{6}Li scattering cross section are included in this model. We examine theoretically both evaporation from a time-independent trap and forced evaporative cooling in which the well depth of the optical trap is adiabatically reduced. Based on this model, we find that forced evaporative cooling of ^{6}Li from an optical trap is a viable means of attaining degeneracy in a Fermi gas. Chapter 7 contains the corresponding experimental studies of interactions and evaporative cooling in the optically trapped ^{6}Li gas. We begin by describing our observation of evaporation of ^{6}Li from a well of fixed depth. Based on a measurement of the rate of evaporation, a comparison with the theory developed in Chapter 6 allows us to extract the collision cross section for ^{6}Li. We find that ^{6}Li exhibits an exceptionally large elastic collision cross section in agreement with the predictions of Chapter 2. We then describe our experimental studies of forced evaporative cooling. By adiabatically lowering the well depth over a period of 40 seconds we cool ^{6}Li atoms to 2.4 μK

which is approximately five times the Fermi temperature for the gas.

In Chapter 8 we summarize the major results and contributions of this dissertation. Finally, we suggest modest improvements to the experiment which should yield a gas of ^{6}Li atoms with a temperature below the Fermi temperature.

Chapter 2

Ultracold ^{6}Li Interactions

By virtue of the low densities and low energies present in an ultracold, dilute gas of neutral atoms, a simple but rigorous description of the atomic interactions is possible. In an ultracold gas, the de Broglie wavelength of the atoms is enormous in comparison to the range of the interatomic potentials. This, in combination with the low density, allows us to model the interactions as binary collisions with an effective contact potential $\mathrm{V}(\boldsymbol{r}-\boldsymbol{r}') = \mathrm{U}_0\delta(\boldsymbol{r}-\boldsymbol{r}')$ when interactions are treated using first order perturbation theory. As shown below, this potential gives the exact low-energy scattering amplitude if $\mathrm{U}_0 = 4\pi\hbar^2 a/m$ where a is a parameter known as the s-wave scattering length. Thus, the s-wave scattering length completely characterizes the interactions in an ultracold, dilute gas of neutral atoms. Precise knowledge of the s-wave scattering length is obviously of great importance since it determines the behavior of the many-body effects one hopes to study in an ultracold gas.

The primary purpose of this chapter is to relate the exceptional promise ^{6}Li presents as a candidate for investigations of an interacting Fermi gas based on its extraordinary collisional properties. In this chapter we calculate the scattering lengths for ultracold ^{6}Li-^{6}Li collisions for different two-state mixtures. The calculation of these scattering lengths is based on ^{6}Li-^{6}Li molecular interaction potentials which are constructed from a combination of *ab initio* calculations and experimen-

tal Li_2 molecular spectroscopy. Based on these calculations, certain two-state ^{6}Li mixtures are expected to exhibit an interaction strength that is widely tunable in an applied external magnetic field. For certain two-state combinations and fields resonant features are found where the scattering length greatly exceeds the range of the molecular potential. In Chapters 6 and 7, we will describe experiments in which we directly observe an extremely large collision cross section in an ultracold ^{6}Li gas in agreement with these predictions.

Of particular interest is the fact that *very large* and *negative* scattering lengths can be obtained in an ultracold ^{6}Li gas which correspond to large and attractive interatomic interactions. Because of these large and attractive interactions, it has been predicted that a quantum degenerate gas of ^{6}Li should exhibit a number of spectacular many-body quantum phenomena. The most exciting of these is the prediction that below a critical temperature T_C, ^{6}Li should become a superfluid due to the formation of Cooper pairs according to the theory of Bardeen,Cooper and Schreiffer (BCS theory). The formation of Cooper pairs requires an effective attractive interaction. Also, the critical temperature T_C for the formation of Cooper pairs depends exponentially on the magnitude of the scattering length a, $T_C \simeq 0.61\, T_F\, e^{-\pi/2k_F|a|}$ where T_F is the Fermi temperature and k_F is Fermi wavenumber. Thus, a large and negative scattering length is essential in order for T_C to be experimentally attainable.

A secondary purpose of this chapter is to calculate the inelastic collision rates expected for magnetically trappable two-state ^{6}Li mixtures. This is of central concern to the feasibility of studying of an interacting two-state ^{6}Li mixtures confined in a magnetic trap. We find that the rate of inelastic spin-flip collisions is prohibitively high for magnetically trapped mixtures of ^{6}Li. These spin-flip collisions

cause transitions to untrapped states in the magnetic trap and thus lead to trap loss. Inelastic collisions can be strongly suppressed by using two-state mixtures of ^{6}Li atoms which can only be confined in an optical trap. Thus, this chapter also serves as the motivation for developing the ultrastable optical trap described in Chapters 3 and 4.

In this chapter we will explore the different interactions that can occur in an ultracold gas of ^{6}Li. We will begin this chapter by outlining basic low temperature scattering theory. We will motivate the concept of a scattering length and elucidate its relationship to the contact potential given above. We will also explore the role that the Pauli exclusion principle plays in low temperature collisions between fermions. ^{6}Li atoms can interact via a singlet molecular potential or a triplet molecular potential depending on how the spins of the valence electron from each atom are coupled. We will calculate the scattering length for both the singlet and triplet ^{6}Li - ^{6}Li molecular potentials and will find that ^{6}Li is expected to exhibit a large and negative *triplet* scattering length. In the later half of the chapter, we will explore the scattering of ^{6}Li atoms in arbitrary hyperfine states. The hyperfine structure of the ^{6}Li atom complicates the calculation of the scattering length because the hyperfine interaction couples the singlet and the triplet states. This leads to a scattering length that is magnetic field dependent. We will explore the field dependence of the scattering length for several combinations of hyperfine states. Finally, we will consider possible inelastic collision channels and will present two mixtures of hyperfine states that can be optically trapped and which provide a large, negative scattering length with a small inelastic collision rate.

2.1 S-Wave Elastic Scattering

Neutral alkali atoms interact primarily via an electrostatic molecular potential $\mathrm{V}(r)$ which only depends on the distance r between the particles. By working in the center of mass frame, we can treat the collision between two ultracold atoms as a single particle of reduced mass μ scattering from a potential $\mathrm{V}(\boldsymbol{r})$.

Consider an incident particle traveling in the $+\hat{\boldsymbol{z}}$ direction with momentum $\hbar k$. The asymptotic single particle wavefunction will consist of an incident plane wave plus an outgoing spherical wave due to scattering from the potential:

$$\psi_{\boldsymbol{k}} \underset{r\to\infty}{\longrightarrow} e^{ikz} + f(\theta,\phi)\frac{e^{ikr}}{r}. \tag{2.1}$$

The function f is known as the *scattering amplitude*. The differential cross section $d\sigma/d\Omega$ is equal to the square of the scattering amplitude:

$$\frac{d\sigma}{d\Omega} = |f(\theta,\phi)|^2. \tag{2.2}$$

The electrostatic molecular potential we will be considering is a central potential, $\mathrm{V}(\boldsymbol{r}) = \mathrm{V}(r)$. This allows us to express the scattering process in a partial wave expansion. Since the potential has no angular dependence, by symmetry, the scattering amplitude is only a function of θ, the angle between the incident direction $\hat{\boldsymbol{z}}$ and the direction to which the particle is scattered. This allows us to express $f(\theta)$ as a series expansion in Legendre polynomials $\mathrm{P}_l(x)$:

$$f(\theta,\phi) = f(\theta) = \sum_{l=0}^{\infty}(2l+1)\frac{e^{2i\delta_l}-1}{2ik}\mathrm{P}_l(\cos\theta). \tag{2.3}$$

This is an expansion in the orbital angular momentum eigenstates $|l\rangle$. Since $\mathrm{V}(r)$

is a central potential the orbital angular momentum is conserved in the scattering process and each angular momentum eigenstate scatters independently.

The terms δ_l in Eq. (2.3)are called partial wave phase shifts. Asymptotically far away from the potential, the radial wavefunction has the form:

$$\mathrm{R}_l(r) \underset{r\to\infty}{\longrightarrow} \frac{\sin[kr - l\pi/2 + \delta_l(k)]}{r}. \tag{2.4}$$

The effect of the potential is to cause the phase shift δ_l in the asymptotic wavefunction. If the potential were absent $\delta_l = 0$ for all l.

In the case of an *ultracold* gas of neutral atoms, the partial wave expansion greatly simplifies the analysis. Due to the extremely low collision energies, only the lowest angular momentum partial wave, the s-wave, contributes to the scattering process. This can be seen in the following heuristic argument. Let us assume that the potential has some finite range r_0. Consider a collision in which two atoms have a relative linear momentum p. The maximum relative orbital angular momentum that is relevant to the scattering process is approximately given by

$$L \simeq r_0\, p \simeq r_0\, h/\lambda_{dB}, \tag{2.5}$$

where we have expressed p in terms of the de Broglie wavelength λ_{dB}. Since angular momentum is quantized, $L = \ell\hbar$ where ℓ is an integer. We find that

$$\ell \simeq \frac{r_0}{\lambda_{dB}} << 1, \tag{2.6}$$

since the typical range for an interatomic potential is $r_0 \sim 10$ $\mathring{\mathrm{A}}$ and we found in Chapter 1 that the typical size of the de Broglie wavelength for ^{6}Li atoms at

$\simeq 1\,\mu$K is $\lambda_{dB} \sim 1\,\mu$m. Thus, only collisions for which $\ell = 0$ are relevant to the scattering process at the ultracold temperatures being considered. Only s-wave (*i.e.*, $\ell = 0$) scattering collisions will be considered in this dissertation.

If we consider only s-wave ($l = 0$) scattering, then equation (2.3) for the scattering amplitude simplifies to

$$f = e^{i\delta_0}\frac{\sin(\delta_0)}{k}, \tag{2.7}$$

which is independent of θ. The total cross section σ becomes

$$\sigma = \int d\Omega\,|f|^2 = \int d\Omega\left|\frac{\sin\delta_0}{k}\right|^2 = 4\pi\frac{\sin^2\delta_0}{k^2}. \tag{2.8}$$

Therefore, in order to calculate the total scattering cross section, we simply find the phase shift δ_0 caused by potential V(r). Note that for a collision with relative momentum $\hbar k$, the s-wave cross section $\sigma \leq 4\pi/k^2$ since $\sin(\delta_0) \leq 1$. This maximum cross section is known as the unitarity limit.

In spherical coordinates the solution to the time-independent Schrödinger equation has the form

$$\Psi_{Elm}(r,\theta,\phi) = \frac{u_{E\,l}(r)}{r}Y_l^m(\theta,\phi), \tag{2.9}$$

where the Y_l^m's are the spherical harmonic functions. The function $u_{E\,l}$ must satisfy the relation

$$\left\{\frac{d^2}{dr^2} + \frac{2\mu}{\hbar^2}\left[E - \mathrm{V}(r) - \frac{l(l+1)\hbar^2}{2\mu r^2}\right]\right\}u_{E\,l}(r) = 0, \tag{2.10}$$

where μ is the reduced mass of the colliding ^{6}Li atoms. Since we are only considering

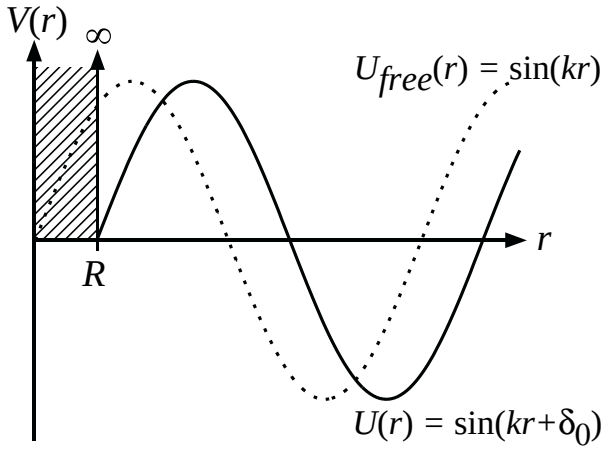

Figure 2.1: Phase shift due to hard sphere potential of radius R

s-wave scattering, we will consider solutions to Eq. (2.10) with $l = 0$. In the absence of a potential V(r), Eq. (2.10) with $l = 0$ has the free particle solution

$$u_E(r) = \sin(kr), \tag{2.11}$$

where $k = (2\mu E/\hbar^2)^{1/2}$. If a potential V($r$) exists but approaches zero at infinity then the asymptotic form of the wave function must give the free particle solution

$$u_E(r) \underset{r\to\infty}{\longrightarrow} \sin(kr + \delta_0), \tag{2.12}$$

although there is a phase shift δ_0 due to the effect of the potential near the origin.

To illustrate these concepts in a simple physical example, consider a hard sphere potential of radius R. For $r > R$ the potential is zero whereas for $r < R$ the potential is infinite. Figure 2.1 shows the function $u_E(r)$ that satisfies the Schrödinger equation for this potential. Also shown in Figure 2.1 is the free particle solution u_{free}. As can be seen in the figure, the hard sphere potential causes a phase shift

$\delta_0 = -kR$. Inserting this result into Eq. (2.8), we find that the s-wave cross section in the low energy limit is given by

$$\sigma = \lim_{k\to 0} 4\pi \frac{\sin^2 \delta_0}{k^2} = \lim_{k\to 0} 4\pi \frac{\sin^2(ka)}{k^2} = 4\pi R^2. \tag{2.13}$$

This gives the unexpected result that the low-energy quantum mechanical cross section for the hard sphere potential is 4 times the classical cross section πR^2.

2.2 The S-Wave Scattering Length

In the limit of zero energy, s-wave collisions are characterized by a single parameter known as the s-wave scattering length. For a broad range of potentials, it is possible to show that $\tan(\delta_0) \propto k$ as $k \to 0$ [59]. Thus, at low collision energies, it is useful to define a scattering length a as

$$a \equiv -\lim_{k\to 0} \frac{\tan \delta_0(k)}{k}. \tag{2.14}$$

We find that the scattering amplitude, Eq. (2.7), in the low energy limit is

$$\lim_{k\to 0} f = \lim_{k\to 0} \frac{\sin \delta_0(k)}{k} = -a. \tag{2.15}$$

Hence, the total cross section, Eq. (2.8), is simply

$$\sigma \underset{k\to 0}{\longrightarrow} 4\pi a^2. \tag{2.16}$$

Note that for the hard sphere example given in the previous section, we found that $\delta_0 = -kR$. Thus, the scattering length is equal to the radius of the hard sphere R.

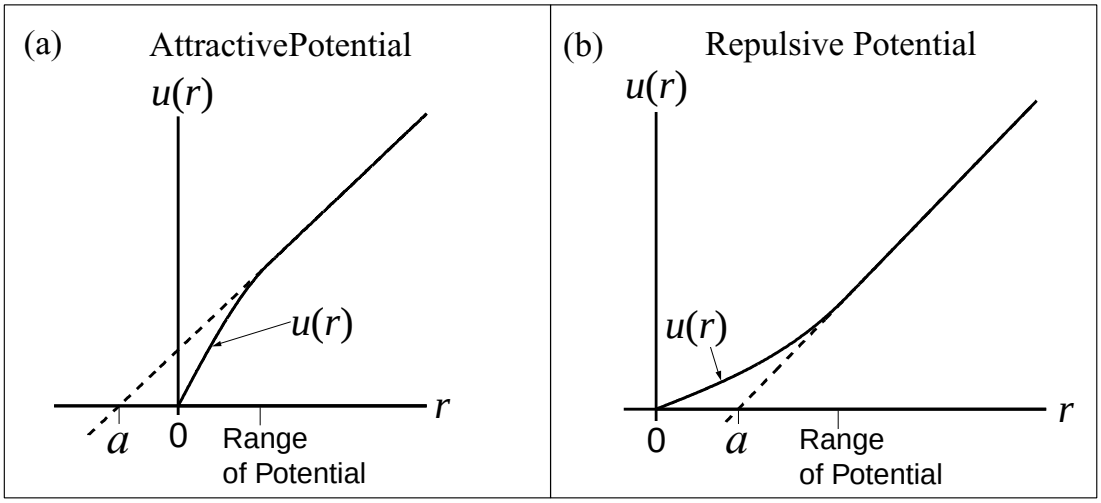

Figure 2.2: The wave function $u(r)$ in the low energy limit for an attractive (a) and repulsive (b) square well potential. The scattering length a is given by the intercept of the asymptotic wave function with the $u(r) = 0$ axis.

Using Eq. (2.16) we again find that the s-wave cross section is $\sigma = 4\pi R^2$.

The scattering length a has a simple physical interpretation. In the low energy limit, the asymptotic wave function has the form $\sin(kr + \delta_0) \simeq \sin(kr) + \delta_0 \cos(kr) \underset{k\to 0}{\longrightarrow} k(r - a)$. Thus, the scattering length a is the intersection of the asymptotic form of $u_{k\to 0}(r)$ with the r axis. Figure 2.2 (a) and (b) illustrate this concept for an attractive and repulsive square well, respectively. The wave function $u(r)$ and its asymptotic form are shown for each case. Note that for a predominately attractive potential the scattering length a is negative and for a predominately repulsive potential the scattering length a is positive.

2.3 Effective Contact Interaction

For a gas of neutral atoms at temperatures $\sim 1\,\mu$K, the de Broglie wavelength of the atoms is enormous in comparison to the range of the molecular potential. In

this case, the atoms experience an averaged effect of the potential. In addition, the effective interactions between the particles are small since the average interparticle spacing is also much larger than the range of the potential. These properties allow us to treat the interactions between particles in first-order perturbation theory (the Born approximation) using an effective contact interaction $V(\mathbf{r}) = V_0\delta(\mathbf{r})$.

We require that this effective contact interaction gives the correct low-energy scattering amplitude $f(\theta, \phi) = -a$ in first-order perturbation theory. In the 1$^{\text{st}}$ Born approximation the scattering amplitude due to a potential $V(\mathbf{r})$ is given by

$$f(\theta, \phi) = \frac{-\mu}{2\pi\hbar^2} \int e^{-i\mathbf{q}\cdot\mathbf{r}'} V(\mathbf{r}')\, d^3\mathbf{r}', \tag{2.17}$$

where $\hbar\mathbf{q}$ is the momentum transferred to the particle of reduced mass μ. This is the standard Born approximation result. Substituting in the effective contact interaction $V(\mathbf{r}) = V_0\delta(\mathbf{r})$ we obtain

$$f(\theta, \phi) = \frac{-V_0\mu}{2\pi\hbar^2} \tag{2.18}$$

Since we require that this potential gives the same low-energy scattering amplitude as the partial wave analysis we find that $V_0 = 2\pi\hbar^2 a/\mu$. Thus, we will use the effective contact potential

$$V(\boldsymbol{r}) = \frac{2\pi\hbar^2 a}{\mu}\delta(\boldsymbol{r}) = \frac{4\pi\hbar^2 a}{M}\,\delta(\boldsymbol{r}) \tag{2.19}$$

when we wish to consider interactions in first-order perturbation theory. Note that the scattering length a completely characterizes the interactions in an ultracold, weakly interacting, dilute gas of neutral atoms. We will now turn our attention

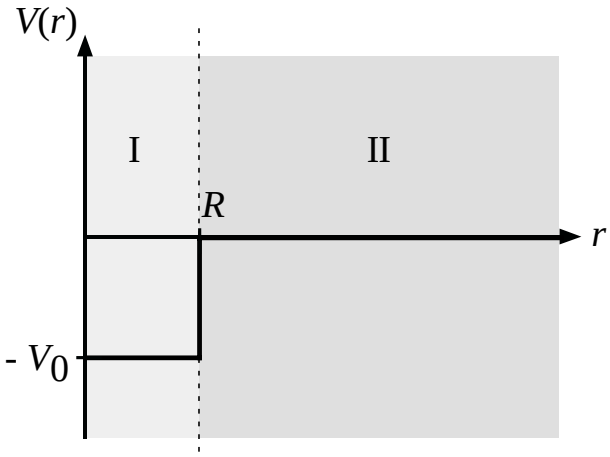

Figure 2.3: Square well potential.

toward calculating the scattering length for ^{6}Li.

2.4 Scattering by a Square Well Potential

Before we calculate the scattering length for the actual ^{6}Li molecular potentials we will first explore scattering due to a square well potential, which shares several salient features. The square well potential provides a simple model which, under certain conditions, exhibits a zero-energy resonance. A near zero-energy resonance in the ^{6}Li molecular potential is responsible for the very large scattering length that is observed in Chapters 6 and 7. From the square well model we will derive an analytical form for the low-energy dependence of the s-wave cross section for a near zero-energy resonance. In section Section 2.5 we will numerically calculate the s-wave cross section for the ^{6}Li triplet potential and will find that it is well approximated by the analytical form we find here.

Consider s-wave scattering by a central potential

$$V(r) = \begin{cases} -V_0 & \text{for } r < R \\ 0 & \text{for } r > R \end{cases} \tag{2.20}$$

A particle of momentum $\hbar k$ has a radial wave function $R(r) = u(r)/r$ where $u(r)$ satisfies the radial Schrödinger equation, Eq. (2.10), with $l = 0$. For the square well in Figure 2.3, $u(r)$ has the form

$$u(r) = \begin{cases} A\sin(\kappa r) & \text{for } 0 \leq r < R \\ B\sin(kr + \delta_0) & \text{for } r > R \end{cases} \tag{2.21}$$

where $\kappa^2 \equiv k^2 + k_0^2$ and $k_0^2 \equiv 2\mu V_0/\hbar^2$. We have used the fact that $u(r = 0)$ must be zero so that the radial wave function does not diverge at $r = 0$. By requiring that $u(r)$ and $u'(r)$ be continuous at $r = R$, we find that the s-wave phase shift δ_0 is given by

$$\delta_0(k) = \tan^{-1}\left(\frac{k}{\kappa}\tan(\kappa R)\right) - kR. \tag{2.22}$$

If k is small ($k << \kappa$) then $\kappa \cong k_0$ and δ_0 becomes

$$\begin{aligned} \delta_0 &= \frac{k}{k_0}\tan(k_0 R) - kR \\ &= -k\left[-R\left(\frac{\tan(k_0 R)}{k_0 R} - 1\right)\right] \\ &= -ka_s \end{aligned} \tag{2.23}$$

where $a_s = -R\,[\tan(k_0R)/(k_0R) - 1]$. We identify a_s as the scattering length since

$$-\lim_{k\to 0}\frac{\tan\delta_0}{k} = -\lim_{k\to 0}\frac{\tan(-ka_s)}{k} = a_s. \tag{2.24}$$

In the low-energy limit, the cross section is given by $\sigma = 4\pi a_s^2$.

Note that the scattering length diverges if $k_0R = n\pi/2$ for integer n. If this is the case, the zero energy phase shift $\delta_0 = \pi/2$ and, according to Eq. (2.8), the s-wave cross section diverges at low energy as $1/k^2$. This is an example of a zero-energy resonance. One can show that the square well potential supports n bound states if $n\pi/2 < k_0R < (2n+1)\pi/2$. Thus, when the condition $k_0R = n\pi/2$ is satisfied an unbound state is about to become bound. The existence of this virtual state at zero energy causes the resonant behaviour of the zero-energy s-wave cross section.

Let us now consider the low energy behaviour of the s-wave cross section for a near zero-energy resonance. In this case, k_0R is nearly but not exactly $\pi/2$ causing the scattering length a_s to be much larger than R. For $k << k_0$, we can rewrite Eq. (2.22) using the definition of a_s given above as

$$\begin{aligned}\delta_0 &= \tan^{-1}\left[k(-a_s + R)\right] - kR \\ &\cong -\tan^{-1}[ka_s]\end{aligned} \tag{2.25}$$

where we have used the fact that $a_s >> R$ and $kR << 1$. This implies that $\tan[\delta_0] = -ka_s$ from which we can show that

$$\begin{aligned}\sigma &= \frac{4\pi}{k^2}\sin^2\delta_0 \cong \frac{4\pi}{k^2}\left[\frac{(ka_s)^2}{1+(ka_s)^2}\right] \\ &= \frac{4\pi a_s^2}{1+k^2a_s^2}.\end{aligned} \tag{2.26}$$

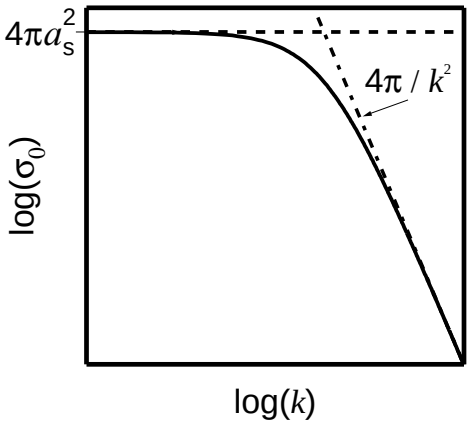

Figure 2.4: Energy dependent s-wave cross section for a near zero-energy resonance. Note that at low energy the cross section approaches the constant cross section $\sigma = 4\pi a_s^2$ (dashed line) whereas at high energy σ approaches the unitarity limit $\sigma = 4\pi/k^2$ (dot-dashed line).

Thus, the s-wave cross section for a near zero energy resonance exhibits a lorentzian dependence on k in the low-energy limit. Figure 2.4 shows a log-log plot of the s-wave cross section as a function of k. Note that at zero-energy the cross section is $\sigma = 4\pi a_s^2$. The dashed line in Figure 2.4 is given by $\sigma = 4\pi a_s^2$. When $ka_s >> 1$ the cross section is unitarity limited in which case $\sigma = 4\pi/k^2$. The dot-dashed line in Figure 2.4 is a plot of $\sigma = 4\pi/k^2$. In section Section 2.5 we will find that the near zero-energy resonance that exists for the ^{6}Li triplet potential will give almost exactly the same energy dependence. We will use this analytical form of the energy dependent cross section when analyzing the energy dependence of elastic collisions in evaporative cooling in Chapters 6 and 7.

2.5 ^{6}Li Scattering Lengths

We now turn our attention to calculating the s-wave cross section for elastic collisions between ^{6}Li atoms using the best ^{6}Li potentials known to date. ^{6}Li atoms in their ground states can interact via either a singlet or triplet molecular potential depending on whether the valance electron from each atom couple to form a singlet or triplet spin state. In this section, we calculate the singlet and triplet scattering lengths for ^{6}Li-^{6}Li collisions. By numerically integrating the radial Schrödinger equation we compute the wave function $u(r)$ for each of these potentials. In the low energy limit, the singlet and triplet scattering lengths a_s and a_t are given by the intercept of the asymptotic wave function $u(r)$ with the $u(r) = 0$ axis. The singlet scattering length is found to be $\simeq 40\, a_0$. Due to a near zero-energy resonance, the triplet scattering length, on the other hand, is predicted to have a very large and negative value of $-2160\, a_0$.

2.5.1 ^{6}Li Singlet and Triplet Molecular Potentials

^{6}Li atoms approach along a singlet potential $V_s(r)$ if the electron spins of the single valance electron from each atom ($\mathbf{S_1}$ and $\mathbf{S_2}$) combine to form a singlet spin state ($\mathbf{S} = \mathbf{S_1} + \mathbf{S_2} = 0$). In this case, the valance electrons are in a symmetric spatial wave function so that the overall valance electron wave function is antisymmetric under exchange of the electrons. Since the spatial wave function is symmetric, the probability density for a valance electron to be found between the nuclei is nonzero. Thus, the valance electrons can shield the repulsive force between the positively charged ^{6}Li nuclei. Conversely, ^{6}Li atoms approach along a triplet potential $V_t(r)$ when the valance electrons combine in a triplet spin state ($\mathbf{S} = 1$). In this case, the

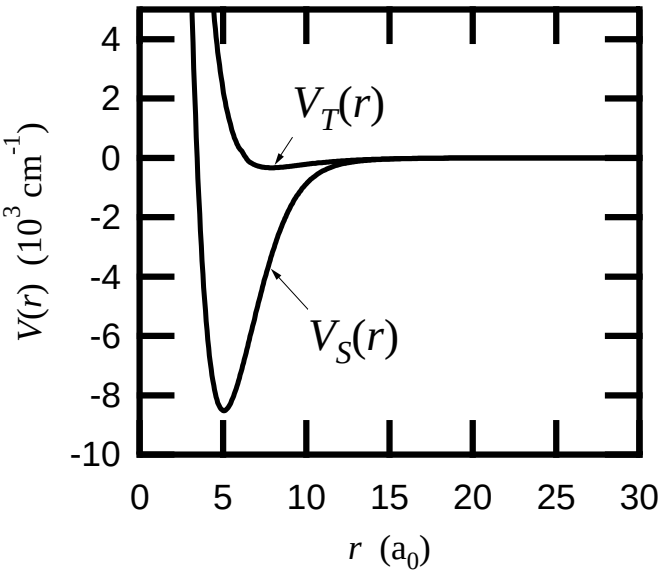

Figure 2.5: Singlet $V_S(r)$ and triplet $V_T(r)$ ^{6}Li molecular potentials.

electrons are in an antisymmetric spatial wave function and the probability density between the nuclei is zero. Thus, the valance electrons cannot shield the repulsive force between the nuclei. Therefore, we expect that the triplet potential is much shallower than the singlet potential.

Figure 2.5 shows the most up-to-date singlet and triplet molecular potentials for ^{6}Li in cm^{-1} as a function of separation r in Bohr radii a_0. As expected, the singlet potential is much deeper than the triplet potential. These potentials were constructed using data from a number of publications [16,60–66]. Different regions of the potential were obtained by several different authors by methods ranging from *ab initio* calculations to fitting experimental molecular spectra. The recipe for constructing the singlet potential is given in Ref. [60] modified by the improved long-range coefficients [64] and the dissociation energy as suggested in Ref. [16]. The inner wall potential between 2.75 and 3.25 a_0 is that of Refs. [62, 63]. The

intermediate potential from 3.4-23.9 a_0 is found in Ref. [61] except for two misprints corrected in [60]. The long-range potential is given by Refs. [60, 64]. The intermediate potential is fit to the inner wall and long-range data by subtracting the dissociation energy $D_e = 8516.70\,\mathrm{cm}^{-1}$ found in Ref. [16] from the data given by Ref. [61]. To obtain values of $V_s(r)$ at arbitrary r a cubic spline curve is used to interpolate between the data points given in these references.

The recipe for constructing the triplet potential is given in Ref. [16]. The inner wall potential from 3 to 6 a_0 is given in Ref. [66] and the long-range potential is given by Refs. [60, 64]. The intermediate potential is given by Ref. [65] and is adjusted to fit the inner wall and long-range potentials by subtracting off the dissociation energy $D_e = 333.74\,\mathrm{cm}^{-1}$ given in Ref. [16]. Again, a cubic spline curve is used to find $V_t(r)$ at arbitrary r.

To calculate the s-wave scattering length and low-energy cross section for the singlet and triplet potentials we must first find the phase shift δ_0 in the asymptotic wave function as defined in (2.12). To find the asymptotic wave function we integrate the s-wave radial wave function (Eq. (2.10) with $l = 0$). We can rewrite the s-wave radial Schrödinger equation in dimensionless parameters as

$$\left\{ \frac{d^2}{d\rho^2} + k_0^2 - \frac{2\mu}{m_e} V(\rho) \right\} u_{k_0}(\rho) = 0, \tag{2.27}$$

where ρ is the separation in bohr, k_0 is the wave number in inverse bohr, m_e is the electron mass, μ is the reduced mass of two ^{6}Li atoms and $V(\rho)$ is the potential in Hartree (1 Hartree $= \alpha^2 m_e c^2$ where α is the fine structure constant and c is the speed of light). We can find $u_{k_0}(\rho)$ by numerically integrating Eq. (2.27) starting with the initial conditions at $\rho = 0$ of $u_{k_0} = 0$ and $u'_{k_0} = C$ where C is arbitrary since it determines the amplitude of u_{k_0} with which we are not concerned. If we

numerically integrate Eq. (2.27) out to a large distance ρ_f such that $2\mu V(\rho_f)/m_e << k_0^2$, u_{k_0} will converge to its asymptotic form $u_{k_0} = \sin(\rho_f k_0 + \delta_0)$. In this case, $k_0 u_{k_0}(\rho_f)/u'_{k_0}(\rho_f) = \tan(k_0\rho_f + \delta_0)$ and we can find δ_0 numerically by computing

$$\delta_0(k_0) = \tan^{-1}\left[\frac{k_0 u_{k_0}(\rho_f)}{u'_{k_0}(\rho_f)}\right] - k_0\rho_f. \tag{2.28}$$

Once $\delta_0(k_0)$ is found numerically, the energy dependent s-wave cross section can be found using Eq. (2.8) and the scattering length is given by Eq. (2.14).

2.5.2 The Singlet Scattering Length

Using *Mathematica*, Eq. (2.27) was numerically integrated using the singlet potential V_s obtained from Refs. [16, 60–64] as described above. The reduced mass $\mu = 3.0075607$ atomic mass units (amu) used was that given by Ref. [16] and the value for $m_e = 5.48579903 \times 10^{-4}$ amu as given by Ref. [67]. Since the value of the potential is not known at $\rho = 0$, the initial conditions actually used for the numerical integration are $u(\rho = \rho_i) = 0$ and $u'(\rho = \rho_i) = 1$ where $\rho_i = 2.75a_0$ at which point the potential is large and positive. Since the wave function is strongly damped for $\rho \leq 3.5a_0$, the use of these initial conditions causes negligible error in the results. Figure 2.6 shows the wave function $u_{k_0}(\rho)$ obtained from numerical integration for $k_0 = 1\,a_0^{-1}$. Also shown are the singlet potential $V_s(\rho)$ and the free particle wave function $u_{free}(\rho) \sim \sin(k_0\rho)$ that would exist in the absence of the potential. Note that for large ρ, $u_{k_0}(\rho) \sim \sin(k_0\rho + \delta_0)$.

The s-wave phase shift is computed numerically as a function of k_0 using Eq. (2.28). The singlet scattering length a_s can then be found by computing $a_s = -\tan(\delta(k_0))/k_0$ in the limit that $k_0 \to 0$. For the singlet potential described

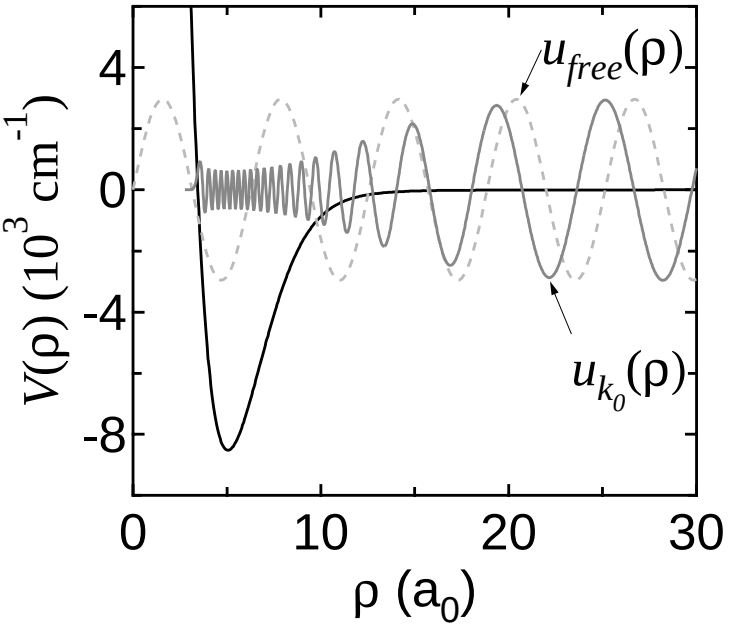

Figure 2.6: Singlet potential wave function (solid grey). The free particle wave function (dashed grey) is also shown for comparison.

above, a_s is found numerically to be $+38.75a_0$. This is in good agreement with the results of [16]. Figure 2.7 shows the wave function $u_{k_0}(\rho)$ in the low energy limit. Note that the asymptotic wave function (shown as the dashed line) intersects the ρ axis at $\rho = a_s$. The energy dependent cross section can also be calculated numerically as $\sigma(k_0) = 4\pi \sin^2(\delta_0(k_0))/k_0^2$. The cross section is found to be constant (to within 1%) for wave numbers k_0 between 10^{-4} and $10^{-2}\, a_0^{-1}$ and is equal to $\sigma = 4\pi a_s^2$ for $|a_s| = 38.75\, a_0$, as expected. These wave numbers correspond to relative kinetic energies T between 300 nanoKelvin - 3 milliKelvin (where $k_B T = \hbar^2 k^2/(2\mu)$). Thus, the s-wave singlet cross section is constant over the range of temperatures considered in this dissertation.

2.5.3 The Triplet Scattering Length

The triplet s-wave phase shift and scattering length are computed in a similar fashion. Equation (2.27) was numerically integrated using the triplet potential V_t obtained from Refs. [16,60,64–66] as described above. The boundary conditions for the numerical integration are $u(\rho = \rho_i) = 0$ and $u'(\rho = \rho_i) = 1$ where $\rho_i = 4a_0$. Figure 2.8 shows the wave function $u_{k_0}(\rho)$ in the low energy limit. Note that the asymptotic wave function intersects the ρ-axis at a large and negative value. The triplet scattering length a_t is found numerically to be $-2240a_0$. This enormous s-wave scattering length is the largest known of all the alkali atoms. This anomalously large scattering length arises from a near zero-energy resonance as described below. That a_t is negative indicates that the potential causes an effective attractive s-wave interaction between the atoms. As discussed in Chapter 1, the existence of a large, attractive interaction between the ^{6}Li atoms is a prerequisite for observing a superfluid transition at an experimentally obtainable temperature.

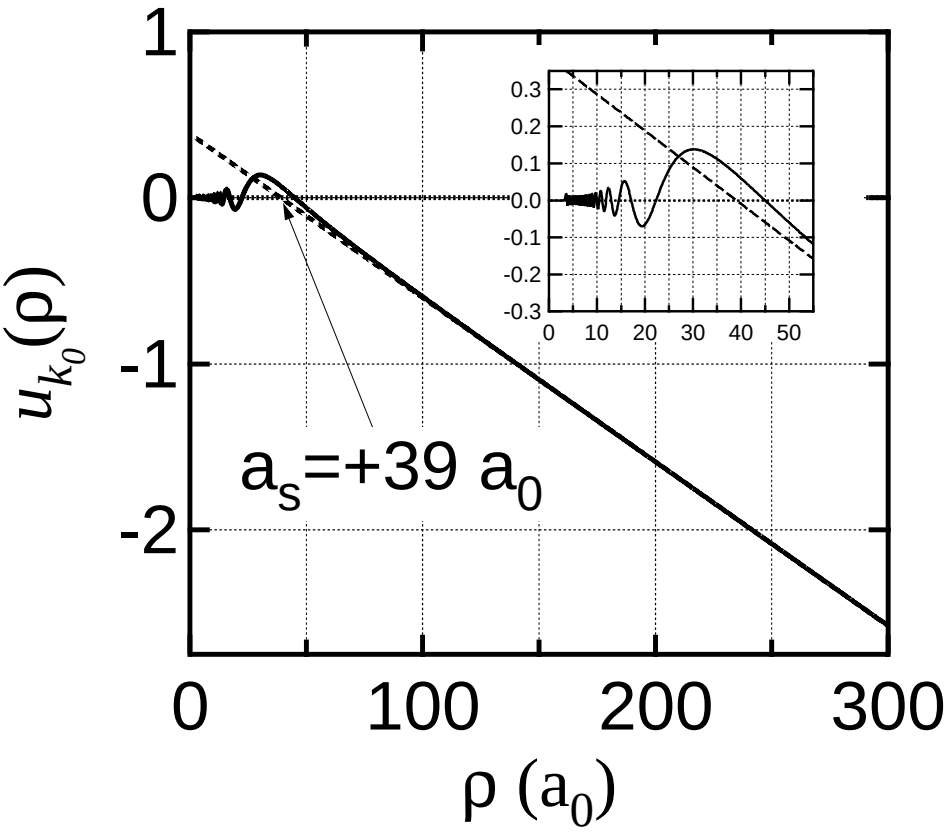

Figure 2.7: Singlet potential scattering length. The singlet scattering length a_s is given by the intercept of the asymptotic wavefunction with the $u(\rho) = 0$ axis. We find that $a_s \simeq 39\, a_0$.

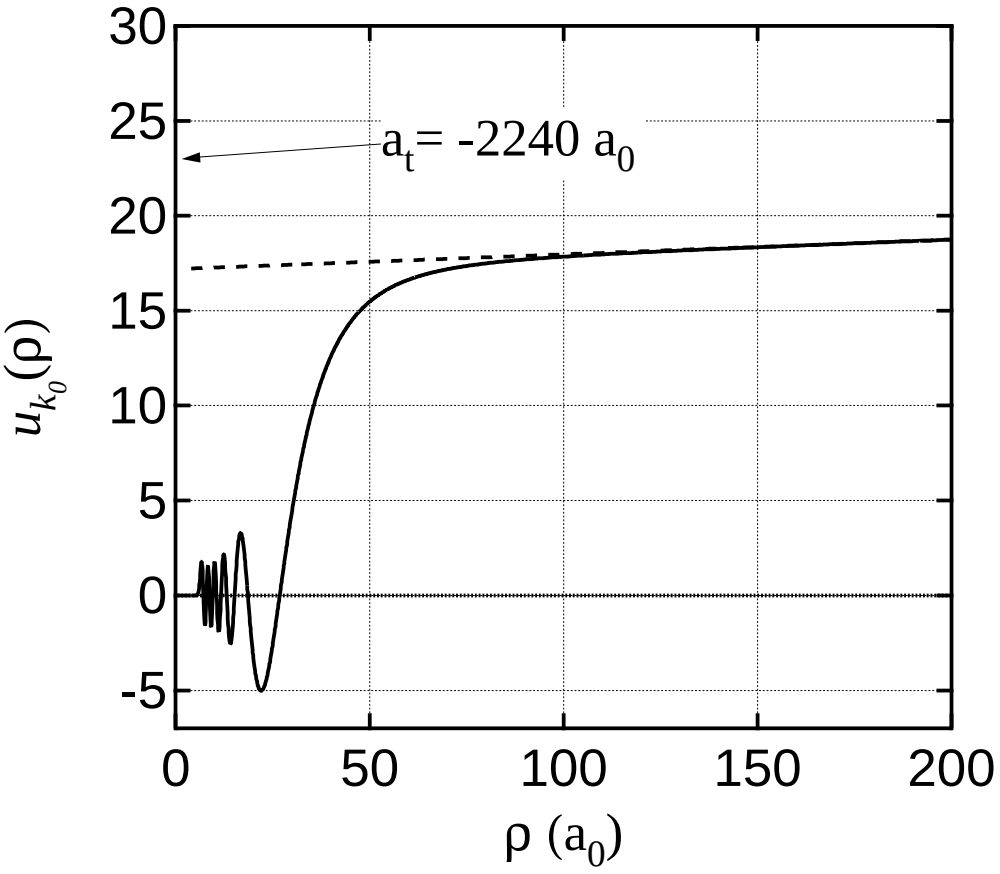

Figure 2.8: Triplet potential scattering length. The triplet scattering length a_t is given by the intercept of the asymptotic wavefunction with the $u(\rho) = 0$ axis. We find that this intercept occurs at a very large and negative value which is found numerically to be $a_t = -2240\, a_0$.

The large, triplet scattering length predicted to exist for ^{6}Li is due to a near zero-energy resonance in the triplet molecular potential. As with the square well potential, a zero-energy scattering resonance arises due to the existence of a vibrational state at the dissociation energy of the molecular potential for which the scattering length diverges. A slightly deeper molecular potential yields a barely bound vibrational state and a large and positive scattering length. On the other hand, a slightly shallower potential yields an unbound virtual state giving rise to a large and negative scattering length. In the case of the ^{6}Li triplet molecular potential, the potential will support an additional vibrational level if the dissociation energy is increased by less than 0.03%. Figure 2.9 shows the triplet scattering length as a function of dissociation energy. For a dissociation energy of $D_E = 333.82\,\mathrm{cm}^{-1}$, a $\nu = 10$ vibrational state becomes bound and the scattering length diverges. Obviously, the precise value of a_t is extremely sensitive to the dissociation energy near a zero-energy resonance. In Ref. [16], the dissociation energy $D_E = 333.74\,\mathrm{cm}^{-1}$ is determined by measuring the binding energy of the highest vibrational level ($\nu = 9$) of the triplet potential. Using this measured binding energy, the dissociation energy of the triplet potential is adjusted such that the $\nu = 9$ binding energy numerically predicted from the Schrödinger equation agrees with the measured value.

In Chapters 6 and 7 we describe evaporative cooling experiments which are directly sensitive to the magnitude of the scattering length. The evaporation rate is sensitive to the scattering length since the probability that an atom experiences collision yielding enough energy to escape the well depends on the elastic collision cross section. The scattering lengths measured in these experiments are in agreement with the results found here. These measurements provide independent confirmation that very large scattering lengths for ^{6}Li collisions indeed exist.

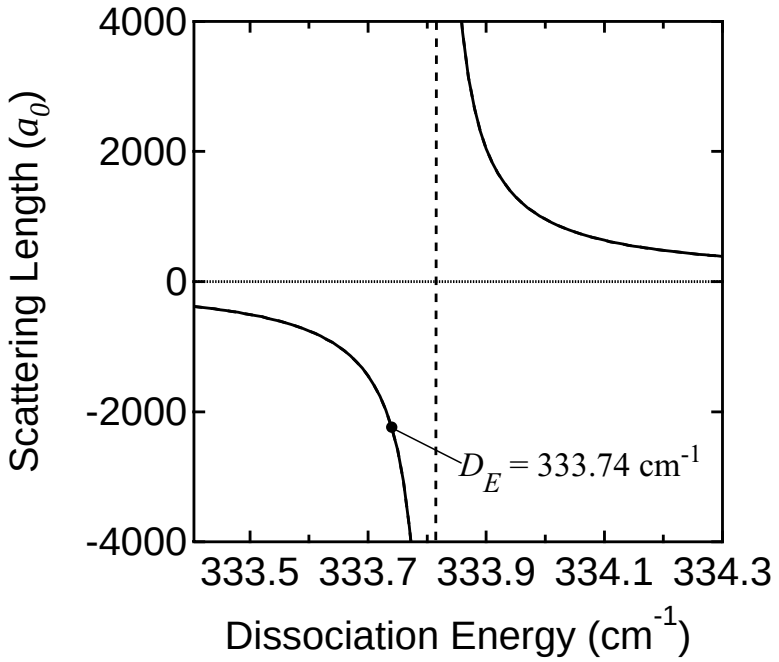

Figure 2.9: Sensitivity of a_t to dissociation energy

In Section 2.4 we calculated the s-wave cross section for a square well potential which exhibits a near zero energy resonance. We found that the s-wave cross section for the square well is energy dependent, exhibiting a Lorentzian dependence on the relative momentum wavenumber k. The energy dependent s-wave cross section for the ^{6}Li triplet molecular potential is also well approximated by a Lorentzian. Figure 2.10 shows both the s-wave cross section for the triplet cross section calculated by numerically integrating the radial Schrödinger equation as well as the function $\sigma(k) = 4\,\pi\,a_t^2/(1 + k_0^2\,a_t^2)$. The Lorentzian provides a good fit over the range of temperatures of interest in this dissertation. This analytical form of the energy dependent cross section will be useful in Chapter 6 where we model the evaporative cooling of ^{6}Li atoms from the optical trap. Since the evaporative cooling rate depends on the elastic collision cross section the energy dependence of the cross sec-

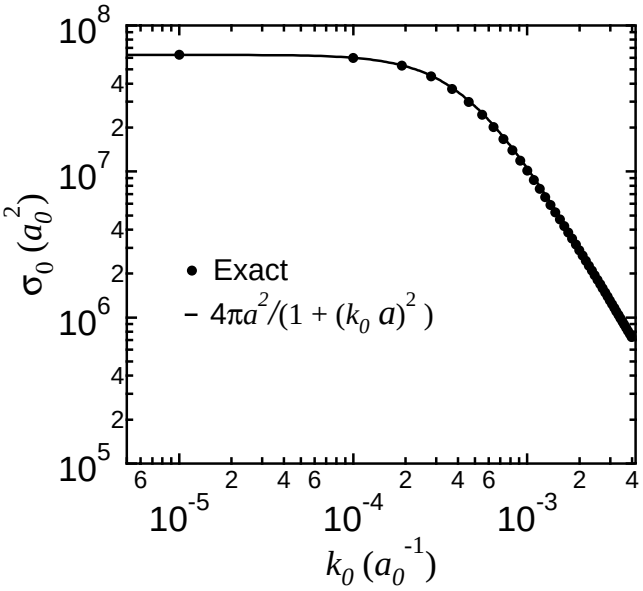

Figure 2.10: Comparison of the calculated triplet cross section (circles) to lorentzian dependent cross section (solid line).

tion needs to be included. Having an analytical model of this cross section makes the modeling of evaporative cooling tractable.

2.6 *S*-Wave Collisions between Fermions

In the preceding analysis we have not yet considered the fact that the colliding ^{6}Li atoms are identical particles. Since the composite ^{6}Li atom has a half-integral total spin (see Appendix A), ^{6}Li atoms obey Fermi-Dirac statistics. The total wave function describing the collision of two ^{6}Li atoms must therefore be antisymmetric under exchange of the atoms.

The unsymmetrized total wave function for two ^{6}Li atoms is

$$\Psi(\mathbf{r}_1, \mathbf{r}_2) = \psi^{CM}(\mathbf{R})\,\psi(\mathbf{r})\;|\chi_1\rangle\;|\chi_2\rangle \tag{2.29}$$

where $\mathbf{r}_1$ and $\mathbf{r}_2$ are the positions of each atom, $\mathbf{R} = (\mathbf{r}_1 + \mathbf{r}_2)/2$ is the center-of-mass coordinate, $\psi^{CM}(\mathbf{R})$ is the center-of-mass wave function, $\mathbf{r} = \mathbf{r}_1 - \mathbf{r}_2$ is the relative coordinate, $\psi(\mathbf{r})$ is the relative wave function and $|\chi_1\rangle$ and $|\chi_2\rangle$ are the spin state of each atom. Under exchange of the atoms $\mathbf{R}$ and therefore $\psi^{CM}(\mathbf{R})$ is invariant. Conversely, $\mathbf{r}$ changes sign under the exchange $\mathbf{r}_1 \leftrightarrow \mathbf{r}_2$. The symmetrized and antisymmetrized relative spatial wave functions are given by

$$\psi_{S/A}(\mathbf{r}) = (e^{ikz} \pm e^{-ikz}) + [f(\theta,\phi) \pm f(\pi-\theta,\phi+\pi)]e^{ikr}/r. \tag{2.30}$$

We can identify $f_{S/A}(\theta,\phi) = f(\theta,\phi) \pm f(\pi-\theta,\phi+\pi)$ as the properly symmetrized scattering amplitude. Note that for s-wave collisions which are dominant in an ultracold ^{6}Li gas, $f(\theta,\phi) = f$ and $f_A = 0$. Thus, s-wave collisions can only occur for a symmetric relative spatial wave function. In this case $f_S = 2f$ and $d\sigma/d\Omega = 4|f|^2$. The total cross section $\sigma = 8\pi|f|^2$ since we integrate $d\sigma/d\Omega$ over 2π instead of 4π in order to avoid double counting. Thus, the low energy cross section for identical ^{6}Li fermions in a symmetric spatial wave function is given by

$$\sigma = 8\pi a^2, \tag{2.31}$$

where a is the s-wave scattering length.

In order for the total wave function Ψ to be antisymmetric with a symmetric relative spatial wave function $\psi_S(\mathbf{r})$, the total spin wave function must by anti-symmetric. Thus, for interactions to exist in an ultracold ^{6}Li gas we require an antisymmetric spin wave function

$$|\{\chi_1,\chi_2\}_-\rangle = \frac{1}{\sqrt{2}}\left(|\chi_1\rangle\,|\chi_2\rangle - |\chi_2\rangle\,|\chi_1\rangle\right). \tag{2.32}$$

In the future we will use the brackets $|\{,\}_-\rangle$ to denote an antisymmetric combination. Note that s-wave collisions between atoms in the same spin state are forbidden since, in this case, $\chi_1 = \chi_2$ and $|\{\chi_1, \chi_2\}_-\rangle = 0$. Thus, s-wave collisions do not exist in a ^{6}Li gas containing only one spin state. Higher partial wave collisions are possible since they can allow for antisymmetric relative spatial wave functions. However, collisions with orbital angular momentum $l > 0$ are strongly suppressed in an ultracold gas. Therefore, a spin polarized gas of ultracold fermions are essentially noninteracting. To study interacting fermions, one must trap a mixture of atoms in different spin states.

In summary, we will account for the effect of fermion statistics on s-wave scattering by computing the low energy cross section as $\sigma = 8\pi a^2$ for atoms in an antisymmetric spin state and will assume that atoms in a symmetric spin state do not interact. Note that for a collision between two atoms where one atom is from each state, the antisymmetric spin combination given by (2.32) occurs with a probability of 1/2.

2.7 Elastic and Inelastic Collisions

The collision between two ground state ^{6}Li atoms is complicated by the fact that the spin of the valence electron is coupled to the spin of the nucleus through the hyperfine interaction. Therefore, as two colliding ^{6}Li atoms approach one another from infinite separation, the valance electrons from each atom are, in general, coupled into a *superposition* of triplet and singlet states. Thus, the collision between two ^{6}Li atoms is not described simply by scattering from either the singlet or triplet potential as described earlier. In addition since the ^{6}Li atoms have internal degrees of freedom there is the additional possibility of inelastic internal-state-changing

collisions. Thus, to properly treat the collision between two ^{6}Li atoms one must solve a coupled-channel Schrödinger equation that treats the internal state structure and internal-state-changing collisions. The general theory of two-body collisions that include inelastic collisions is treated in a number of textbooks (see for example, Ref. [68,69]). Here, we will summarize the derivation of the coupled-channel Schrödinger equation.

Before we delve into the derivation of the coupled-channel Schrödinger equation describing the collision between two ^{6}Li atoms, it is worthwhile to first familiarize ourselves with the internal structure of a single ^{6}Li atom. Appendix A gives a thorough account of the structure of the ground state. We summarize the salient features here.

The single unpaired valance electron of a ^{6}Li atom has spin $s = 1/2$ and is coupled via a magnetic dipole interaction to the ^{6}Li nucleus which has a spin $i = 1$ giving rise to six internal spin states. This interaction is referred to as the hyperfine interaction. In an arbitrary external magnetic field, both the electron and nuclear spins are also coupled to the external field $\mathbf{B}$. The internal state Hamiltonian for ^{6}Li in its electronic ground state is given by

$$H^{int}(\mathbf{B}) = \frac{a_{hf}}{\hbar^2}\,\mathbf{s}\cdot\mathbf{i} + \left(\frac{2\mu_e}{\hbar}\,\mathbf{s} - \frac{\mu_n}{\hbar}\,\mathbf{i}\right)\cdot\mathbf{B}, \tag{2.33}$$

where a_{hf} is the hyperfine constant, μ_e is the Bohr magneton and μ_n is the nuclear magnetic moment. For $\mathbf{B} = 0$, this Hamiltonian is diagonal in the $|f\,m_f\rangle$ basis where $\mathbf{f} = \mathbf{s} + \mathbf{i}$ and m_f is the projection of $\mathbf{f}$ onto the quantization axis. For an arbitrary magnetic field, the internal state Hamiltonian can be diagonalized by six eigenstates $|1\rangle$-$|6\rangle$ which can be expressed in terms of superpositions of the product states $|m_s\,m_i\rangle$ where m_s and m_i are respectively the projections of $\mathbf{s}$ and $\mathbf{i}$ onto the

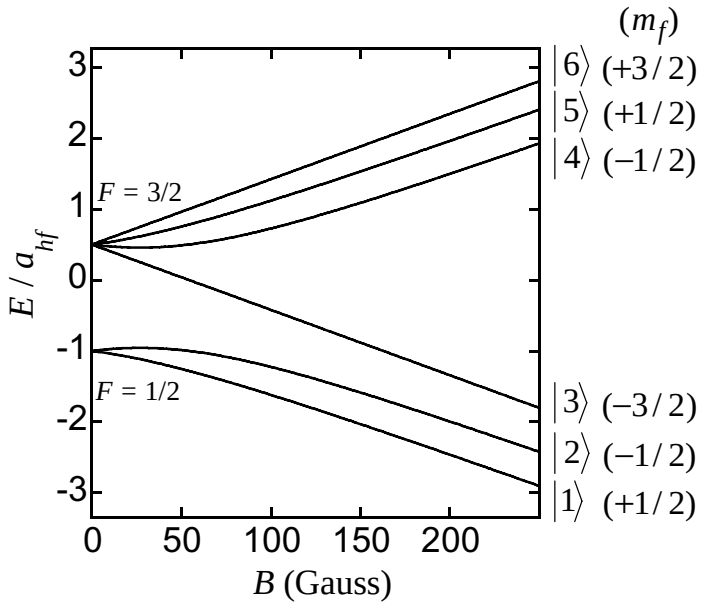

Figure 2.11: Hyperfine state energies of ^{6}Li in an external B-field. The states are labeled $|1\rangle - |6\rangle$ in order of increasing energy. These states are states with definite m_f where the values of m_f are shown on the far right hand side.

quantization axis. The states are given in Appendix A. Note that the coefficients of the product states are magnetic field dependent. It is also important to note that the internal state Hamiltonian (2.33) conserves the quantity $m_f = m_s + m_i$. Thus, the states $|1\rangle$-$|6\rangle$ which diagonalize the internal state Hamiltonian are states with definite m_f.

Figure 2.11 shows the energy of the six internal states in an arbitrary magnetic field. Since the levels do not cross, they can simply be labeled 1 through 6 in order of increasing energy in the **B** field. This labeling convention is identical to that used in Refs. [17, 39, 55]. Since the states $|1\rangle$-$|6\rangle$ are states with definite m_f, the states are also labeled on the right hand side by m_f.

When two colliding ^{6}Li atoms are separated by an infinite distance, the states $|1\rangle$ through $|6\rangle$ are the eigenstates of the atoms. Thus, when two atoms collide

they will approach one another in an antisymmetric combination $|\{\alpha,\beta\}_-\rangle$ of spin states where α and β are one of these six states. The antisymmetric spin state $|\{\alpha,\beta\}_-\rangle$ can be expressed with the help of Clebsch-Gordan coefficients in terms of a superposition of electron spin singlet and spin triplet states. In general, the two-body spin wavefunction is neither purely triplet nor purely singlet but rather a superposition of both. Thus, the scattering length for an antisymmetric combination in an arbitrary $\mathbf{B}$ field is not in general given by either the singlet or the triplet scattering length.

We will now turn our attention toward deriving the coupled channel Schrödinger equation which describes the collision between two ^{6}Li atoms. The collision of two ground state ^{6}Li atoms is described in the center-of-mass frame by the Hamiltonian

$$\mathcal{H} = \frac{\mathbf{p}^2}{2\mu} + \sum_{i=1}^{2} H_i^{int} + V(\mathbf{r}) \tag{2.34}$$

where $\mathbf{p}$ is the relative momentum, $\mathbf{r}$ is the relative coordinate, H_i^{int} is the internal Hamiltonian for each of the atoms (described above and in Appendix A) and $V(\mathbf{r})$ is the interaction potential.

We will denote the eigenstates of the internal state Hamiltonian

$$H_0 = \sum_{i=1}^{2} H_i^{int} \tag{2.35}$$

as $|\{\alpha,\beta\}_-\rangle$ with eigenvalue $\epsilon_\alpha+\epsilon_\beta$ (i.e. $H_0\ |\{\alpha,\beta\}_-\rangle = (\epsilon_\alpha+\epsilon_\beta)\ |\{\alpha,\beta\}_-\rangle$). These eigenstates are antisymmetric combinations of the internal-spin-state eigenstates given in Appendix A. As discussed in Section 2.6, s-wave collisions only occur if the spin wave function is antisymmetric. The states $|\{\alpha,\beta\}_-\rangle$ are referred to as channel states since the product of a state $|\{\alpha,\beta\}_-\rangle$ and a free particle spatial wave

function are the eigenstates of the asymptotic Hamiltonian. Thus, asymptotically, the colliding particles will approach one another in an entrance channel $|\{\alpha,\beta\}_-\rangle$ and will recede from one another in one or more exit channels $|\{\alpha',\beta'\}_-\rangle$.

The total wave function Ψ representing the relative motion of the ^{6}Li atoms can be written as a sum over these channel states with spatially dependent coefficients

$$\Psi = \sum_{\{\alpha'\,\beta'\}} \sum_{l',m'} \frac{F_{l'\,m'\,\{\alpha'\beta'\}}(r)}{r}\, Y_{l'}^{m'}(\theta,\phi)\; |\{\alpha',\beta'\}_-\rangle\,. \tag{2.36}$$

Substitution into the time-independent Schrödinger equation $\mathcal{H}\,\Psi = E\,\Psi$ and projection onto $Y_l^m(\theta,\phi)\; |\{\alpha,\beta\}_-\rangle$ yields the coupled channel Schrödinger equation

$$\begin{aligned}\left[-\frac{\hbar^2}{2\mu}\frac{d^2}{dr^2} + \frac{l(l+1)\hbar^2}{2\mu r^2} + \epsilon_\alpha + \epsilon_\beta - E\right] F_{lm\,\{\alpha\beta\}}(r) = \\ - \sum_{\{\alpha'\,\beta'\}} \sum_{l',m'} V_{lm\{\alpha\beta\},l'm'\{\alpha'\beta'\}}(r)\, F_{l'm'\{\alpha'\beta'\}}(r),\end{aligned} \tag{2.37}$$

which is an infinite set of coupled differential equations that determine the functions $F_{lm\{\alpha\beta\}}(r)$. The coupling matrix is defined as

$$V_{lm\{\alpha\beta\},l'm'\{\alpha'\beta'\}}(r) \equiv \int d\Omega\, Y_{lm}^*(\theta,\phi)\, Y_{l'm'}(\theta,\phi)\; \langle\{\alpha,\beta\}_-|\, V(\mathbf{r})\, |\{\alpha',\beta'\}_-\rangle \tag{2.38}$$

Eq. (2.37) is solved subject to the boundary conditions

$$\begin{aligned} F_{lm\,\{\alpha\beta\}}(0) &= 0 \\ F_{lm\,\{\alpha\beta\}}(r) &\underset{r\to\infty}{\longrightarrow} e^{i\,\mathbf{k}_{\alpha\beta}\cdot\mathbf{r}} + f(\theta,\phi)\,\frac{e^{i\,k_{\alpha\beta}\,r}}{r}\end{aligned} \tag{2.39}$$

for the entrance channel, and

$$\begin{aligned} F_{lm\,\{\alpha\beta\}}(0) &= 0 \\ F_{lm\,\{\alpha\beta\}}(r) &\underset{r\to\infty}{\longrightarrow} f(\theta,\phi)\,\frac{e^{i\,k_{\alpha\beta}\,r}}{r} \end{aligned} \tag{2.40}$$

for all outgoing channels. The wave number $k_{\alpha\beta}$ satisfies the condition $\hbar^2 k_{\alpha\beta}^2/2\mu = E - \epsilon_\alpha - \epsilon_\beta$.

Note that we do *not* consider here the possibility that one or both of the atoms involved in the collision are in an electronic excited state. As long as the atoms are not excited into these states by an external optical field, the electronic excited molecular states do not need to be considered when describing an ultracold collision between two ground state ^{6}Li atoms. This is due to the fact that the electronic excited state molecular potential for Li_2 is not deep enough for the electronic excited state to become energetically allowed. Thus, even during the collision when the atoms are in close proximity to one another, the possibility that the atoms are in a state containing an admixture of an electronic excited state is energetically forbidden and therefore does not need to be considered.

For two ground state alkali atoms, the interaction potential is relatively simple compared to other multi-electron atoms. It is given by the sum of a central electrostatic interaction potential and a magnetic dipole-dipole interaction potential

$$V(\mathbf{r}) = V^c(r) + V^d(\mathbf{r}). \tag{2.41}$$

The electrostatic interaction potential $V^c(r)$ is given by

$$V^c(r) = V_0(r)\,\mathcal{P}^{(0)} + V_1(r)\,\mathcal{P}^{(1)}, \tag{2.42}$$

where $\mathcal{P}^{(0)}$ and $\mathcal{P}^{(1)}$ denote projection operators onto the singlet and triplet total-electron-spin subspaces respectively. $V_0(r)$ and $V_1(r)$ are the singlet and triplet potentials described in section Section 2.5. $V^d(\mathbf{r})$ represents the sum of the electron-electron and electron-proton magnetic dipole interactions. $V^d(\mathbf{r})$ is much weaker than the electrostatic interaction $V^c(r)$. We will neglect this interaction whenever V^c gives nonzero elastic and inelastic rate constants. However, in situations in which the inelastic collision rate due to $V^c(r)$ vanishes, V^d gives the dominant inelastic rate constant. In Section 2.10 we will discuss its implications for inelastic rate constants.

Neglecting $V^d(\mathbf{r})$, we are left with the central potential $V(\mathbf{r}) = V^c(r)$ which only couples channel states with the same orbital angular momentum. For an ultracold gas we need only consider s-wave collisions. Under these assumptions, the coupled channel equation reduces to

$$\left[-\frac{\hbar^2}{2\mu}\frac{d^2}{dr^2} + \epsilon_\alpha + \epsilon_\beta - E\right] F_{\{\alpha\beta\}}(r) = - \sum_{\{\alpha'\beta'\}} \langle\{\alpha,\beta\}_-|\, V^c(r)\,|\{\alpha',\beta'\}_-\rangle\; F_{\{\alpha'\beta'\}}(r). \tag{2.43}$$

Symmetry considerations allow us to group the channel states into uncoupled subsets. Since $V^c(r)$ is a central potential, the total angular momentum is conserved. As shown in Appendix A, the internal Hamiltonian eigenstates $|\{\alpha,\beta\}_-\rangle$ have definite projection of the total spin $M_F = m_{f1} + m_{f2}$. Since $V^c(r)$ conserves angular momentum, only channels with the same M_F are coupled. For example, consider a mixture of ^{6}Li atoms with half in state $|6\rangle$ and half in state $|5\rangle$ (where the states are those defined in Appendix A). State $|6\rangle$ has a spin projection $m_{f1} = 3/2$ and state $|5\rangle$ has $m_{f2} = 1/2$ giving a total $M_F = 2$. Only one other combination

of states has $M_F = 2$: $|6\rangle$ and $|1\rangle$. Thus, the channel state $|\{6,5\}_-\rangle$ is coupled to the channel state $|\{6,1\}_-\rangle$ via $V^c(r)$ and Eq. (2.43) reduces to two coupled differential equations. These coupled equations describe both the elastic collision $|\{6,5\}_-\rangle \to |\{6,5\}_-\rangle$ and the inelastic collision $|\{6,5\}_-\rangle \to |\{6,1\}_-\rangle$.

From integration of Eq. (2.43) we can obtain the s-wave scattering length for elastic collisions and the inelastic spin-exchange rate. To simplify our notation we will denote the entrance channel state as $|i\rangle$ and all other coupled channel states as $|j\rangle$. Asymptotically far from the potential $V^c(r)$, the total wave function is the sum of a plane wave in the entrance channel and the product of a scattering amplitude and an outgoing spherical wave for each exit channel. Considering only the $l = 0$ partial wave, the plane wave is given by $\sin(k_i r)/k_i r$ and the scattering amplitudes are independent of θ and ϕ. The asymptotic total wave function Ψ is

$$\begin{aligned} \Psi &\sim \left(\frac{\sin(k_i r)}{k_i r} + f_{ii}\frac{e^{ik_i r}}{r}\right)|i\rangle + \sum_j f_{ji}\frac{e^{ik_j r}}{r}|j\rangle \\ &= -\frac{1}{2ik_i r}\left\{\left(e^{-ik_i r} + \tilde{S}_{ii}e^{ik_i r}\right)|i\rangle + \sum_j \tilde{S}_{ji}e^{ik_j r}|j\rangle\right\} \end{aligned} \tag{2.44}$$

where $\tilde{S}_{ii} = -1 - 2ik_i f_{ii}$ and $\tilde{S}_{ji} = -2ik_i f_{ji}$. The wave numbers k_j depend on the energy gained in the transition to the respective outgoing channel. Thus, $k_j = \sqrt{k_i^2 + 2\mu\Delta_{i\to j}/\hbar^2}$ where $\Delta_{i\to j}$ is the energy gained in the transition (i.e. $\Delta_{i\to j} = \epsilon_i - \epsilon_j$). Note that in cases where $\epsilon_j > \epsilon_i$ the corresponding wave number k_j may be imaginary yielding an exponentially decaying wave function. In such a case, this channel is said to be "closed".

$\tilde{S}_{ii}$ and $\tilde{S}_{ji}$ are related to the S matrix as defined in most textbooks on scattering theory by $S_{ii} = -\tilde{S}_{ii}$ and $S_{ji} = -\sqrt{k_j/k_i}\,\tilde{S}_{ji}$. In terms of the s-wave phase shift $\tilde{S}_{ii} = -e^{2i\delta_0}$. The elastic s-wave scattering length a is related to the low energy $\tilde{S}$

matrix by

$$\lim_{k\to 0} \tilde{S}_{ii} = -\lim_{k\to 0} e^{2i\delta_0} = -\lim_{k\to 0} e^{-2ik_i a} = -1 + 2ik_i a. \tag{2.45}$$

Note that δ_0 and a may now be complex where the imaginary part corresponds to the loss of flux to other channels.

By considering the ratio of the flux into a solid angle $d\Omega$ to the incoming flux we find the elastic and inelastic differential cross sections

$$\begin{aligned} \frac{d\sigma_{ii}}{d\Omega} &= |f_{ii}|^2 = \left| \frac{1+\tilde{S}_{ii}}{2ik_i} \right|^2 = |a|^2 \\ \frac{d\sigma_{ji}}{d\Omega} &= \frac{k_j}{k_i} |f_{ji}|^2 = \frac{1}{4k_i^2} |S_{ji}|^2 . \end{aligned} \tag{2.46}$$

The total elastic cross section $\sigma_{ii} = 4\pi a^2$. The rate for spin-exchange transitions from state $|i\rangle$ to state $|j\rangle$ in the low-energy limit is $R_{i\to j} = n_i \, v_i \, \sigma_{ji} \equiv G_{i\to j} \, n_i$ where

$$G_{i\to j} = \frac{\pi\hbar}{\mu k_i} |S_{ji}|^2 , \tag{2.47}$$

n_i is the density of atoms, and v_i is their relative velocity.

After numerically integrating the coupled Schrödinger equation Eq. (2.43) subject to the boundary conditions Eqs. (2.39), the S matrix can be extracted from the asymptotic form of the wave function. The elastic scattering length a and the inelastic spin-exchange rate constant G can then be determined as shown above. Two groups have computed the scattering length a and inelastic spin-exchange rate constants G for a select number of two-state ^{6}Li mixtures using this method [55, 70]. Some of these results will be discussed below. Since numerical integration of Eq. (2.43) is not entirely trivial, the authors of Ref. [55] present an approximate

method by which the low-energy S matrix can be obtained analytically. This approximation is the subject of Section 2.7.

2.8 Asymptotic Boundary Condition Approximation

In this section we will outline the asymptotic boundary condition (ABC) approximation presented in Ref. [55] which provides an analytical method for obtaining the magnetic field dependent elastic scattering length and spin exchange rate constant for two-state mixtures of ultracold ^{6}Li atoms. The ABC approximation is based on a boundary condition model presented in Ref. [71].

In the ABC approximation, the relative coordinate space is divided into two regions where the division occurs at a position $r = R$. In the exterior region $r > R$, the hyperfine energy dominates over the singlet and triplet potentials. In this region the wave function has its asymptotic form:

$$\begin{aligned} |\psi(r_>)\rangle &= \left(e^{-ik_i r} + \tilde{S}_{\{\alpha\beta\},\{\alpha\beta\}} e^{ik_{\alpha\beta} r}\right) |\{\alpha,\beta\}_-\rangle \\ &\quad + \sum_{\{\alpha'\beta'\}} \tilde{S}_{\{\alpha'\beta'\},\{\alpha\beta\}} e^{ik_{\alpha'\beta'} r} |\{\alpha',\beta'\}_-\rangle \,. \end{aligned} \tag{2.48}$$

Note that we have dropped the $1/r$ dependence of the wavefunction here for simplicity. In Eq. (2.48), the states $|\{\alpha,\beta\}_-\rangle$ and $|\{\alpha',\beta'\}_-\rangle$ all have the same total spin projection M_F since they are the only state which are coupled.

In the interior region $r < R$ the singlet and triplet potentials dominate over the hyperfine energy which is neglected. Thus, the interior wave function can be written as a linear combination of singlet and triplet wave functions. For $r \simeq R$

the singlet and triplet wave functions are well approximated by their asymptotic forms sin $k_{\alpha\beta}(r - a_s)$ and sin $k_{\alpha\beta}(r - a_t)$ where a_s and a_t are the singlet and triplet scattering lengths found in sections Section 2.5.2 and Section 2.5.3 respectively. Thus, near R, $|\psi(r_<)\rangle$ can be written as a linear superpostion of singlet and triplet asymptotic wave functions which are each multiplied by a singlet or triplet spin state respectively. By requiring that $|\psi(r)\rangle$ and $|\psi'(r)\rangle$ be continuous at $r = R$ we can solve for the unknown coefficients $\tilde{S}_{\{\alpha'\beta'\},\{\alpha\beta\}}$ and $\tilde{S}_{\{\alpha\beta\},\{\alpha\beta\}}$. Finally, the elastic scattering length a and the inelastic spin-exchange rate constants $G_{\alpha\beta\to\alpha'\beta'}$ can be obtained using Eqs. (2.45) (2.47).

In the following sections we will use the ABC approximation to calculate a and $G_{\alpha\beta\to\alpha'\beta'}$ for several two-state mixtures. We will examine the strengths and weaknesses of different two-state mixtures for use in fundamental studies of a dilute, ultracold, interacting fermi gas. We use the ABC approximation to obtain the magnetic field dependent scattering length a_{31} for a mixture of atoms in states $|3\rangle$ and $|1\rangle$ in Section 2.10. We find that this previously unexamined mixture of ^{6}Li atoms is well suited for studies of degenerate Fermi effects in an optical trap.

2.9 Collisions in a $|6\rangle$-$|5\rangle$ Mixture

In this section we will use the ABC approximation to calculate the scattering properties of a mixture of ^{6}Li atoms in states $|6\rangle$ and $|5\rangle$. We have chosen this mixture because it is a simple application of the ABC approximation since only two states are coupled. In addition, these states are of interest because they can both be confined in a magnetic trap. As shown in Appendix B, only a minimum in $|\mathbf{B}|$ can be obtained in free space. Thus, the weak field seeking states ($|4\rangle$, $|5\rangle$ and $|6\rangle$) whose internal energies are minimized at a field minimum can be trapped in a magnetic

field.

The antisymmetrized spin state $|\{6,5\}_-\rangle = (|6\rangle_1 |5\rangle_2 - |5\rangle_1 |6\rangle_2)/\sqrt{2}$ can be written either in terms of the product states $|m_{s1}\, m_{i1}\rangle\, |m_{s2}\, m_{i2}\rangle$ as in Appendix A or in terms of the total electron and nuclear spin states $|S\, M_S\rangle |I\, M_I\rangle$ where $\mathbf{S} = \mathbf{s_1} + \mathbf{s_2}$ is the total electron spin, $\mathbf{I} = \mathbf{i_1} + \mathbf{i_2}$ is the total nuclear spin and M_S and M_I are their projections along the quantization axis. Transformation from one basis to the other is easily accomplished by use of the appropriate Clebsch-Gordan coefficients. The $|\{6,5\}_-\rangle$ channel is coupled to $|\{6,1\}_-\rangle$ since they both have total spin projection $M_F = 2$. $|\{6,1\}_-\rangle$ can also be expressed in terms of the total electron and nuclear spin states. Using the results from Appendix A, we have in the $|S\, M_S; I\, M_I\rangle$ basis

$$\begin{aligned} |\{6,5\}_-\rangle &= \sin\theta_+ \,|0\,0;2\,2\rangle + \cos\theta_+ \,|1\,1;1\,1\rangle \\ |\{6,1\}_-\rangle &= \cos\theta_+ \,|0\,0;2\,2\rangle - \sin\theta_+ \,|1\,1;1\,1\rangle \end{aligned} \tag{2.49}$$

Note that the parameter θ_+ is magnetic field dependent. In the asymptotic boundary condition approximation, the interior wave function is given by a linear superposition of singlet and triplet wave functions and the exterior wave function is given by the asymptotic form (Eq. (2.48)):

$$\begin{aligned} |\psi(r_<)\rangle &= \psi_S(r)\,|0\,0;2\,2\rangle + \psi_T(r)\,|1\,1;1\,1\rangle\,, \\ |\psi(r_>)\rangle &= \left(e^{-ik_{65}r} + \tilde{S}_{\{65\},\{65\}} e^{ik_{65}r}\right) |\{6,5\}_-\rangle + \tilde{S}_{\{61\},\{65\}} e^{ik_{61}r}\,|\{6,1\}_-\rangle\,. \end{aligned} \tag{2.50}$$

We require that $|\psi(r)\rangle$ and be continuous at $r = R$. By projecting Eqs. (2.50) onto

the states $|0\,0;2\,2\rangle$ and $|1\,1;1\,1\rangle$ and using Eqs. (2.49) and (2.50) we find

$$\begin{aligned}\psi_S(R) &= \sin\theta_+\left(e^{-ik_{65}R}+\tilde{S}_{\{65\},\{65\}}e^{ik_{65}R}\right)+\cos\theta_+\tilde{S}_{\{61\}\{65\}}e^{ik_{65}R},\\ \psi_T(R) &= \cos\theta_+\left(e^{-ik_{65}R}+\tilde{S}_{\{65\},\{65\}}e^{ik_{65}R}\right)-\sin\theta_+\tilde{S}_{\{61\},\{65\}}e^{ik_{61}R}.\end{aligned} \tag{2.51}$$

We also know that for $r = R$ the singlet and triplet spatial wave functions are given by their asymptotic forms $\psi_S(R) = A_S \sin k_{65}(R - a_S)$ and $\psi_T(R) = A_T \sin k_{65}(R - a_T)$ where A_S and A_T are undetermined coefficients. Thus, to first order in k_{65} we have that $\psi_S(R)/\psi_S'(R) \cong (R - a_S)$ and $\psi_T(R)/\psi_T'(R) \cong (R - a_T)$. Since we are only interested in determining $\tilde{S}$ to first order in k_{65} we can find $\tilde{S}_{\{65\},\{65\}}$ and $\tilde{S}_{\{61\},\{65\}}$ by solving the 2 algebraic equations

$$\begin{aligned}\psi_S(R) &= (R-a_S)\,\psi_S'(R)\\ \psi_T(R) &= (R-a_T)\,\psi_T'(R)\end{aligned} \tag{2.52}$$

where $\psi_S(R)$ and $\psi_T(R)$ are given by Eq.(2.51).

To first order in k_{65} we find that

$$\begin{aligned}\tilde{S}_{\{65\},\{65\}} &= -1+2ik_{65}\left\{R+\frac{ik_{61}^{(0)}(R-a_S)(R-a_T)}{D(k_{61}^{(0)})}\right.\\ &\qquad\left.-\frac{\cos^2\theta_+(R-a_T)+\sin^2\theta_+(R-a_S)}{D(k_{61}^{(0)})}\right\},\\ \tilde{S}_{\{61\},\{65\}} &= \frac{2ik_{65}\cos\theta_+\sin\theta_+(a_S-a_T)}{D(k_{61}^{(0)})},\end{aligned} \tag{2.53}$$

where $k_{61}^{(0)} = \sqrt{2\mu\Delta_{65\to61}/\hbar^2}$ is the wave number for the outgoing channel to zeroth order in k_{65}, $\Delta_{65\to61} = [(\epsilon_6+\epsilon_5)-(\epsilon_6+\epsilon_1)]$ is the energy gained in making the

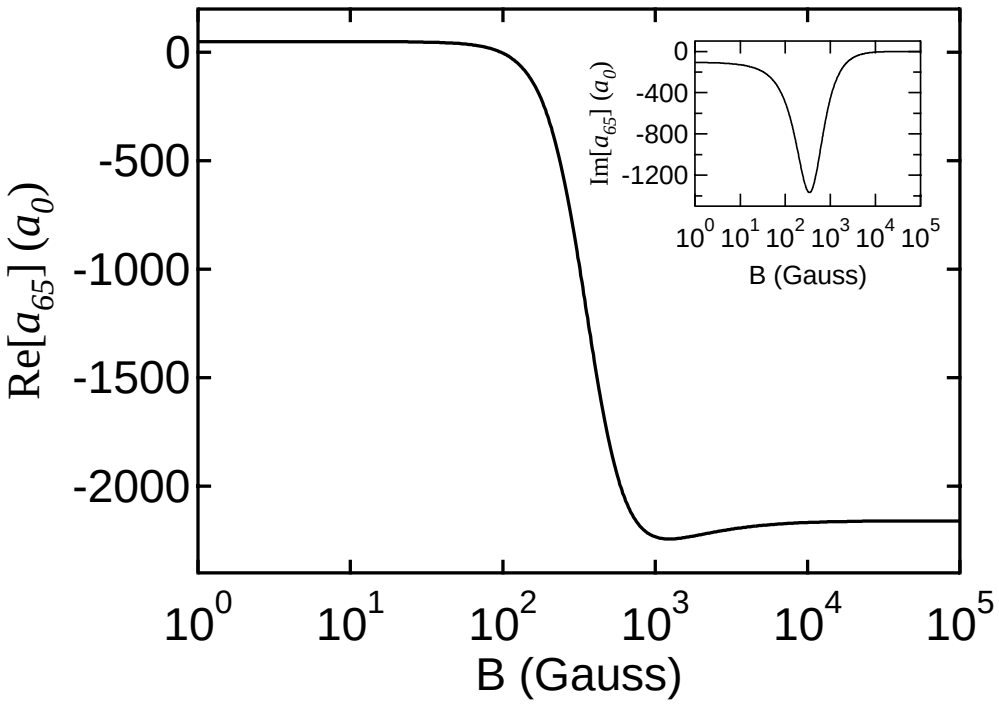

Figure 2.12: Magnetic field dependence of a_{65}. Since inelastic collisions are possible a_{65} has both a real (main figure) and imaginary (inset) part.

transition from $65 \rightarrow 61$ and

$$D(k_{61}^{(0)}) = 1 - ik_{61}^{(0)}[\cos^2\theta_+(R - a_S) + \sin^2\theta_+(R - a_T)]. \tag{2.54}$$

The scattering length $a_{65} = (1+\tilde{S}_{\{65\},\{65\}})/2ik_{65}$ and the spin-exchange rate constant $G_{65\rightarrow 61}$ is given by Eq. (2.47). The best value to use for R is not known *a priori*. However, in Ref. [55] a value of $R = 40a_0$ gives surprisingly good agreement with the exact result obtained by numerically integrating the coupled Schrödinger equation.

Figure 2.12 is a plot of the real part of a_{65} as a function of magnetic field B. Since the $|\{6,1\}_-\rangle$ inelastic channel is open, a_{65} also has an imaginary part which is shown as a function of B in the inset. Note that the triplet scattering length $a_T = -2160a_0$

is only obtained for fields above 750 Gauss. This is a somewhat surprising result since at zero field $|\{6,5\}_-\rangle = 1/\sqrt{3}|0\,0;2\,2\rangle + \sqrt{2/3}|1\,1;1\,1\rangle$ which is predominately composed of the triplet state $|1\,1;1\,1\rangle$. One might naively have expected a_{65} to be $2/3\,a_T$. This, in fact, is what one obtains if the hyperfine interaction is neglected (*i.e.*, $a_{hf} = 0$). Although the large triplet scattering length can be obtained for fields beyond 750 Gauss, the large inelastic spin-exchange rate constant that accompanies it makes this mixture a poor candidate for studies of interacting degenerate Fermi effects.

The inelastic process $|\{6,5\}_-\rangle \rightarrow |\{6,1\}_-\rangle$ releases enough energy to expel both atoms involved in the collision from a standard magnetic trap. Figure 2.13 shows the magnetic field dependence of the inelastic spin-exchange rate constant $G_{65\rightarrow 61}$. As shown in Chapter 1, to study quantum degenerate effects we want to obtain densities between $10^{12}\,\mathrm{atoms/cm^3}$ and $10^{14}\,\mathrm{atoms/cm^3}$. Thus, this rate constant is prohibitively large for evaporative cooling (which proceeds over 10's or 100's of seconds) and unfavorable for studies of quantum degenerate effects.

A large inelastic spin-exchange decay rate is found for each of the two-state mixtures that can be trapped magnetically (the $|6\rangle$-$|4\rangle$ and $|5\rangle$-$|4\rangle$ mixtures). Thus, magnetically trapped two-state mixtures of ^{6}Li atoms are unfavorable for evaporative cooling and studies of quantum statistical effects. However, in Chapter 3 we will show that optical traps can store any hyperfine state of ^{6}Li in a nearly conservative potential. Therefore, we will now turn our attention toward mixtures which cannot be magnetically trapped. We are interested in mixtures that do not exhibit a large inelastic collision rate while at the same time provide a large and negative elastic scattering length that is beneficial for efficient evaporative cooling and essential for observing a superfluid transition.

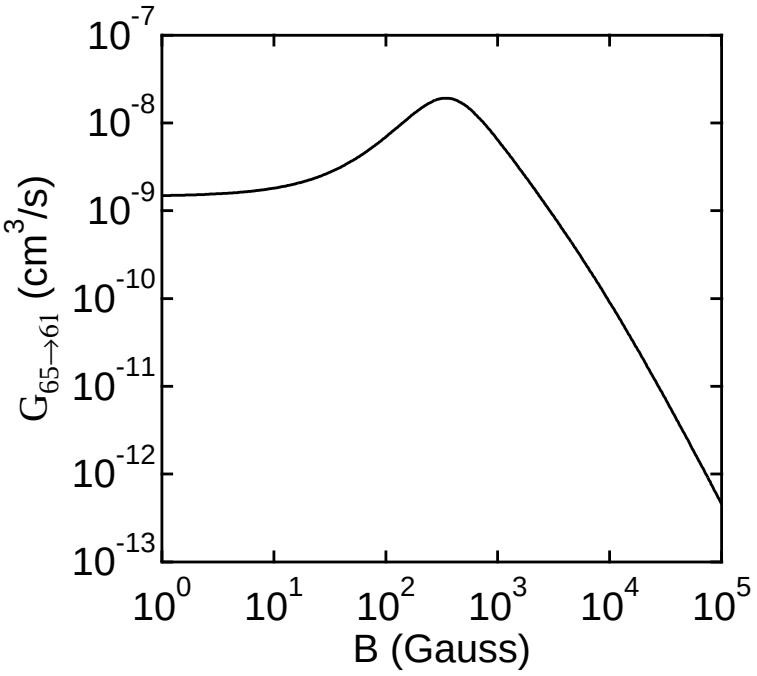

Figure 2.13: Magnetic field dependence of $G_{65\to 61}$.

2.10 Stable Mixtures of ^{6}Li

Since we wish to avoid exothermic inelastic collisions, we will first examine a mixture of the two lowest energy hyperfine states: $|1\rangle$ and $|2\rangle$. The $|\{2,1\}_-\rangle$ channel has a total spin projection $M_F = 0$. Thus, the $|\{2,1\}_-\rangle$ channel is coupled to the four other channels with $M_F = 0$: $|\{4,5\}_-\rangle$, $|\{6,3\}_-\rangle$, $|\{5,2\}_-\rangle$, and $|\{4,1\}_-\rangle$. However, all of these states are have a much higher energy than the $|\{2,1\}_-\rangle$ mixture. To make a spin-exchange transition to the nearest higher lying channel a thermal energy of at least 10 milliKelvin is required. Thus, for the ultracold ^{6}Li vapors considered here these higher-lying channels are closed. However, although these channels are closed they must be considered in the coupled-channel calculation of the elastic scattering length. The presence of these closed channels has a profound effect on the $|\{2,1\}_-\rangle$ scattering length through a Feshbach resonance as described below.

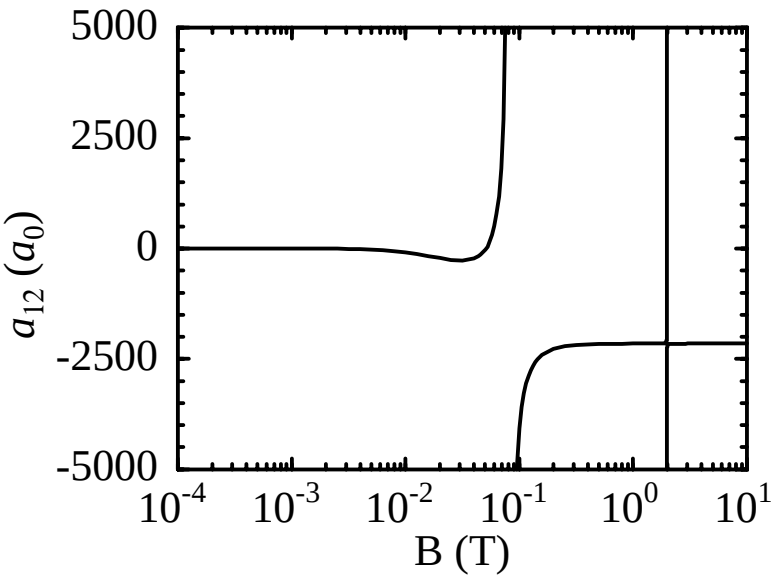

Figure 2.14: Magnetic field dependence of a_{12}.

A calculation based on the ABC approximation and includes all five coupled channels gives reasonably good agreement with the exact coupled-channel calculation. However, it doesn't precisely predict the low-field dependence of the scattering length nor the exact location of a Feshbach resonance. We present here the results obtained in Ref. [55] using an exact coupled-channel calculation. Figure 2.14 shows the scattering length a_{21} as a function of applied magnetic field in Tesla . The low-energy inelastic spin-exchange rate constant for the $|\{2,1\}_-\rangle$ mixture is identically zero since all other coupled channels are closed. Thus, the scattering length is purely real.

There are several notable features in Fig. Figure 2.14. First, at $B = 0$ the scattering length is predicted to be exactly zero. To our knowledge, the absence of a scattering length at zero field is not due to any fundamental constraints but rather must be due to an accidental interference effect. This property can be useful since it

allows one to "turn off" interactions in this mixture by simply zeroing the applied field. We will make use of this effect in Chapter 4 and Chapter 7. The other important features of interest are the resonant behaviours that occur at ~ 0.1 Tesla and 2 Tesla. These "Feshbach" resonances allow the scattering length to be tuned to $\pm\infty$ by adjusting the magnetic field strength. This is a very exciting prospect since it might allow quantum degenerate effects to be studied in a system in which the interaction strength can be continuously tuned over a wide range including both attractive and repulsive interactions.

The physical origin of these Feshbach resonances deserves a brief explanation. Resonance features in scattering can be divided into two classes: shape resonances and Feshbach resonances. Both resonant features arise when a continuum state energy is degenerate with a bound state. In shape resonances, the bound and continuum states belong to the same internal state of the system. In a Feshbach resonance, the bound and continuum states belong to different internal states. Figure 2.15 is a schematic of a Feshbach resonance. A resonance occurs whenever the continuum energy for an open channel is resonant with a bound state of the closed channel.

In the case of the $|\{2,1\}_-\rangle$ resonances, the $|\{2,1\}_-\rangle$ mixture is almost a pure triplet state with a small singlet admixture at these large magnetic fields. The $|\{2,1\}_-\rangle$ state has a field dependent energy of about $-2\mu_e B$ since it is almost a pure triplet state. Conversely, the singlet state, having a negligible dipole moment, doesn't tune in a magnetic field. Thus, by adjusting the magnetic field, the energy of the $|\{2,1\}_-\rangle$ entrance channel can be tuned such that it is in resonance with a bound singlet state of higher lying closed channels. The features at ~ 0.08 Tesla and ~ 2 Tesla in Fig. Figure 2.14 are due to resonances with the $\nu = 38$ and 37

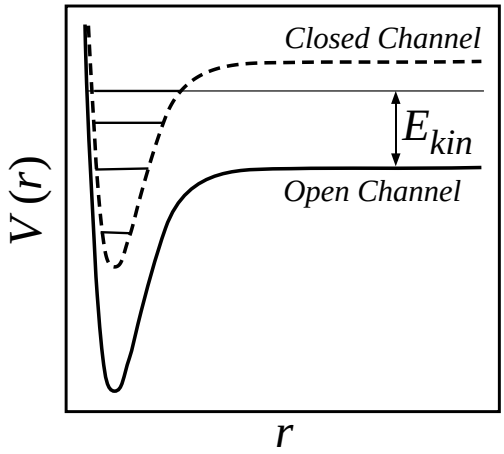

Figure 2.15: Physical origin of a Feshbach resonance. In a Feshbach resonance, the continuum state energy for an open channel comes into resonance with the bound state energy for a closed channel.

vibrational states of the singlet potential respectively.

We have shown that optical trapping of a $|2\rangle$-$|1\rangle$ mixture is an extremely useful system since it provides a highly tunable scattering length and does not suffer from an inelastic spin-exchange rate. These properties make it a promising candidate for fundamental studies of interacting fermions and may also provide a means for efficient evaporative cooling to achieve ultralow temperatures. Unfortunately, the scattering length is relatively small at low fields. To take advantage of either the Feshbach resonance or the large triplet scattering length a magnetic field of approximately 1 kG is required. Although this field is relatively easy to obtain at the center of a moderate power solenoid, the competing requirements of good optical access and compatibility with an ultra-high vacuum environment make achieving this field extremely difficult.

An excellent alternative is provided by the $|3\rangle$-$|1\rangle$ mixture, which also cannot be confined in a magnetic trap. The $|\{3,1\}_-\rangle$ channel has a total spin projection

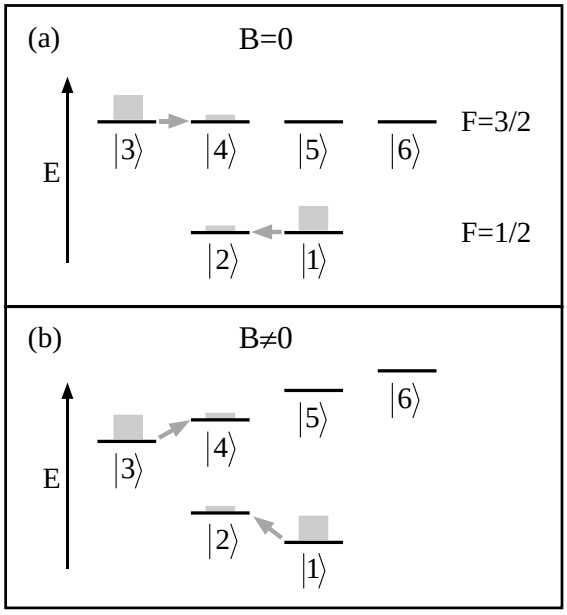

Figure 2.16: Spin exchange collisions for $|\{3,1\}_-\rangle$ mixture. (a) For $B = 0$ spin-exchange collisions can occur in which $|\{3,1\}_-\rangle \rightarrow |\{4,2\}_-\rangle$. (b) However, for $B \neq 0$, spin-exchange collisions for which $|\{3,1\}_-\rangle \rightarrow |\{4,2\}_-\rangle$ require energy in order to occur.

$M_F = -1$. There are two other channels with $M_F = -1$ to which this state is coupled. These are the $|\{4,2\}_-\rangle$ and $|\{5,3\}_-\rangle$ states. At zero field, the $|\{4,2\}_-\rangle$ state is degenerate with the $|\{3,1\}_-\rangle$ state while the $|\{5,3\}_-\rangle$ state energy is higher by the hyperfine splitting $3a_{hf}/2$. Thus, for a low energy collision along the $|\{3,1\}_-\rangle$ entrance channel the $|\{4,2\}_-\rangle$ channel is open while the $|\{5,3\}_-\rangle$ channel is closed for $B = 0$. Barring any fortuitous interference effects, the inelastic spin-exchange rate constant $G_{31\to 42}$ will therefore be finite at zero field. However, as shown in Figure 2.16, the inelastic spin-exchange transition $|\{3,1\}_-\rangle \to |\{4,2\}_-\rangle$ requires a relative kinetic energy $E_{req} = -\Delta_{31\to 42} = (\epsilon_4 + \epsilon_2) - (\epsilon_3 + \epsilon_1)$ for a nonzero B field. Thus, the $|\{4,2\}_-\rangle$ channel can be closed if a field B is applied such that the required relative kinetic energy E_{req} is greater than that which is available to atoms in the trap. Since we can eliminate spin-exchange collisions in the $|\{3,1\}_-\rangle$ mixture by an appropriate choice of B-field, we wish to calculate the elastic scattering length for this combination.

The field dependent elastic scattering length for the $|\{3,1\}_-\rangle$ mixture was not calculated in either Refs. [55, 70]. Using a three-channel ABC approximation we calculated a_{31}, the results of which are shown in Figure 2.17. At our request, these results were later verified by F. A. van Abeleen and B. J. Verhaar by an exact coupled channel calculation. At zero field the scattering length goes to the large and negative value of $-1615a_0$. At high field, a_{31} goes to the triplet scattering length $a_T = -2160a_0$ since at high field the $|\{3,1\}_-\rangle$ combination is almost purely in the triplet state. We believe that a Feshbach resonance should also exist for the $|\{3,1\}_-\rangle$ combination at ~ 0.1 Tesla (not shown). Thus, at low magnetic fields an optically trapped $|3\rangle$-$|1\rangle$ mixture can provide a large and negative scattering length and is stable against spin-exchange collisions for ultracold atoms.

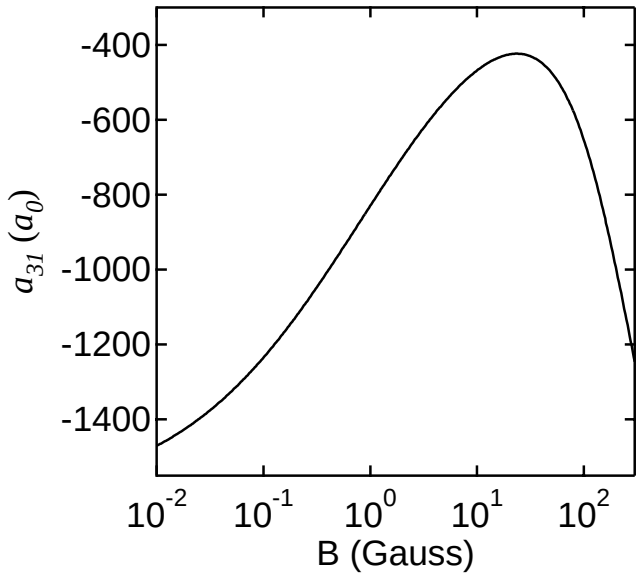

Figure 2.17: Magnetic field dependence of a_{31}.

The scattering length a_{31} is widely tunable at low magnetic field, varying from $a_{31} = -1615\,a_0$ at $B = 0$ to $a_{31} \simeq -400\,a_0$ at $B = 20$ G. The wide tunability of a_{31} at low field is made possible by the presence of the near zero energy resonance in the triplet potential. A near zero energy resonance occurs whenever a molecular potential supports a barely bound or barely unbound state. The binding energy of this state is given approximately by $E_b \sim \hbar^2/Ma^2$. For large $|a|$, this energy scale can be quite small and only a modest change in the incoming channel state energy is required to cause a large change in the scattering length. For example, the energy scale for the triplet scattering length $E_b \sim \hbar^2/Ma_t^2 \simeq 6\,\mu$K. By applying a magnetic field such that $\mu_b B \sim \hbar^2/Ma_t^2$ the a_{31} scattering length can be dramatically changed. This requires a magnetic field $B \sim \frac{1}{10}$ G. Thus, the scattering length a_{31} can be widely tuned by applying only a small magnetic field as shown in Figure 2.17.

2.11 Dipolar Relaxation Collisions

In Section 2.10 we found that both the $|2\rangle$-$|1\rangle$ and $|3\rangle$-$|1\rangle$ mixtures can be made stable with respect to spin-exchange collisions, which can arise in the coupled channel Schrödinger equation due to coupling via the central electrostatic interaction potential $V^c(r)$. However, these mixtures are not completely immune to inelastic internal-state-changing collisions. In the preceding analysis we neglected coupling between channel states due to the non-central dipolar interaction potential $V^d(\mathbf{r})$ since it is much weaker than $V^c(r)$. However, in the event that the spin-exchange collision rate due to coupling via $V^c(r)$ vanishes, the dominant inelastic loss rate will be due to channel coupling via $V^d(\mathbf{r})$.

The magnetic dipolar interaction potential $V^d(\mathbf{r})$ arises from the electron-electron, electron-nucleon and nucleon-nucleon magnetic dipole moment interactions. Since the nuclear magnetic moment μ_n is several orders of magnitude smaller than the Bohr magneton μ_e, we can neglect the electron-nucleon and nucleon-nucleon dipolar interactions compared to the electron-electron dipolar interaction. The interaction potential between two magnetic moments is

$$V^d(\mathbf{r}) = \left(\frac{3(\hat{\mathbf{n}} \cdot \mathbf{s_1})(\hat{\mathbf{n}} \cdot \mathbf{s_2}) - \mathbf{s_1} \cdot \mathbf{s_2}}{r^3} \right), \tag{2.55}$$

where μ_0 is the permeability of free space. It is instructive to rearrange this potential into the form

$$V^d(\mathbf{r}) = -\frac{\mu_0 \mu_e^2}{4\pi r^3} \sum_{\mu=-2}^{2} \left(\frac{4\pi}{5} \right)^{1/2} (-1)^{\mu} Y_{2,-\mu}(\hat{\mathbf{r}}) \, \Sigma^{ee}_{2\mu}, \tag{2.56}$$

the derivation of which can be found in [72]. Here $\Sigma^{ee}_{2,\mu}$ is a tensor operator arising

from the coupling between the electron spins to a tensor of rank 2. Note that the spherical harmonic $Y_{2,-\mu}$, which operates on the angular part of the relative spatial coordinate, can couple channel states with different angular momenta because it is a rank 2 spherical tensor operator.

The calculation of inelastic dipolar rates due to the coupling caused by Eq. (2.56) is beyond the scope of this dissertation. However, it is worthwhile to examine what channels can be coupled by V^d based on the Wigner-Eckart theorem. Let us first consider the $|3\rangle$-$|1\rangle$ mixture in a bias field for which spin-exchange collisions have been suppressed. In this case, there are three possible exothermic inelastic transitions that might occur: $|\{3,1\}_-\rangle \rightarrow |\{2,1\}_-\rangle$, $|\{3,1\}_-\rangle \rightarrow |2\rangle_1|2\rangle_2$ and $|\{3,1\}_-\rangle \rightarrow |1\rangle_1|1\rangle_2$ (the subscripts in the last two cases label the colliding atoms 1 and 2). In the first case, the final state has an antisymmetric spin wave function that requires a symmetric spatial wave function, whereas for the other two cases the final state has a symmetric spin wave function requiring an antisymmetric spatial wave function. Since the interaction V^d contains the rank 2 spherical tensor operator $Y_{2,-\mu}(\hat{\mathbf{r}})$, an s-wave entrance channel wave function can only couple to a d-wave outgoing channel wave function. Since a d-wave spatial wave function is symmetric, the final spin state must be an antisymmetric combination. Thus, in the low-energy limit for which only s-wave entrance channels exist, there will exist a finite s-wave $\rightarrow$ d-wave dipolar inelastic rate in which $|\{3,1\}_-\rangle \rightarrow |\{2,1\}_-\rangle$. At our request, F. A. van Abeelen and B. J. Verhaar calculated this inelastic dipolar rate constant by numerically integrating the coupled channel Schrödinger equation and found that $G^d_{\{31\}\rightarrow\{21\}} \sim 10^{-15}\,\mathrm{cm}^3/\mathrm{sec}$. Thus, this small inelastic rate will only become important at high densities.

For the $|2\rangle$-$|1\rangle$ mixture there exists only one possible exothermic inelastic tran-

sition $|\{2,1\}_-\rangle \rightarrow |1\rangle_1 |1\rangle_2$ for which the final state is a symmetric spin state. Thus, the final state spatial wave function must be antisymmetric (i.e. p-wave, f-wave, etc...) for this inelastic collision. Again, the dipolar interaction V^d only allows s-wave to d-wave transitions for an s-wave entrance channel wave function. Thus, the $|2\rangle$-$|1\rangle$ combination is virtually impervious to inelastic collisions in the low-energy limit.

2.12 Summary

We have shown in this chapter that an ultracold ^{6}Li gas is expected to exhibit a widely tunable interaction strength that can be adjusted by application of a uniform magnetic field $\mathbf{B}$. For certain values of $\mathbf{B}$, several two-state mixtures exhibit a very large and negative scattering length suitable for the observation and study of a superfluid phase transition via the formation of Cooper pairs. In addition, the widely tunable interaction strength will permit systematic studies of collective phenomena in an interacting Fermi gas. In certain cases the scattering length can greatly exceed the range of the molecular interaction potential. These anomalously large scattering lengths arise from one of two resonant scattering effects, either a zero energy resonance in the ^{6}Li-^{6}Li triplet molecular potential or a Feshbach resonance. However, the magnetically trappable two-state mixtures of ^{6}Li also exhibit prohibitively large inelastic spin-exchange collisions rendering them unsuitable for evaporative cooling and investigations of an interacting Fermi gas.

Optically trapped two-state mixtures of ^{6}Li fermions have been shown to provide an appealing alternative to magnetically trapped mixtures. Certain two-state mixtures, which can only be trapped optically, have been shown to be stable against inelastic collisions. In addition, these mixtures exhibit large and widely tunable in-

teraction strengths. A two-state mixture of ^{6}Li atoms in the two lowest energy states (states $|1\rangle$ and $|2\rangle$) has no open inelastic decay channels in the limit of zero energy and exhibits both a Feshbach resonance near $B = 800$ G and, for fields exceeding 1 kG, approaches the triplet scattering length of $-2160\,a_0$. However, for $B < 800$ G, the scattering length for the $|1\rangle$-$|2\rangle$ mixture is small, approaching zero bohr for $B = 0$. As an alternative, a two-state mixture of ^{6}Li atoms in states $|1\rangle$ and $|3\rangle$ provides a large and negative scattering length at low field. In zero field, the $|3\rangle$-$|1\rangle$ mixture is expected to yield a scattering length of $-1600\,a_0$. The scattering length a_{31} is also widely tunable in a low field, rising to $-480\,a_0$ for an applied field of 10 G. By applying a small bias magnetic field, spin-exchange collisions arising from the central electrostatic molecular potential can be suppressed in the $|3\rangle$-$|1\rangle$ mixture. A small dipolar spin-relaxation process exists for the $|3\rangle$-$|1\rangle$ mixture. However, the decay rate is small enough that this process only becomes problematic at extremely high densities.

In conclusion, we have shown that an optically trapped two-state mixture of lithium fermions is well suited for systematic studies of an interacting Fermi gas. In the next several chapters we will discuss the design and construction of a stable optical trap for lithium fermions. We will then turn our attention toward studies of evaporative cooling and interactions in optically confined two-state mixtures of ^{6}Li. In Chapter 7, we directly verify several of the collisional properties of ultracold ^{6}Li discussed here.

Chapter 3

Optical Dipole Traps

We found in Chapter 2 that in order to study interactions in a gas of ultracold fermionic atoms one must be able to confine a two-state mixture of atoms. This is due to the fact that s-wave collisions are forbidden by the exclusion principle for a single state fermionic vapor. In addition, we found that while ^{6}Li provides large and tunable interaction strengths that make it particularly attractive for studies of collective phenomena, there are correspondingly large inelastic rates that exist for certain two-state mixtures. To avoid these detrimental collisions, one wishes to confine a two-state mixture of ^{6}Li in the lowest energy magnetic substates. Magnetic traps unfortunately are unable to confine the lowest energy states because Maxwell's equations forbid a static magnetic field maximum in free space (for a further discussion see Appendix B). Optical dipole traps, on the other hand, can provide a potential that is independent of the internal magnetic substate of the atom. Thus, all magnetic substates can be confined, permitting the study of stable, interacting two-state mixtures of fermionic atoms.

In this chapter, we will explore the properties of optical dipole traps. We begin with a simple derivation of the optical dipole potential which arises from the interaction between the induced electric dipole moment of an atom and an optical beam. We find that a three-dimensional confining potential can be formed from a single focused laser beam. Although atoms in this trap are heated by optical excita-

tion, we find that the heating rate can be made negligible in the limit of extremely large detunings of the trap laser from the atomic resonance frequency. However, in reviewing the literature, we find that optical traps have suffered from unexplained heating and loss mechanisms that have limited their lifetime to several seconds. We explore heating due to fluctuations in the intensity and position of the trap laser beam as a source of non-optical heating. We find that the achievement of storage times beyond 10 seconds requires stringent control of the trap laser intensity and position noise. We also examine trap loss and heating due to residual background gas atoms in the vacuum system. Finally, we motivate the choice of using a CO_2 laser trap to confine lithium fermions. The large detuning from resonance and inherent stability of CO_2 lasers make them ideally suited for confining atoms with minimal heating.

3.1 The Optical Dipole Trap

In this section we will derive the induced electric dipole interaction potential and the photon scattering rate for an atom in the presence of an optical field. The optical dipole force arises from the interaction between the induced electric dipole moment $\mathbf{d}$ of an atom and the electric field $\mathbf{E}$ of the optical beam. The optical field induces a dipole moment $\mathbf{d} = \alpha\mathbf{E}$ where α is the polarizability of the atom. The interaction potential U between the induced dipole and the optical field is given by

$$U = -\frac{1}{2}\overline{\mathbf{d}\cdot\mathbf{E}}, \tag{3.1}$$

where the factor of $1/2$ is due to the fact the dipole is induced rather than permanent and the bar indicates a time average over a few optical periods. Thus the potential

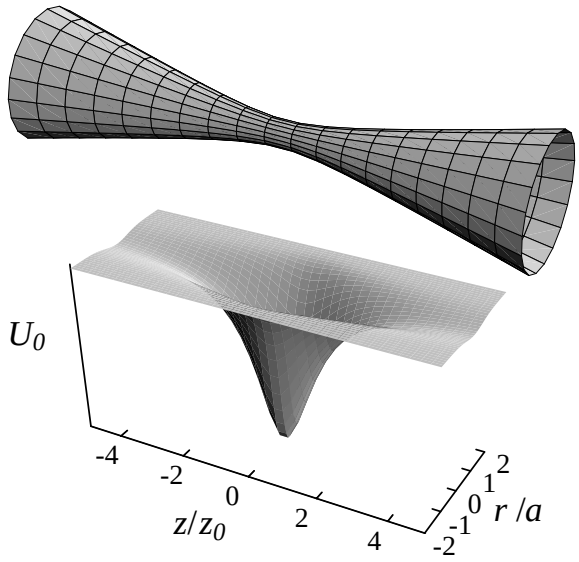

Figure 3.1: Optical trap fromed from a single focused laser beam. The upper half of the figure shows a focused Gaussian laser beam and the lower half of the figure shows the potential energy U for an atom in a plane that includes the z-axis.

is given by

$$U = -\frac{1}{4}\,\alpha\,\mathcal{E}^2 = -\frac{2\pi}{c}\,\alpha\,I, \tag{3.2}$$

where $\mathcal{E}$ is the electric field amplitude, c is the speed of light and I is the optical field intensity. Note that this potential is proportional to the intensity of the field and atoms are attracted (repelled) from regions of high intensity for positive (negative) α.

Thus, for positive α, three-dimensional confinement of neutral atoms can be easily achieved by using a single focused laser beam as was first suggested by [73] and demonstrated by [74]. The atoms are attracted to the region of highest intensity, which occurs at the laser focus. Figure 3.1 illustrates a focused laser beam as well

as the corresponding trapping potential for a slice through the center of the focused beam. For a focused Gaussian laser beam the laser intensity has the form

$$I(r,z,\phi) = \frac{I_0}{1+(z/z_0)^2}\,\exp(-2r^2/a^2) \tag{3.3}$$

where I_0 is the peak intensity, a is the $1/e^2$ intensity radius, $z_0 = \pi a^2/\lambda$ is the Rayleigh length and λ is the wavelength of the light. Thus, the dipole potential has the form

$$U(r,z,\phi) = -\frac{U_0}{1+(z/z_0)^2}\,\exp(-2r^2/a^2) \tag{3.4}$$

where the well depth $U_0 = (2\pi\alpha/c)I_0$.

Note that, for ultracold atoms at a temperature $T << U_0$, the atoms are confined near the focus of the Gaussian beam where the potential is approximately harmonic. If we expand (3.4) for small values of z/z_0 and r/a we find that

$$U(r,z,\phi) \simeq -U_0 + \frac{U_0}{z_0^2}\,z^2 + \frac{2\,U_0}{a^2}\,r^2 = -U_0 + \frac{1}{2}\,M\,\omega_z^2\,z^2 + \frac{1}{2}\,M\,\omega_r^2\,r^2. \tag{3.5}$$

Thus, for a focussed Gaussian laser beam of $1/e^2$ intensity radius a, an atom of mass M near the bottom of the trap experiences an anisotropic harmonic potential where the oscillation frequencies are given by $\omega_r^2 = 4\,U_0/M\,a^2$ in the radial direction and $\omega_z^2 = 2\,U_0/M\,z_0^2$ in the axial direction. Since the well depth U_0 is directly proportional to the intensity of the trap laser beam, the square of the trap oscillation frequencies in the axial and radial directions are also directly proportional to the intensity.

An important quantity of interest is the photon scattering rate. The scattering

of photons by the confined atoms causes optical heating through mechanisms such as recoil heating, excited state inelastic collisions and dipole force fluctuations (arising from the fact that the polarizability for the excited state is, in general, different from that of the ground state). Thus we wish to minimize the scattering rate. The power radiated by the oscillating dipole is given by the Larmor power formula

$$P = \frac{2\overline{\ddot{\mathbf{d}}^2}}{3\,c^3} = \frac{1}{3c^3}\,\omega^4\,\alpha^2\,\mathcal{E}^2, \tag{3.6}$$

where ω is the frequency of the optical field. The photon scattering rate at the trap center can be written in terms of a scattering cross section σ_s as

$$R_{sc} = \frac{P}{\hbar\omega} = \frac{\sigma_s\,I_0}{\hbar\,c\,k}, \tag{3.7}$$

where

$$\sigma_s = \frac{8\pi}{3}\,\alpha^2\,k^4. \tag{3.8}$$

In order to compute both the well depth and the scattering rate we must first calculate the polarizability of the atom.

The polarizability of the atom α can be found by modeling the atom as an electron harmonically bound to the nucleus. This derivation provides physical insight and reproduces the quantum mechanical results found using first-order time dependent perturbation theory [75].

The equation of motion for the harmonically bound electron driven by the optical

field is:

$$\ddot{\mathbf{x}} + \omega_0^2 \mathbf{x} = \frac{e\mathbf{E}(t)}{m_e}, \tag{3.9}$$

where ω_0 is the natural oscillation frequency, e is the charge of the electron and m_e is the mass of the electron. Solving the equation of motion for this driven oscillator one finds $\mathbf{d} = e\,\mathbf{x} = \alpha\,\mathbf{E}$ with

$$\alpha = \frac{e^2}{2\omega_0 m_e}\left[\frac{1}{\omega_0 - \omega} + \frac{1}{\omega_0 + \omega}\right] = \frac{\mu^2}{\hbar}\left[\frac{1}{\omega_0 - \omega} + \frac{1}{\omega_0 + \omega}\right], \tag{3.10}$$

where we have expressed α in terms of the dipole matrix element $\mu \equiv e\sqrt{\hbar/2m_e\omega_0}$, which is the product of the electron charge e and the natural length scale for the quantized harmonic oscillator $\sqrt{\hbar/2m_e\omega_0}$.

Note from (3.10) that the induced dipole oscillates in phase ($\alpha > 0$) with the applied electric field for optical fields tuned below resonance ($\omega < \omega_0$) and the atom is attracted to the region of highest intensity. For fields tuned above resonance ($\omega > \omega_0$), the induced dipole oscillates 180° out-of-phase ($\alpha < 0$) with the electric field and the atom is repelled from the region of highest intensity.

The polarizability of an atom can also be calculated semiclassically. In this case we consider the atom as a two-level quantum system coupled to a classical electric field $\mathbf{E}$ via the dipole interaction $\boldsymbol{\mu} \cdot \mathbf{E}$ where $\boldsymbol{\mu} = e\,\mathbf{r}$ is the electric dipole operator. Using first order time-dependent perturbation theory we can find the expectation value of the dipole operator $\langle \boldsymbol{\mu} \rangle$. We find that $\langle \boldsymbol{\mu} \rangle = \alpha\,\mathbf{E}$ with

$$\alpha = \frac{\mu_{eg}^2}{\hbar}\left[\frac{1}{\omega_0 - \omega} + \frac{1}{\omega_0 + \omega}\right], \tag{3.11}$$

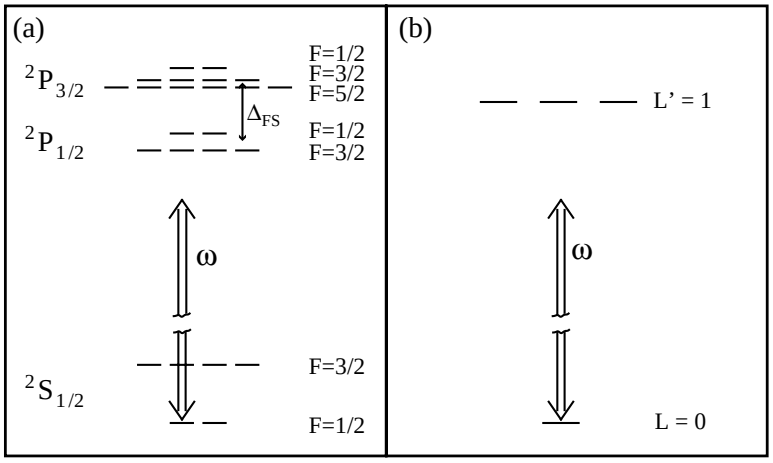

Figure 3.2: Alkali atom energy level diagram. (a) An alkali atom has a number of internal states. (b) If a linearly polarized laser beam is detuned from resonance by more that the fine structure splitting Δ_{FS}, the fine and hyperfine structure in the atom is unresolved.

where $\mu_{eg} = \langle e|\mu|g\rangle$ is the dipole matrix element between the ground and excited state of the atom. This is identical to (3.10) once we replace $\mu = e\sqrt{\hbar/2m_e\omega_0}$ with μ_{eg}

Of course, a real atom contains multiple levels, which complicates the derivation of the polarizability. For example, alkali atoms have a structure similar to that shown in Figure 3.2(a). In this case, the polarizability of an atom in a ground state $|g\rangle$ is given by a sum over excited states $|e\rangle$:

$$\alpha = \frac{1}{\hbar}\sum_e |\mu_{eg}|^2 \left[\frac{1}{\omega_{eg}-\omega} + \frac{1}{\omega_{eg}+\omega}\right], \tag{3.12}$$

where $\omega_{eg} = E_{eg}/\hbar$ and E_{eg} is the energy splitting between the states $|e\rangle$ and $|g\rangle$. However, in most cases, equation (3.12) can be simplified as we now show.

In order to minimize the photon scattering rate, the detuning $\Delta \equiv \omega_0 - \omega$ of the optical field from the atomic resonance frequency is chosen to be large with

respect to the natural linewidth Γ of the atomic transition. In many cases the detuning Δ is chosen to be much larger than the fine structure splitting Δ_{FS} shown in Figure 3.2(a). If this is the case, the fine structure and hyperfine structure shown in Figure 3.2(a) cannot be resolved. Instead, the transition can be simply thought of as occurring between states of orbital angular momentum $L = 0$ and $L' = 1$ as shown in Figure 3.2(b). For linearly polarized light, which can only make $\Delta m = 0$ transitions, we regain our two level atom picture.

Formally, this simplification comes from the fact that in the limit of large detuning $\Delta >> \Delta_{FS}$ the frequency dependent terms in (3.12) can be pulled in front of the summation. We are then left with a sum over matrix elements μ_{eg}. According to the Wigner-Eckart theorem, each matrix element can be written as a product of a reduced matrix element $||\mu||$ and a 3j-symbol. 6j recoupling coefficients and sum rules can then be used to simplify the result so that it only depends on a reduced matrix element between states $|L = 0\rangle$ and $|L' = 1\rangle$. Thus, in this limit of large detuning using a linearly polarized trap laser beam, the ground state potential is independent of the choice of magnetic substate.

3.1.1 Far-Off Resonance Traps

As mentioned above, the detuning of the trap laser beam is chosen such that $\Delta >> \Gamma$ in order to minimize the photon scattering rate. However, in most experiments, while $|\Delta| >> \Gamma$ the detuning is much smaller than the optical frequency $|\Delta| << \omega_0$. In this case, we can make the so-called rotating-wave approximation and neglect the counter-rotating term $1/(\omega_0 + \omega)$ in α as it is much smaller than $1/(\omega_0 - \omega) = 1/\Delta$.

Then,

$$\alpha = \frac{\mu_{eg}^2}{\hbar\,\Delta}, \tag{3.13}$$

and the dipole potential becomes

$$U = -\frac{\mu_{eg}^2 \mathcal{E}^2}{4\,\hbar\,\Delta} = -\frac{\hbar\,\Omega^2}{4\,\Delta}, \tag{3.14}$$

where $\Omega \equiv \mu_{eg}\mathcal{E}/\hbar$ is the Rabi oscillation frequency. Note that the quantity Ω^2 is proportional to the intensity.

Substituting (3.13) into (3.7) and (3.8) gives the scattering rate in the limit $|\Delta| >> \Gamma$ and $|\Delta| << \omega_0$

$$R_{sc} = \frac{4\,\omega_0^3\,\mu_{eg}^2}{3\,\hbar\,c^3}\left(\frac{\omega}{\omega_0}\right)^3 \frac{\Omega^2}{4\,\Delta^2} \cong \frac{\Gamma\,\Omega^2}{4\,\Delta^2}, \tag{3.15}$$

where $\Gamma \equiv 4\omega_0^3\mu^2/3\hbar c^3$ is the spontaneous emission rate (the Einstein A coefficient) and we have used the fact that in this limit $\omega/\omega_0 \sim 1$.

Upon examining equations (3.14) and (3.15) one finds that the well depth for a red-detuned, focused Gaussian beam is $\propto I_0/\Delta$ while the photon scattering rate is $\propto I_0/\Delta^2$. The photon scattering rate can be expressed in terms of the well depth U_0 as

$$R_{sc} = \frac{\Gamma}{\hbar\Delta}\,U_0 \tag{3.16}$$

Thus, one can reduce the photon scattering rate while maintaining a given well depth by tuning the trap laser further from resonance and using more power. The photon scattering rate can be drastically reduced if intense laser beams with large

detunings from resonance are used.

The initial demonstration of optically trapped atoms [74] used a 220 mW trap laser beam focused to a waist radius $a = 10\,\mu$m tuned ~ 650 GHz below resonance. This produced a 5 mK deep potential well depth for neutral sodium atoms. For these parameters, the large photon scattering rate limited the trap lifetime to 4 ms. By employing a large detuning from resonance, Miller *et al.* [76] demonstrated a far-off-resonance optical trap (FORT) in which the photon scattering rate was reduced. In this experiment a 0.80 W laser focused to a waist radius $a = 10\,\mu$m tuned 19 nm below resonance provided a 6 mK deep well depth for rubidium atoms. In this case, the photon scattering rate $R_{sc} = 400$ Hz was expected to increase the optical heating lifetime for atoms at the bottom of the well to 43 seconds. However, collisions with background gas atoms inside the vacuum system limited the lifetime to 200 ms.

3.1.2 Quasi-Electrostatic Traps

In a small number of experiments, lasers producing $10.6\,\mu$m radiation with detunings greatly exceeding the resonance frequency ($\Delta >> \omega_0$) have been employed in order to reduce optical heating to negligible amounts [20, 77–79]. Due to the large detuning and extremely low frequency of the radiation, the optical scattering rate is dramatically reduced. As was pointed out by Takekoshi *et al.* [80], one cannot make the rotating-wave approximation when calculating the polarizability of the atom for such extremely large detunings. When the counter-rotating term is included in computing α one finds that the scattering rate is significantly smaller than that predicted by (3.15) for $\Delta >> \omega_0$.

For large detunings $\Delta >> \omega_0$, the polarizability can be expressed as

$$\alpha = \alpha_s \frac{1}{1 - \omega^2/\omega_0^2}, \tag{3.17}$$

where $\alpha_s \equiv 2\mu^2/\hbar\omega_0$ is the *static* polarizability of the two-level atom. Thus, for $\omega << \omega_0$ the dipole interaction potential for the oscillating field is identical to that for a *static* field with the same root-mean-squared field strength

$$U = -\frac{1}{2}\,\alpha_s\, E_{rms}^2 = -\frac{1}{4}\,\alpha_s\, \mathcal{E}^2. \tag{3.18}$$

The optical scattering rate is given by the Larmor power formula

$$R_{sc} = \sigma_s\, I_0/\hbar\, c\, k, \tag{3.19}$$

with the scattering cross section

$$\sigma_s = \frac{8\pi}{3}\,\alpha_s^2\, k^4. \tag{3.20}$$

For comparison with the rotating-wave approximation result (3.16) we can rewrite the scattering rate in terms of the well depth $U_0 = 2\pi\alpha_s I_0/c$ as

$$R_{sc} = \frac{2\,\Gamma}{\hbar\,\omega_0}\,\left(\frac{\omega}{\omega_0}\right)^3\, U_0, \tag{3.21}$$

where we have used the fact that $\alpha_s = 2\mu_{eg}^2/\hbar\omega_0$ and $\Gamma = 4\mu_{eg}^2\omega_0^3/3\hbar c^3$for a two-level atom . In comparing (3.16) to (3.21) we find that the photon scattering rate in the quasi-electrostatic limit is suppressed by a factor $2(\omega/\omega_0)^3$ beyond that predicted using the rotating-wave approximation. Because of the drastic reduction attainable

for low infrared frequency radiation where $\omega << \omega_0$, scattering rates for quasi-electrostatic traps are typically $< 10^{-3}$ Hz.

Takekoshi *et al.* [77] demonstrated a quasi-electrostatic trap by confining cesium atoms using a focused CO_2 laser which produces $\lambda = 10.6\,\mu$m radiation. A 20 W beam focused to a 100 μm radius spot size provided a 115 μK deep well depth for cesium. The estimated photon scattering rate $R_{sc} = 2 \times 10^{-4}$ Hz. Thus, heating due to optical scattering is expected to be completely negligible in this system. The number of trapped atoms decayed exponentially with a 1 second time constant. The short lifetime was caused by collisions with background gas atoms in the vacuum system.

3.2 Unexplained Trap Heating and Loss

Although heating due to optical scattering is expected to become negligible in the limit of extreme detuning, unexplained heating and trap loss rates have been observed in a number of optical dipole traps [51, 81–85]. In all of these traps, storage times have been limited to several seconds. For example, Ref. [81] employed a Nd:YAG laser to trap 140 μK sodium atoms in a 900μK deep well. The large detuning from resonance ($\omega = \omega_0/2$) gave a predicted photon scattering rate $R_{sc} = 1.25$ Hz which would produce a small 1 μK/s recoil heating rate. Although the trap lifetime was expected to exhibit an exponential decay with a 14 s time constant due to the finite vacuum pressure, the number of trapped atoms was observed to decay exponentially with a 0.8 s time constant instead. The lifetime was reported to be inversely proportional to the laser intensity and independent of density.

In a 1997 review article [84] on laser cooling and trapping, C. S. Adams and E. Riis discussed observations made with a red-detuned optical dipole trap:

> "In the limit of far detuning, one expects the light to create an almost *conservative potential*, such that in practice the lifetime of the trap is only limited by the background pressure. [Our observations show that] the lifetime varies linearly with pressure, except at very low pressures ($\sim 10^{-11}$ Torr) where it tends to saturate at a few seconds due to other possible heating mechanisms."

Optical traps had fallen short of providing the ideal of a conservative potential with a long lifetime.

Attempts have been made to circumvent the heating problem by using blue-detuned traps [51,82,83]. For a blue-detuned ($\Delta > 0$) optical field, the polarizability is negative and atoms are repelled from regions of high intensity. Traps can then be formed by using multiple sheets of blue-detuned laser light. For example, six sheets could be combined to form the six faces of a cube. Atoms could then be confined inside this box potential. Since atoms are repelled from the optical beams, they spend a minimum time in the optical field and hopefully experience less heating.

Blue-detuned traps have failed to provide storage times beyond several seconds and have been observed to exhibit heating beyond the expected optical heating rates. H. J. Lee *et al.* confined atoms in an inverted pyramid trap formed from the intersection of four sheets of blue detuned light [51]. The number of trapped atoms exhibited a rapid decay for the first second followed by an exponential decay with a 7.0 second time constant. The observed lifetime was independent of background pressure from 7×10^{-11} down to 2×10^{-11} Torr. The lifetime was believed to be limited by an unexplained heating mechanism which produced an observed heating rate ~ 30 times that estimated due to photon scatter.

3.3 Laser-Noise-Induced Heating

One source of non-optical heating in optical traps is that due to fluctuations in the intensity and position of the trapping laser beam. While it has been appreciated for some time that such processes can cause heating, explicit expressions for the heating rates in terms of the laser noise spectrum were nonexistent until recently. In 1997, our group published a theoretical paper in which the heating rates for a red-detuned optical trap could be estimated from the intensity and position noise power spectra of the trap laser. One finds that the achievement of heating time constants well beyond 10 sec imposes stringent requirements on the laser noise power spectra. While these heating rates are derived in the context of a red-detuned, focussed Gaussian beam, they are applicable to fluctuations in any trap that confines atoms in a harmonic potential. Simple extensions to this model might also explain the unexplained heating rates observed in blue-detuned traps.

3.3.1 Intensity-Noise-Induced Heating

Fluctuations in the laser intensity leads to exponential heating for atoms near the bottom of the trap as we now show. In Section 3.1 we found that for a focussed Gaussian laser beam of $1/e^2$ intensity radius a, an atom of mass M near the bottom of the trap experiences a harmonic potential $V(x) = \frac{1}{2}M\omega_{tr}^2$ where the square of the trap oscillation frequency ω_{tr}^2 is proportional to the trap laser intensity I. For a fluctuating intensity $I(t)$ the time dependent Hamiltonian is

$$H = \frac{p^2}{2M} + \frac{1}{2}M\omega_{tr}^2[1 + \epsilon(t)]x^2, \tag{3.22}$$

where $\epsilon(t)$ is the fractional fluctuation in the laser intensity

$$\epsilon(t) = \frac{I(t) - I_0}{I_0}. \tag{3.23}$$

Here I_0 is the time averaged laser intensity. We can define the correlation function for the fractional intensity fluctuations as

$$\langle \epsilon(t)\, \epsilon(t+\tau) \rangle = \frac{1}{T} \int_0^T dt\ \epsilon(t)\, \epsilon(t+\tau). \tag{3.24}$$

The one-sided power spectrum of the fractional intensity noise is given by

$$S_\epsilon(\omega) = \frac{2}{\pi} \int_0^\infty d\tau\ \cos\omega\tau\, \langle \epsilon(t)\epsilon(t+\tau) \rangle. \tag{3.25}$$

Note that the one-sided power spectrum is defined so that

$$\int_0^\infty d\omega\ S_\epsilon(\omega) = \langle \epsilon^2(t) \rangle \equiv \epsilon_0^2, \tag{3.26}$$

where ϵ_0 is the root-mean-square fractional intensity fluctuation.

The heating rate is easily determined by using first-order time-dependent perturbation theory to calculate the average transition rates between quantum states of the harmonic trap. The perturbation is given by

$$H'(t) = \frac{1}{2}\, \epsilon(t)\, M\, \omega_{tr}^2\, x^2. \tag{3.27}$$

The average heating rate is found to be

$$\langle \dot{E} \rangle = \Gamma \langle E \rangle \tag{3.28}$$

where $\langle E \rangle$ is the average energy of the trapped atoms. The rate constant Γ is given by

$$\Gamma \equiv \pi^2 \nu_{tr}^2 S_\epsilon(2\nu_{tr}), \tag{3.29}$$

where ν_{tr} is the trap oscillation frequency $\nu_{tr} = \omega_{tr}/2\pi$. Thus, we find that intensity fluctuations cause exponential heating where the rate constant is proportional to ν_{tr}^2. That the heating rate is sensitive to the noise spectrum evaluated at $2\nu_{tr}$ shows that this is a parametric heating process.

Optical traps with trap oscillation frequencies ranging from 10 Hz to 100 kHz have been used in Refs. [51, 77, 81]. According to Eq. (3.29), to achieve an energy e-folding time of 100 sec in a trap with an oscillation freuqency of 10 kHz requires $\sqrt{S_\epsilon(2\,\nu_{tr})} = 3 \times 10^{-6}\,\mathrm{Hz}^{-1/2}$. Hence, if most of the intensity noise were evenly distributed over a 40 kHz bandwidth, the rms fractional intensity noise must be better than $\epsilon_0 = 6 \times 10^{-4}$.

3.3.2 Position-Noise-Induced Heating

In addition to intensity noise, laser position noise also causes heating. In this case, the effective Hamiltonian is given by

$$H = \frac{p^2}{2M} + \frac{1}{2}\,M\,\omega_{tr}^2\,[x - \epsilon(t)]^2, \tag{3.30}$$

where $\epsilon(t)$ is now the fluctuation in the location of the trap center. Again, an application of first-order time-dependent perturbation theory yields the transition

rates between quantum states of the trap from which we can find the heating rate

$$\langle \dot{E} \rangle = \frac{\pi}{2} M \omega_{tr}^4 S_x(\omega_{tr}). \tag{3.31}$$

We find that shaking the trap causes a heating rate that is independent of energy. Here, $S_x(\omega)$ is the one-sided power spectrum of the position fluctuations in the trap center defined so that $\int_0^\infty d\omega\, S_x(\omega) = \epsilon_x^2$ is the mean-square variation in the trap center position.

An energy-doubling time T_x can be defined as the time needed to increase the energy by the average energy at $t = 0$: $\langle \dot{E} \rangle / \langle E(0) \rangle \equiv 1/T_x$. Then, using $\langle E(0) \rangle = M\omega_{tr}^2 \langle x^2 \rangle$, where $\langle x^2 \rangle$ is the mean-square position of an atom in the trap at $t = 0$, one obtains

$$\frac{\langle \dot{E} \rangle}{\langle E(0) \rangle} \equiv \frac{1}{T_x(\text{sec})} = \pi^2 \nu_{tr}^2 \frac{S_x(\nu_{tr})}{\langle x^2 \rangle}. \tag{3.32}$$

According to (3.32), if an atom is confined in a trap to a dimension of 1 μm with an oscillation frequency of 10 kHz, achievement of an energy-doubling time of 100 sec requires a position stability of $\sqrt{S_x(\nu_{tr})} = 3 \times 10^{-6}\, \mu\text{m/Hz}^{1/2}$.

3.4 Intensity and Postion Noise of a Commercial Ar^+ Laser

In order to illustrate that intensity and position fluctuations can cause significant heating in optical traps based on commercial laser sources, Tom Savard measured the intensity and position noise power spectra for a Coherent model Innova 310-argon-ion laser. Figure 3.3(a) shows the measured intensity noise power spectrum

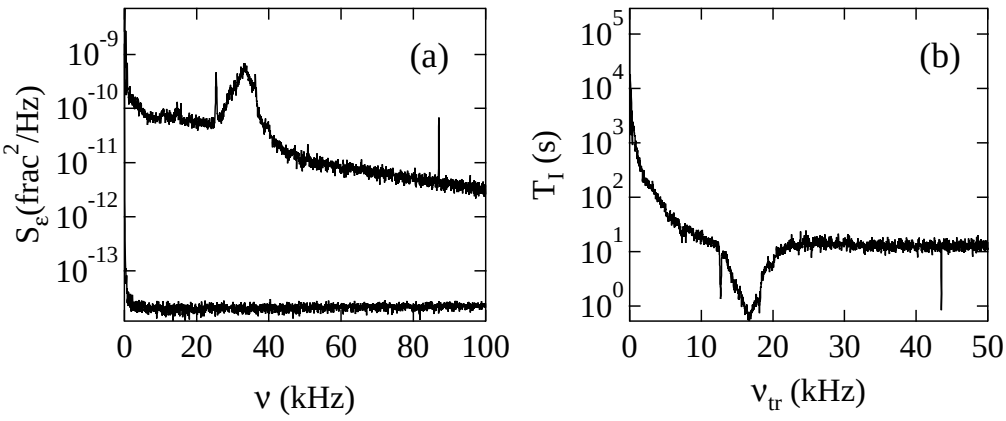

Figure 3.3: Intensity-noise-induced heating for an Ar^+ laser. The upper curve in (a) shows the one-sided fractional intensity noise power spectrum for the Ar^+ laser which greatly exceeds the electronic noise shown as the lower curve. (b) The exponential heating time constant T_I predicted for the Ar^+ laser based on the intensity noise spectrum shown in (a).

$S_\epsilon(\nu)$ for the argon laser. The upper curve is the noise spectrum of the laser and the lower curve shows the electronic noise of the detection system. The integrated power spectrum yields a rms noise $\epsilon_0 = 0.26 \times 10^{-2}$, consistent with the manufacturer's specification and with the directly measured rms intensity fluctuations. Figure 3.3(b) shows how the energy e-folding time T_I calculated from (3.29) varies with the choice of trap frequency for a laser with this noise power spectrum. A poor choice of trap frequency is near 17 kHz; however, low trap frequencies yield long heating times. Unfortunately, low trap frequencies usually correspond to smaller well depths, and less confinement. At high frequencies, the spectrum scales as ν^{-2}, and the energy e-folding time is constant at 10 sec.

Figure 3.4(a) shows the position noise power spectrum $S_x(\nu)$ for the argon ion laser in units of micrometers squared per hertz. Again, the lower curve shows the electronic noise contributed to the spectrum. This spectrum includes pointing

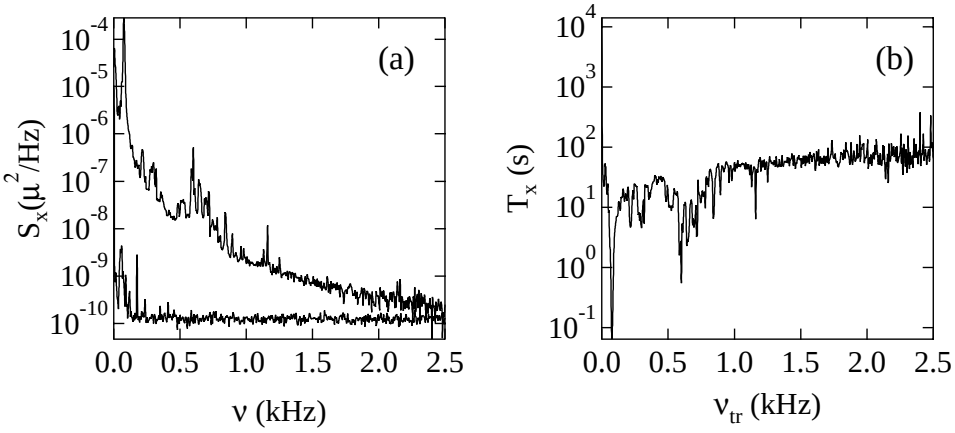

Figure 3.4: Position-noise-induced heating for an Ar^+ laser. The upper curve in (a) shows the one-sided power spectrum for the position noise and the electronic noise of the detection system is shown in the lower curve. (b) The energy doubling time T_x predicted for the Ar^+ laser based on the position noise spectrum shown in (a).

noise from both the laser and the optical mounts. Figure 3.4(b) shows the energy-doubling time T_x calculated from this spectrum assuming the sample of atoms is initially confined to a rms distance $x_{rms} = \sqrt{\langle x^2 \rangle} = 1\,\mu$m. Micrometer dimensions are typical for the quantum scale of a low-frequency trap (100 Hz, Rb atoms) and for temperatures of a few hundred μK in a tight trap.

The measured noise spectra for the argon-ion laser demonstrate that laser intensity and position fluctuations can cause significant heating in optical traps. While laser-noise-induced heating may not be the only source of heating and trap loss observed in optical traps, intensity and position fluctuations of the trap laser must be stringently controlled in order to achieve trap lifetimes beyond 10 seconds.

3.5 Loss and Heating due to Background Gas Collisions

Another source of trap loss and heating arises from elastic collisions between the cold trapped atoms and the much hotter residual gas atoms and molecules in the vacuum system [86–88]. Since the background gas atoms are at a temperature $T \simeq 300°\text{K}$ and the well depths for neutral atom traps are typically ~ 1 mK, glancing angle collisions between residual background gas atoms and the trapped atoms are sufficient to eject atoms from the trap causing trap loss. However, for extremely small-angle collisions, a trapped atom receives an energy kick but is not ejected from the trap. If a mechanism for thermalization exists, the energy kick received by one atom can cause heating of the entire atomic sample. In this section we calculate the expected heating and loss rates.

Consider a collision between a trapped atom with velocity $\boldsymbol{v}_a$ and a residual background gas atom with velocity $\boldsymbol{v}_b$. The initial relative velocity $\boldsymbol{v}_r = \boldsymbol{v}_a - \boldsymbol{v}_b$. During the collision, the relative velocity changes by $\Delta\,\boldsymbol{v}_r$ and the trapped atom velocity changes by $\Delta\,\boldsymbol{v}_a = \mu\,\Delta\,\boldsymbol{v}_r/m_a$ where μ is the reduced mass, m_a is trapped atom mass. For an elastic collision $|\Delta\,\boldsymbol{v}_r|^2 = 2\,v_r^2\,(1-\cos\theta)$ where θ is the scattering angle between the final and initial relative velocity. As shown below, a glancing angle collision for which $\theta << 1$ is sufficient to eject an atom from the trap. In the small-angle limit $|\Delta\,\boldsymbol{v}_r| \simeq v_r\,\theta$ and $|\Delta\,\boldsymbol{v}_a| \simeq \mu\,v_r\,\theta/m_a$.

An atom near the bottom of the well is ejected from the trap if

$$\Delta E_a \equiv \frac{1}{2}\,m_a\,(\Delta \boldsymbol{v}_a)^2 \geq U_0. \tag{3.33}$$

The condition $\Delta\,E_a = U_0$ yields a threshold angle θ_0 such that for $\theta > \theta_0$ the atom

is ejected from the trap while for $\theta < \theta_0$ the atom remains in the trap and can cause heating. Using the small angle approximation for $|\Delta \boldsymbol{v}_a|$, we find

$$U_0 = \frac{1}{2}\,\frac{\mu^2}{m_a}\,v_r^2\,\theta_0^2. \tag{3.34}$$

For atoms trapped in a 1 mK deep well in a vacuum system containing residual lithium atoms at a temperature of 300°K the threshold angle $\theta_0 \simeq 4$ mrad justifying our use of the small angle approximation.

Since these are relatively high energy collisions in comparison to the collisions studied in Chapter 2, one might hope to use a classical small-angle scattering approximation to calculate the loss and heating rates. However, when the scattering angles required to eject atoms from the trap are sufficiently small, they fall into the diffractive cone of the scattering amplitude, where a classical small-angle approximation is not valid. It is therefore of interest to calculate the diffraction angle θ_d. The diffraction angle is of order $\theta_d = \lambda_{dB}/(\pi\,R) = 2/(k\,R)$ where $k = 2\pi/\lambda_{dB} = \mu\,v_r\,/\hbar$ is a thermal wave vector and R is the range of the collision potential. R can be related to the total scattering cross section σ in the hard sphere approximation for which $\sigma \simeq 2\pi R^2$. Using the small-angle approximation, the trapped atom velocity change in a diffractive collision is $|\Delta \boldsymbol{v}_a| \simeq \mu\,v_r\,\theta_d/m_a \simeq 2\hbar/(m_a\,R)$ and the natural scale for a diffractive energy change of a trapped atom is

$$\epsilon_d = \frac{m_a(\Delta \boldsymbol{v}_a)^2}{2} = \frac{4\pi\hbar^2}{m_a\sigma}. \tag{3.35}$$

For neutral atom collisions, the total elatic cross section σ used in (3.35) is determined from the Van der Waals constants as described below.

Since we are only interested in glancing angle collisions which occur at a large

impact parameter, the interaction potential is well approximated by the long range Van der Waals interaction potential $V(r) = -C_6/r^6$. The total elastic cross section σ for a power-law potential is given in Ref. [69]. For $V(r) = -C_6/r^6$

$$\sigma(v_r) = 8.083 \left(\frac{C_6}{\hbar\, v_r}\right)^{2/5}. \tag{3.36}$$

For Li-Li collisions, $C_6 = 1390$ a.u. ($1\,\text{a.u.} = e^2\, a_0^5$). We assume that the Li background gas speed distribution is described by an isotropic Maxwellian distribution with a $1/e$ width $u_b = \sqrt{2\, k_B\, T/m_b}$. At $T = 300°\text{K}$, $\sigma(u_b) = 920$ $\mathring{\text{A}}^2$ for Li-Li collisions. Inserting this result for the total cross section into (3.35) gives the energy scale for a diffractive collision $\epsilon_d = 110$ mK. Since $\epsilon_d >> U_0$ for shallow well depths typical of optical traps, the threshold scattering angle $\theta_0 << \theta_d$.

3.5.1 Loss Rate due to Background Gas Collisions

The collision rate to scatter into a solid angle $d\Omega$ is $n_b\, v_r\, (d\sigma/d\Omega)\, d\Omega$, where $d\sigma/d\Omega$ is the differential scattering cross section and n_b is the background gas density. For a central force interaction potential, $d\sigma/d\Omega = |f(\theta)|^2$, where $f(\theta)$ is the scattering amplitude. The loss rate γ_C is given by the integral over all collisions for which the scattering angle exceeds the threshold scattering angle θ_0

$$\gamma_C = n_b\, v_r \int_{\theta_0}^{\pi} 2\,\pi\, d\theta\, \sin\theta\, |f(\theta)|^2. \tag{3.37}$$

Due to the fact that $\theta_0 << \theta_d$ and $\theta_0 << 1$, the lower limit of the integration can be replaced by zero since the integrand is constant for $\theta << \theta_d$. In this case, the integral over θ yields essentially the total cross section and the loss rate due to atoms with relative velocity v_r is simply $\gamma_C \simeq n_b\, v_r\, \sigma(v_r)$ where $\sigma(v_r)$ is the total

cross section given by (3.36). This loss rate is averaged over a Maxwellian speed distribution with a $1/e$ width $u_b = \sqrt{2\,k_B\,T/m_b}$ to give the loss rate

$$\gamma_C = 1.05\,n_b\,u_b\,\sigma(u_b). \tag{3.38}$$

For a residual background gas of lithium atoms in an ultra-high vacuum system at a pressure $P = 10^{-9}$ Torr (1 Torr = 1 mm Hg = 1/760 atm) and a temperature $T = 300°$K, the ideal gas law can be used to find $n_b = 3.2 \times 10^7$ atoms/cm^3. In this case $\gamma_C = 0.28$ s^{-1}. The constant loss rate causes the trapped atoms to decay exponentially with a time constant $\tau_C = 1/\gamma_C = 3.55$ sec. Note that the time constant τ_C scales inversely with background pressure P. Thus to achieve a time constant of several hundred seconds, a background pressure $P \leq 10^{-11}$ Torr is required.

3.5.2 Heating Rate due to Background Gas Collisions

A collision for which the scattering angle $\theta < \theta_0$ does not eject an atom from the trap but instead causes heating. The atom has received an energy kick $\Delta E(\theta) = \frac{1}{2}\,m_a\,(\Delta \boldsymbol{v}_a)^2 \simeq \frac{1}{2}\,\mu^2\,v_r^2\,\theta^2/m_a$. The heating rate $\dot{Q}$ due to collisions which do not eject atoms from the trap is given by

$$\dot{Q} = n_b\,v_r \int_0^{\theta_0} 2\,\pi\,d\theta\,\theta\,|f(\theta)|^2\,\Delta E(\theta), \tag{3.39}$$

where we have approximated $\sin\theta \simeq \theta$. Since $\theta_0 << \theta_d$ and $\theta_0 << 1$ we can use a small angle approximation for the scattering amplitude in the diffractive regime. Ref. [69] gives a suitable approximation for power-law potentials. For

$V(r) = -C_6/r^6$

$$|f(\theta)|_d^2 = 1.53 \left(\frac{k\,\sigma}{4\,\pi}\right)^2 \left[1 - 2.07\,\frac{k^2\,\sigma}{8\,\pi}\,\theta^2 + \cdots\right], \tag{3.40}$$

where σ is the total cross section given by (3.36). Since $\theta^2\,k^2\,\sigma/8\,\pi \simeq \theta^2/\theta_d^2 << 1$ we only need to use $|f(\theta)|^2 \simeq |f(0)|_d^2$ in evaluating the heating rate integral (3.39). The heating rate integral yields a simple result

$$\dot{Q} = \frac{1.53}{4}\,n_b\,v_r\,\sigma(v_r)\,\frac{U_0^2}{\epsilon_d(v_r)}. \tag{3.41}$$

This heating rate is averaged over a Maxwellian speed distribution with a $1/e$ width u_b to give the total heating rate

$$\dot{Q} = 0.37\,\gamma_C(u_b)\,\frac{U_0^2}{\epsilon_d(u_b)} \tag{3.42}$$

where $\gamma_C(u_b)$ is the loss rate given by (3.38).

For a residual background gas of lithium atoms at a pressure $P = 10^{-9}$ Torr and a temperature $T = 300°$K, the heating rate for Li atoms confined in a $U_0 = 1$ mK deep harmonic potential is $\dot{Q} \simeq 1\,\mu$K/sec assuming there exists a mechanism for thermalization inside the trapped atomic sample. For a pressure $P = 10^{-11}$ Torr, the heating rate is reduced to 10 nK/s.

3.6 Heating from Black Body Radiation

While contemplating the possible mechanisms that can heat atoms in an optical trap, it is interesting to consider the heating rate that arises from the scattering of black body radiation. In condensed matter low temperature physics, heating due to

the presence of black body radiation creates a serious impediment to cooling bulk matter to low temperature. Bulk matter can absorb a substantial portion of the room temperature black body spectrum as the absorption spectrum of bulk matter is in general a broad continuum. Thus, black body radiation can cause a substantial amount of heating and is therefore a major concern when attempting to cool bulk matter to low temperature.

The situation for an ultracold sample of Li atoms is quite different. The absorption spectrum of a Li atom is discrete rather than continuous and the first resonance transition occurs at a wavelength of 671 nm. At room temperature the peak in the black body radiation spectrum occurs at 17 μm. Therefore, the majority of the black body spectrum is off resonance with the atomic resonance frequency and the amount of light scattered by the atom is substantially reduced compared to a piece of bulk matter. Furthermore, the atoms do not absorb the full energy of the scattered photon but are only heated by the recoil energy. Thus, in contrast to bulk matter, black body radiation does not cause a substantial heating rate for an ultracold gas of Li atoms.

The heating rate for ^{6}Li atoms due to black body radiation is easily estimated. If the atoms are confined inside a cavity at temperature T, the spectral density $u(\omega)$ of energy in the electromagnetic field is given by the Planck radiation law

$$u(\omega)\,d\omega = \frac{\hbar}{\pi^2\,c^3}\,\frac{\omega^3}{\exp(\hbar\omega/k_BT)-1}\,d\omega, \tag{3.43}$$

where $u(\omega)$ gives the energy per unit volume per unit frequency range and ω is given in units of rad/s. Photons from the black body radiation can scatter off of the ^{6}Li atoms and cause heating. The photon scattering rate can be obtained by first calculating the power radiated by the oscillating dipole moment $\mathbf{d}$ of the atom

which is given by the Larmor power formula

$$P(\omega)\,d\omega = \frac{2\overline{\ddot{\mathbf{d}}^2}}{3\,c^3}\,d\omega = \frac{\omega^4\,|\alpha|^2}{3c^3}\,\mathcal{E}(\omega)^2\,d\omega. \tag{3.44}$$

Here we have used the fact that $\mathbf{d} = \alpha\,\mathbf{E}$ where α is the polarizability of the atom and $\mathbf{E}$ is the electric field of the black body radiation. In Eq. (3.44), $\mathcal{E}$ is the electric field amplitude. For a two-level atom where the energy splitting is given by $\hbar\,\omega_0$, the polarizability α of the atom can be calculated from first order perturbation theory and is found to be

$$\alpha = \frac{2\omega_0\,\mu^2}{\hbar}\,\frac{1}{\omega_0^2 - \omega^2 - i\,\omega\,\Gamma}, \tag{3.45}$$

where we have included the fact that the excited state decays exponentially with a time constant Γ^{-1}. In Eq. (3.45), μ is the dipole matrix element. Since the spectral density of the electromagnetic field $u(\omega) = \mathcal{E}(\omega)^2/8\pi$ we find that

$$P(\omega)\,d\omega = \frac{32\pi\,\omega^4\,\omega_0^2\,\mu^4}{3\,\hbar^2\,c^3}\,\frac{u(\omega)\,d\omega}{(\omega_0^2 - \omega^2)^2 + \omega^2\,\Gamma^2}, \tag{3.46}$$

where $u(\omega)$ is given by Eq. (3.43). The photon scattering rate

$$R_{sc}(\omega) = P(\omega)/\hbar\omega. \tag{3.47}$$

The scattering of photons causes a random walk in momentum space which causes a heating rate

$$\dot{Q} = \int d\omega\,R_{sc}(\omega)\,\frac{\hbar^2 k^2}{2M}\,\cdot 2 \tag{3.48}$$

where we have used the fact that for each scattered photon the atom takes two random steps in momentum space each of size $\hbar\, k$ due to absorption and emission of a photon. Substituting Eq. (3.46) into Eq. (3.48) yields the total heating rate

$$\dot{Q} = \left(\frac{6}{\pi}\right)\, \left(\Gamma \frac{\hbar^2\, \omega_0^2}{M\, c^2}\right)\, \left(\frac{\Gamma}{\omega_0}\right)\, \frac{1}{\omega_0^9} \int_0^\infty \frac{d\omega\, \omega^8}{\exp(\hbar\omega/k_B T) - 1}\, \frac{\omega_0^4}{(\omega_0^2 - \omega^2)^2 + \omega^2\, \Gamma^2}, \tag{3.49}$$

where we have used the fact that $\Gamma = 4\, \omega_0^3\, \mu^2/3\, \hbar\, c^3$. Note that Eq. (3.49) is expressed in terms of the resonant recoil heating rate $\Gamma\, \frac{\hbar^2\, \omega_0^2}{M\, c^2}$.

The total heating rate $\dot{Q}$ can be evaluated analytically by writing the integral which appears in Eq. (3.49) as the sum of a contribution from off resonant light for which $\omega << \omega_0$ and a contribution from resonant light $\omega \simeq \omega_0$. Physically, the separation into a nonresonant and a resonant contribution arises from the fact that the peak of the black body distribution occurs for a wavelength of 17 μm whereas the scattering resonance occurs at a wavelength of 671 nm. Thus, the integrand in Eq. (3.49) exhibits two peaks and the total heating rate $\dot{Q} = \dot{Q}_{nonres} + \dot{Q}_{res}$ is given by the sum of the contributions from each of those peaks.

For the nonresonant contribution $\omega << \omega_0$ and $\omega_0^4/((\omega_0^2 - \omega^2)^2 + \omega^2\, \Gamma^2) \simeq 1$. Consequently, for $\omega << \omega_0$ the nonresonant contribution to the integral is given by

$$\begin{aligned} \frac{1}{\omega_0^9} \int_0^\infty \frac{d\omega\, \omega^8}{\exp(\hbar\omega/k_B T) - 1} &\simeq \left(\frac{k_B T}{\hbar\omega_0}\right)^9 \int_0^\infty dx\, x^8\, \exp(-x) \\ &= \left(\frac{k_B T}{\hbar\omega_0}\right)^9\, 8!. \end{aligned} \tag{3.50}$$

Thus, the nonresonant contribution to the heating rate

$$\dot{Q}_{nonres} \simeq \left(\frac{6}{\pi}\right) \left(\Gamma \frac{\hbar^2 \omega_0^2}{M c^2}\right) \left(\frac{\Gamma}{\omega_0}\right) \left(\frac{k_B T}{\hbar \omega_0}\right)^9 8!. \tag{3.51}$$

For ^{6}Li atoms confined in a cavity at temperature $T = 300°$K the nonresonant contribution $\dot{Q}_{nonres}$ can be evaluated to yield

$$\dot{Q}_{nonres} \simeq 5 \times 10^{-18}\,°\text{K/s} \tag{3.52}$$

where we have used the fact that $\Gamma^{-1} = 27$ ns, $\lambda_0 = 671$ nm and $M = 10^{-26}$ kg.

For the resonant contribution, $\omega \simeq \omega_0$ and the integral appearing in Eq. (3.49) can be expressed as

$$\begin{aligned} \frac{1}{\omega_0^9} \int_0^\infty \frac{d\omega\, \omega^8}{\exp(\hbar\omega/k_B T) - 1} \frac{\omega_0^4}{(\omega_0^2 - \omega^2)^2 + \omega^2\, \Gamma^2} & \\ \simeq \omega_0^3 \exp\left[-\frac{\hbar\omega_0}{k_B T}\right] \int_0^\infty \frac{d\omega}{(\omega_0^2 - \omega^2)^2 - \omega_0^2\, \Gamma^2} & \\ \simeq \frac{\omega_0}{4} \exp\left[-\frac{\hbar\omega_0}{k_B T}\right] \int_{-\infty}^\infty \frac{d\Delta}{\Delta^2 - (\Gamma/2)^2} & \\ = \frac{\pi}{2} \frac{\omega_0}{\Gamma} \exp\left[-\frac{\hbar\omega_0}{k_B T}\right], & \end{aligned} \tag{3.53}$$

where we defined $\Delta \equiv \omega_0 - \omega$. Thus, for the resonant contribution

$$\dot{Q}_{res} \simeq \left(\frac{6}{\pi}\right) \left(\Gamma \frac{\hbar^2 \omega_0^2}{M c^2}\right) \left(\frac{\Gamma}{\omega_0}\right) \frac{\pi}{2} \frac{\omega_0}{\Gamma} \exp\left[-\frac{\hbar\omega_0}{k_B T}\right] \tag{3.54}$$

Evaluating $\dot{Q}_{res}$ for ^{6}Li inside a cavity at temperature $T = 300°$K gives

$$\dot{Q}_{res} = 6 \times 10^{-29}\,°\text{K/s}. \tag{3.55}$$

We have found that the dominant contribution of heating from black body radiation for trapped ^{6}Li atoms arises from the nonresonant scattering of photons. However, this process only yields a heating rate of $\dot{Q} \simeq 5 \times 10^{-18}\,^\circ$K/s and is thus completely negligible. Thus, while black body radiation poses significant challenges to cooling bulk matter it causes insignificant heating in a trapped atomic sample.

3.7 Ultrastable CO_2 Laser Trap

Since we are interested in studies of *ultracold* fermionic vapors in an optical trap, heating due to optical scattering and laser intensity and position fluctuations are of central concern. In Section 3.3 we have seen that these problems can be overcome by using extreme detunings from resonance and a laser with exceptional intensity and pointing stability. Fortunately, these qualities can be provided by a properly designed CO_2 laser. In this section we investigate the properties of a CO_2 laser trap for fermionic ^{6}Li atoms.

CO_2 lasers operate at a wavelength of $\lambda_{CO_2} = 10.6\mu$m. The resonant transition for ^{6}Li occurs for $\lambda_{Li} = 671$ nm light. Thus, for CO_2 laser confinement of ^{6}Li atoms $\omega/\omega_0 = 1/15.8$ which is in the quasi-electrostatic limit. Properly designed CO_2 lasers are powerful and extremely stable in both frequency and intensity. Single mode, 50 Watt lasers with root mean square fractional intensity fluctuations $< 10^{-4}$ can be constructed [89,90]. Therefore these lasers promise to have negligible optical heating and minimal laser-noise-induced heating.

We also require that the well depth of the optical trap be several hundred μK since a magneto-optical trap for ^{6}Li (described in Chapter 4) produces atoms at between $\sim 140\mu$K and 1 mK. A $P = 50$ Watt CO_2 laser beam focused to $a = 50\mu$m spot size gives a peak intensity $I_0 = 2P/\pi a^2 = 1.3\text{MW/cm}^2$. The ground state

CO_2 Laser Trap Parameters	
Wavelength	10.6 μm
Power	50 Watts
Waist Radius (a)	50 μm
Rayleigh Length (z_0)	0.75 mm
Trap Depth U_0/k_B	500 μK
Radial Frequency	5.3 kHz
Axial Frequency	250 Hz
Photon Scattering Rate	3.6×10^{-4} Hz
Photon Recoil Heating Rate	10 pK/s
Intensity Noise Time Constant (Γ^{-1})	$\geq 5 \times 10^4$ s
Position Noise Heating Rate ($\dot{Q}$)	$\leq$ 46 nK/s

Table 3.1: CO_2 Laser Trap for ^{6}Li

static polarizability for lithium has been measured to be $\alpha_s = 24.3 \times 10^{-24}$ [91]. Thus, the well depth in Kelvin is $U_0/k_B = 2\pi\alpha_s I_0/k_B c = 500\mu$K.

In the next chapter we describe the construction of an ultrastable CO_2 laser which is used to form an optical trap for ^{6}Li fermions. Typically, this laser provides 50 W of power at the vacuum system which is used to form the trap. Table 3.1 lists the parameters for the CO_2 laser trap Note that due to the extremely low frequency of the 10.6 μm radiation and the large detuning from the ^{6}Li resonance frequency, the photon scattering rate is only 3.6×10^{-4} Hz. Thus, the time required for an atom to have scattered a single photon is 2700 sec, over 3/4 of an hour. The photon recoil heating rate corresponding to this scattering rate is only 10 pK/s. In Chapter 4, we describe measurements of the intensity and pointing noise for this laser. We find that the intensity noise induced exponential heating time constant Γ^{-1} is measured in hours and the position noise induced heating rate is measured in nK/s for this system. By combining the ultrastable CO_2 laser trap with an ultra-high vacuum system operating at a pressure $\leq 10^{-11}$ Torr, we demonstrate optical storage of ^{6}Li

for hundreds of seconds.

Chapter 4

Ultrastable CO_2 Laser Trapping of ^{6}Li

In this chapter, we recount the experimental development of the first stable optical trap for neutral atoms. We confine fermionic ^{6}Li atoms at the focus of an ultrastable CO_2 laser for hundreds of seconds in an ultra high vacuum environment operating at $\simeq 10^{-11}$ Torr. We begin with a description of the ultrastable CO_2 laser itself which is the heart of the system. This laser was custom built to provide maximal intensity and pointing stability in order to minimize laser noise induced heating. The focused beam from this laser provides a 400μK deep well depth for ^{6}Li atoms. We then describe the cooling and trapping apparatus which includes the ultra high vacuum system and the magneto-optical trap. The magneto-optical trap (MOT) provides a cold and dense source of lithium atoms for loading the CO_2 laser trap. We discuss the experimental techniques used to overlap the CO_2 laser trap with the MOT and the procedure used to load atoms from the MOT into the CO_2 laser trap. Finally, we report on our observation of optical confinement of atoms in the CO_2 laser trap and the measurement of the trap lifetime.

Figure 4.1: The ultrastable CO_2 laser.

4.1 The Ultrastable CO_2 Laser

Figure 4.1 shows the custom-built ultrastable CO_2 laser which was constructed to provide a stable source of 10.6 μm radiation for use as an optical trap. The laser is approximately 2 meters in length and produces 65 Watts in an nearly TEM_{00} mode. In Section 4.1.2 we find from the measured intensity and pointing noise power spectra that predicted noise induced heating times are measured in hours for this laser.

Properly designed CO_2 lasers are powerful and extremely stable in both frequency and intensity [89,90]. Several design considerations contribute significantly to the increased stability of the laser. High-voltage power supplies which power the plasma discharge tube should be extremely stable to reduce discharge current fluctuations. Proper electrode design minimizes plasma instabilities within the amplifying region. Heavy mechanical construction reduces mechanical vibration. Finally, the use of thermally and acoustically shielded Invar rods as spacers for the resonator cavity mirrors reduce the effect of thermal fluctuations and room noise. We are indebted to Dr. Charles Freed (Lincoln Laboratory, MIT) with whom we collaborated on the design of the ultrastable CO_2 laser described below. The design used

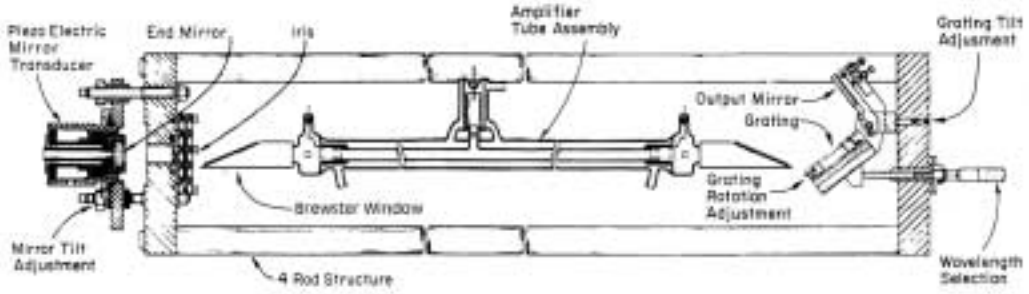

Figure 4.2: Overview of the ultrastable CO_2 laser

is based on similar lasers built by C. Freed and J. E. Thomas *et al.* [89,90] at MIT. The major modifications to these designs include the use of a high output coupling efficiency diffraction grating optimized for high output power operation and the use of Brewster windows to reduce the hazard of electrical shock.

4.1.1 Design and Construction

The resonator is a 2.0 meter semiconfocal cavity consisting of a 5 meter radius of curvature mirror and a diffraction grating as shown in Figure 4.2. The mirror is silver-coated and dielectrically enhanced to provide a reflectivity of 99.6% for 10.6 μm radiation. The output coupling for the laser is via the zero order reflection off of the grating and feedback is provided by the first order reflection (i.e. a Littrow configuration). Two fold mirrors following the grating direct the radiation away from the laser at a 90° angle to the cavity axis (the second fold mirror is not shown in Figure 4.2). A conical, polished brass iris with a 10.5 mm diameter aperture placed at mirror end of the cavity restricts oscillation to the TEM_{00} transverse mode [92]. The conical shape ensures that light falling outside the aperture is removed from the resonator.

The diffraction grating has a groove density of 150 lines per mm which is chosen such that only zero and first order reflections occur for 10.6 μm light. The grating is ruled on a stainless steel substrate and coated with gold. The grating is specially blazed such that in the Littrow configuration, 30% of incident 10.6 μm radiation is reflected into the zeroth order. By providing 30% reflection into the zeroth order, this grating yields the optimum output coupling for peak output power for a CO_2 laser of this length [92]. This grating was purchased from Hyperfine Inc. (Boulder, Colorado). However, this grating is not one of their standard products and may be difficult to replace. It was fabricated under the request and with the assistance of Dr. K. Evenson of NIST (Boulder).

The grating is mounted in an assembly that is designed to give a fixed output direction when rotated for wavelength selection. The assembly is shown in Figure 4.2. The assembly contains a mirror mounted at 90° with respect to the grating. The entire assembly rotates about the axis defined by the intersection between the plane of the mirror and the plane of the grating. Rotation of the assembly about this axis does not cause a change in the output beam direction as described in Ref. [93]. Coarse wavelength selection is achieved by rotation of this assembly using a micrometer head mounted to the laser frame. The entire assembly can also be tilted for initial alignment of the grating.

Fine adjustments of the cavity length is realized using a piezoelectrical transducer (PZT) attached to the high reflectivity mirror. The PZT assembly consists of an aluminum piston-stainless steel cylinder arrangement which conducts heat away from the piezoelectric crystal to reduce thermal frequency drift. The piston is machined to have a tight but sliding fit inside the stainless cylinder to provide good stability for the mirror. The aluminum piston retains the mirror by means of

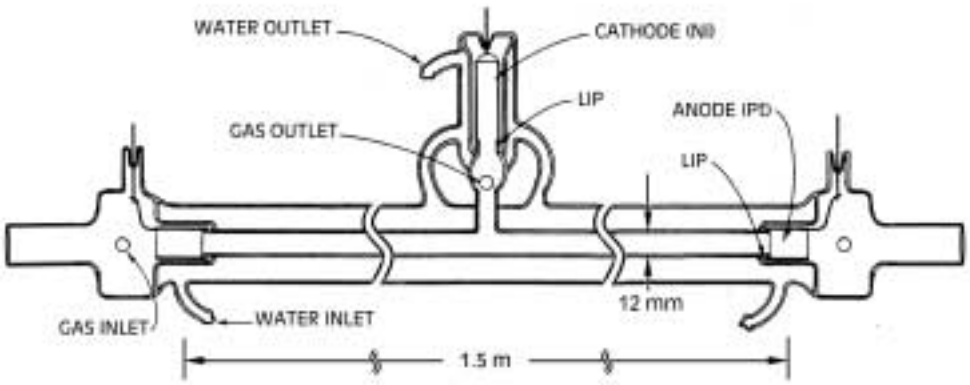

Figure 4.3: CO_2 laser amplifier tube.

a cap and phosphor-bronze spring.

A four rod structure is used to support the grating and mirror assemblies as shown in Figure 4.2. The rods are $1\frac{1}{4}$ inch diameter solid invar rods. These rods are each wrapped in lead filled foam that damps mechanical vibrations in the structure. Armaflex insulation tubing is also wrapped around each rod. The Armaflex provides thermal insulation and acoustic shielding.

The laser amplifier tube is made of pyrex and consists basically of a 12 mm inner bore and a water cooling jacket as shown in Figure 4.3. The amplifying region runs the length of the central bore between the two platinum anodes that are seperated by 1.5 m. Each platinum anode fits snugly around a lip protruding from the inner bore so that instabilities due to sharp ends of the cylindrical electrode are eliminated. The nickel cathode is located such that the cathode fall region and tube outlet are external to the central bore. This minimizes plasma instabilities within the amplifying region. The cathode also fits snugly around a lip. Two gas inlets and a central outlet are provided to achieve a uniform gas flow throughout the gain region. In order to electrically insulate the plasma tube from the laser

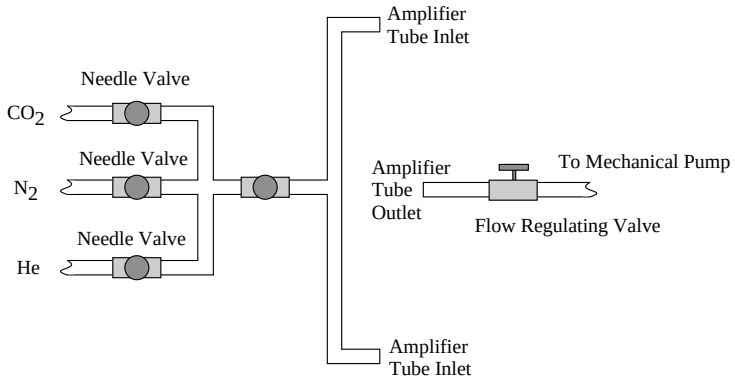

Figure 4.4: CO_2 laser gas handling system.

structure, Brewster window holders made of machinable ceramic (MACOR) slide onto each end of the tube. Each window holder contains two O-ring seals for vacuum compatibility. Uncoated ZnSe windows are simply epoxied to the machinable glass surface using Hardman epoxy. One drawback of using Brewster windows is that mechanical vibrations of the Brewster windows may cause intensity and pointing fluctuations of the laser. To minimize these effects, the pyrex tube is firmly held at each end and in the middle by heavy aluminum mounts.

A slow flow gas handling system, shown schematically in Figure 4.4, is utilized to avoid the complexity and cost of a sealed off laser system. Mechanical pump vibrations are isolated from the CO_2 laser by a long PVC tube rigidly mounting to the floor. The laser is operated with a gas mixture ratio He:N_2:CO_2 = 78:12:10 and with a total gas pressure of 32.5 mbar. This Helium rich gas mixture was suggested by Dr. K. Evenson of NIST (Boulder) for high output power performance.

The plasma discharge is maintained by two Northeast High-Voltage power supplies rated for 7.5 kV/65 mA output on loan from Lincoln Laboratory (Bedford, MA). By utilizing vacuum tube technology and careful transformer design, these high-voltage power supplies are rated for 10^{-6} fractional stability at full voltage.

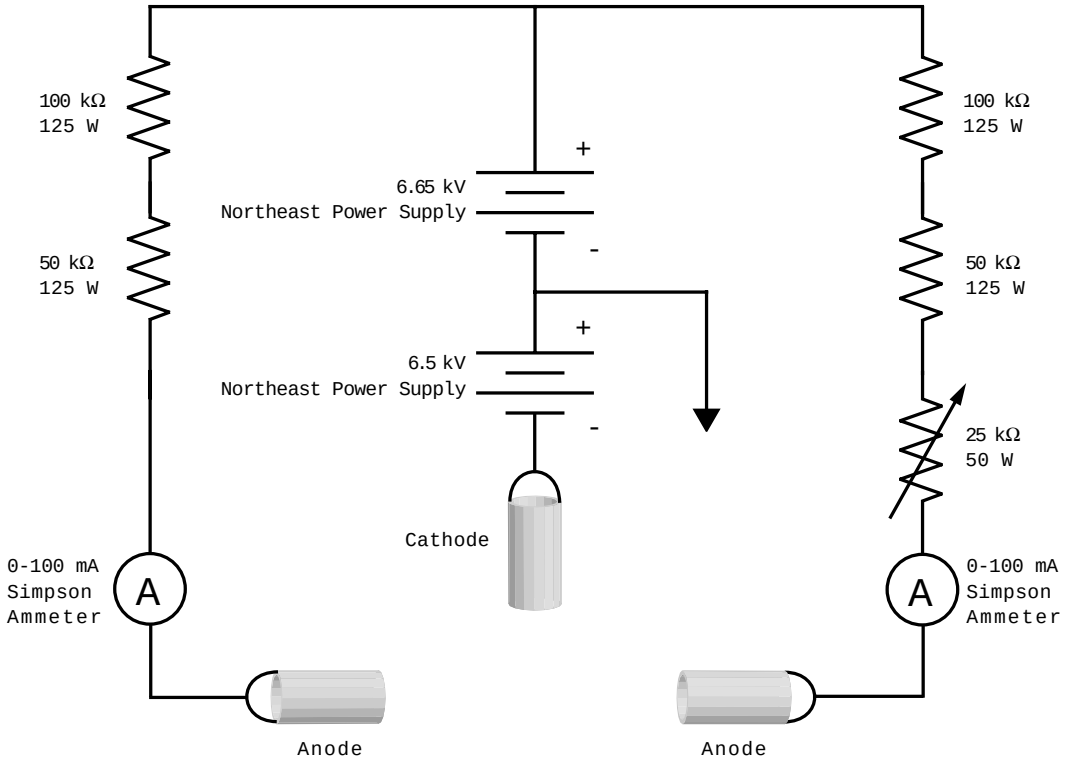

Figure 4.5: CO_2 laser electronic system.

The electrical system is shown in Figure 4.5. Ceramic, low-inductance resistors made by Cesiwid Inc. are used for ballast resistance in each arm. A 50 W 50 kΩ variable resistor is used to balance the current in the two arms. The laser is operated with 6.8 kV and 6.5 kV on the high voltage supplies. For the gas mixture and pressure described above, these voltages maintain a 30 mA discharge current in each arm. The discharge is initiated with a hand held tesla coil.

We are indebted to Dr. C. Primmerman and Dr. R. Heinrichs of MIT Lincoln Laboratory for loaning us the two stable Northeast high voltage power supplies used to operate the laser.

4.1.2 Laser Noise Spectra

As we found in Chapter 3, heating can arise from laser intensity noise and beam pointing fluctuations. There, we developed equations which predict the noise-induced heating rates for a harmonic potential based on laser-noise spectra. We will now use the measured CO_2 laser noise spectra to estimate the expected heating rates based on these formula. Of course, the trap formed by the focused laser is gaussian in the radial direction and lorentzian in the axial direction. Only atoms near the bottom of the well experience a harmonic potential. Thus, while these formula accurately predict the expected heating rates for cold atoms, they provide only a rough estimate of the expected heating rates when the confined atoms are at a temperature comparable to the well depth.

Figure 4.6 shows the experimental setup for measuring the laser intensity and pointing noise spectrum of the ultrastable CO_2 laser. A small ($\sim 5\%$) amount of CO_2 laser power is split off by an uncoated ZnSe wedge. The faces of the ZnSe wedge have a 3° angle between them so that the spots reflected off the front and

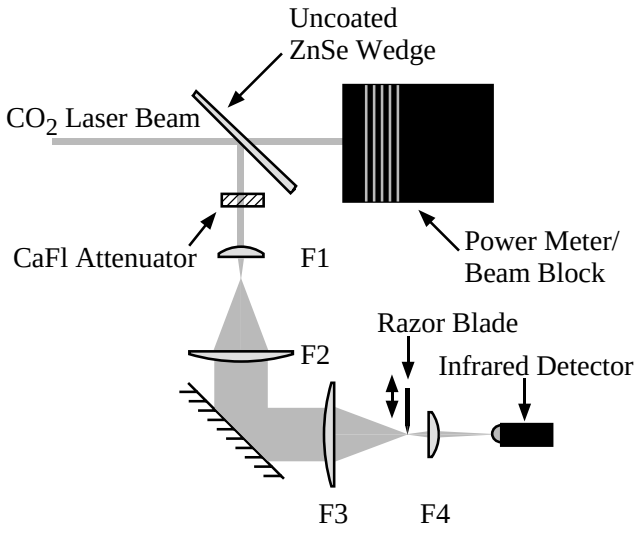

Figure 4.6: Experimental setup for measuring the intensity and position noise of the CO_2 laser.

back surfaces of the wedge are easily distinguished. One beam is sent to a beam dump (not shown) and the other beam is used for the noise measurement. This beam is sent through a CaFl attenuator to reduce the laser power to ~ 80 mW. The beam is then expanded by a telescope and focused to a $53\,\mu$m radius spot size by lens $F3$. The configuration of lenses $F1$, $F2$ and $F3$ is identical to that used when they are employed to form the trap. The CO_2 laser trapping potential is formed at the focus of lens $F3$. At the focus of $F3$, a razor blade can be moved across the laser beam. For intensity noise measurements the razor blade is moved completely out of the way. For position noise measurements the position of the razor blade is adjusted so that the razor blade blocks half of the laser beam. Beyond the razor blade the beam expands and is refocused by $F4$ to a $225\,\mu$m radius spot size onto a low-noise infrared detector.

The infrared detector is a model PD-3 from the PD-10.6 series of detectors made by Boston Electronics. The $225\,\mu$m spot size is chosen so that the beam does not

locally saturate the detector. The output of the detector is connected to a low-noise preamplifier supplied by Boston Electronics. The output of the preamplifier is connected to a Tektronix TDS644B digital oscilloscope with either a 5 kHz or a 50 kHz low pass filter.

The digital oscilloscope records a time series $V(t)$ of the voltage output by the preamplifier. A LabView program written by Tom Savard reads the time series from the oscilloscope and calculates the one-sided power spectrum of the fractional fluctuations as defined by (3.25):

$$S_V(\omega) \equiv \frac{2}{\pi} \int_0^\infty d\tau \cos \omega\tau \langle \epsilon(t)\epsilon(t+\tau) \rangle, \tag{4.1}$$

where $\epsilon(t) = (V(t) - V_0)/V_0$ and V_0 is the average voltage. The process is repeated and the power spectra are averaged together.

Intensity Noise Spectrum

To measure the intensity noise power spectrum, the razor blade in Figure 4.6 is removed so that it does not obstruct the beam. The one-sided power spectrum of the fractional voltage fluctuations is recorded. The one-sided power spectrum with the laser completely blocked is also acquired to record the electronic noise spectrum. The difference in these spectra yields the one-sided power spectrum of the intensity fluctuations.

Both a high-frequency, low-resolution spectrum and a low-frequency high-resolution spectrum are obtained. These spectra are shown in Figures 4.7 and 4.8. The spectrum in Figure 4.7 is obtained using a 50 kHz (3-dB point) low-pass filter at a sample rate of 500 kSamples/s providing data out to the Nyquist frequency of 250 kHz. Aliasing effects are avoided by setting the Nyquist frequency at 5 times

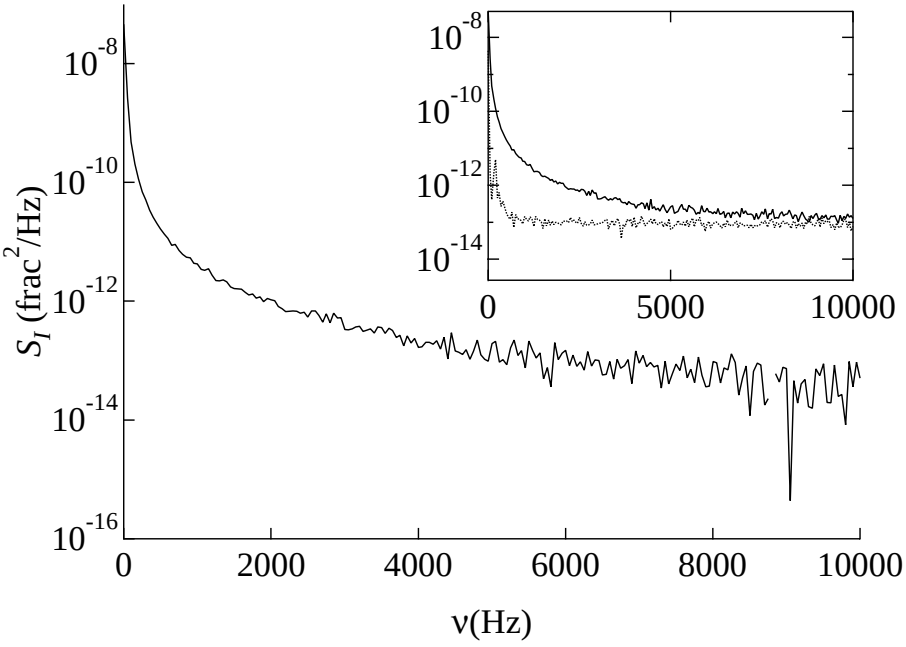

Figure 4.7: CO_2 laser intensity noise spectrum (low resolution). The main figure shows the one-sided fractional intensity noise power spectrum after the electronic noise power spectrum has been subtracted off. The inset shows the intensity noise power spectrum with the CO_2 laser blocked (lower curve in inset) which yields the electronic noise power spectrum and with the CO_2 laser unblocked (upper curve in inset) which gives the sum of the laser intensity noise and the electronic noise background. Note that at high freqeuncy ($\nu \simeq 10$ kHz), the CO_2 laser intensity noise falls below the sensitivity of the detector.

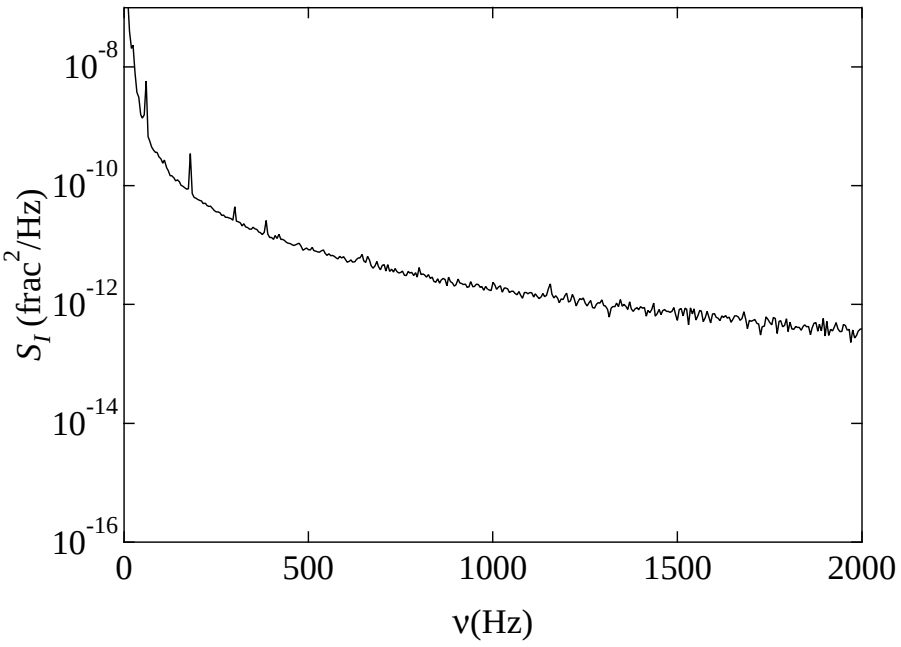

Figure 4.8: CO_2 laser intensity noise spectrum (high resolution). The figure shows the one-sided fractional intensity noise power spectrum after the electronic noise power spectrum has been subtracted off.

the filter 3-dB point. The inset shows the fractional noise spectrum with the laser unblocked (solid line) and blocked (dashed line). The blocked spectrum shows the electronic noise of the detection system. The intensity noise spectrum shown in the main part of the figure is obtained from the difference in these spectra. Note that above 5 kHz the laser intensity noise spectrum is comparable to the detector noise of 1×10^{-13}/Hz. Thus, at ~ 10 kHz we estimate that the laser noise is $< 1 \times 10^{-13}$/Hz. This is nearly three orders of magnitude smaller than the laser intensity noise for a commercial Argon ion laser (see Figure 3.3).

The spectrum in Figure 4.8 is obtained using a 5 kHz low-pass filter at a sample rate of 50 kSamples/s providing data out to 25 kHz. This high resolution spectrum allows one to clearly see the noise peaks at 60 Hz and at 180 Hz that are not observable in the lower resolution spectrum (Figure 4.7).

For atoms near the bottom of the well that experience a harmonic potential, we can calculate the exponential heating rate based on the intensity noise spectrum. Recall that the average energy increases exponentially $\langle \dot{E} \rangle = \Gamma \langle E \rangle$ where the rate constant

$$\Gamma = \pi^2 \nu^2 S_I(2\nu). \tag{4.2}$$

Figure 4.9 shows Γ^{-1} as a function of trap frequency ν_{tr} as calculated from the intensity noise power spectra. The main figure shows the low-resolution data and the inset shows the low-frequency, high resolution data. Due to the greatly reduced intensity noise of the CO_2 laser, exponential heating time constants exceeding 10^4 seconds are expected for a trap based on this laser.

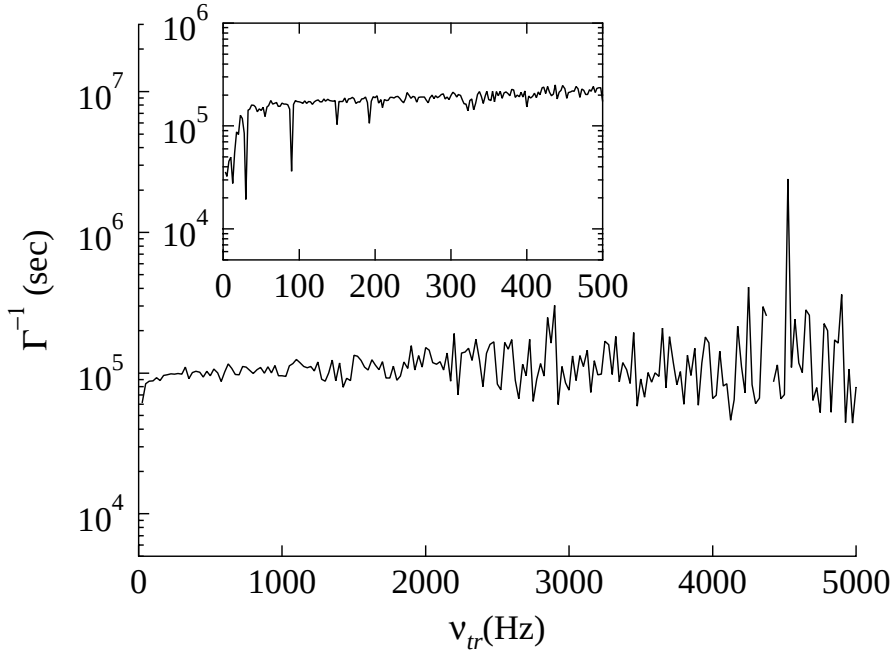

Figure 4.9: Predicted exponential heating time constant for the CO_2 laser trap. The main figure shows the exponential heating time constant based on the low resolution intensity noise power spectrum shown in Figure 4.7. Note that for trap frequencies beyond $\nu_{tr} \simeq 5$ kHz, the intensity noise has fallen below the detectors sensitivity. The inset shows the predicted exponential heating time constant based on the high resolution intensity noise power spectrum shown in Figure 4.8.

Position Noise Spectrum

To measure the position noise power spectrum, the razor blade shown in Figure 4.6 is adjusted so that it blocks exactly half of the beam. With the razor blade dividing the beam in half vertically, a displacement $\epsilon(t)$ of the beam in the horizontal direction causes a fluctuation in the power reaching the detector. The power fluctuation corresponding to a displacement $\epsilon(t)$ is given by $\Delta P = \sqrt{2}P_0\epsilon(t)/(a\sqrt{\pi})$ where a is the $1/e^2$ intensity radius of the Gaussian laser beam and P_0 is the total power in the unblocked beam. Thus, neglecting intensity fluctuations for the moment, the one sided power spectrum of the position fluctuations $S_x(\nu)$ is given by

$$S_x(\nu) = \frac{\pi}{2}\, a^2\, S_\epsilon(\nu), \tag{4.3}$$

where $S_\epsilon(\nu)$ is 1/4 the one-sided power spectrum of the fractional voltage fluctuations from the detector. The factor of 1/4 arises from the fact that 1/2 the beam is blocked.

Of course, the measured $S_\epsilon(\nu)$ will contain fluctuations arising from both position fluctuations and intensity fluctuations of the laser. However, we can subtract off the intensity fluctuation spectrum shown in Figure 4.7 obtained without the razor blade to yield the fractional fluctuation spectrum due to displacement fluctuations alone. This spectrum can then be used in (4.3) to yield the position fluctuation spectrum.

Figure 4.10 shows the fractional detector voltage fluctuation $S_\epsilon(\nu)$ with the razor blade blocking half of the beam (solid line) and with the razor blade removed from the beam (dashed line). Note that for the majority of the frequencies the two spectra are nearly identical except for two position noise peaks at 680 and 800 Hz.

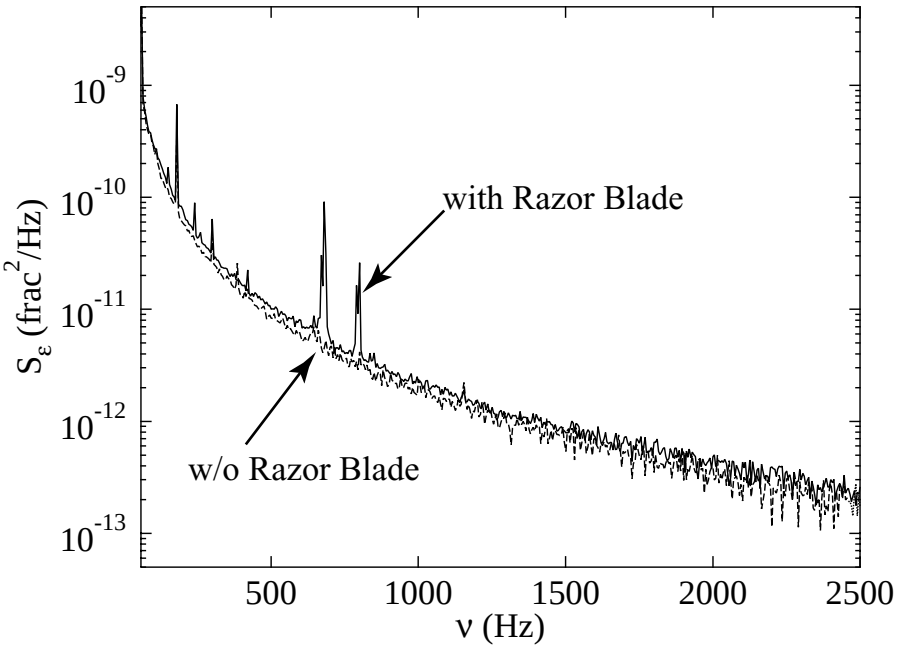

Figure 4.10: Fractional voltage fluctuation power spectrum with and without the razor blade. Note that the curves lie on top of one another for the majority of frequencies except for the peaks at 680 and 800 Hz which only occur when the razor blade is inserted into the beam.

Thus, we conclude that the position noise is below the noise floor of our detection system for most of the spectrum.

The position fluctuation spectrum $S_x(\nu)$ is given by the difference in the two spectra shown in Figure 4.10 multiplied by $\pi\, a^2/2$. The resulting spectrum is shown in Figure 4.11. The main figure shows the low resolution spectrum while the inset displays the high resolution spectrum.

As we found in Chapter 3, position fluctuations cause a constant heating rate $\langle \dot{E} \rangle = \dot{Q}$ given by

$$\dot{Q} = 4\pi^4\, M\, \nu_{tr}^4\, S_x(\nu_{tr}) \tag{4.4}$$

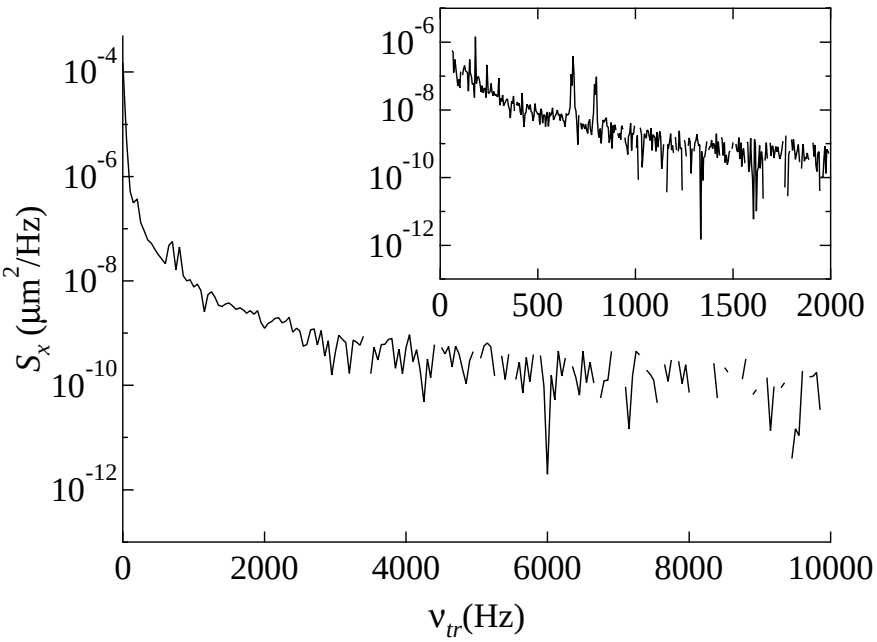

Figure 4.11: Position noise spectrum $S_x(\nu)$ of the CO_2 laser. The main figure shows the low resolution spectrum extending out to 10 kHz. The inset shows the high resolution spectrum which clearly indicates the position noise peaks at 680 and 800 Hz. Except for these peaks, the position noise is comparable to or below the sensitivity of the detection system.

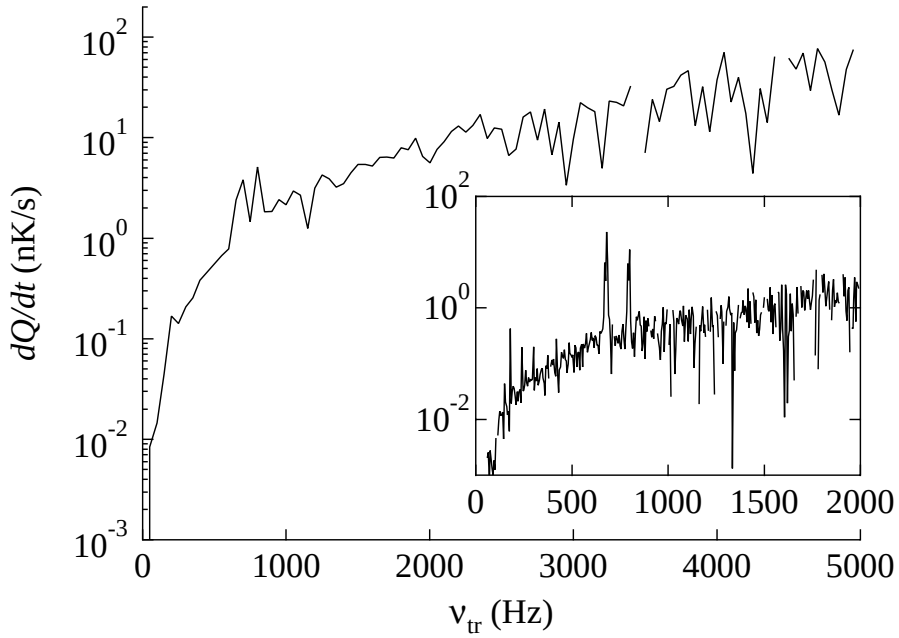

Figure 4.12: Predicted position noise induced heating rate $\dot{Q}$ for the CO_2 laser trap based on the spectrum shown in Figure 4.11. The main figure shows the low resolution data and the inset shows the high resolution data. Except for the peaks at 680 and 800 Hz the curve shown gives an upper bound on the predicted heating rate since the position noise is less than or comparable to the sensitivity of our detection method.

where M is the mass of the atom and ν_{tr} is the harmonic oscillation frequency for atoms confined at the bottom of the trap. The expected constant heating rate for the CO_2 laser trap is shown in Figure 4.12 as a function of the harmonic trap oscillation frequency. For the majority of the spectrum, the position noise is below the noise floor of the detection system except for the peaks at 680 and 800 Hz. The position noise heating rate is below ~ 50 nK/s for all trap frequencies shown.

4.2 The Cooling and Trapping Apparatus

In this section, we describe the cooling and trapping apparatus which includes both the ultra high vacuum system and the ^{6}Li magneto-optical trap. The magneto-optical trap (MOT) provides a source of cold ^{6}Li atoms for loading the shallow CO_2 laser trap. The ultra high vacuum system provides a low pressure environment in which atoms can be stored for hundreds of seconds.

In Chapter 3, we found that a 50 W CO_2 laser beam focused to a 50 μm spot size produces a 500 μK deep well for ^{6}Li atoms. To load atoms into this shallow well we need a source of cold atoms. The magneto-optical trap (MOT) has become a standard method for providing a cold and dense source of atoms [94,95]. The MOT has a well depth of ~ 1 K and can be loaded from the slowed atomic beam produced by a Zeeman slower [96,97]. The operation of both the MOT and the Zeeman slower are based on the radiation pressure force. A brief explanation of their operation is given in this section in order to understand how the CO_2 laser trap is loaded. For a more thorough description of the Zeeman slower and magneto-optical trap see Tom Savard's dissertation [98]

4.2.1 The Vacuum System

The Zeeman slowed atomic beam and the magneto-optical trapped atoms are contained inside a vacuum system. As was pointed out in Chapter 3, achieving storage times of several hundred seconds requires an ultra high vacuum (UHV) environment operating at or below 10^{-11} Torr. In this section we describe the UHV vacuum system used in these experiments and point out the issues critical to achieving this low pressure.

The vacuum system consists of three sections: (1) the oven region, (2) the

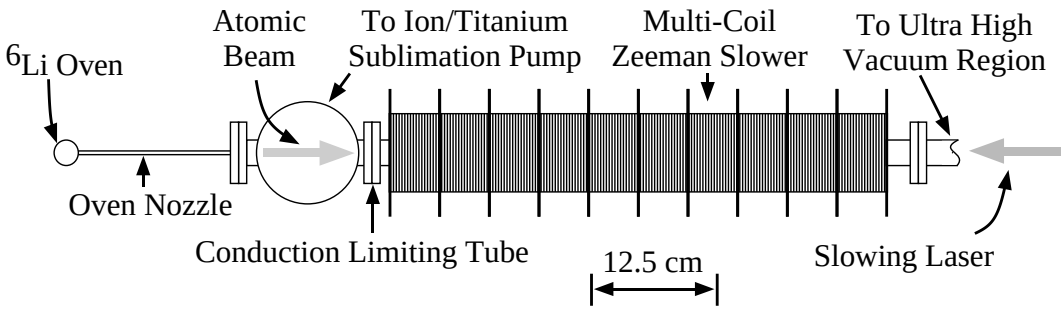

Figure 4.13: ^{6}Li oven and Zeeman slower.

Zeeman slower region and (3) the trapping region. The oven region contains the ^{6}Li oven which, in order to produce the atomic beam, is heated to $\simeq 400°$C during operation. Due to outgassing of the hot oven, the pressure in the oven region can be as high as 10^{-8} Torr. In order to maintain a pressure $< 10^{-11}$ Torr in the the trapping region where the optical trap is formed, the trapping region must be isolated from the oven region. The isolation is provided by the Zeeman slower region. The Zeeman slower vacuum region has a small conductance and limits the flow of gas between the oven and trapping regions. This permits a large pressure differential to be built up across the Zeeman slower. At the end of the slowing region a large ion pump and a titanium sublimation pump maintain the pressure in the trapping region at $< 10^{-11}$ Torr. Both the magneto-optical trap and the CO_2 laser trap are formed there.

Figure 4.13 is a top view of the oven region and the Zeeman slower. A thorough description of the ^{6}Li oven is given in [98]. Basically, the oven consists of a 2.5 in. tall, 3/4 in. diameter cylinder which contains approximately 2 grams of Lithium when it is newly filled. This cylinder is heated to $\simeq 400°$C to melt the ^{6}Li (melting point 180°C). The molten ^{6}Li rests in the bottom 1/4 of the cylinder while a ^{6}Li vapor fills the remainder of the volume. At this temperature, liquid ^{6}Li has a vapor

pressure $\simeq 10^{-4}$ Torr corresponding to a density of 10^{12} atoms/cc [98]. Half way up the cylinder, a 1/8 in. diameter circular aperture in the side of the cylinder allows the ^{6}Li vapor to escape into a 6.25 in. long nozzle. The inside diameter of the nozzle is 1/8 in. except at the end away from the oven where it opens to 3/16 in. diameter. The collimation angle provided by the nozzle is 21 mrad. The inside of the oven and the nozzle is lined with a stainless steel wire mesh. A temperature gradient is maintained across the nozzle such that the temperature drops from 400°C to 200°C across the length of the nozzle. In combination with the wire mesh, this temperature gradient causes condensed ^{6}Li to wick back to the oven reservoir. By recirculating unused ^{6}Li in this manner, the lifetime of the oven should be extended.

The oven is connected to a 4 in. diameter stainless steel tube that leads down to a 300 liter/sec ion pump made by Physical Electronics and a titanium sublimation filament made by Varian Vacuum Inc. The titanium sublimation pump operates by sublimating a monolayer of titanium atoms onto the walls of the vacuum system. Titanium is highly reactive with many elements and acts as a getter in the vacuum system. The pumping speed provided by the titanium film depends on the surface area coated. The pumping speed can be extremely high. For example, the titanium monolayer coated on the walls of the 4 in. diamter 10 in. tall tube in the oven region yields a pumping speed of $\cong 10^4$ liter/sec for O_2. However, certain elements such as Helium are not as reactive with Titanium. Luckily, the 300 liter/sec ion pump is effective at pumping these unreactive elements. With the oven operating at 400°C, the titanium sublimation pump and the ion pump maintain a pressure $< 5 \times 10^{-9}$ Torr in the oven region. The pumping speed of the titanium film eventually degrades as the titanium atoms react and form stable bonds. The pumping speed can be restored by applying a fresh monolayer of titanium. A fresh monolayer is applied

by running 47 Amps through a filament for 7 minutes. When the oven is used regularly ($\simeq$ 3 times a week for 8 hours a day) the titanium film needs to be sublimated about once every two weeks to maintain the full pumping speed.

One advantage to using ion and titanium sublimation pumps is that they operate without mechanical vibrations. Diffusion pumps also provide quiet operation but are not compatible with UHV systems. Turbomolecular pumps backed by mechanical pumps are compatible with UHV systems but generate acoustic noise and mechanical vibration. In fact, before the ion and titanium sublimation pumps were installed on the oven region, a 300 liter/sec Alcatel turbomolecular pump backed by a Leybold mechanical pump were used to pump out the oven region. The noise and vibration generated by these pumps was found to limit the lifetime of atoms in the CO_2 laser trap. To eliminate this problem the ion and sublimation pumps were installed on the oven region. When the system is initially pumped down from atmosphere, a small 20 liter/sec turbomolecular pump is used to reduce the pressure below 10^{-5} Torr so that the ion pump can be started. However, once the ion pump is started the turbomolecular pump can be isolated from the system by a metal seal valve and turned off.

The slower region is connected to the oven region by a $2\frac{3}{4}$ in. conflat flange opposite the oven (see Figure 4.13). Since we want to limit the flow of gas between the oven region and the trapping region, a long tube with a small diameter is installed at this point to limit the conductance between these two regions. The conduction limiting assembly consists of a 6 in. long copper tube with a 1/4 in. inside diameter mounted to a solid copper gasket. These assemblies are sold by Varian Vacuum Inc. for use as pinch off tubes. The tube and gasket assembly is simply installed on the system in place of the standard $2\frac{3}{4}$ in. copper gasket.

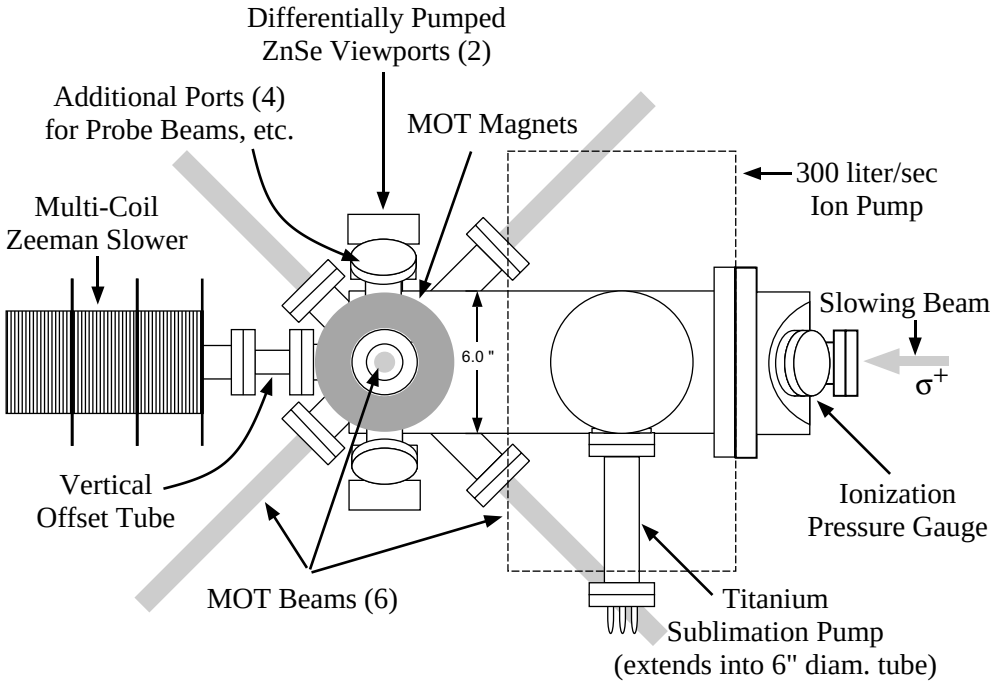

Figure 4.14: The trapping region.

Considered as a vacuum component, the slower region itself is simply a long tube which further limits the conductance between the oven and trapping regions. The slower tube is approximately 22 in. long and has an inner diameter of 1.5 in.

Figure 4.14 shows a top view of the trapping region. The slower region is connected to the trapping region by an offset tube which offsets the center of the trapping region vertically from the center of the slower tube by 3/8 in. This is done so that the magneto-optical trap, which forms in the center of the trapping region, is above the center of the atomic beam. Otherwise, unslowed atoms in the atomic beam would, through elastic collisions, eject atoms from the MOT.

The bulk of the trapping region consists of two 6 in. diameter stainless steel tubes connected at right angles to one another. Twelve viewports are mounted on the horizontal tube to provide ample optical access. The viewport for the slowing

laser beam and an ionization gauge are attached to the 8 in. port at the end of the horizontal tube. The vertical tube leads to a 240 liter/sec. ion pump made by Varian Vacuum Inc. Six inch diameter tubes are used so that the pumping speed of the ion pump is not compromised by the conduction of the tubes. A titanium sublimation filament extends into the vertical tube. The titanium sublimation filaments are located such that there is no direct path between the filaments and any of the viewports to ensure that the viewports are not subject to titanium deposition. This of course assumes that the titanium atoms stick to the first wall they encounter and do not bounce around in the vacuum system. The pumping speed for a monolayer of titanium is estimated to be 10^4 liters/sec. Titanium must be sublimated once every two months to maintain the pumping speed if the oven is used regularly. When the oven is run at 400°C, the pressure is $< 10^{-11}$ Torr, below the sensitivity of the ionization gauge.

As shown in Figure 4.14, six of the viewports are used for the six laser beams used to form the MOT. Two viewports are used to allow the CO_2 laser beam to enter and exit the vacuum system. This leaves four viewports that are free to be used for probe beams, imaging, etc.

One challenge posed by using a CO_2 laser beam to form the optical trap is finding UHV compatible viewports to admit the CO_2 laser beam into the vacuum system. Glass viewports cannot be used since glass strongly absorbs 10.6 μm radiation. Crystalline ZnSe is well suited for CO_2 optics since it does not absorb 10.6 μm radiation and is transparent at optical wavelengths. Unfortunately, ZnSe viewports are not readily made UHV compatible. The vacuum seal that can be obtained with crystalline ZnSe has a substantially higher leak rate compared to glass viewports. To achieve UHV compatibility, a differentially pumped ZnSe view-

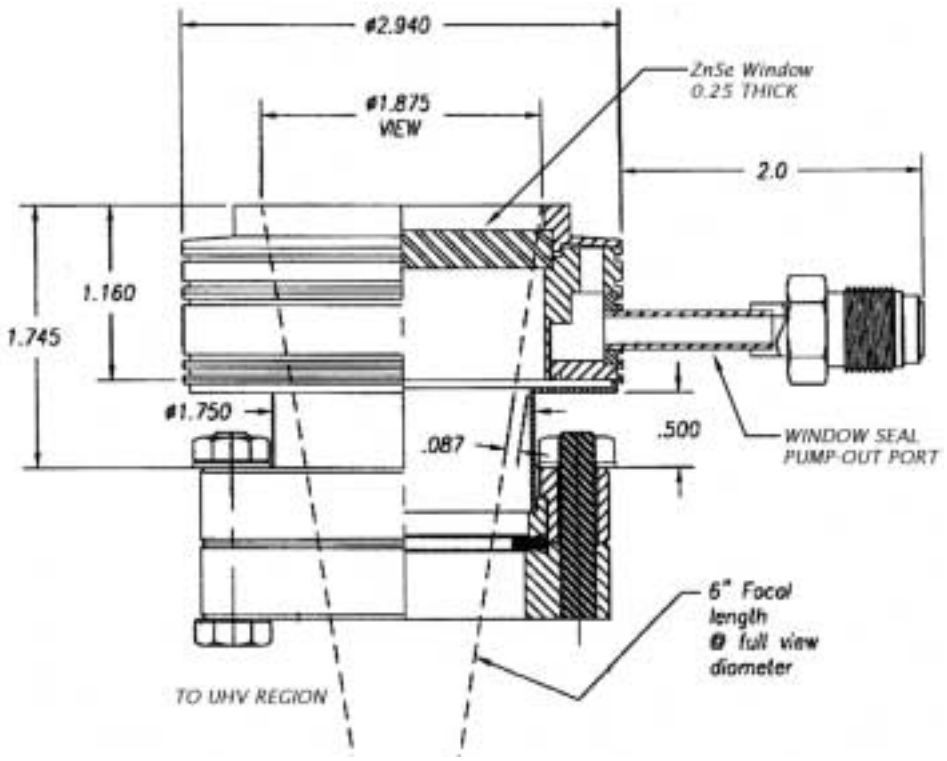

Figure 4.15: ZnSe UHV-compatible viewports.

port made by Insulator Seal, Inc. is used. Figure 4.15 shows the viewport custom built for our vacuum system. This design employs a double sealed, differentially pumped ZnSe window. The leak rate into the UHV system is substantially reduced by maintaining the region between the seals at a modest vacuum with an additional pump. Although a mechanical pump would be sufficient to maintain the vacuum between the seals, a 20 liter/sec ion pump is used instead as it provides a noise and maintenance free alternative and keeps the pressure between the seals $\leq 10^{-9}$ Torr. The ZnSe viewport was designed to provide as large an aperture as could be accommodated to permit tight focusing.

To prevent contamination of the vacuum parts, latex gloves were worn during assembly of the vacuum system. Most vacuum parts have been cleaned by the manufacturer. However, all flanges and gaskets are cleaned with acetone and methanol (in that order) prior to assembly.

In order to achieve ultra high vacuum operation, the entire vacuum system must be baked out for several days. Most components are baked at 250°C with a few exceptions. The ion pumps are baked at temperatures below 200°C since higher temperatures threaten to partially demagnetize the internal permanent magnets. The slower region is baked at 100°C since the copper cooling fins of the electromagnets were soft-soldered in assembly and cannot withstand higher temperatures. To bake the slower region, 8 Amps are driven through each of the ten coils without air or water cooling. The temperature, as measured by a thermocouple mounted to the slower coils, should be monitored to keep the temperature below 100° C. The gate valve which is located in the oven region between the oven and the ion pump, is baked at 150°C when it is in the open position. The oven is baked at 500°C for several 1/2 hour periods if recently filled with lithium. Finally, the seals on the

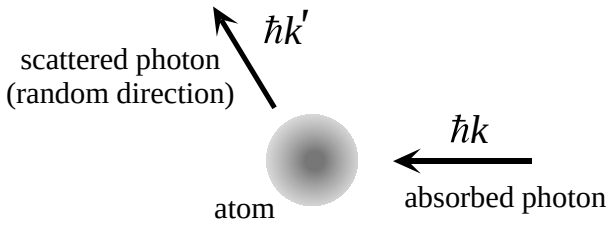

Figure 4.16: The radiation pressure force. By absorbing a photon, an atom recieves a momentum kick $\hbar\boldsymbol{k}$ in the direction of propagation of the laser beam. Since the subsequent reemission of the photon occurs in a random direction, on average, the atom receives a momentum kick equal to $\hbar\boldsymbol{k}$ in the direction of propagation of the laser beam for each absorption-emission cycle.

ZnSe viewports may be damaged for temperatures above 200°C. In addition, the titanium filaments must be outgassed during the bakeout process. This is accomplished by running 30 Amps through each filament for 2.5 minutes at a time and cycling through all filaments over the course of the entire bakeout. After several days of baking, the pressure in the system falls into the 10^{-7} Torr region and the bakeout is terminated.

4.2.2 "The Slower"- Introduction to the Radiation Pressure Force

Both the Zeeman slower and the magneto-optical trap are based on the radiation pressure force. Radiation pressure causes a force on the atom in the direction of propagation of the incident light. This force arises from the absorption and subsequent spontaneous emission of photons by the atom. Since it relies on the absorption of photons, the radiation pressure force is significant for light nearly resonant with the atomic transition.

Figure 4.16 illustrates the origin of the radiation pressure force. During the

absorption process, the atom receives a momentum kick $\hbar\mathbf{k}$ equal to the momentum of the incident photons. The atom then spontaneously emits a photon and receives another momentum kick $\hbar k$ in a random direction. On average, each absorption-spontaneous emission cycle imparts to the atom a momentum kick $\hbar\mathbf{k}$ equal to the momentum of the incident photons. Thus, the magnitude of the radiation pressure force is given by $\mathbf{F}_{rad} = \Gamma_{sc}\,\hbar\,\mathbf{k}$ where Γ_{sc} is the photon scattering rate.

For a two-level atom, the photon scattering rate is given by

$$\Gamma_{sc} = \frac{\Gamma}{2}\,\frac{s}{1+s+4(\Delta - k\,v)^2/\Gamma^2} \tag{4.5}$$

where Γ^{-1} is the excited state lifetime, v is the velocity of the atom, $\Delta = \omega - \omega_0$ is the detuning of the laser frequency from the atomic resonance frequency and s is the saturation parameter given by

$$s \equiv \frac{2\Omega^2}{\Gamma^2} = I/I_{sat}. \tag{4.6}$$

Here Ω is the Rabi frequency, I is the intensity of the laser beam and we have defined the saturated intensity $I_{sat} \equiv c\,\pi\,h\,\Gamma/3\lambda^3$.

The presence of the $k\,v$ term in (4.5) accounts for the Doppler shift. If an atom is moving toward the laser beam, the sign of v is negative and the photon scattering rate has a maximum for $\omega < \omega_0$. This reflects the fact that in the reference frame of the atom the laser field is blue shifted. Conversely, if an atom moves away from the laser beam, the photon scattering rate has a maximum for $\omega > \omega_0$ due to the fact that the laser field is red shifted in the atom's reference frame.

The two-level atom approximation is appropriate for an alkali atom illuminated with circularly polarized light. For circularly polarized light there exists a cycling

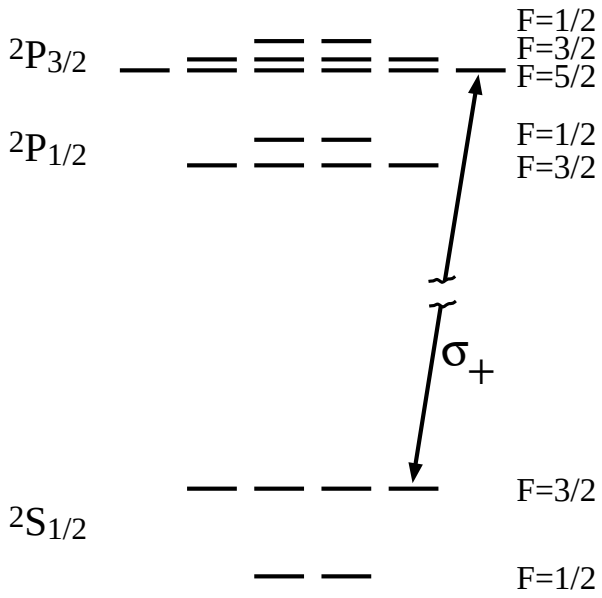

Figure 4.17: The photon burst transition in ^{6}Li

transition that only involves two levels. Figure 4.17 shows the level structure for the first excited state ($2S \rightarrow 2P$) transition in ^{6}Li. For right hand circularly polarized (σ^+) light, only $\Delta m = +1$ ground state to excited state transitions are allowed. The atoms are quickly optically pumped into the $F = 3/2$, $M_F = 3/2$ ground state (there is usually an additional "repumping" laser beam that pumps atoms out of the $F = 1/2$ state). From the $F = 3/2$, $M_F = 3/2$ state atoms can only make transitions to the excited $F' = 5/2$, $M_{F'} = 5/2$ which in turn can only decay back to the $F = 3/2$, $M_F = 3/2$ state. This cycling transition is also referred to as a photon burst transition.

For a saturated transition, $I >> I_{sat}$, $s >> 1$, the photon scattering rate $\Gamma_{sc} = \Gamma/2$ and the saturated radiation pressure force is $F_{rad} = \hbar\, k\, \Gamma/2$. For the photon burst transition in ^{6}Li, $I_{sat} = 2.55$ mW/cm^2 and $\Gamma^{-1} = 27$ ns. The acceleration due to this saturated radiation force $\hbar k\Gamma/2M = 2 \times 10^6$ m/s^2 for ^{6}Li, i.e. $2 \times 10^5\, g$!

The radiation pressure force can be used to decelerate a beam of atoms. If a laser beam counterpropagates with an atomic beam and is tuned below resonance such that the atoms' motion Doppler shifts the light into resonance, the atoms will experience a force opposite to their direction of motion. However, as an atom's velocity decreases the Doppler shift changes and the atom is no longer in resonance. Thus, to slow an atomic beam down, the frequency of the laser must be continuously adjusted. Alternatively, an applied magnetic field can be used to tune the atom's transition frequency via the Zeeman effect. In this way atomic beams can be continuously slowed by using a fixed frequency laser counterpropagating with an atomic beam which travels through a spatially varying magnetic field. The spatial profile of this magnetic field is chosen to compensate for the changing Doppler shift and keeps the atoms in resonance with the slowing laser.

A schematic of the Zeeman slower used in our experiment is shown in Figure 4.13. A ^{6}Li atomic beam travels from left to right in the figure inside the vacuum system. A counterpropagating laser beam enters the vacuum system on the right and produces the radiation pressure force that slows the atomic beam. Ten independently controllable electromagnets produce a spatially varying magnetic field that Zeeman shifts the frequency such that the atoms remain in resonance with the slowing laser as their velocity decreases. For a more complete description of the Zeeman slower see [98,99].

4.2.3 The Magneto-Optical Trap

The Zeeman slower provides a beam of slow atoms that can be captured by a magneto-optical trap. The MOT in turn cools the atoms further and builds up a cold and dense sample of atoms that can be loaded into the CO_2 laser trap. In

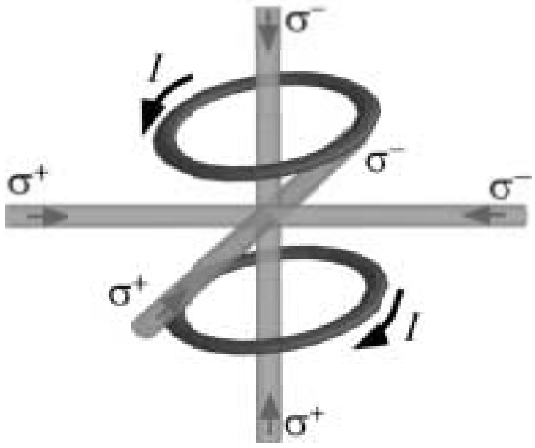

Figure 4.18: The magneto-optical trap.

a MOT, the radiation pressure force provides both a viscous damping force and spatial restoring force. In this section we present a simple picture of how the MOT works. We discuss the expected temperature and density limitations. Finally we discuss how we implement the MOT experimentally.

The standard magneto-optical trap is shown in Figure 4.18. Three sets of counterpropagating $\sigma^+ - \sigma^-$ laser beams propagate along three mutually orthogonal axes. These beams are tuned below resonance to provide a viscous damping force in three dimensions as described below. Two loops of wire at the top and bottom of the figure carry current in opposite directions and produce a quadrupole magnetic field. Between the two magnets the field is zero and its magnitude increases linearly in all directions from this point. The six laser beams intersect at this field zero point. The spatially varying magnetic field in combination with the choice of $\sigma^\pm$ polarizations gives rise to a spatial dependence of the radiation pressure force. The polarizations are chosen to produce a three-dimensional restoring force as described below. Thus, atoms are both confined and cooled in a magneto-optical trap yielding a cold and dense source of atoms. In this section, we first discuss the cooling

mechanism in the MOT followed by an explanation for the spatial restoring force.

Doppler Cooling

By tuning the laser beams below resonance, the radiation pressure force creates a viscous damping force for the atoms. To see this, consider the forces on an atom in one dimension illuminated by two counterpropagating laser beams tuned below resonance. This is illustrated in Figure 4.19(a). If the atom moves to the right, the beam propagating to the left will be Doppler shifted closer to resonance with the atom while the beam propagating to the right will be Doppler shifted further out of resonance. The atom will thus absorb more photons from the beam propagating to the left and will feel a net force to the left opposing its motion. Similarly, if the atom moves to the left, the radiation pressure force imbalance due to the Doppler shift gives rise to a net force to the right.

For low intensity light $s << 1$, the two beams act independently and the resulting force on the atom is given by the sum of the radiation pressure force from each beam

$$F_{tot} = \hbar\, k\, \frac{\Gamma}{2} \frac{s}{1 + [2(\Delta - kv)/\Gamma]^2} - \hbar\, k\, \frac{\Gamma}{2} \frac{s}{1 + [2(\Delta + kv)/\Gamma]^2}. \tag{4.7}$$

Figure 4.19(b) shows the individual forces from each beam (dashed curves) as a function of velocity in dimensionless units for the particular detuning $\Delta = -\Gamma/2$. The net force (solid line) is also plotted. Note that for small velocities ($|kv| << |\Delta|, \Gamma$), the net force is linear in velocity.

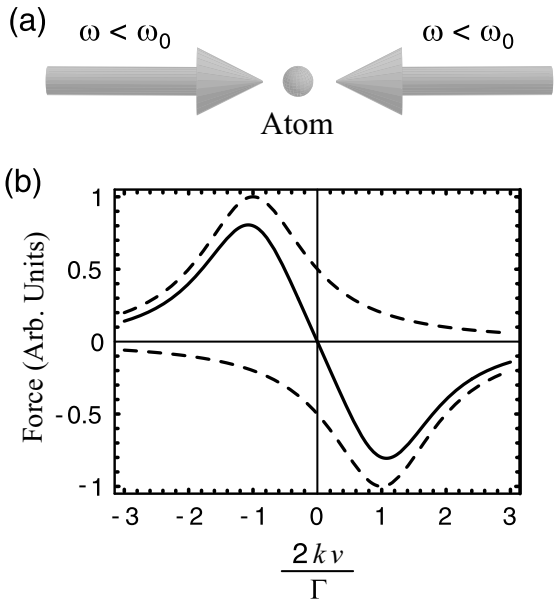

Figure 4.19: One-dimensional optical molasses. (a) Two counterpropagating beams tuned below the atomic resonance frequency ω_0 illuminate an atom. (b) The dashed lines show the force on the atom as a function of the atom's velocity for each beam individually. The net force is indicated by the solid curve.

For small v, $F_{tot} = -\alpha\, v$ where

$$\alpha = -4\,\hbar\, k^2 \frac{I}{I_0}\, \frac{2\Delta/\Gamma)}{[1+(2\Delta/\Gamma)^2]^2}. \tag{4.8}$$

This viscous damping force causes the energy of the atom to decrease at a rate

$$\left(\frac{dE}{dt}\right)_{cool} = Fv = -\alpha v^2. \tag{4.9}$$

However, the energy of the atom is not reduced to zero. Due to the fact that the atom is continuously scattering photons, the atom is executing a random walk in momentum space. For each absorption-emission cycle, the atom takes two steps in momentum space each in a random direction with a step size given by the recoil momentum $\hbar k$. The mean square momentum of the atom grows by the number of steps times the square of the step size i.e. $d\langle p^2\rangle/dt = 2\Gamma_{sc}\hbar^2k^2 = 2\mathcal{D}_p$ where Γ_{sc} is the photon scattering rate and $\mathcal{D}_p$ is the momentum diffusion constant. Thus, momentum diffusion due to photon scatter causes a heating rate

$$\left(\frac{dE}{dt}\right)_{heat} = \frac{1}{2M}\frac{d\langle p^2\rangle}{dt} = \frac{1}{2M}\,2\Gamma_{sc}\hbar^2k^2. \tag{4.10}$$

In equilibrium, the heating and cooling rates must be equal. Setting $(dE/dt)_{heat} + (dE/dt)_{cool} = 0$ and substituting in the low intensity and low velocity limit for the damping coefficient α and the photon scattering rate $\Gamma_{sc} = (I/I_0)\Gamma/(1+(2\Delta/\Gamma)^2)$ we find a condition on v^2:

$$v^2 = \frac{\hbar\Gamma}{4M}\frac{1+(2\Delta/\Gamma)^2}{2|\Delta|/\Gamma}, \tag{4.11}$$

which gives the mean squared velocity of the atom. This equation has a minimum

of $v^2 = \hbar\Gamma/2M$ for $\Delta = -\Gamma/2$. By the equipartition theorem $k_B T/2 = Mv^2/2$, and the corresponding minimum temperature is

$$k_B T_{min} = \frac{\hbar\Gamma}{2}. \tag{4.12}$$

This temperature is known as the Doppler limit. For ^{6}Li, $\Gamma/2\pi = 5.9$ MHz and $T_{min} = 140\,\mu$K.

The six beams used in a magneto-optical trap are a three-dimensional generalization to the one-dimensional molasses discussed above. Motion of the atom in any direction in three-dimensions causes a Doppler shift induced imbalance in the radiation pressure forces which opposes the atom's motion. The atoms are cooled by this viscous damping force but heated by photon scattering. A three-dimensional generalization of the arguments given above leads to the same results that the temperature has a minimum $T_{min} = \hbar\Gamma/2$ for a detuning $\Delta = -\Gamma/2$ [100].

It is interesting to note that temperatures well below the Doppler limit have been observed [101] for several different alkali atoms. These observations have been explained by going beyond the assumption of independent beams interacting with a two-level atom used in the preceding argument [102]. The explanation for the observed sub-Doppler temperatures relies on the fact that counterpropagating laser beams of different polarization give rise to polarization gradients and different ground state levels experience different coupling strengths to the excited state depending on the polarization. In the case of the $\sigma^+ - \sigma^-$ standing wave used in a MOT, the polarization of the combined field is linear everywhere however it's orientation rotates about the optical axis forming a helix. The mechanism for sub-Doppler cooling in this case hinges on the fact that for linearly polarized light, ground states with a different magnetic quantum number magnitude $|m|$ experience

different light shifts (AC Stark effect). This is true if the detuning of the laser field is comparable to or less than the excited state hyperfine splitting. However, in ^{6}Li the excited state hyperfine splitting is less than the natural linewidth of the excited to ground state transition. In this case, the hyperfine structure cannot be resolved and the difference in light shifts for ground states with different $|m|$ are negligible for linearly polarized light. Thus, sub-Doppler cooling mechanisms are not expected for ^{6}Li in a standard $\sigma^+ - \sigma^-$ magneto-optical trap.

Spatial Restoring Force

In addition to damping, the six laser beams of the MOT also generate a spatial restoring force due to the presence of an inhomogeneous magnetic field [94]. As described above, two current loops are used to create a quadrupole magnetic field $\mathbf{B}$ which goes to zero at the center of the loops where the laser beams intersect. The field magnitude $|B|$ grows linearly as you move away from the field zero in any direction. This magnetic field causes a spatially dependent and state dependent Zeeman shift. For an appropriate choice of optical polarizations, this Zeeman shift causes an imbalance in the radiation pressure force that pushes atoms toward the field zero.

To better understand the origin of the spatial restoring force, consider the energy level diagram for an atom along one of the laser propagation axes of the MOT shown in Figure 4.20. For clarity, the level scheme for this atom has been simplified so that the ground state has total angular momentum $\mathbf{F} = 0$ and the excited state $\mathbf{F}' = 1$. At $z = 0$ the magnetic field $B = 0$. The linear gradient in the field near $z = 0$ creates a spatially dependent Zeeman shift for the magnetic sublevels of the excited state. The laser beam propagating to the left is σ^- polarized and

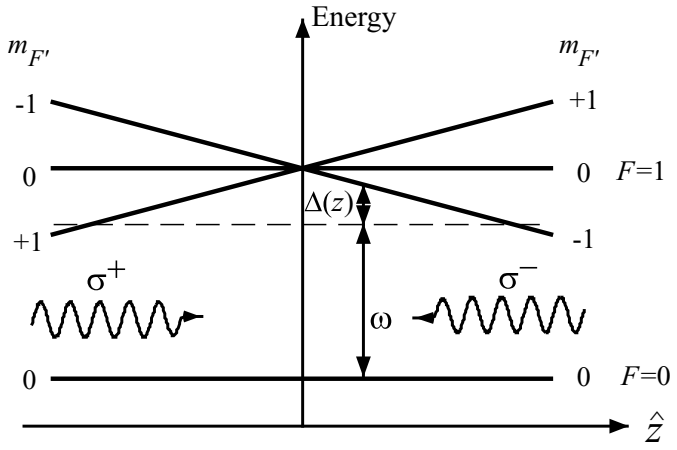

Figure 4.20: Spatial restoring force in one-dimension.

can only make transitions from the ground state to the $m_{F'} = -1$ state. The laser beam propagating to the right, being σ^+ polarized, only makes transitions to the $m_{F'} = +1$ state. As mentioned above, these beams are detuned below resonance. If an atom is displaced such that $z > 0$, the Zeeman effect causes the $m_{F'} = -1$ excited state to be shifted closer into resonance with the σ^- beam while the $m_{F'} = +1$ state is shifted further from resonance with the σ^+ beam. Thus, the atom will absorb more photons from the σ^- beam than the σ^+ beam and will experience a net radiation pressure force to the left toward $z = 0$. Similarly, if the atom is displaced such that $z < 0$, the σ^+ beam will be shifted into resonance and the atom will experience a net force to the right toward $z = 0$.

The energy level diagram for ^{6}Li shown in Figure 4.17 is slightly more complicated than that assumed in the argument above. However, the restoring force mechanism is basically the same. For ^{6}Li, the trapping beams are tuned to the red of the $|F = 3/2, m_F = \pm 3/2\rangle \leftrightarrow |F' = 5/2, m'_F = \pm 5/2\rangle$ cycling transition frequency. These transitions are akin to the $|m_F = 0\rangle \rightarrow |m'_F = \pm 1\rangle$ transitions in the simple example above. Since the trapping beams are circularly polarized, atoms

displaced from center are quickly optically pumped into the appropriate cycling transition state. The spatial restoring force then operates in an identical manner to the example described above. The only complication arises from the existence of a lower $F = 1/2$ ground state. By spontaneous emission atoms can decay into this state before being pumped into the cycling transition. To circumvent this problem, a repumping beam tuned into resonance with the $|F = 1/2, m_F = \pm 1/2\rangle \rightarrow |F' = 3/2, m'_F\rangle$ transition copropagates with each of the trapping laser beams and optically pumps atoms out of the $F = 1/2$ state.

By reproducing this one dimensional restoring force scheme on three mutually orthogonal axes, the MOT shown in Figure 4.18 produces a three-dimensional restoring force. The combination of spatial restoring and viscous damping forces allow atoms to be captured from the Zeeman slowed atomic beam. Initially, the number of atoms increases as $\dot{N} = R - \Gamma N$ where R is the loading rate and Γ is the loss rate due to collisions with background gas atoms inside the vacuum system. However, as the density increases several mechanisms eventually limit the maximum attainable density [103]. If the sample becomes optically thick, the inward radiation pressure force is reduced due to absorption of the incident photons. In addition, radiation trapping due to multiple scattering of the photons within the sample creates an outward radiation pressure force. Finally, inelastic collisions between atoms in which one or both are in the excited state release enough energy for atoms to be ejected from the trap.

We have seen a simple picture of how the Zeeman slower and MOT work. In the following sections we will describe how these techniques have been implemented experimentally and how the magneto-optical trap is used to load the CO_2 laser trap.

4.2.4 Magneto-Optical Trapping Apparatus

Generation of Required Optical Frequencies

To excite the ground to first excited state transition ($2S \rightarrow 2P$) in ^{6}Li, 671 nm wavelength light is required. Light of this wavelength is provided by a Coherent Model 699-21 Ring Dye Laser which circulates LD688 dye dissolved in 2-phenoxyethanol. The dye is pumped by a Coherent Innova Model 310 Argon Ion Laser which produces 6 Watts of power distributed between the visible argon lines (488 nm and 514.5 nm). With new dye, this system produces 750 mW of 671 nm radiation. The peak-to-peak frequency jitter is 5 MHz as measured by an external Fabry-Perot etalon. A thorough description of this dye laser system is given in Tom Savard's thesis [98].

A number of different optical frequencies near the ^{6}Li $F = 3/2 \rightarrow F' = 5/2$ resonance frequency ω_0 are required for operation of the MOT and Zeeman slower and for use as probe beams. The required optical frequencies are listed in Table 4.1. In addition, all of these beams need to be turned on and off during the course of the experiment. Fortunately, acousto-optic modulators provide a means for creating frequency shifts of several hundred MHz and can be used to turn the beams on and off.

An acousto-optic modulator (AOM) is used to shift the frequency of incident optical radiation be several hundred MHz. An AOM consists of a crystal with a piezo-electric transducer at one end. When radio frequency energy is supplied, the transducer generates a traveling sound wave in the crystal. Since the index of refraction of the crystal depends on the local density, the traveling sound wave is seen by the light as a modulated index of refraction. Thus, Bragg scattering of the incident light off of the traveling sound wave can occur. Usually, the angle of the

Beam	Frequency
reference	ω_0
slower	$\omega_0 - 200\,\mathrm{MHz}$
trapping	$\omega_0 - \Delta$
trap repumper	$\omega_0 + 225\,\mathrm{MHz}$
probe	$\omega_0 - 3\,\mathrm{MHz}$
probe repumper	$\omega_0 + 225\,\mathrm{MHz}$

Table 4.1: The laser beams required for trapping, cooling and probing ^{6}Li. Δ is the detuning of the trap laser beams below resonance. Δ may be up to 7 Γ where $\Gamma = 5.9$ MHz is the linewidth of the ^{6}Li transition.

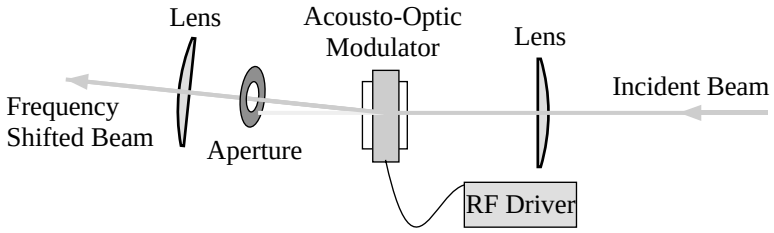

Figure 4.21: An Acousto-Optic Modulator

AOM crystal relative to the incident optical radiation is optimized such that the majority of the light is scattered into a first order Bragg reflection when rf power is applied. The optical frequency of the light is either upshifted or downshifted by the rf frequency depending on which first order reflection is optimized. Of course, if rf power is not applied the incident light passes through the crystal undeflected (and unshifted).

Figure 4.21 shows a typical implementation of an AOM. Two lenses are used to focus and recollimate the incident laser beam. The acousto-optic modulator is placed at the focus of the first lens. The focal length of the lens is chosen such that the optical beam is smaller than the height of the sound wave. By placing an aperture around the desired first order reflection, an acousto-optic modulator can be used as an optical shutter. If the rf power is turned off, the incident light is

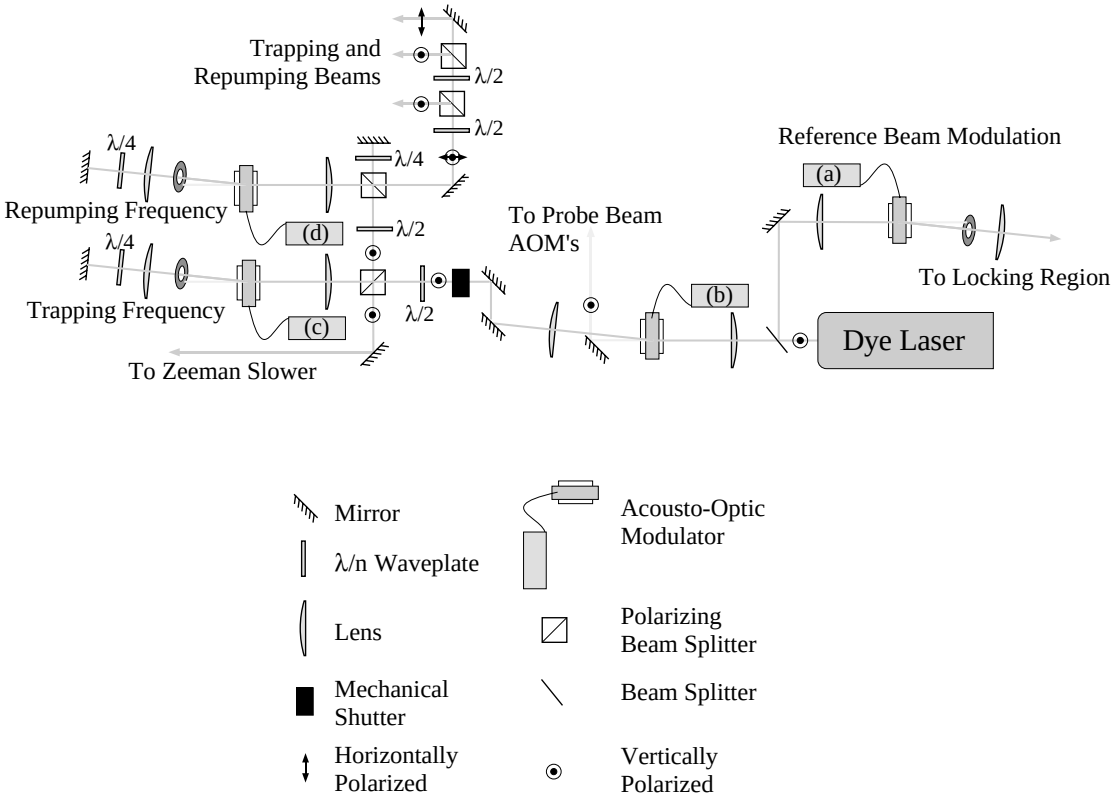

Figure 4.22: Generation of Required Frequencies

undeflected and does not pass through the aperture.

To generate the required frequencies given in Table 4.1 the optical system shown in Figure 4.22 is used. The laser frequency is locked to the ^{6}Li resonance frequency using the fluorescence signal from an atomic beam in a separate vacuum system (the locking region). This oven and vacuum system are described in [104]. The reference beam frequency is modulated at $\simeq$ 1.5 kHz by acousto-optic modulator (a) (Figure 4.22). The modulation amplitude is 2.5 MHz. This reference beam propagates perpendicular to the atomic beam in the locking region. Since this atomic beam is not perfectly collimated, the linewidth of the transition is Doppler broadened to 40 MHz. By modulating the reference beam frequency, the fluorescence from the

atomic beam is also modulated. Lock-in detection of this signal produces a signal proportional to the derivative of the lineshape. This can be used as an error signal for the dye laser frequency since the derivative is zero at the center of the lineshape. A servo-loop [105] sends this error voltage to the laser to adjust the laser frequency. Acousto-optic modulator (a) causes a DC frequency offset of 90 MHz. Thus, the laser is locked 90 MHz below resonance.

Acousto-optic modulator (b) downshifts the frequency by an additional 110 MHz producing a total detuning of 200 MHz below resonance. The downshifted light from AOM (b) provides optical power for the Zeeman slower and is also directed to AOM (c) and (d) which generate the trapping and repumping frequencies required for the MOT. AOM (b) also provides a means of turning on and off the trapping and slowing beams. When AOM (b) is off, all of the incident light passes through undeflected and is directed toward additional acousto-optic modulators (not shown) which generate the required frequencies for the probe beam.

A mechanical shutter placed in front of AOM (b) is used to block the slower and trapping beams whenever these beams are not needed. Although AOM (b) can be used to turn off the trapping, repumping and slowing beams, there is usually a small amount of leakage light which the mechanical shutter blocks. In addition, as discussed in Section 4.3.2, the rf power to AOM (b) needs to remain on for most of the time in order to keep the modulator crystal in thermal equilibrium. Thus, whenever trapping and slowing beams are unwanted but rf power is being supplied to AOM (b), the mechanical shutter is used to block the slower and trapping beams.

AOM (c) and (d) are used to generate the required trapping and repumping frequencies for the MOT. AOM (c) and (d) both upshift incident light by nominally 100 MHz per pass. Both modulators are double passed to produce the required

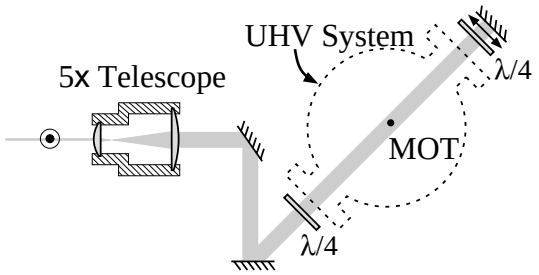

Figure 4.23: Generation of $\sigma^{\pm}$ Light for the MOT

frequencies. The frequency of the rf power supplied to each modulator can be adjusted by applying a DC voltage to the AOM driver. Polarizing beamsplitters and waveplates are used so that the modulators can be double passed without wasting optical power.

The trapping and repumping beams are combined into a single laser beam which contains vertically polarized trapping light and horizontally polarized repumping light. Three beams are generated by using a combination of waveplates and polarizing beamsplitters to divide the optical power shown in Figure 4.22. Each of the three beams contain trapping and repumping beams of the same polarization. The $\lambda/2$ plates can be adjusted such that the trapping beam power in each beam is equal. However, the repumping power in each beam is, in general, unequal. All three beams are expanded by a telescope such that their $1/e^2$ intensity diameter is $\simeq 0.75$ cm. These three beams are used to generate the six beams required for the MOT by retroreflecting each beam along one of three orthogonal axes. $\lambda/4$ plates are used to generate the appropriate circular polarization as shown in Figure 4.23 for one arm of the MOT. Since the $\lambda/4$ plates and the vacuum viewports do not transmit 100% of the incident light, the retroreflected beam will have less total power than the incident beam. In order to compensate for this, the beam expand-

ing telescope in each arm is adjusted so that the beams are slightly focusing such that the retroreflected beam has the same intensity at the MOT as the incident beam.

4.2.5 Observation of the MOT

The previous section described how the optical beams required to form the MOT are generated. The MOT is typically formed using 10 mW per trapping beam (3 beams, each of which are retroreflected) and a total of 7.5 mW unevenly distributed between the repumping beams (in a ratio of 1:1:5.5). These gaussian beams have a $1/e^2$ intensity diameter $\simeq 0.75$ cm. This corresponds to an intensity $I \simeq 25\mathrm{m}W/cm^2 \simeq 10I_{sat}$ per beam. Two electromagnetic coils in an anti-helmholz configuration (described in detail in [98]) provide the quadrupole magnetic field for the MOT. These coils provide a field gradient of 15 G/cm (7.5 G/cm) along the axis (in the radial direction) of the coils.

According to Doppler cooling theory (see Section 4.2.3), we expect the lowest temperature to occur when the beams are at low intensity and are detuned one half-linewidth ($\Gamma/2$) below resonance. However, when the beams are tuned this close to resonance, atoms with a high velocity are not captured by the MOT since the trapping beams are blue shifted away from resonance for the high velocity atoms. Experimentally, the number of atoms trapped in the MOT is maximized when the trapping beams are detuned $5-6\Gamma$ below resonance and high intensity light is used. The repumping frequency is left at $\Gamma/2$ below resonance. Unfortunately, these are not the conditions required to achieve the Doppler limit $T_D = 140\mu$K. As discussed in Section 5.2.3, the temperature of the MOT under these conditions is found to be $\simeq 1$ mK. However, temperatures approaching the Doppler limit can

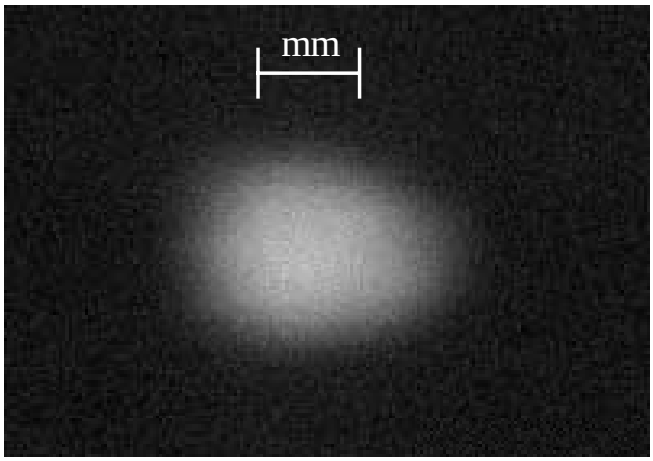

Figure 4.24: Image of MOT Fluorescence

be achieved with a large number of atoms by using a transient technique in which a high intensity, large detuning loading stage is followed by a low intensity, small detuning cooling stage (see Section 5.2.3).

The fluorescence from the MOT is easily seen by eye. Figure 4.24 shows an image of the MOT fluorescence obtained using a charge coupled device (CCD) camera made by Cohu, Inc. As can be seen in this image, the diameter of the MOT is approximately 1.5 mm. Thus, the MOT volume is $\simeq 2\text{mm}^3$.

A calibrated photomultiplier tube is used to determine the approximate number of atoms in the MOT. This optical detection system is also used to detect the number of atoms confined in the CO^2 laser trap (see Section 4.3.2). The optical detection system consists of a Hamamatsu 1894 PMT optically coupled to an optical fiber bundle which is easily positioned to observe the MOT. A 660-680 nm bandpass filter is mounted inside the PMT housing to block unwanted background light at other wavelengths. A 10 cm focal length lens images the fluorescence from the MOT with unity magnification onto the optical fiber bundle. This optical detection system is calibrated by coupling light of known power into the optical fiber bundle

and recording the resulting electron current produced in the PMT when the PMT is biased at a given voltage. This yields the gain α measured in Amps/Watt.

To measure the number of atoms in the MOT or the CO_2 laser trap, the atoms are illuminated with intense, resonant probe light. The probe light causes the atoms to fluoresce and the fluorescence is detected by the calibrated optical detection system. For a two level atom, the photon scattering rate is given by

$$\Gamma_{sc} = \frac{\Gamma}{2} \frac{s}{1 + s + 4(\Delta/\Gamma)^2} \tag{4.13}$$

where $s = I/I_{sat}$ is the saturation parameter, I_{sat} is the saturation intensity and Δ is the detuning of the probe light from resonance. $I_{sat} = 2.55$ mW/cm^2 for the cycling transition in lithium. For resonant light with $s >> 1$ half of the atomic population is in the excited state and the photon scattering rate $\Gamma_{sc} = \Gamma/2$. In this case, the atoms radiate a power $P_{rad} = \hbar\,\omega_0\,\Gamma/2$ into a 4π solid angle. For lithium $P_{rad} = 5.5 \times 10^{-9}$ mW. The fluorescence collection optics collect a fraction $d\Omega/4\pi$ of the scattered light. The current output by the PMT generates a voltage across a resistive load R which is measured by an oscilloscope. The voltage measured by the oscilloscope per atom is given by

$$V_a = P_{rad} \frac{d\Omega}{4\pi} \alpha\, R \tag{4.14}$$

assuming the transition is fully saturated. The solid angle for the fluorescence collection optics is limited by the solid angle presented by the viewport of the vacuum system and is estimated to be $d\Omega/4\pi = 3.9 \times 10^{-3}$. A typical voltage gain used for measuring the number of atoms in the MOT is 4.6 Amps/W which is obtained at a PMT bias voltage of 600 Volts. Thus, if the voltage is measured

across a resistive load $R = 1\mathrm{M}\Omega$ the number of volts per atom is $V_a = 0.1\,\mu\mathrm{V/atom}$. To measure the number of atoms in the CO_2 laser trap the PMT bias voltage is normally increased to 1450 V which typically yields a gain $\alpha = 1304$ Amps/W. In addition a spherical mirror placed in front of the viewport opposite the fiber bundle is sometimes used to approximately double the solid angle in order to detect small numbers of atoms.

Using the calibrated optical detection system the number of atoms in the MOT can be determined. For the parameters described above, the MOT typically stores $\sim 10^8$ atoms. Since the MOT volume $\simeq 2\,\mathrm{mm}^3$, this corresponds to a density of $\simeq 5 \times 10^{10}\,\mathrm{atoms/cm}^3$.

4.3 CO_2 Laser Trapping of ^{6}Li

In this section we describe how ^{6}Li atoms are loaded into the CO_2 laser trap and the observation of optical confinement for several hundred seconds of a two-state mixture of lithium fermions. The CO_2 laser trap is loaded by spatially overlapping the CO_2 laser focus with the MOT. The procedures used to overlap the CO_2 laser beam focus with the MOT and techniques used to verify this overlap are reviewed. Finally, we describe the observation of optically confined ^{6}Li atoms and the measurement of the CO_2 laser trap lifetime.

Both the excited and ground states are attracted to the focus of a CO_2 laser trap since the infrared frequency is small compared to the excited state resonance frequencies. Thus, for moderate intensities, the trap-induced light shift of the optical transition frequency is small compared to the MOT detuning, so that the trap can be continuously loaded. The MOT serves as a reservoir in thermal and diffusive contact with the CO_2 laser trap. The optical molasses of the MOT laser fields provides the

viscous damping needed to cool atoms into the CO_2 laser trap potential. Thus, to load the CO_2 laser trap, one needs to simply overlap the CO_2 laser focus with the MOT and allow time for the atoms to come into thermal and diffusive equilibrium. A more comprehensive discussion of loading dynamics is given in Chapter 5.

4.3.1 Aligning the CO2 Laser Beam

CO_2 Laser Optics

The gaussian beam which emerges from the CO_2 laser has a $1/e^2$ intensity radius of 3.7 mm. This beam is expanded by a $\times 4.5$ telescope formed from 28.6 cm and 6.35 cm focal length lenses. The lenses of the telescope are made of crystalline ZnSe and are anti-reflection coated for 10.6 μm light. The expanded CO_2 laser beam is then focused using a 19 cm focal length plano-convex spherical ZnSe lens into the ultra-high vacuum system through the differentially pumped ZnSe viewports described in Section 4.2.1. The gaussian beam is focused to a spot with a $1/e$ intensity radius of 53 μm as verified by measuring the beam intensity profile using a pinhole. Spherical aberration causes the spot size to exceed the diffraction limit.

The CO_2 laser optics need to be aligned such that the focus of the CO_2 laser beam overlaps with the MOT. The longitudinal and transverse position of the focal point are aligned separately. The following two sections describe this alignment procedure.

Split Image Technique

The distance between the 19 cm ZnSe lens and the MOT needs to be adjusted such that the optical path length for 10.6 μm radiation is exactly 19 cm. This adjustment ensures that the longitudinal location of the CO_2 laser focal point overlaps with the

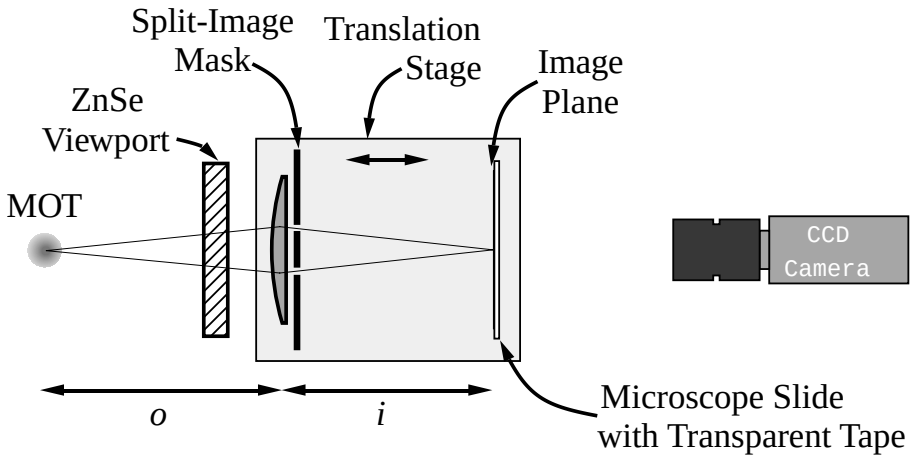

Figure 4.25: Split-image alignment technique used for alignment of lens focal point.

MOT. However, since the Rayleigh length of the focused CO_2 laser beam is only 0.75 mm, the ZnSe lens needs to be placed with sub-millimeter accuracy. Split-image detection of fluorescence from the MOT can be used to accurately determine the distance between the MOT and the 19 cm focal length ZnSe lens.

Figure 4.25 illustrates the procedure used. A 10 cm focal length plano-convex lens is mounted on a translation stage. The translation stage also supports the mount for the 19 cm ZnSe focal length lens and a microscope slide. The purpose of this procedure is to position the ZnSe lens mount the appropriate distance from the MOT. The desired object distance for the 10 cm lens is easily calculated based on the desired distance between the MOT and the ZnSe mount. The image distance corresponding to this object distance is then calculated. The microscope slide is carefully placed at the resulting image distance from the 10 cm lens. A mask containing two apertures is attached to the 10 cm lens mount. Fluorescence from the MOT passes through each aperture. The rays from each aperture intersect at the image plane of the 10 cm lens. Only when the translation stage is adjusted

such that the MOT is at the desired object distance will the rays intersect at the microscope slide.

A piece of transparent tape is affixed to one side of the microscope slide to diffuse the light rays striking the tape. The light from each aperture can then be visibly seen on the transparent tape. The translation stage is simply adjusted such that these two spots overlap. Since the light reaching the transparent tape is extremely dim, a CCD camera is normally used to monitor the overlap of these spots. However, note that as the translation stage is moved the CCD camera lens must be adjusted so that the transparent tape remains in focus.

Since sub-millimeter resolution is desired in this technique, the desired object and image distances must be determined with care. For example, the ZnSe window has a different index of refraction for 10.6 μm light than for 671 nm light. This must be considered when calculating the desired object distance since both the MOT fluorescence and the CO_2 laser beam pass through 1/4 in. of ZnSe. Also, when considering the object and image distances one must remember that these distances are not measured from the plano or spherical surface of the lenses but rather are measured from the primary principle point which is a point internal to the lens. The Melles Griot catalog provides an excellent and concise review of lens design.

In practice, this technique provided positioning of the lens with millimeter accuracy. Thus, this technique positions the focal point of the CO_2 laser beam near but not necessarily overlapping with the MOT. The light shift of the $2p - 3d$ transition in Li is used to accurately position the focal point as described below.

Transverse Alignment Procedure

To facilitate alignment of the CO_2 laser beam with the MOT in the direction transverse to the propagation direction, a several milliWatt 671 nm laser beam resonant with the Li transition frequency is made to propagate along the same path as the CO_2 laser beam. This resonant beam causes a visible disturbance to the MOT, due to the radiation pressure force, whenever it passes through the MOT. Using this beam, the CO_2 laser optics can be aligned such that a visible disturbance of the MOT is observed during the alignment procedure. This ensures that the CO_2 laser passes through (or at least close to) the MOT. The alignment of the CO_2 laser focal point along the direction of propagation was described previously.

Before any lenses are placed in the CO_2 laser beam path, the visible 671 nm beam is overlapped with the CO_2 laser beam at two points in space separated by 5 meters. To overlap the beams at these two locations, the 50 Watt beam of the CO_2 laser burns marks into index cards mounted at each location (first the downstream location followed by the upstream location). The CO_2 laser beam is extinguished and the 671 nm beam is made to overlap with the two burn marks.

Once this alignment is complete, a fold mirror along the laser beam path is used to adjust the direction of the 671 nm beam such that it passes through the MOT. This causes a visible disturbance to the MOT. The 19 cm focal length ZnSe lens is then inserted into the lens chuck which was pre-aligned using the split-image technique (see above). The vertical and horizontal position of this lens are adjusted such that the 671 nm beam passes through the center of the lens. This can be verified by making sure the insertion of the lens does not deflect the beam. The rotation of the lens is adjusted such that the lens is perpendicular to the beam propagation direction. Once the focusing lens is in place, the lenses for the $\times 4.5$

telescope are inserted in the beam in a similar manner such that the 671 nm beam is centered on each lens and the lenses are perpendicular to the propagation direction. Following the alignment of theses optics, a visible disturbance to the MOT due to the 671 nm beam should still occur. Once this has been confirmed the 671 nm beam can be removed. The CO_2 laser focus should now occur reasonably close to the position of the MOT.

Light Shift of $2p - 3d$ Transition

It is useful to identify a technique that can confirm the spatial overlap of the MOT and the CO_2 laser focus that does not depend on observation of optically confined atoms. For optical traps that are nearer to resonance than the CO_2 laser trap, a technique often used to verify the spatial overlap is the observation of the light shift caused by the optical potential. Unfortunately, the near equality of the Li excited and ground state polarizabilities, while ideal for continuous loading of atoms from the MOT, makes locating the focus of the CO_2 laser by light shift methods difficult. For a 50 W CO_2 laser focused to a 100 μm diameter spot, the peak light shift for the $2s - 2p$ transition in Li is 2 MHz. Several unsuccessful attempts at observing this light shift were made. To circumvent this problem, the light shift of an excited state transition is observed instead.

In order to initially verify the spatial overlap between the CO_2 laser focus and the MOT, the light shift of the $2p - 3d$ transition caused by the CO_2 laser is observed. While the polarizabilities of the 2s and 2p state are nearly identical, leading to a negligible light shift of the $2s - 2p$ transition, the $3d$ state in ^{6}Li has a sizable shift. For 10.6 μm light, we estimate that the $3d$ state has a scalar polarizability of approximately 700×10^{-24} cm^3 [106], nearly 30 times that of the $2s$ or $2p$ state. In

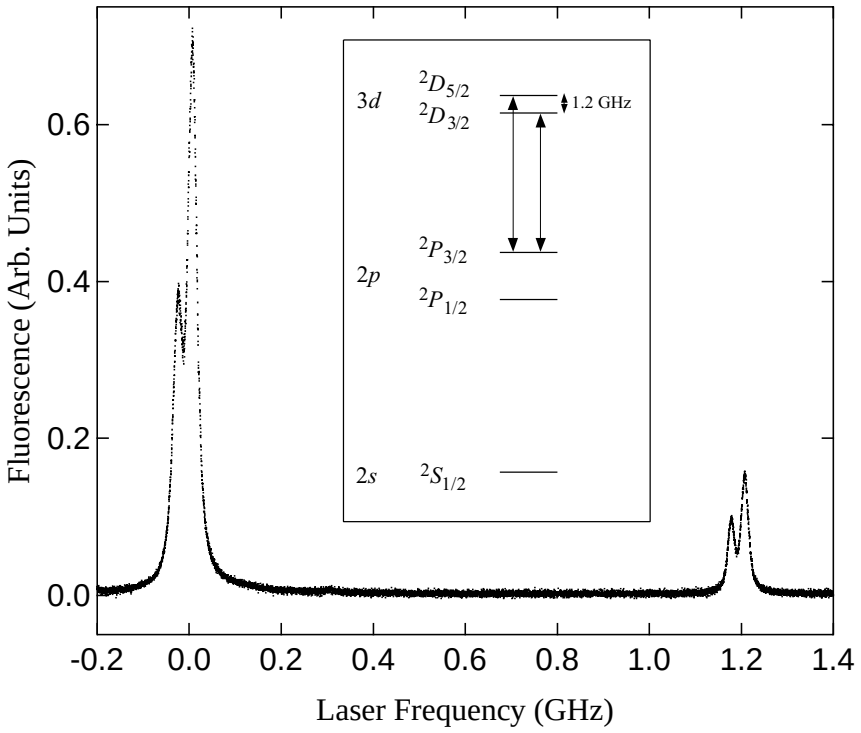

Figure 4.26: $2p - 3d$ Transition Spectrum

the focus of the CO_2 laser, the corresponding light shift is $\simeq -300$MHz.

In order to excite the $2p - 3d$ transition, 610 nm wavelength light is required. A Spectra-Physics dye laser circulating Rhodamine 6G dye, normally used for experiments in the adjacent laboratory, can be used to provide several hundred milliWatts of 610 nm radiation. To observe the $2p - 3d$ transition, 80 μW of 610 nm light in a 2-mm diameter, retroreflected beam illuminates the MOT. The MOT trapping and repumping beams are kept on continuously as they are required to provide population in the excited $2p$ state. Low intensity 610 nm light is used so as not to seriously disturb the operation of the MOT. Fluorescence from the $2p - 3d$ transition is easily observed with the naked eye as an orange glow which accompanies the normal red glow of the MOT. The fluorescence can also be observed with the pho-

tomultiplier tube that normally monitors the MOT. However, the 660-680 nm filter that is normally used to only transmit light at 671 nm is replaced by a 600-620 nm bandpass filter. Figure 4.26 shows the spectrum of the $2p-3d$ as the 610 nm laser is scanned in frequency over 1.6 GHz. The two resonant features that appear in the spectrum arise from the $2p\,^2P_{3/2} \rightarrow 3d\,^2D_{3/2}$ and $2p\,^2P_{3/2} \rightarrow 3d\,^2D_{5/2}$ transitions. The $2p\,^2P_{3/2}$ state is populated by the MOT beams. The splitting between $3d\,^2D_{3/2}$ and $3d\,^2D_{5/2}$ states is 1.2 GHz [107].

Figure 4.27(a) shows the fluorescence from one of the $2p-3d$ transitions. The CO_2 laser was blocked while recording this spectrum. The fact that the lineshape appears to be composed of two separate peaks is not well understood. Although both the $2p$ and $3d$ states contain hyperfine structure, the hyperfine splitting should be too small to be observed in these spectra. This two-peaked structure persists even when the retroreflection of the 610 nm beam is blocked. Also, the relative peak heights can be adjusted with adjustment of the power in the 610 nm beam. Although we never came to a resolution on this issue, the light shift of this lineshape provided a valuable diagnostic for overlapping the CO_2 laser with the MOT.

The CO_2 laser was pre-aligned using the split-image technique described above. With the CO_2 laser properly aligned, the lineshape shown in Figure 4.27 (a) is expected to shift to lower frequency. In order to detect this shift, the CO_2 laser beam is chopped at 2 kHz and lock-in detection of the 610 nm fluorescence is employed as the 610 nm light is scanned in frequency. The lock-in signal gives the difference between the fluorescence signal with the CO_2 laser blocked and unblocked. Since the light shift of the $2p-3d$ transition frequency is rather large ($\simeq$ 300 MHz at the focus of the CO_2 laser beam), this technique provides a great deal of sensitivity. The split-image alignment technique is usually accurate enough that the lock-in

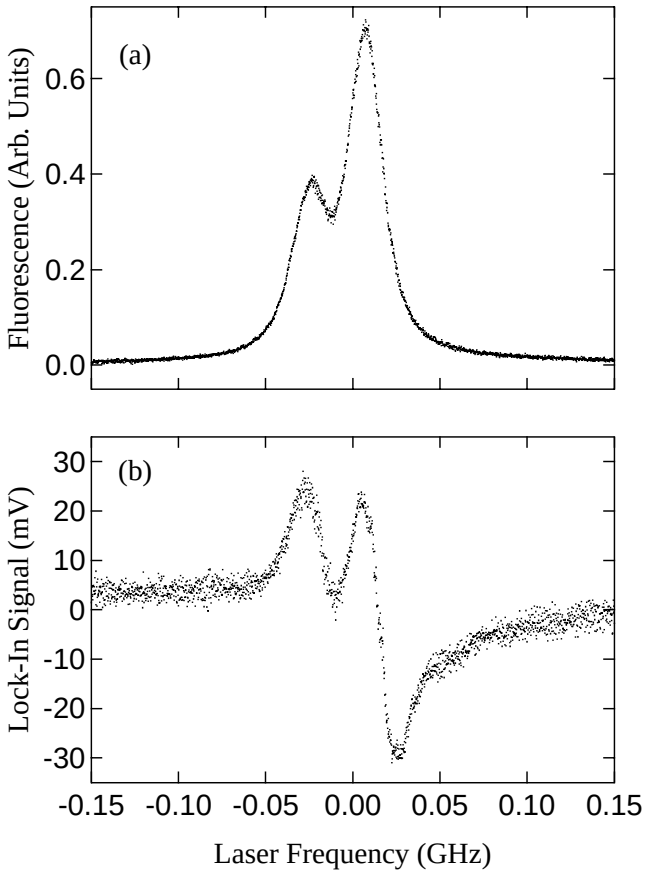

Figure 4.27: $2p - 3d$ lineshape and CO_2-laser-induced light shift. (a) The fluorescence spectrum from one of the lines shown in Figure 4.26 with the CO_2 laser blocked. (b) Output from a lock-in amplifier while scanning over the resonance shown in (a) while the CO_2 laser is being chopped. This signal gives the difference between the fluorescence signal with the CO_2 laser blocked and the fluorescence signal with the CO_2 laser unblocked. The difference in these signals arises from the light shift in the $2p - 3d$ transition frequency due to the presence of the CO_2 laser beam.

detection signal immediately shows a feature that can be peaked up. With the CO_2 laser properly aligned, the signal shown in Figure 4.27 (b) is obtained. This signal is the difference between the shifted and unshifted lineshape. At the ideal focusing lens position, the amplitude and the frequency separation of these peaks are maximized.

4.3.2 Optical Confinement and Long-Term Storage of ^{6}Li

Once the CO_2 laser beam focus is overlapped with the MOT, the CO_2 laser trap can be loaded with ^{6}Li atoms. To load the trap, the CO_2 laser remains on continuously while the MOT is loaded from the Zeeman slower. The time required to load the MOT to steady state is approximately 10 sec. The viscous damping forces present in the MOT cool the ^{6}Li atoms into the potential provided by the CO_2 laser. As discussed in Chapter 5, the 10 second MOT loading time provides an ample amount of time for the atoms in the CO_2 laser trap to come into thermal and diffusive equilibrium with atoms in the MOT.

After the magneto-optical trap and CO_2 laser trap are loaded for 10 seconds, the MOT is shut off so that the atoms are left to evolve solely in the CO_2 laser potential. To shut off the MOT, the repumping beams are first extinguished by an acousto-optic (A/O) modulator so that ^{6}Li atoms are optically pumped into the lower lying $F = 1/2$ hyperfine state by the trapping beams which remain on. By optically pumping atoms into the lower hyperfine state, exothermic inelastic collisions between atoms that remain in the $F = 3/2$ state are avoided. Without this optical pumping step, the number of atoms confined in the CO_2 laser trap would rapidly decay due to these inelastic collisions. After 25 μsec, the MOT trapping beams and the slower are turned off by an acousto-optic modulator. The MOT

gradient magnets are turned off within 0.2 ms. A mechanical shutter in front of the dye laser is closed within 1 ms to eliminate all MOT light at 671 nm. The mechanical shutter eliminates trap loss arising from near resonant light leakage which can optical pump atoms into the unstable $F = 3/2$ hyperfine state. After a variable delay, a probe beam illuminates the CO_2 laser trap to detect the number of atoms that remain.

To measure the number of ^{6}Li atoms confined in the CO_2 laser trap, a 1 mW, 2-mm diameter probe beam ($I/I_{sat} = 25$) which overlaps the CO_2 laser trap focus is pulsed on and causes the atoms to fluoresce. The fluorescence is detected by the photomultiplier tube used to monitor the MOT as described in Section 4.2.5. With the PMT at full voltage, the fluorescence from the MOT would cause an electron current exceeding the PMT's tolerance. Hence, the photomultiplier tube is mechanically shuttered so that it only monitors fluorescence during the probe pulse. This allows the photomultiplier tube to be run at full voltage giving it maximum sensitivity. The probe beam contains two frequencies to excite both the $F = 1/2$ and $F = 3/2$ ground hyperfine states. Both frequencies are detuned approximately 1/2 linewidth below the respective resonance frequencies. The probe beam is circularly polarized and retroreflected. The use of red-detuned, retroflected light ensures that atoms are not instantly pushed out of the probe volume by radiation pressure forces.

The probe beam power is derived from the optical power formerly used to produce the MOT beams. Since these beams are off when the probe beam is required, the optical power is available. The probe beam frequencies are generated using acousto-optic modulators in a manner similar to that used to generate the MOT beams (see Section 4.2.4). The probe beam is pulsed on and off by pulsing the rf power supplied to the acousto-optic crystal which generates these frequencies. To

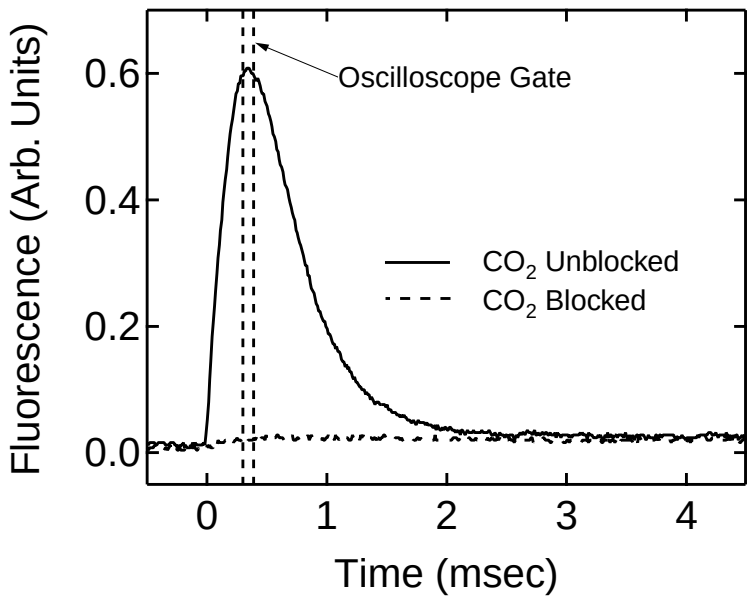

Figure 4.28: Optical Detection of ^{6}Li Atoms Trapped in CO_2 Laser Beam

further ensure that 671 nm light does not illuminate the CO_2 laser trap when the probe beam is off, the probe beam is double blinded by two additional acousto-optic modulators.

The same pulse used to trigger the probe pulse also triggers a Tektronix digital oscilloscope which monitors the photomultiplier tube current by measuring the voltage across a resistive load. Figure 4.28 shows a typical fluorescence pulse shape observed using this technique. In this case, the probe pulse is fired 100 ms after the MOT is extinguished. The fluorescence signal decays after $\cong$ 1 msec as atoms are heated out of the probe beam. Thus, this optical detection method is destructive. To demonstrate that the CO_2 laser is providing confinement the entire loading and probe sequence is repeated with the CO_2 laser blocked and unblocked generating the signals shown in Figure 4.28. The pulse peak height is proportional to the number of trapped atoms. To record the number of atoms trapped, a gate on the digital

oscilloscope is set such that the oscilloscope records the mean value of the points within the gate. The value recorded can be transferred to a digital computer using the oscilloscope's GPIB port. The gate used is illustrated in Figure 4.28 by the two dashed vertical lines.

Using the detection system calibration discussed in Section 4.2.5, the number of ^{6}Li atoms confined in the CO_2 laser can be estimated from the height of the fluorescence signal. Note that a small resistive PMT load needs to be used in order to faithfully reproduce the optical pulse shape observed by the PMT. For large resistive loads, the RC time constant of the circuit formed by the resistive load and the capacitive coaxial cable limits the response of the system. Typical trapped atom numbers measured in these initial experiments are 3.5×10^4 assuming that an excited state fractional population of 1/3 is produced by the probe beam.

Measurement of the trapped atom number versus time is accomplished by varying the probe beam delay and recording the fluorescence peak height as the entire timing sequence described above is repeated. A digital computer running LabView is used to control the experiment. A LabView program written by Stephen Granade is used to repeatedly trigger the pulse generator timing sequence, control the mechanical shutter in front of the dye laser, adjust the probe delay via GPIB communication with the Stanford pulse generators, retrieve the number of atoms measured by the oscilloscope and record the number versus time data. Two pulse generators produce digital signals used to turn various pieces of equipment such as A/O drivers and the MOT gradient field on and off during the course of the experiment.

To measure the long lifetime of the CO_2 laser trap, the probe delay is adjusted between 0 and 600 seconds. In order to avoid systematic errors when delays are

changed over such long time scales, several issues need to be addressed. First, the alignment of acousto-optic modulators is sensitive to thermal drift. Since the rf power supplied to these crystals generate a substantial amount of heat, large thermal fluctuations can occur on the scale of seconds if the rf power level is changed for substantial amounts of time. Left uncorrected, this can cause the power in the probe beam to change for different delay lengths. To solve this problem, the experiment is designed such that A/O modulators which need to be on for large periods of time (e.g. the MOT A/O modulators) are only shut off for short (millisecond) time scales. For example, when the MOT is extinguished the MOT A/O modulators are shut off only long enough for the mechanical shutter in front of the dye laser to shut before they are turned on again. They are turned off again briefly when power needs to be diverted to generate the probe beam. This keeps the A/O modulators in thermal equilibrium. Second, if separate components are required to agree to millisecond accuracy on time scales of hundreds of seconds, the separate frequency references must be carefully synchronized. For example, both the computer and Stanford pulse generators need to agree on the passage of 600 seconds to sub-millisecond accuracy. Finally, one must be aware that electronic equipment can drift over hundred second time scales. Originally, a boxcar averager was used to record the peak height of the probe fluorescence signal. However, a small leakage current caused the measured peak height to be erroneously high for long time delays. This issue was resolved by using the digital oscilloscope to measure the peak height.

The ultrastable CO_2 laser trap is expected to store atoms for several hundred seconds. The optical heating rate in this system is negligible since the time for an atoms to scatter a 10.6 μm photon is measured in hours. The time constant for heating due to intensity fluctuations is also measured in hours and the heating rate

due to beam jitter is expected to be less than 50 nK/sec. The primary trap loss rate is expected to arise from collisions between trapped atoms and background gas atoms in the vacuum system. As discussed in Section 3.4, a vacuum system containing background ^{6}Li atoms at a pressure of 10^{-11} Torr causes an exponential loss with a time constant $\simeq 300$ sec.

Figure 4.29 shows the decay of the trapped atom number on a time scale of 0-600 seconds. Each data point is the mean obtained from four separate measurement sequences through the complete decay curve. The error bars are the standard deviation from the mean. Atoms in the $F = 1/2$ state exhibit a single exponential decay with a time constant of 297 sec. This is the longest storage time ever reported for an optical trap. The 300 second lifetime observed is two orders of magnitude larger than previously reported storage times for optical traps of comparable well depth.

The inset to Figure 4.29 shows the data points between 0 and 10 seconds. We have observed that an initial 10-15% decrease in the signal can occur during the first second. This arises from inelastic collisions between atoms in the $F = 1/2$ state with atoms that are not optically pumped out of the upper $F = 3/2$ state. During optical pumping, fluorescence from the F=3/2 state decays in $\simeq 5\,\mu$sec to a $\simeq 5\%$ level which persists for many milliseconds, consistent with a residual $F = 3/2$ population. In experiments described in Chapter 7, this initial loss has been avoided by adjusting the intensity of the optical pumping light which enables nearly 100% of the atoms to be optically pumped into the $F = 1/2$ state.

Since a two-state mixture of ^{6}Li atoms is being confined, s-wave elastic collisions between the atoms can occur. In this case, one might expect that the confined mixture will undergo evaporative cooling by thermal escape of energetic atoms

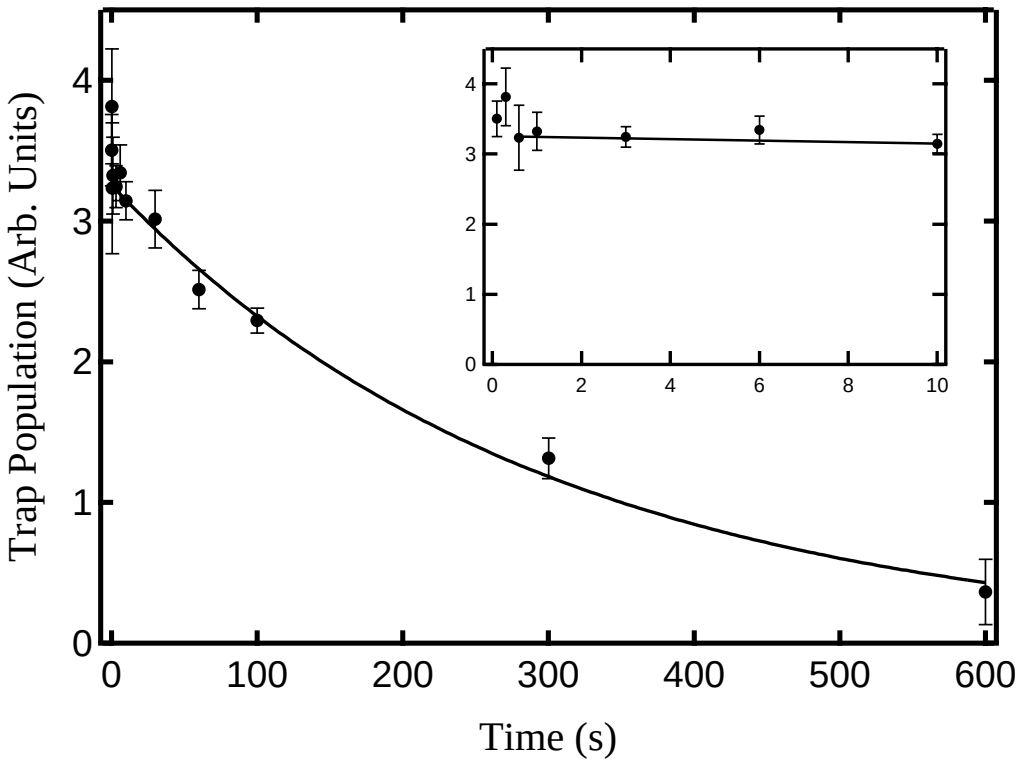

Figure 4.29: CO_2 laser trap lifetime. The main figure shows the number of atoms confined in the CO_2 laser trap as a function of time. The data is fit by a single exponential with a exponential time constant $\simeq 300$ sec. The inset shows the same data from 0 to 10 sec.

(see Chapter 6). Evaporation would cause a rapid initial loss of atoms since the temperature of the atoms loaded into the trap is comparable to the well depth. However, the long lifetime observed is expected, based on the prediction of a negligible s-wave elastic scattering length ($<<$ 1 Bohr) at zero magnetic field [55]. As discussed in Section 2.10, the s-wave cross section in this mixture is predicted to vanish at zero field due to an accidental cancellation between the triplet and singlet scattering amplitudes. Hence, spontaneous evaporation should not occur.

The lifetime of atoms in the $F = 1/2$ state can be limited by processes that cause heating or direct loss. If we attribute the trap lifetime entirely to residual heating, the heating rate from all sources would be at most 400μK/300sec $\simeq 1\mu$K/sec, which is quite small. However, if the loss were due to heating, one would expect a multimodal decay curve, analogous to that predicted in Ref. [46]. Instead, we observe a single exponential decay as expected for direct loss mechanisms, such as collisions with background gas atoms or optical pumping by background light at 671 nm (into the unstable $F = 3/2$ state). If we assume that the lifetime is background gas limited and that Li is the dominant constituent, the measured lifetime of 297 sec is consistent with a pressure of $\simeq 10^{-11}$ Torr.

We are not certain of the the dominant constituent of the residual background gas in our vacuum system. The flux of ^{6}Li atoms into the system is far greater than any other element supporting the idea that ^{6}Li is the dominant constituent of the residual gas. However, ^{6}Li is highly reactive and is therefore readily pumped by the titanium getter which is used in the vacuum system. Therefore, it is possible that a relatively unreactive element such as He which is not as readily pumped by the titanium may be the dominant constituent of the background gas. If the background gas is composed of He, the measured lifetime of 297 sec is consistent with a He

background pressure of $\simeq 5 \times 10^{-11}$ Torr. This result is obtained using Eqs. (3.36) and (3.38) where the C_6 constant for ^{6}Li-He collisions is found in Ref. [108] to be $C_6 = 21.9$ a.u. Although atoms in a He gas have a larger velocity at room temperature as compared to ^{6}Li atoms, the loss rate is reduced compared to a residual ^{6}Li background gas since the ^{6}Li-He collision cross section is reduced from that for ^{6}Li-^{6}Li collisions.

Note that, regardless of what the primary constituent of the background gas is, since the trap population exhibits an exponential decay the dominant loss of atoms appears to arise from a direct loss process such as collisions with background gas atoms as opposed to a residual heating rate. This conclusion is supported by experiments described in Chapter 7 in which a gas of atoms evaporatively cooled to a temperature $\simeq 1/10$ of the well depth exhibits a lifetime comparable to that of a gas for which the temperature is $\simeq 1/2$ of the well depth. Thus, residual heating of the trapped atoms does not appear to be the dominant loss process in this system.

4.4 Summary

In this chapter, we have recounted the first experimental realization of a stable optical trap for neutral atoms. By utilizing an ultrastable CO_2 laser we have demonstrated confinement of ^{6}Li atoms for several hundred seconds. The trap lifetime is limited by collisions between trapped atoms and residual background gas atoms in the vacuum system which operates at a pressure $\simeq 10^{-11}$ Torr. The observed 300 second exponential decay is consistent with a background ^{6}Li gas at a pressure of 10^{-11} Torr. Due to the high stability of the CO_2 laser, laser-noise-induced heating of the trapped atoms is expected to be extremely small. The measured intensity and position noise spectra for the ultrastable CO_2 laser yield predicted intensity-

noise-induced heating time constants measured in hours and position-noise-induced heating rates ≤ 50 nK/s. Due to the long wavelength of the CO_2 laser radiation, optical heating due to photon scattering is negligible in this system as the time for an atom to scatter a single photon is measured in hours.

The observed trap lifetime is the longest ever reported for an optical trap and is comparable to the best lifetimes achieved with magnetic traps. The 300 second lifetime observed is two orders of magnitude larger than previously reported storage times for optical traps of comparable well depth. The demonstration of long term storage of atoms in an optical trap serves as a proof-of-principle that long term confinement can be obtained with optical traps. This result has important ramifications for a wide variety of applications for optical traps which can benefit from long term storage times and low residual heating rates. Applications which stand to benefit from this result include precision measurements such as improved atomic frequency standards or measurements of the atomic electric dipole moment, investigations of dilute, degenerate atomic vapors and quantum computing methods which utilize trapped neutral atoms.

Optical traps are particularly well suited to studies of interactions in an ultracold Fermi gas as they provide a means for confining stable two-state mixtures of fermions thus enabling s-wave interactions between the atoms. The stable optical trap for ^{6}Li fermions discussed in this chapter provides a foundation for investigations of an ultracold gas of fermionic atoms. Having discussed the successful development of a stable optical trap we focus our attention in the following chapters on improved loading techniques in Chapter 5 and finally on the study of interactions and evaporative cooling in an optical trap in Chapters 6 and 7.

Chapter 5

Loading Dynamics of the CO_2 Laser Trap

For many applications, it is important to maximize the number of atoms loaded into an optical dipole force trap. Therefore, it is of interest to understand the loading dynamics of dipole force traps in order to identify strategies for maximizing the transfer of atoms into these traps. In this chapter, we present a simple model which predicts the equilibrium trap number and describes the loading dynamics for the CO_2 laser trap. The model assumes that the atoms in the magneto-optical trap come into thermal and diffusive equilibrium with the CO_2 laser potential. The approach to this equilibrium state is governed by a Fokker-Planck equation in which the optical fields of the magneto-optical trap provide a viscous damping force. This simple model predicts that the equilibrium number of trapped atoms in the CO_2 laser trap grows exponentially with the ratio of the trap depth U_0 to the MOT temperature T. Thus, the number of atoms loaded into the trap can be greatly enhanced by lowering the temperature of the MOT or increasing the well depth U_0.

By employing a transient cooling phase we find that we can lower the temperature of the MOT to temperatures approaching the Doppler cooling limit and thereby substantially increase the number of atoms transferred to the CO_2 laser trap. We have measured the number of atoms loaded into the CO_2 laser trap for several different values of U_0/k_BT and found the results to be in good agreement with the

predicted equilibrium number. In addition, we observe that the equilibration time concurs with that predicted by the Fokker-Planck equation.

5.1 Simple Model for Equilibrium Trap Number

In Chapter 4 we noted that the electrostatic polarizabilities of the ground and first excited state of Li are nearly identical. Due to this fact, the $2s - 2p$ transition frequency experiences only a small shift for atoms in the optical potential. For a CO_2 laser trap with a well depth of $500\,\mu$K, the maximum shift which occurs at the focus of the laser beam is only 2 MHz for Li. Thus, the presence of the CO_2 laser trap does not disturb the operation of the magneto-optical trap since the frequency shift over most of the volume is much less than the linewidth of the optical transition. Therefore, we expect that the equilibrium trap number for atoms in the CO_2 laser trap is simply given by considering the potential to be in thermal and diffusive equilibrium with a reservoir of atoms at density $n_{\rm MOT}$ and temperature T. In the simplest model we consider the volume of the MOT to greatly exceed the volume of the CO_2 laser trap in which case the density $n_{\rm MOT}$ is a constant in the absence of the CO_2 laser potential.

The number of atoms trapped in the CO_2 laser potential is readily determined from the phase space distribution. The phase space distribution function $W(\boldsymbol{x},\boldsymbol{p})$ gives the number of atoms within a phase space volume $d^3x\,d^3p$ about the point $(\boldsymbol{x},\boldsymbol{p})$ and is normalized such that the total number of atoms N is given by

$$N = \int d^3x\,d^3p\,W(\boldsymbol{x},\boldsymbol{p}). \tag{5.1}$$

The potential due to the CO_2 laser trap is given approximately by

$$U(\boldsymbol{x}) = -U_0 \exp\left[\frac{x^2}{a^2} + \frac{y^2}{b^2} + \frac{z^2}{c^2}\right] \tag{5.2}$$

where a, b and c are the $1/e$ intensity radii of the focused gaussian beam in the $x-$, $y-$ and $z-$ directions respectively. Here we approximate the lorentzian dependence on the axial position z by a gaussian dependence on z to simplify the calculations which follow. The single particle Hamiltonian is $\mathcal{H}(\boldsymbol{r},\boldsymbol{p}) = p^2/2M + U(\boldsymbol{x})$. In equilibrium the phase space density is given by

$$W_{eq}(\boldsymbol{x},\boldsymbol{p}) = \frac{n_{\rm MOT}}{(2\pi M k_B T)^{3/2}} \exp\left[-\frac{\mathcal{H}(\boldsymbol{x},\boldsymbol{p})}{k_B T}\right]. \tag{5.3}$$

We have normalized $W(\boldsymbol{x},\boldsymbol{p})$ such that the spatial density $n(\boldsymbol{x}) = \int d^3p\, W(\boldsymbol{x},\boldsymbol{p})$ approaches the unperturbed MOT density $n_{\rm MOT}$ for $r >> a, b, c$. We are implicitly assuming here that the fraction of atoms stored in the CO_2 laser trap is much smaller than the number of atoms confined in the MOT.

Note that the density of atoms at the center of the trap is given by

$$n_0 \equiv n(0) = n_{\rm MOT} \exp\left[\frac{U_0}{k_B T}\right]. \tag{5.4}$$

Therefore, the peak density is enhanced by a Boltzmann factor $\exp(U_0/k_B T)$ at the center of the CO_2 laser potential.

The number of atoms confined in the CO_2 laser trap N_T is found by integrating the phase space density over the region where the total energy is negative

$$N_T = \int d^3x\, d^3p\, \Theta\left(-\frac{p^2}{2M} - U(\boldsymbol{r})\right) W(\boldsymbol{x},\boldsymbol{p}). \tag{5.5}$$

The integral is easily performed to yield

$$N_T = N_0 \, \mathcal{F}\left[\frac{U_0}{k_B T}\right] = n_{\rm MOT} \, V_{\rm trap} \, \mathcal{F}\left[\frac{U_0}{k_B T}\right], \tag{5.6}$$

where N_0 is the number of atoms at the MOT density $n_{\rm MOT}$ which fall inside the effective volume of the CO_2 laser trap $V_{\rm trap} \equiv \pi^{3/2} abc$. The factor $\mathcal{F}[q]$ is given by

$$\mathcal{F}[q] = \frac{q^{3/2}}{2} \int_0^1 dx \, x^2 \, g_1(x) \, \exp[q(1-x)], \tag{5.7}$$

where

$$g_1(x) = \frac{\beta^{3/2}(1-x)^{1/2}}{x^2} \, \frac{16}{\pi} \int_0^1 du \, u^2 \, \sqrt{\exp[\beta(1-u^2)] - 1}, \tag{5.8}$$

and $\beta \equiv -\ln(1-x)$. The integrals in (5.7) and (5.8) are easily evaluated numerically. $\mathcal{F}(U_0/k_B T)$ is the trapping factor which gives the ratio of the number of atoms confined in the CO_2 laser trap to the number of atoms which fall inside the trap volume $V_{\rm trap}$ for atoms at a uniform density $n_{\rm MOT}$. Figure 5.1 shows $N_T/N_0 = \mathcal{F}(q)$ as a function of $q = U_0/k_B T$ for values of q between 0 and 5. Substantial improvement in N_T is expected as q increases. For $q = 4$, $N_T/N_0 = 10$. For $q >> 1$, $\mathcal{F}(q) \simeq \exp[q]/q^{3/2}$. Thus, by increasing the ratio of the trap depth to the temperature of atoms in the MOT, the number of atoms confined in the CO_2 laser trap can be greatly enhanced. Of course, once the number of atoms in the CO_2 laser trap becomes a significant fraction of the atoms in the MOT, this simple model must eventually break down for large q.

It is interesting to compare the predictions of this simple model with the experimental results described in Section 4.3.2. In Section 4.3.2, we reported on the

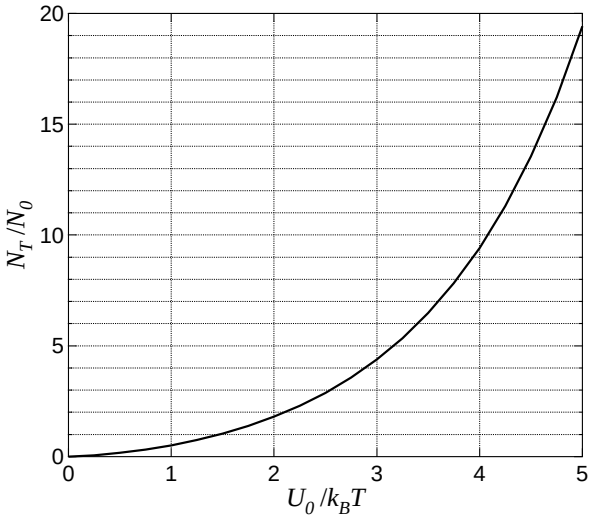

Figure 5.1: N_T/N_0 as a function of $q = U_0/k_BT$

confinement of 3.5×10^4 atoms in a CO_2 laser trap with a well depth of $U_0 \simeq 450\,\mu$K. In this case, the gaussian CO_2 laser beam is focused to a waist with a $1/e$ intensity radius $a = b = 37.5\,\mu$m which has a corresponding Rayleigh length $c = 833\,\mu$m yielding an effective trap volume $V_{\rm trap} = 6.5 \times 10^{-6}\,{\rm cm}^3$. The density of the MOT was estimated to be $n_{\rm MOT} \simeq 5\times10^{10}\,{\rm atoms/cm}^3$. Thus, the number of atoms in the MOT which fall inside the effective trap volume $V_{\rm trap}$ is $N_0 = n_{\rm MOT}\,V_{\rm trap} = 3.25 \times 10^5$. By using time-of-flight methods described in Section 5.2.3, the temperature of the MOT in this case is measured to be $T \simeq 1$ mK. Thus, the ratio $q = U_0/k_BT = 0.45$ in this case. Numerical integration of (5.7) and (5.8) gives the trapping factor $\mathcal{F}(0.45) = 0.135$. Thus, the number of atoms predicted to be confined in the CO_2 laser trap in this case is $N_T = 4.4 \times 10^4$, which is in good agreement with the observed value of $N_{meas} = 3.5 \times 10^4$.

Given the success with which this simple model predicts the number of atoms confined in the CO_2 laser trap, we are encouraged that the loading efficiency can

be substantially improved by increasing the ratio $q = U_0/k_BT$. In Section 5.2, we report on our attempts at increasing the density and lowering the temperature of the MOT in order to increase the number of atoms transferred into the CO_2 laser trap. By lowering the intensity and tuning the MOT beams closer to resonance for a short period of time before extinguishing the MOT beams we find that we can maintain the spatial density of the MOT while at the same time lowering the temperature to near the Doppler cooling limit. We describe the experimental techniques used to measure the spatial density and temperature of the MOT. In Section 5.3, we develop a more complete model of the loading dynamics which takes into account the finite size of the MOT and models the approach to equilibrium using a Fokker-Plank equation. Finally, in Section 5.4 we compare the predictions of the model with our experimental observations.

5.2 Density and Temperature of the MOT

In this section we describe the experimental techniques used to characterize the temperature and density of the MOT. In addition, we recount our attempts at increasing the density and lowering the temperature of the MOT in order to increase transfer efficiency into the CO_2 laser trap. We find that the maximum number of atoms in the MOT is obtained by employing high intensity laser beams tuned approximately 6 linewidths below resonance. However, these parameters yield a relatively high temperature ($\simeq 1$ mK). When the MOT laser beams are tuned close to resonance and have low intensity, the temperature of the MOT approaches the Doppler cooling limit of $140\,\mu$K. However, the number of atoms in the MOT is substantially reduced. We find that by using a transient technique in which a MOT loading phase is followed by a short cooling phase we can maintain the high spatial

density of the loading phase while at the same time lowering the temperature of the atoms to near the Doppler limit. By employing this technique we have improved the number of atoms loaded into the CO_2 laser trap by more than a factor of 20.

5.2.1 The MOT Loading and Cooling Phases

The steady state number of atoms loaded into the MOT is found to be maximized for high intensity laser light tuned far from resonance. In an attempt to achieve a high spatial density in the MOT, we load the MOT using trapping beams tuned 6 linewidths below the $|F = 3/2\rangle \rightarrow |F' = 5/2\rangle$ resonance. The peak intensity at the center of each of the 6 MOT trapping beams is $I = 92\,\mathrm{mW/cm^2}$. This corresponds to $I_0/I_{sat} = 36$ for each of the six beams. The gaussian beams have a $1/e^2$ intensity diameter $\simeq 0.75\,\mathrm{cm}$ as measured using a diode array. Each of these six beams is overlapped with a repumping beam tuned 1/2 linewidth below the $|F = 1/2\rangle \rightarrow |F' = 5/2\rangle$ transition. The peak intensity at the center of each of the repumping beams is $I_0 \simeq 12\,\mathrm{mW/cm^2}$, approximately 1/3 of that used for the MOT trapping beams.

The optical power required for the MOT trapping and repumping beams is provided in a manner similar to that described in Section 4.2.4. However, instead of dividing the trapping beam power into three equal beams with unequal repumping beam power, we divide the total optical power equally between two beams. Each beam contains a 3:1 ratio of trapping to repumping beam power. One beam is used for both the vertical MOT beams by retroreflection of the light as described in Section 4.2.4. The other beam is used to produce all four horizontal MOT beams in the manner shown in Figure 5.2. Since the MOT beams are circularly polarized, mirrors $M1$ and $M2$ need to be first surface metallic mirrors (as opposed to dielectric mir-

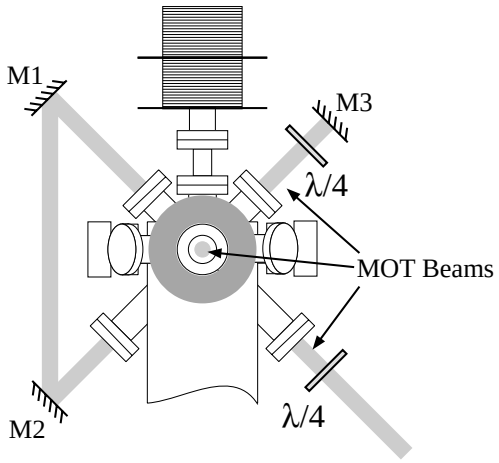

Figure 5.2: MOT Beam Configuration

rors) in order for the reflected light to maintain its circular polarization. However, even for metallic mirrors, there still exists a small relative phase shift between the $S-$ and $P-$polarized light upon reflection. The advantages of using this technique for generating the MOT laser beams over that described in Section 4.2.4, is (1) each beam contains more power and (2) the repumping light is distributed evenly over the six MOT beams. The major disadvantage of this technique is that the MOT beams are not as easily aligned since the horizontal beams are coupled together.

During the MOT loading phase, which lasts for several seconds, the MOT beams are described by the parameters given above. At steady state the MOT is observed using the calibrated optical detection system described in Section 4.2.5 to contain 5×10^8 atoms.

In order to increase the number of atoms loaded into the CO_2 laser trap, the MOT beams are tuned closer to resonance and the intensity is lowered in order to cool the atoms to temperatures near the Doppler limit (see Section 4.2.3 for a discussion of the Doppler cooling limit). The trapping beam intensity is reduced to $I_0 = 0.25\,\mathrm{mW/cm^2}$ which corresponds to $I_0/I_{sat} = 0.1$ and the repumping beam

intensity is reduced to $I_0 = 0.08\,\mathrm{mW/cm^2}$ per beam. Both the trapping and repumping beams are tuned approximately 1/2 linewidth below their respect resonant transition frequencies. The steady state number of atoms in the cooling phase is substantially lower than the steady state number of atoms in the loading phase. However, the cooling phase can be maintained for tens of milliseconds following the loading phase before a loss of atoms begins to take place. Thus, by using a transient scheme in which a short cooling phase follows the MOT loading phase, we hope to maintain the density obtained during the loading phase while cooling the atoms to near the Doppler limit.

5.2.2 Measurement of the MOT Density

A measurement of the number of atoms in the MOT in combination with a measurement of the MOT's spatial distribution yields the MOT spatial density. By imaging the fluorescence from the MOT using a charge-coupled device (CCD) camera we can measure the spatial distribution of atoms in the MOT. Figure 5.3(a) shows an image of the fluorescence from the MOT obtained using a COHU CCD camera. The MOT is formed using the parameters for the loading phase given above and has reached a steady state distribution after loading for 10 seconds. Figure 5.3(b) gives the intensity distribution along a vertical line that passes through the peak intensity value in the fluorescence image. A gaussian distribution $\exp(-x^2/R_v^2)$ is fit to the intensity distribution in the vertical direction by minimizing χ^2. The best fit to the distribution is given for $R_v = 1.03$ mm. Similarly, Figure 5.3(b) shows the intensity distribution of the MOT in the horizontal direction. In this case, the best fit to a gaussian distribution $\exp(-x^2/R_h^2)$ is given by $R_h = 1.27$ mm.

A vertical line through the center of the MOT in Figure 5.3(a) corresponds to the

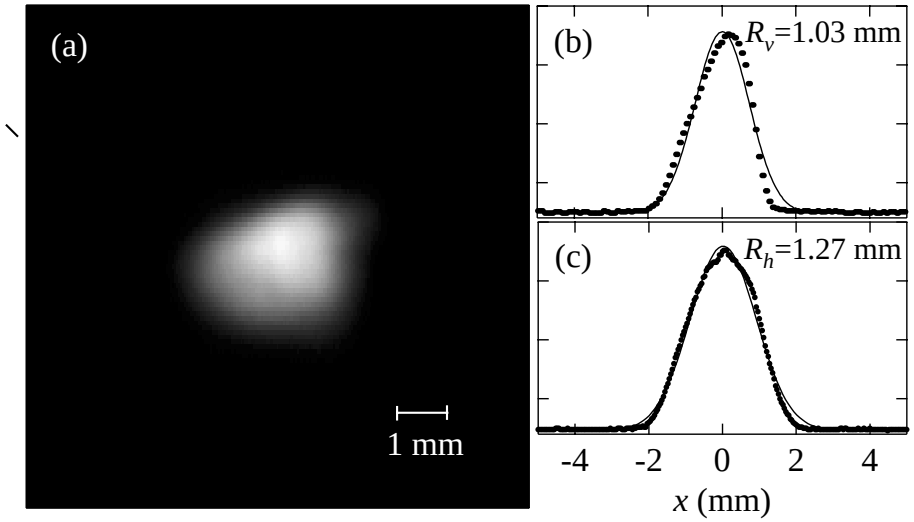

Figure 5.3: Fluorescence Measurement of the Size of the MOT

axis of the current loops used to form magnetic quadrupole field. This vertical line through the center of the MOT is an axis of symmetry. Thus, from the fluorescence image, we expect that the spatial distribution of the MOT is well approximated by a cylindrically symmetric gaussian distribution

$$n_{\mathrm{MOT}}(\rho, z) = n_0 \, \exp\left[-\frac{\rho^2}{R_h^2} - \frac{z^2}{R_v^2}\right] \tag{5.9}$$

where z is the dimension along the symmetry axis, ρ is the radial dimension and $n_0 = N_{\mathrm{MOT}}/(\pi^{3/2}\, R_h^2\, R_v)$ is the peak density in the center of the trap. Here, N_{MOT} is the number of atoms confined in the MOT.

For the MOT loading parameters described above we observe that $N_{\mathrm{MOT}} = 5 \times 10^8$ atoms are confined in the MOT. For $R_h = 1.27$ mm and $R_v = 1.03$ mm this corresponds to a peak density $n_0 \simeq 5 \times 10^{10}\,\mathrm{atoms/cm}^3$ at the center of the MOT. Thus, we find that while using the higher intensity beams gives a larger number of

atoms in the MOT (by a factor of 5), the peak density at the center of the MOT does not appear to be greatly improved. The size of the MOT simply increases in order to accommodate the larger number of atoms while maintaining the same peak density. However, while the high intensity beams do not provide an increase in MOT density, we have chosen to continue using this configuration since the loading rate is enhanced by a factor of three over the lower intensity configuration. In addition, the high intensity configuration provides a simple means of producing equal repumping power in each of the MOT beams.

Note that the spatial distribution in the horizontal (Figure 5.3(a)) and vertical (Figure 5.3(b)) directions are well approximated by a gaussian distribution. This implies that the effective confining potential for the MOT is approximately harmonic since, in equilibrium, the spatial distribution is given by $\exp(-U_{\rm MOT}(\boldsymbol{x})/k_BT)$ which gives a gaussian distribution for a harmonic potential $U_{\rm MOT}(\boldsymbol{x})$. For a spherical gaussian distribution with $1/e$ radius R at temperature T, the effective confining potential $U_{\rm MOT}(\boldsymbol{x}) = (k_BT/R^2)\,x^2$. Note that this phenomenological potential even includes the effect of radiation trapping forces in the event that the MOT is optically thick.

5.2.3 Temperature Measurements via Time of Flight

The temperature of the atoms in the MOT can be determined by measuring the time-of-flight for atoms released from the MOT to reach a given region of space [101]. Figure 5.4 illustrates how this technique is implemented experimentally. Atoms in the MOT are released at a time $t = 0$ by extinguishing the MOT laser beams and magnetic field gradient. Once released, the atomic vapor expands and accelerates under the force of gravity. A sheet of light tuned near resonance is placed a dis-

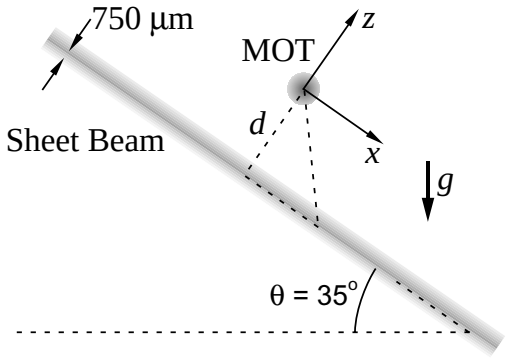

Figure 5.4: Time of Flight Temperature Measurement

tance d away from the MOT. As atoms enter the sheet beam they fluoresce. The fluorescence is imaged with unity magnification onto an optical fiber bundle which transmits the light to a photomultiplier tube. The time dependent signal is related to the temperature of the atoms as it depends on the initial velocity distribution of the atoms.

The sheet beam consists of two low-intensity, counterpropagating σ^+ probe beams detuned below the $F = 3/2, M_F = 3/2 \leftrightarrow F' = 5/2, M'_F = 5/2$ cycling transition by $\Delta = -\Gamma/2$ so that atoms are not heated as they enter the beam. The sheet beam is an elliptical gaussian beam with $1/e$ radii of 1 cm and 750μm. The intensity of the beams is approximately $0.1\, I_{sat}$. The sheet beam makes an angle $\theta = 35°$ with respect to the horizontal direction due to the availability of vacuum viewports in this direction. The distance $d = 10$ cm in the experiments considered below.

Immediately following release from the MOT, the phase space distribution of the atoms is given by:

$$W_0(\boldsymbol{x}, \boldsymbol{v}) = \frac{1}{\pi^3\, u^3\, R^3}\, \exp\left[-\frac{\boldsymbol{v}^2}{u^2}\right]\, \exp\left[-\frac{\boldsymbol{x}^2}{R^2}\right] \tag{5.10}$$

where R is the $1/e$ radius of the MOT spatial distribution, $u \equiv \sqrt{2k_BT/M}$, T is the temperature that the atoms had in the MOT and M is the mass of ^{6}Li.

In order to calculate the expected time dependent fluorescence signal, we want to find $n(\boldsymbol{x},t)$ the spatial distribution of atoms at time t. The time dependent fluorescence signal is then given by the convolution of the spatial distribution $n(\boldsymbol{x},t)$ with a spatial sampling function describing the probe beam. In terms of the initial phase space distribution W_0

$$n(\boldsymbol{x},t) = \int d\boldsymbol{v}_0\, W_0(\boldsymbol{x} - \boldsymbol{v}_0\, t - 1/2\, \boldsymbol{g}\, t^2, \boldsymbol{v}_0), \tag{5.11}$$

since an atom found at a position $\boldsymbol{x}$ at time t was initially at $\boldsymbol{x}_0 = \boldsymbol{x} - \boldsymbol{v}_0\, t - 1/2\, \boldsymbol{g}\, t^2$ where $\boldsymbol{v}_0$ is the initial velocity. Integrating the distribution over all possible initial velocities gives the probability that an atom is found at $\boldsymbol{x}$ at time t independent of velocity.

The fluorescence signal $S_{TOF}(t)$ is given by the convolution of $n(\boldsymbol{x},t)$ with a spatial sampling function

$$S_{TOF}(t) = \int d^3x \exp[-(x^2+y^2)/\sigma_{x,y}^2 - z^2/\sigma_z^2]\, n(\boldsymbol{x},t). \tag{5.12}$$

To simplify the integration we have assumed a gaussian dependence for the sampling function. Here, $\sigma_{x,y}$ is the $1/e$ radius of the sampling region in the x,y plane and σ_z is the $1/e$ radius of the sampling region along z. Performing the integration yields

$$\begin{aligned} S_{TOF}(t) &= \frac{A_1}{(\sigma_{x,y}^2 + u^2t^2)\sqrt{\sigma_z^2 + u^2t^2}} \exp\left[-\frac{(1/2\, g\, \sin\, t^2)^2}{\sigma_{x,y}^2 + u^2\, t^2}\right] \\ &\quad \times \exp\left[-\frac{(1/2\, g\, \cos\theta\, t^2 - d)^2}{\sigma_z^2 + u^2\, t^2}\right], \end{aligned} \tag{5.13}$$

up to an overall normalization A_1. We have included the fact that the probe beam makes an angle θ with respect to the horizontal direction.

For the experimental setup illustrated in Figure 5.4, σ_z is the $1/e$ intensity radius of the elliptical sheet beam in the thin direction. For the sheet beam described above $\sigma_z = 750\mu$m. The aperture of the optical fiber bundle is expected to limit the region of the probe beam observed in the $x-y$ plane. The aperture has a 0.25 in. diameter. Thus, we assume $\sigma_{x,y} \simeq 0.125\text{in.} \times 2.54\text{cm/in.} = 3.2$ mm.

To determine the temperature of atoms in the MOT, the time dependent fluorescence signal is recorded and (5.13) is fit to the data. The normalization A_1, an additive offset A_2 and the temperature T are all adjusted to minimize χ^2. $\sigma_{x,y}$ is also adjusted within reason, however, when $\sigma_{x,y}$ is allowed to vary it has little effect on the temperature T. The distance $d = 10$ cm and $\sigma_z = 750\mu$m.

By employing a low-intensity cooling phase using the MOT beam parameters described above, temperatures approaching the Doppler limit can be obtained. Figure 5.5 shows the time-of-flight signal obtained for atoms released from the MOT following a 4 ms cooling phase which cools the atoms collected during the MOT loading phase. During the cooling phase the trapping beam intensity is reduced to $I_0/I_{sat} = 0.1$ per beam and the trapping and repumping beam frequencies are tuned to 1/2 linewidth below their respective resonances. The best fit to the time-of-flight signal is given for a temperature $T = 185\,\mu$K. The theoretical time-of-flight signals for $T = 350\,\mu$K and $T = 140\,\mu$K are also shown for comparison.

Time-of-flight signals corresponding to $T \simeq 185\,\mu$K as shown in Figure 5.5 are typical for the cooling phase parameters described above. However, time-of-flight signals corresponding to temperatures approaching the Doppler cooling limit $T = 140\,\mu$K have also been observed. We believe that achieving temperatures ap-

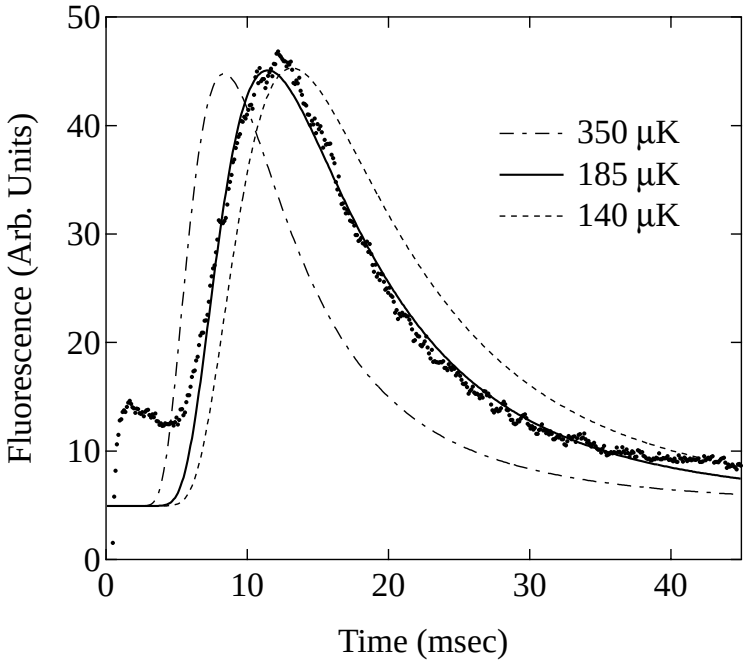

Figure 5.5: Time of flight signal for atoms released from the MOT.

proaching the Doppler cooling limit is sensitive to the frequency stability of the dye laser. The dye laser has been observed to exhibit peak-to-peak frequency fluctuations as large as 5 MHz. Since the Doppler cooling limit requires that the trapping beams be tuned to 1/2 linewidth ($\simeq$ 3 MHz) below resonance, reliably achieving the Doppler cooling limit with 5 MHz peak-to-peak fluctuations in the dye laser frequency can be challenging. Improvement of the frequency stability of the dye laser would be desirable.

5.2.4 Density Measurement via Absorption Imaging

Although we have demonstrated that by employing a low-intensity, near resonant cooling phase we can cool ^{6}Li atoms to near the Doppler cooling limit, it is not obvious that during this cooling phase the density of the atoms in the MOT remains

constant. In order to compare the density obtained in the loading phase to that present in the cooling phase we employ absorption imaging of the atoms in the MOT. To obtain the absorption image we use the experimental setup shown in Figure 5.6. A collimated probe beam with a $1/e$ diameter of 0.5 cm and peak intensity of $40\,\mu\mathrm{W/cm}^2$ illuminates the MOT from one side. Two lenses and a CCD camera are placed opposite to this probe beam in order to image the probe beam after it passes through the MOT. The lenses each have a focal length f. The first lens is placed a optical path length f from the MOT. The second lens is placed a distance $2\,f$ from the first. The image plane occurs at a distance f from the second lens at which point an image with unity magnification forms. Note that at the image plane both the spatial and momentum distribution of the light as it passes through the MOT is reconstructed. This is desirable for absorption imaging since the probe beam is recollimated before it travels to the CCD camera. Normally a ruler is placed at the image plane. The ruler provides an object for the CCD camera lens to focus on and provides a length scale for comparison with the absorption image. The probe beam remains on for a duration of $4\,\mu$s. The CCD camera digitizes the intensity striking each pixel into 256 bins. In order to avoid digitization error, the probe beam is tuned off resonance such that the maximum attenuation of the probe beam is $\simeq e^{-2}$.

In order to obtain the density distribution of the MOT from absorption images a small amount of post-processing of the images is required. To extract the density distribution both an image of the intensity distribution $I(x, y)$ after it passes through the cloud and an image of the unobstructed intensity distribution of the probe beam $I_0(x, y)$ need to be recorded. Here x and y are the coordinates in the horizontal and vertical direction respectively in the plane of the image. We will use

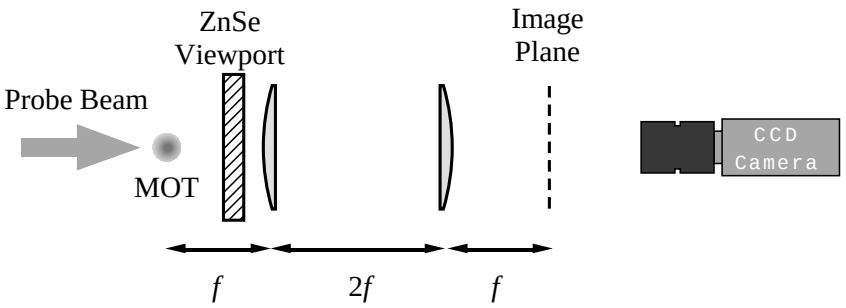

Figure 5.6: Experimental Setup for Measuring MOT Absorbtion

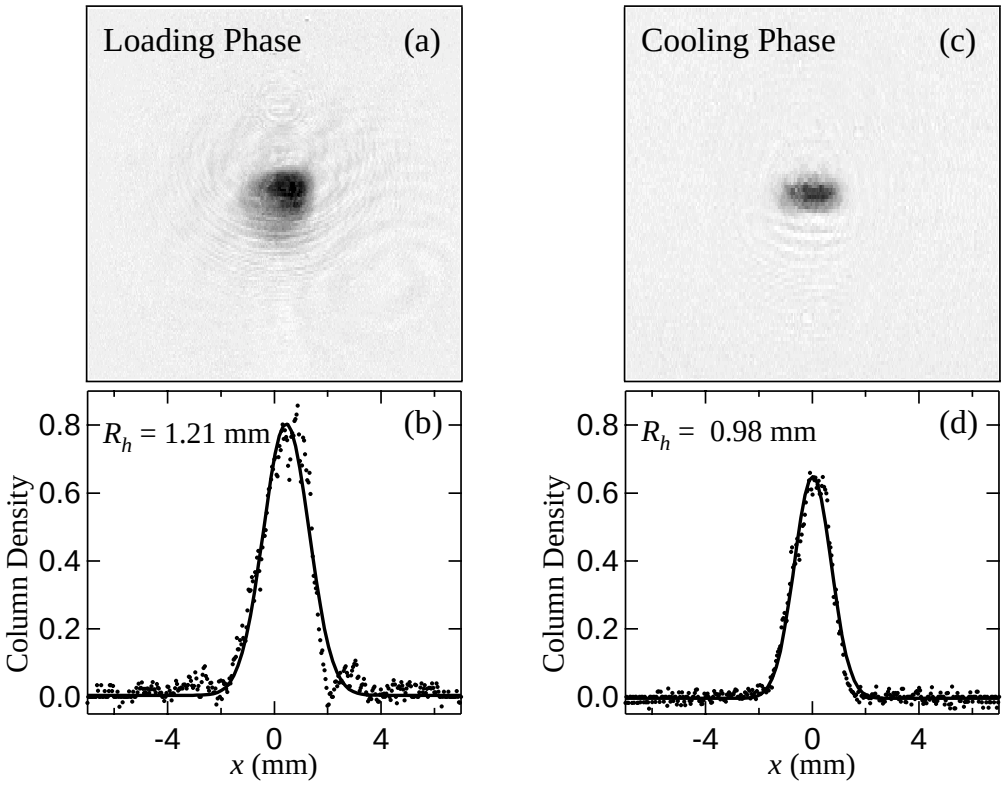

Figure 5.7: Absorption Images of the MOT During the Loading Phase and the Cooling Phase

the variable z to denote the direction of propagation of the probe beam. As the probe beam passes through the cloud of atoms, the intensity of the light is reduced due to scattering of light out of the probe beam according to

$$\frac{dI}{dz} = -I\, n(x,y,z)\, \sigma, \tag{5.14}$$

where σ is the cross section for a photon to scatter off of an atom. Assuming that the density distribution of the cloud is given by $n(x,y,z) = n_0 \exp\left[-\frac{x^2}{R_h^2} - \frac{y^2}{R_v^2} - \frac{z^2}{R_h^2}\right]$, integration of both sides of (5.14) yields

$$I(x,y) = I_0(x,y)\, e^{-\sigma\, n(x,y)}, \tag{5.15}$$

where $n(x,y) \equiv n_0 \sqrt{\pi}\, R_h \exp\left[-\frac{x^2}{R_h^2} - \frac{y^2}{R_v^2}\right]$ is the column density of the cloud. Thus, by dividing the absorption image by the probe beam image and taking the natural logarithm of the resulting image we arrive at an image proportional to the column density $n(x,y)$.

We wish to determine the density distributions of the MOT during the loading phase and during the cooling phase. In order to determine the density distribution during the loading phase we pulse the probe beam on for $4\,\mu$s several μs after extinguishing the MOT laser beams. The MOT magnetic field gradient remains on since it requires $\simeq 200\,\mu$s to shut this field off over which time the ^{6}Li cloud would expand substantially. The absorption image and an image of the probe beam in the absence of the atomic cloud is recorded. From these images, the column density distribution of the atoms during the loading phase can be found. Similarly, the density distribution of the atoms during the cooling phase is measured by recording an absorption image several μs after the MOT beams are extinguished following a

4 ms cooling phase.

Figure 5.7 shows the density distribution $n(x, y)$ obtained for the ^{6}Li cloud immediately following the MOT loading phase (a) and immediately following the MOT cooling phase (c). Below each density distribution is a gaussian fit to the distribution $n(x, y_0)$ along a horizontal line passing through the point of maximum absorption. The best fit to the horizontal distribution during the loading phase (b) is given by $R_h = 1.21$ mm in good agreement with the fit to the fluorescence image discussed previously. The best fit to the horizontal distribution during the cooling phase gives $R_h = 0.98$ mm. Although the column densities $n(x, y_0)$ are not given in absolute units, the relative height of the peaks give a true indication of the relative column density in each case. As can be seen in Figure 5.7, the maximum column density during the loading phase exceeds that of the cooling phase by a factor 1.2. However, since the column density is proportional to the $1/e$ radius of the cloud R_h as well as the peak spatial density n_0, we find that since R_h is reduced by a factor of 0.8 during the cooling phase, the peak spatial density n_0 during the cooling phase is nearly identical to that during the loading phase. Thus, we find that during the cooling phase, the peak density at the center of the atomic cloud remains the same as the peak density during the loading phase. The cloud has lost a small number of atoms and shrinks slightly in size while keeping n_0 constant.

Since the number of atoms confined in the MOT during the cooling phase decreases over time to a steady state value substantially less than during the loading phase, it is important to estimate the time scale required for the atoms come into thermal and diffusive equilibrium with the CO_2 laser potential. If the time scale is long, the density of atoms in the cooling phase might be greatly reduced before equilibrium is achieved. In the following section we develop a model which considers the

loading dynamics of the CO_2 laser trap. We find that the momentum distribution of the atoms is expected to come into equilibrium very rapidly. The approach to equilibrium in the spatial degrees of freedom is governed by a Fokker-Plank equation and is found to be quite long if the ratio U_0/k_BT is large.

5.3 Loading Dynamics

In this section, we present a simple Fokker-Planck model for the evolution of the trapped atom spatial distribution in a CO_2 laser trap which is loaded from a magneto-optical trap. Deep CO_2 laser traps can achieve very high densities, but reach equilibrium slowly compared to shallow traps. Equilibrium times range from milliseconds for shallow traps to seconds in traps which are deep compared to the thermal energy. A universal function for the equilibrium number of trapped atoms is given. The purpose of this section is to provide a simple radial loading model of the dynamics for the CO_2 laser trap, as well as the equilibrium number of trapped atoms. We find that the equilibrium density in the trap can be greatly enhanced compared to that of the MOT when the trap depth is large compared to the thermal energy. This is a consequence of the Boltzmann factor. However, the time scale to achieve equilibrium can be quite long.

The model described here provides a simple picture of what we believe are the dominant mechanisms at work in the loading dynamics of the CO_2 laser trap. The model is meant to provide physical insight into the loading dynamics of the CO_2 laser trap so that strategies to increase the transfer efficiency from the MOT into the CO_2 laser trap can be contemplated. However, this model neglects a number of phenomena that may become very relevant to the loading dynamics especially as the density in the CO_2 laser trap becomes very high. For example, we have

neglected density-dependent loss processes as well as absorption of the MOT beams and the effects of radiative atom-atom repulsion in the CO_2 laser trap. However, the current model will serve as a starting point for including these features in future work.

As assumed previously, the MOT serves as a reservoir in thermal and diffusive contact with the CO_2 laser trap. The optical molasses of the MOT laser fields provides the viscous damping needed to cool atoms into the CO_2 laser trap potential.

The conservative part of the potential for the trapped atoms arises from the MOT and from the focused CO_2 laser beam:

$$U(\rho, z) = \frac{k_B T}{R^2}\left(\rho^2 + z^2\right) - U_0 \exp\left(-\frac{\rho^2}{a^2} - \frac{z^2}{z_0^2}\right). \tag{5.16}$$

The first term describes the effective harmonic restoring force of the MOT in the radial ρ and axial z directions. Here z is along the direction of propagation of the CO_2 laser beam. The first term in (5.16) includes both the MOT laser forces and the atom-atom radiative repulsion forces [103] that determine the MOT radius R, i.e., the effective MOT restoring force is reduced at high MOT density. For simplicity, the MOT is taken to be spherically symmetric with a radius R which can be estimated experimentally using absorption imaging as described in Section 5.2.4. This term yields a Boltzmann factor for the equilibrium MOT density which is a gaussian distribution of radius R in the absence of the CO_2 laser trap. The second term describes the CO_2 laser trap, where a is the intensity $1/e$ radius and $z_0 = 2\pi a^2/\lambda$ is the Rayleigh length. We assume $a << R$ and neglect atom-atom radiative repulsion forces in the CO_2 laser trap. Here we approximate the lorentzian dependence on the axial position z by a gaussian dependence on z as described above. U_0 is the well depth, which is proportional to the static polarizability and

to the maximum intensity (see Chapter 3). For simplicity, we also assume that the ground and excited state polarizabilities are nearly identical so that the force on the atoms does not change when the atoms are excited in the MOT laser beams. This is approximately the case for Li.

In addition to the conservative potential, the atoms experience viscous damping in the MOT optical molasses which provides cooling (see the discussion of optical molasses in Section 4.2.3). The local momentum distribution is damped very rapidly according to $\dot{p} = -\alpha v$. We assume that the viscous damping coefficient α is spatially constant in the CO_2 laser trap. Then, $\dot{v} = -\gamma_v\, v$, where $\gamma_v = \alpha/M$, so that an atom loses memory of its velocity after traveling a distance v/γ_v. For the ideal MOT detuning and intensity in the trap region, the maximum value of α for simple Doppler cooling is $\hbar k^2/2$ [100], so that $\gamma_v \simeq \epsilon_{rec}/(\hbar)$. For lithium, γ_v is $2\pi \times 70$ kHz. Hence, at MOT temperatures of 0.2 mK, where the velocity is of order 1 m/s, the atom travels only a few microns before losing memory of the velocity. Thus, we can assume the momentum distribution is in local equilibrium.

In this case, the position distribution, $n(\boldsymbol{x}, t)$, will obey approximately a Fokker-Planck equation [109, 110],

$$\frac{\partial n(\boldsymbol{x}, t)}{\partial t} = \frac{1}{\alpha}\nabla \cdot \left[n(\boldsymbol{x}, t)\, \nabla U(\boldsymbol{x}) \; + \; k_B T\, \nabla n(\boldsymbol{x}, t) \right], \tag{5.17}$$

where $D_x = k_B T/\alpha$ is the spatial diffusion constant and T is the temperature. In Eq. (5.17), the right hand side is $-\nabla\cdot\boldsymbol{J}$, where $\boldsymbol{J}$ is the sum of the drift and diffusion currents. The local drift velocity is determined by the spatially varying trap force and the viscous damping coefficient. In equilibrium, the drift and diffusion currents balance and the solution to Eq. (5.17) is the usual Boltzmann factor. To lowest

order, the phase space density $W(\boldsymbol{x}, \boldsymbol{p}, t)$ is given by the product

$$W(\boldsymbol{x}, \boldsymbol{p}, t) = n(\boldsymbol{x}, t) \frac{\exp(-\boldsymbol{p}^2/(2Mk_BT)}{(2\pi Mk_BT)^{\frac{3}{2}}}, \tag{5.18}$$

where the momentum dependent factor is a normalized Maxwellian distribution. The number of trapped atoms at time t is then obtained by integrating the phase space density over the region where the total energy is negative, i.e., between $-U_0$ and 0, for the potential of Eq. (5.16).

$$N_T(t) = \int d^3x\, d^3p\, \Theta \left[-\frac{\boldsymbol{p}^2}{2M} - U(\boldsymbol{x}) \right] W(\boldsymbol{x}, \boldsymbol{p}, t), \tag{5.19}$$

where $\Theta(E)$ is a unit step function.

We consider for simplicity the case of radial loading and assume that the Rayleigh length of the trap is larger than the radius of the MOT, $z_0 >> R$. In this case, the z dependence of the spatial distribution remains essential unchanged from that of the MOT as discussed below. Then, the effective potential of Eq. (5.16) is approximated by

$$U(\rho, z) = \frac{k_BT}{R^2} \left(\rho^2 + z^2 \right) - U_0 \exp\left(-\frac{\rho^2}{a^2} \right). \tag{5.20}$$

Here, we assume the MOT provides the dominant axial confining potential for the trapped atoms while the CO_2 laser provides the dominant radial potential in the trap assuming $R >> a$.

To describe the radial motion, the Fokker-Planck equation, Eq. (5.17), is written

in terms of the radial coordinate ρ,

$$\frac{\partial n(\rho,t)}{\partial t} = \frac{1}{\alpha}\frac{1}{\rho}\frac{\partial}{\partial \rho}\left[\rho\left(\frac{\partial U}{\partial \rho}n + k_B T\frac{\partial n}{\partial \rho}\right)\right]. \tag{5.21}$$

Eq. (5.21) is integrated numerically using Eq. (5.20) with $z = 0$ and $n(\rho, t = 0) = n_0 \exp(-\rho^2/R^2)$ to determine the evolution of the radial density distribution of atoms in the CO_2 laser trap. The numerical integration of this partial differential equation is accomplished using an explicit forward-time-centered-space finite differencing routine [111]. We assume that $\frac{\partial n}{\partial \rho} = 0$ at $\rho = 0$ and use l'Hôpital's rule for evaluating $\frac{1}{\rho}\frac{\partial n}{\partial \rho}$ at the origin. A von Neumann stability analysis [111] of the discretized diffusion equation neglecting the potential $U(\rho)$ is found to accurately determine the stability criterion for the time step used in the finite differencing routine. Retaining the radial part of the MOT potential assures that the total number of atoms is conserved.

Figure 5.8 shows the radial density distribution, $n(\rho, t)$ for three different times. We choose parameters comparable to those for our trap: $R = 1$ mm, $a = 35\,\mu$m, $U_0 = 0.33$ mK, $k_B T = 0.2$ mK, and a saturation parameter of 0.1, so that $\alpha/M \simeq 0.1\,\hbar k^2/M = 2\pi \times 14$ kHz. The density in the center builds up as atoms are pulled in through the optical molasses by the radial force of the CO_2 laser trap.

Eq. (5.19) can be used to determine the total number of atoms which are trapped at any time t. Since the potential given by Eq. (5.20) is separable, i.e., for $z_0 >> R$, the CO_2 laser radial potential does not exert an axial force, we assume that the axial spatial distribution is in equilibrium at all times, i.e., the density scales as

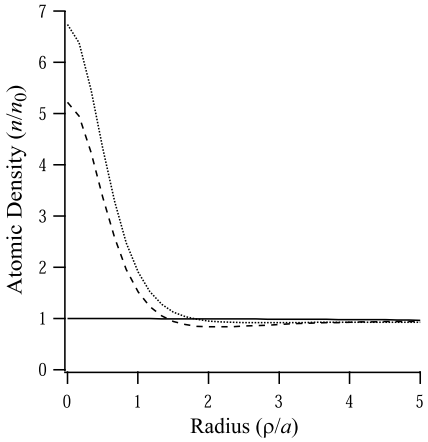

Figure 5.8: Radial spatial distribution of the atoms at several different times. The solid line shows the initial density distribution and the long- and short-dashed lines show the density distribution at two later times.

$\exp(-z^2/R^2)$. Then the phase space distribution takes the form

$$W(\rho, z, \boldsymbol{p}, t) = n(\rho, t)\, \exp\left(-\frac{z^2}{R^2}\right)\, \frac{\exp(-\boldsymbol{p}^2/(2Mk_BT)}{(2\pi Mk_BT)^{\frac{3}{2}}}. \tag{5.22}$$

Using Eq. (5.22), Eq. (5.19) can be rewritten as

$$\begin{aligned} N_T(t) &= \int d^2\boldsymbol{x}_\perp d^2\boldsymbol{p}_\perp n(\rho, t)\, \frac{\exp(-\boldsymbol{p}_\perp^2/(2Mk_BT)}{(2\pi Mk_BT)^{3/2}} \\ &\quad \times \int dE_z \Theta\left[-E_\perp(\rho, \boldsymbol{p}_\perp) - E_z\right]\, \frac{2\pi}{\omega_z}\, \exp\left(-\frac{E_z}{k_BT}\right), \end{aligned} \tag{5.23}$$

where the MOT radial potential is negligible for the trapped atoms so that $E_\perp(\rho, \boldsymbol{p}_\perp) = \boldsymbol{p}_\perp^2/(2M) - U_0\, \exp(-\rho^2/a^2)$. We have used the fact that

$$\int dz\, dp_z \delta\left(E_z - \frac{p_z^2}{2M} - k_BT\frac{z^2}{R^2}\right) = \frac{2\pi}{\omega_z},$$

which is obvious once the integral is recognized as the density of states for a one-

dimensional harmonic oscillator. Here, $\omega_z = \sqrt{2k_BT/(MR^2)}$ is the oscillation frequency corresponding to the effective MOT axial potential, $k_BT\,z^2/R^2$.

The rest of the integrals in Eq. (5.23) can be straightforwardly done to obtain

$$N_T(t) = N_0 \int_0^\infty \frac{2\rho d\rho}{a^2\,n_0}\, n(\rho,t)\, f[\rho, U_0/(k_BT)], \tag{5.24}$$

where

$$f(\rho,q) = 1 - \left(1 + q\exp(-\rho^2/a^2)\right)\, \exp\left(-q\exp(-\rho^2/a^2)\right). \tag{5.25}$$

The number of trapped atoms is given in terms of the number N_0 contained in the overlap volume of the trap with the MOT,

$$N_0 = \pi^{3/2}\,a^2\,R\,n_0, \tag{5.26}$$

where n_0 is the MOT central density.

Using Eq. (5.24), the number of atoms $N_T(0)$ initially contained in the trap is obtained by setting $n(\rho, t=0) = n_0$, the initial MOT density at $\rho = z = 0$. One obtains

$$N_T(0) = N_0\,q^2 \int_0^1 dv\, v\,(-\ln v)\,\exp(-qv), \tag{5.27}$$

where $q = U_0/(k_BT)$. Note that the initial number is equivalent to the number of atoms trapped by turning the CO_2 laser trap on suddenly, since the momentum distribution is assumed to be instantly in equilibrium. Figure 5.9 shows that the maximum initial number is the order of N_0 and increases slowly for large $U_0/(k_BT)$ due to increase in the volume for which the negative potential is comparable to

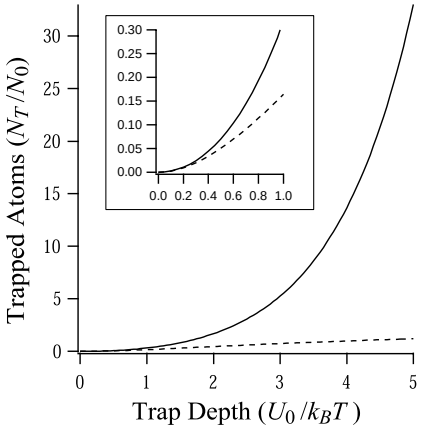

Figure 5.9: Number of trapped atoms N at $t = 0$ (dashed line) and in equilibrium (solid line) as a function of U_0/k_BT, where U_0 is the well depth and k_BT is the thermal energy. N is given in units of the number N_0 contained in the trap volume at the MOT density. The inset shows the same curves for $U_0/k_BT = 0$ to 1.

k_BT.

The equilibrium number of trapped atoms $N_T(t \rightarrow \infty)$ is obtained using $n(\rho, \infty) \simeq n_0 \exp[+q \exp(-\rho^2/a^2)]$, assuming $R >> a$. Then,

$$N_T(\infty) = N_0\, q \int_0^1 dv(-\ln v)[\exp(qv) - 1]. \tag{5.28}$$

Note that for shallow traps, $U_0/(k_BT) << 1$, $N_T(\infty) = N_T(0)$. Figure 5.9 compares the equilibrium number of trapped atoms to the initial number as a function of $q = U_0/(k_BT)$. For deep traps, where $q = U_0/(k_BT) >> 1$, the exponential in the integrand of Eq. (5.28) leads to substantial density enhancement as has been observed in a deep optical traps [112].

The time scale for the trap to reach equilibrium increases with $U_0/(k_BT)$ as shown in Figure 5.10. For large values of $U_0/(k_BT)$, the equilibrium trap number is large compared to N_0, the number contained in the trap volume at the initial MOT

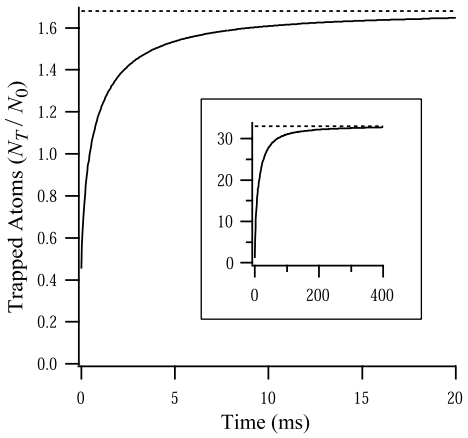

Figure 5.10: Time dependent trap number

density. Atoms must drift in from large ρ to fill the trap fully. Since the force is weak when $\rho >> a$, and the optical molasses of the MOT provides a high viscosity medium, this time scale can be several seconds when $U_0/(k_BT)$ is large. This may account in part for the long time scales observed in Ref. [113]. Note that for fixed $q = U_0/(k_BT)$ and fixed R/a, the equilibrium time scales with the diffusion time, $\tau \simeq \alpha a^2/(k_BT)$.

5.4 Experimental Observations

It is interesting to compare the equilibrium number of trapped atoms predicted by Eq. (5.28) to that obtained in our CO_2 laser trap. In the experiments, the MOT is loaded for 3 seconds and then cooled to near the Doppler limit by reducing the MOT laser intensity and tuning the laser closer to resonance. Using time of flight measurements, the temperature is estimated to be between 0.15 and 0.2 mK. The MOT density is estimated to be $n_0 \simeq 0.5 \times 10^{11}$ atoms/cm^3 by absorption imaging. The MOT radius is measured to be $R \simeq 1.0$ mm in the axial direction both before

and after the cooling phase.

We have measured the equilibrium number of atoms for several different well depths by placing an acousto-optic (AO) modulator in the CO_2 laser beam path (the CO_2 laser AO-modulator will be described in Chapter 7). The maximum well depth is obtained without using the AO-modulator and its parameters were given previously as: $U_0 = 0.45$ mK, $a = b = 37.5\,\mu$m and $c = 833\,\mu$m. In this case, the trap volume $V_{\rm trap} = 6.5 \times 10^{-6}{\rm cm}^3$. Using the AO-modulator, the power of the CO_2 laser can be adjusted to any value. The trap parameters in this case are determined by exciting parametric resonances in the trap as described in Section 7.5. When the AO-modulator is used the trap radii are given by $a = 35\,\mu$m, $b = 47\,\mu$m and $z_0 = 0.8$ mm. In this case, the radii a and b differ due to the fact that the AO-modulator causes astigmatism in the CO_2 laser beam. The corresponding trap volume $V_{\rm trap} = 7.3 \times 10^{-6}{\rm cm}^3$. We have measured the equilibrium number of trapped atoms using the AO-modulator for well depths $U_0 = 0.33$ mK and $U_0 = 0.1$ mK.

Note that the trap radii c is somewhat smaller than R in all of the cases considered contrary to our assumption $c >> R$ given above. However, the trap loading time in the final cooling stage is limited to a maximum of 10 ms, short compared to the axial equilibration time in the trap. Hence, the z dependence of the density cannot change quickly and the faster radial motion dominates the density enhancement. Thus, the radial loading model is approximately valid. The primary error is that the radial force is not constant over the Rayleigh length. We take $N_0 = \pi^{3/2}\, a\, b\, c\, n_0$ as the number of atoms in the overlap volume.

Table 5.1 shows the measured number of trapped atoms and the predictions of Eq. (5.28) for the well depths, 0.45 mK, 0.33 mK and 0.1 mK. Eq. (5.28) is evaluated for temperatures of 0.15 mK and 0.2 mK, and is in reasonable agreement the

		N_{calc}	
U_0(mK)	N_{meas}	$T = 0.2\,\mathrm{mK}$	$T = 0.15\,\mathrm{mK}$
0.45	7.2×10^5	7.5×10^5	1.7×10^6
0.33	4.0×10^5	3.8×10^5	8.1×10^5
0.1	4.4×10^4	2.6×10^4	4.8×10^4

Table 5.1: Number of Trapped Atoms.

measurments. At a well depth of 0.33 mK, the measured loading time is optimized at 4 ms for a saturation parameter of 0.1 with the detuning optimized to give a minimum temperature near the Doppler limit. Increasing the loading time to 30 ms has no effect, while lowering it to 1 ms reduces the atom number. Figure 5.10 shows that for $U_0/(k_B T) \simeq 2$ and $\alpha = 0.1\,\hbar k^2$, the expected equilibrium time is $\simeq 4$ ms, in very good agreement with the measurements.

5.5 Summary

In conclusion, we have presented a simple Fokker-Planck equation treatment of the loading dynamics of a CO_2 laser trap. We find that deep traps can achieve very high densities, but take much longer to fill than shallow traps. The predictions for the number of trapped atoms are in good agreement with our measurements and the equilibrium time scales are consistent with our observations. We have neglected a variety of processes that can affect the loading dynamics. Since our trap lifetime is hundreds of seconds, we have neglected loss arising from background gas collisions. We have also neglected inelastic collisions between the upper and lower hyperfine levels which expel atoms from the trap. This tends to favor loading into the lower hyperfine level at high density. In addition, we have neglected density-dependent loss processes as well as absorption of the MOT beams and the effects of radiative atom-atom repulsion in the CO_2 laser trap. One expects that the effects of high

density will be important in deep wells where the density is greatly enhanced, as obtained in Ref. [112]. The current model will serve as a starting point for including these features in future work.

Since the number of atoms loaded into the CO_2 laser trap is expected to be enhanced by increasing the ratio $q = U_0/k_BT$, we are hopeful that substantial improvements in the number of trapped atoms can be obtained by increasing U_0 or decreasing T. One simple method that can be used to increase the well depth is to retroreflect the CO_2 laser beam back through the focus of the trap. If the retroreflected beam has an orthogonal polarization to the incident beam, interference effects between the beams are avoided and the well depth U_0 is doubled. The temperature of the atoms in the MOT may be reduced by using polarization gradient cooling [102]. In Section 4.2.3 we noted that for a standard $\sigma^+ - \sigma^-$ ^{6}Li MOT, polarization gradient cooling is not expected to occur since the light shift for linear polarized light is independent of the magnetic quantum number $|m|$ in ^{6}Li. However, an alternative configuration of the optical molasses beams (lin$\perp$lin) may provide a mechanism for sub-Doppler cooling in a ^{6}Li gas. In the lin$\perp$lin configuration, the three counterpropagating pairs of beams each consist of two beams which are linearly polarized at right angles to one another. Along each beam axis a polarization gradient exists that alternates between σ^+ and σ^- light. Despite the small hyperfine splitting in the excited state of ^{6}Li, the light shift due to σ^+ and σ^- light is dependent on the magnetic quantum number m. Therefore, polarization gradient cooling mechanisms are expected to exist for ^{6}Li in a lin$\perp$lin configuration of optical molasses. By using lin$\perp$lin optical molasses, other alkali atoms have been cooled to temperatures such that their root mean square velocity v_{rms} is only 3.6 times the velocity of recoil from the absorption or emission of a single photon [114].

The recoil velocity for ^{6}Li is $v_{rec} = \hbar\, k/M = 9.8$ cm/s. Thus, temperatures as low as $\frac{1}{2}\, M\, (3v_{rec})^2/k_B \simeq 50\, \mu$K might be achievable using this technique.

If one or both of these techniques can be implemented to yield ratios $q = U_0/k_B T \geq 4$, the number of trapped atoms expected from the model given in Section 5.3 will exceed 3×10^6 atoms. As discussed in the following chapter, this should provide suitable initial conditions for the successful evaporative cooling of ^{6}Li atoms to temperatures much less than the Fermi temperature.

Chapter 6

Evaporative Cooling in an Optical Trap

Evaporative cooling remains the only means by which dilute, degenerate gases have been produced. Evaporative cooling of a trapped gas proceeds by the preferential removal of energetic atoms from the trap followed by the thermalization of the remaining atoms through elastic collisions. Atoms with an energy exceeding a threshold energy ϵ_t are allowed to escape the confining potential. If ϵ_t is chosen to be greater than the average energy for an atom, the loss of an atom with an energy $\epsilon > \epsilon_t$ reduces the average energy of the atoms that remain in the trap. Since the average energy is reduced, the atoms that remain in the trap thermalize via elastic collisions to a lower temperature. The elastic collisions that permit the thermalization process also produce atoms in the high energy tail of the Boltzmann distribution with energies $\epsilon > \epsilon_t$, thus sustaining the evaporation process. However, as the temperature of the gas cools, the probability that an atom with energy $\epsilon > \epsilon_t$ is produced in an elastic collision is exponentially suppressed by a factor $\exp(-\epsilon_t/k_B T)$. Due to this exponential suppression the evaporation process eventually stagnates and becomes small in comparison to residual loss or heating rates present in the system. In order to force evaporative cooling to continue, the threshold energy is simply lowered as a function of time.

For alkali atoms confined in a magnetic trap, the evaporation threshold ϵ_t is

realized by application of rf radiation of a certain frequency that causes spin-flip transitions to untrapped states for atoms with a specific potential energy. In this case, the trapped atoms are confined in a harmonic potential which is truncated at the threshold energy ϵ_t. The threshold energy ϵ_t can be adjusted simply by changing the frequency of the rf radiation. For atoms confined in an optical trap, the threshold energy ϵ_t is equal to the well depth U_0 of the optical potential. To lower the evaporation threshold energy, one simply needs to lower the power of the trap laser beam. However, since the trap oscillation frequency is proportional to the square root of the well depth, both the well depth and the trap oscillation frequency are adjusted in this case.

In this chapter we apply kinetic theory to model the evaporative cooling of a two-state mixture of fermionic atoms from an optical potential. The evaporative cooling model developed here is an extension to the kinetic theory model developed in Ref. [115]. Ref. [115] treats the evaporative cooling process using a Boltzmann equation under the assumption of sufficient ergodicity (phase-space distribution only a function of energy) and s-wave elastic collisions with an energy-independent cross section. This Boltzmann equation is applied to the problem of evaporative cooling of a single component classical gas from a time-independent truncated harmonic oscillator potential. In this chapter, we extend this kinetic theory model to study evaporative cooling from a *time-dependent gaussian* potential in which the s-wave elastic collisions exhibit an *energy-dependent* cross section. We also include Fermi statistics to examine its effect on the evaporative cooling process for temperatures below the Fermi temperature.

The evaporative cooling model developed in this chapter will be used to analyze the evaporative cooling experiments discussed in Chapter 7. These experiments use

evaporative cooling to verify the existence of a large elastic collision cross section predicted to exist for ultracold ^{6}Li collisions and to increase the phase space density of the ^{6}Li gas by two orders of magnitude over that which is initially loaded into the trap. The model developed in this chapter is also used to examine the feasibility of attaining temperatures below the Fermi temperature by employing evaporative cooling from an optical potential. Although the focus of the chapter concerns the evaporative cooling of fermionic atoms, many of the results are applicable to the evaporative cooling of bosonic atoms from an optical trap. Thus, this work may be of interest to experimentalists attempting to produce Bose condensed cesium atoms in an optical trap.

We begin the chapter with a derivation of the s-wave Boltzmann equation. We first derive the Boltzmann equation for a time-independent gaussian potential and an energy-independent cross section under the assumption of sufficient ergodicity. The resulting integro-differential equation is numerically integrated to study the evolution of the phase space distribution as a function of time. The phase space distribution is found to closely approximate a Boltzmann thermal distribution at temperature T. Starting from high temperature, the temperature of the gas is found to decrease as a function of time until the evaporation process stagnates in the time-independent well depth. The Boltzmann equation for an energy-dependent cross section is then derived assuming a lorentzian dependence to the s-wave cross section, as expected for a potential with a short range compared to λ_{dB}, the thermal de Broglie wavelength. The resulting model will be used to analyze the evaporation of lithium fermions from a time-independent potential studied in Chapter 7 in order to extract the magnitude of the ^{6}Li scattering length. The s-wave Boltzmann equation for a time-dependent gaussian potential is then derived. This model is used for

comparison to experiments in Chapter 7 in which the well depth of the optical trap is adiabatically lowered in order to increase the phase space density. Finally, the effect of Fermi statistics is included and the resulting model is used to examine the feasibility of cooling lithium fermions to temperatures below the Fermi temperature.

6.1 Kinetic Theory of Evaporative Cooling

Evaporative cooling of trapped atoms arises from the thermal escape of energetic atoms from a potential of finite well depth. Binary elastic collisions between the trapped atoms cause the atoms to thermalize and occasionally yield an atom with enough energy for the atom to escape the potential. The escape of energetic atoms causes the average energy of the gas to decrease. The evaporative cooling of atoms confined in a potential of finite depth can be studied using kinetic theory. The trapped gas at time t is described by its phase-space distribution function which evolves according to the Boltzmann equation. The Boltzmann equation takes into account the fact that the atoms evolve in a potential $U(\boldsymbol{r})$ subject to binary elastic collisions. The process of evaporative cooling is modeled by simply evolving the phase space distribution forward in time using the Boltzmann equation under the assumption that atoms with energy $\epsilon > \epsilon_t$ escape the confining potential without suffering a further collision. This assumption is only valid if the gas is in the Knudsen regime where the mean free path exceeds the size of the atomic cloud.

In this treatment, the trapped gas is described by its phase-space distribution function $f(\boldsymbol{r}, \boldsymbol{p}, t)$. The phase-space distribution function is defined such that

$$N(t) = \int \frac{d^3r\, d^3p}{(2\,\pi\,\hbar)^3}\, f(\boldsymbol{r}, \boldsymbol{p}, t) \tag{6.1}$$

where $N(t)$ is the number of atoms confined in the potential at time t. To simplify notation in what follows, the time dependence of $f(\boldsymbol{r},\boldsymbol{p},t)$ will not be indicated explicitly. The evolution of the phase-space distribution function is given by the Boltzmann equation [116]

$$\left(\frac{\partial}{\partial t}+\frac{\boldsymbol{p}}{M}\cdot\nabla_{\boldsymbol{r}}-\nabla_{\boldsymbol{r}}U(\boldsymbol{r})\cdot\nabla_{\boldsymbol{p}}\right)f(\boldsymbol{r},\boldsymbol{p})=\mathcal{I}(\boldsymbol{r},\boldsymbol{p}), \tag{6.2}$$

where $\mathcal{I}(\boldsymbol{r},\boldsymbol{p})$ describes the effect of binary elastic collisions. $\mathcal{I}(\boldsymbol{r},\boldsymbol{p})$ is given by

$$\begin{aligned}\mathcal{I}(\boldsymbol{r},\boldsymbol{p}_4) &= -\frac{1}{2}\sum_{\boldsymbol{p}_1,\boldsymbol{p}_2,\boldsymbol{p}_3} R(\boldsymbol{p}_3\,\boldsymbol{p}_4\rightarrow\boldsymbol{p}_1\,\boldsymbol{p}_2)\,f(\boldsymbol{r},\boldsymbol{p}_3)\,f(\boldsymbol{r},\boldsymbol{p}_4)\\ &\quad+\frac{1}{2}\sum_{\boldsymbol{p}_1,\boldsymbol{p}_2,\boldsymbol{p}_3} R(\boldsymbol{p}_1\,\boldsymbol{p}_2\rightarrow\boldsymbol{p}_3\,\boldsymbol{p}_4)\,f(\boldsymbol{r},\boldsymbol{p}_1)\,f(\boldsymbol{r},\boldsymbol{p}_2),\end{aligned} \tag{6.3}$$

where $R(\boldsymbol{p}_1\,\boldsymbol{p}_2\rightarrow\boldsymbol{p}_3\,\boldsymbol{p}_4)$ gives the rate at which two atoms with initial momenta $\boldsymbol{p}_1$ and $\boldsymbol{p}_2$ scatter into the momentum states $\boldsymbol{p}_3$ and $\boldsymbol{p}_4$. Similarly, $R(\boldsymbol{p}_3\,\boldsymbol{p}_4\rightarrow\boldsymbol{p}_1\,\boldsymbol{p}_2)$ gives the rate at which atoms are scattered out of the momentum states $\boldsymbol{p}_3$ and $\boldsymbol{p}_4$ into the momentum states $\boldsymbol{p}_1$ and $\boldsymbol{p}_2$. The factors of $\frac{1}{2}$ ensure that identical processes are not double counted.

6.1.1 *S*-Wave Boltzmann Equation

Since we are considering ultracold atomic collisions, we will only consider s-wave interactions. Since binary s-wave interactions are time reversal invariant, $R(\boldsymbol{p}_3\,\boldsymbol{p}_4\rightarrow\boldsymbol{p}_1\,\boldsymbol{p}_2)=R(\boldsymbol{p}_1\,\boldsymbol{p}_2\rightarrow\boldsymbol{p}_3\,\boldsymbol{p}_4)$. Fermi's Golden rule gives the rate at which atoms are scattered from the initial two particle state $|i\rangle$ into the final two particle state $|f\rangle$

$$R(\boldsymbol{p}_3\,\boldsymbol{p}_4\rightarrow\boldsymbol{p}_1\,\boldsymbol{p}_2)=R(\boldsymbol{p}_1\,\boldsymbol{p}_2\rightarrow\boldsymbol{p}_3\,\boldsymbol{p}_4)=\frac{2\,\pi}{\hbar}\left|\langle f|H'|i\rangle\right|^2\,\delta(E_f-E_i). \tag{6.4}$$

In Chapter 2, we found that for the ultracold collisions being considered, the interatomic interaction can be approximated by the contact potential

$$H' = \frac{4\,\pi\,\hbar^2\,a}{M}\,\delta(\boldsymbol{x}_1 - \boldsymbol{x}_2), \tag{6.5}$$

where a is the s-wave scattering length. To calculate the scattering rate, we use box normalized, two-particle initial and final states which are spatially symmetric since we are considering s-wave collisions

$$\psi_i(\boldsymbol{x}_1, \boldsymbol{x}_2) = \frac{1}{\sqrt{2}}\left(\frac{e^{i\boldsymbol{p}_1\cdot\boldsymbol{x}_1/\hbar}}{\sqrt{V}}\,\frac{e^{i\boldsymbol{p}_2\cdot\boldsymbol{x}_2/\hbar}}{\sqrt{V}} + \frac{e^{i\boldsymbol{p}_1\cdot\boldsymbol{x}_2/\hbar}}{\sqrt{V}}\,\frac{e^{i\boldsymbol{p}_2\cdot\boldsymbol{x}_1/\hbar}}{\sqrt{V}}\right) \tag{6.6}$$

$$\psi_f(\boldsymbol{x}_1, \boldsymbol{x}_2) = \frac{1}{\sqrt{2}}\left(\frac{e^{i\boldsymbol{p}_3\cdot\boldsymbol{x}_1/\hbar}}{\sqrt{V}}\,\frac{e^{i\boldsymbol{p}_4\cdot\boldsymbol{x}_2/\hbar}}{\sqrt{V}} + \frac{e^{i\boldsymbol{p}_3\cdot\boldsymbol{x}_2/\hbar}}{\sqrt{V}}\,\frac{e^{i\boldsymbol{p}_4\cdot\boldsymbol{x}_1/\hbar}}{\sqrt{V}}\right), \tag{6.7}$$

where V is the box normalization volume. Using these states gives the matrix element

$$H'_{fi} = \frac{8\,\pi\,\hbar^2\,a}{M\,V}\,\delta_k(\boldsymbol{p}_1 + \boldsymbol{p}_2 - \boldsymbol{p}_3 - \boldsymbol{p}_4), \tag{6.8}$$

where δ_k is a Kronecker delta function since the momentum states are discrete. Inserting this result into (6.4) yields the transition rate

$$\begin{aligned} R(\boldsymbol{p}_1\,\boldsymbol{p}_2 \to \boldsymbol{p}_3\,\boldsymbol{p}_4) &= \frac{2\,\pi}{\hbar}\left(\frac{8\,\pi\,\hbar^2\,a}{M\,V}\right)^2 \delta_k(\boldsymbol{p}_1 + \boldsymbol{p}_2 - \boldsymbol{p}_3 - \boldsymbol{p}_4) \\ &\quad \times \delta\left(\frac{p_1^2}{2\,M} + \frac{p_2^2}{2\,M} - \frac{p_3^2}{2\,M} - \frac{p_4^2}{2\,M}\right). \end{aligned} \tag{6.9}$$

Note that the $\delta_k^2 = \delta_k$ since this is a Kronecker delta function.

Eq. (6.9) can be substituted into (6.3) to give $\mathcal{I}(\boldsymbol{r}, \boldsymbol{p})$. At this point the summation over discrete momentum states $\boldsymbol{p}_1$, $\boldsymbol{p}_2$ and $\boldsymbol{p}_2$ can be converted to inte-

grals over continuous momentum variables following the prescription $\sum_{\boldsymbol{p}_1\,\boldsymbol{p}_2\,\boldsymbol{p}_3} \rightarrow (V/(2\,\pi\,\hbar)^3)^3 \int d^3\boldsymbol{p}_1\,d^3\boldsymbol{p}_2\,d^3\boldsymbol{p}_3$. The Kronecker delta function is converted to a Dirac delta function $V/(2\,\pi\,\hbar)^3\,\delta^3_k(\boldsymbol{p}_1+\boldsymbol{p}_2-\boldsymbol{p}_3-\boldsymbol{p}_4) = \delta^3(\boldsymbol{p}_1+\boldsymbol{p}_2-\boldsymbol{p}_3-\boldsymbol{p}_4)$. The resulting equation for the collision integral is

$$\begin{aligned}\mathcal{I}(\boldsymbol{r},\boldsymbol{p}_4) &= \frac{\sigma}{4\,\pi^4\,M\,\hbar^3}\int d^3p_1\,d^3p_2\,d^3p_3\,\delta(\boldsymbol{p}_1+\boldsymbol{p}_2-\boldsymbol{p}_3-\boldsymbol{p}_4)\,\delta(p_1^2+p_2^2-p_3^2-p_4^2)\\ &\quad\times\left[f(\boldsymbol{r},\boldsymbol{p}_1)\,f(\boldsymbol{r},\boldsymbol{p}_2)-f(\boldsymbol{r},\boldsymbol{p}_3)\,f(\boldsymbol{r},\boldsymbol{p}_4)\right],\end{aligned} \tag{6.10}$$

where $\sigma = 8\,\pi\,a^2$ is the total s-wave cross section.

6.1.2 Boltzmann Equation in the Ergodic Approximation

The Boltzmann equation can be greatly simplified by assuming that the motion of the trapped atoms is sufficiently ergodic that the phase-space distribution of particles is a function only of the single-particle energy ϵ. If this is the case

$$f(\boldsymbol{r},\boldsymbol{p}) = \int d\epsilon\,f(\epsilon)\,\delta\left(\epsilon - U(\boldsymbol{r}) - \frac{p^2}{2\,M}\right). \tag{6.11}$$

The function $f(\epsilon)$ is the occupation number for trap eigenstates with energy ϵ. The number of atoms with energy between ϵ and $\epsilon + d\epsilon$ is given by $f(\epsilon)\,\mathcal{D}(\epsilon)\,d\epsilon$ where $\mathcal{D}(\epsilon)$ is the density of states for the gaussian potential given by (6.30). Note that $f(\epsilon)\,\mathcal{D}(\epsilon) = (2\,\pi\,\hbar)^{-3}\int d^3r\,d^3p\,\delta\left(\epsilon - U(\boldsymbol{r}) - \boldsymbol{p}^2/2\,M\right)\,f(\boldsymbol{r},\boldsymbol{p})$.

The Boltzmann equation (6.2) is greatly simplified if the phase-space distribution $f(\boldsymbol{r},\boldsymbol{p})$ is only a function of energy, i.e. $f(\boldsymbol{r},\boldsymbol{p}) = f(\mathcal{H}(\boldsymbol{r},\boldsymbol{p}))$ where $\mathcal{H}(\boldsymbol{r},\boldsymbol{p})$ is the single-particle Hamiltonian. We apply to both sides of (6.2) the operation $(2\,\pi\,\hbar)^{-3}\int d^3r\,d^3p\;\delta\left(U(\boldsymbol{r}) + \frac{p^2}{2\,M} - \epsilon\right)$. Application to the left hand side of (6.2)

yields

$$\int \frac{d^3r\, d^3p}{(2\,\pi\,\hbar)^3}\,\delta\left(\epsilon - U - \frac{p^2}{2\,M}\right)\,\left(\frac{\partial}{\partial t} + \frac{\boldsymbol{p}}{M}\cdot\nabla_{\boldsymbol{r}} - \nabla_{\boldsymbol{r}}\,U\cdot\nabla_{\boldsymbol{p}}\right) f(\boldsymbol{r},\boldsymbol{p}) \tag{6.12}$$

The gradient terms sum to zero since

$$\left(\frac{\boldsymbol{p}}{M}\cdot\nabla_{\boldsymbol{r}} - \nabla_{\boldsymbol{r}}\,U\cdot\nabla_{\boldsymbol{p}}\right)\,f(\mathcal{H}(\boldsymbol{r},\boldsymbol{p}),t) = \frac{\partial f}{\partial \mathcal{H}}\overbrace{\left(\frac{\boldsymbol{p}}{M}\cdot\nabla_{\boldsymbol{r}}\,U - \nabla_{\boldsymbol{r}}\,U\cdot\frac{\boldsymbol{p}}{M}\right)}^{=0} \tag{6.13}$$

where the single-particle Hamiltonian $\mathcal{H}(\boldsymbol{r},\boldsymbol{p}) = U(\boldsymbol{r}) + p^2/2\,M$. Thus, only the time derivative term $\mathcal{D}(\epsilon)\,(\partial f(\epsilon)/\partial t)$ remains on the left hand side.

Applying $(2\pi\,\hbar)^{-3}\int d^3r\,d^3p_4\,\delta\Big(U(\boldsymbol{r}) + \frac{p_4^2}{2\,M} - \epsilon_4\Big)$ to the collision integral $\mathcal{I}(\boldsymbol{r},\boldsymbol{p}_4)$ and substituting (6.11) in for each function $f(\boldsymbol{r},\boldsymbol{p}_i)$ yields

$$\frac{\partial f(\epsilon_4)}{\partial t}\,\mathcal{D}(\epsilon_4) = \frac{\sigma}{(2\pi\,\hbar)^3\,4\pi^4\,M\hbar^3}\int d\epsilon_1\,d\epsilon_2\,d\epsilon_3\,h(\epsilon_1\,\epsilon_2\,\epsilon_3\,\epsilon_4)\,[f(\epsilon_1)\,f(\epsilon_2) - f(\epsilon_3)\,f(\epsilon_4)], \tag{6.14}$$

where the function

$$\begin{aligned} h(\epsilon_1\,\epsilon_2\,\epsilon_3\,\epsilon_4) \;\equiv\; & \int d^3r\,d^3p_1\,d^3p_2\,d^3p_3\,d^3p_4\,\delta^3(\boldsymbol{p}_1+\boldsymbol{p}_2-\boldsymbol{p}_3-\boldsymbol{p}_4) \\ & \times\delta(p_1^2+p_2^2-p_3^2-p_1^2)\,\prod_{i=1}^{4}\,\delta\left(\epsilon_i - U(\boldsymbol{r}) - \frac{p_i^2}{2\,M}\right). \end{aligned} \tag{6.15}$$

To obtain this result we have made use of the identity $\int d\epsilon_i\,\delta\,(\epsilon_i - U(\boldsymbol{r}) - p_i^2/2\,M) = 1$.

The function $h(\epsilon_1\,\epsilon_2\,\epsilon_3\,\epsilon_4)$ can be simplified further. The δ function product $\prod_{i=1}^{4}\delta\,(\epsilon_i - U(\boldsymbol{r}) - p_i^2/2\,M)$ is zero unless $U(\boldsymbol{r}) \le \epsilon_{\min} \equiv \min(\epsilon_1,\epsilon_2,\epsilon_3,\epsilon_4)$ which limits the spatial integral to those values of $\boldsymbol{r}$ for which $U(\boldsymbol{r}) \le \epsilon_{\min}$. To sim-

plify (6.15) further we change the integration variables to center of mass and relative momenta coordinates defined as $\boldsymbol{P} = \boldsymbol{p}_1 + \boldsymbol{p}_2$, $\boldsymbol{q} = (\boldsymbol{p}_1 - \boldsymbol{p}_2)/2$, $\boldsymbol{P}' = \boldsymbol{p}_3 + \boldsymbol{p}_4$ and $\boldsymbol{q}' = (\boldsymbol{p}_3 - \boldsymbol{p}_4)/2$. $\boldsymbol{P}$ and $\boldsymbol{P}'$ are the center of mass momenta before and after the collision respectively. Similarly $\boldsymbol{q}$ and $\boldsymbol{q}'$ are the relative momenta before and after the collision. The momentum conserving delta function $\delta^3\left(\boldsymbol{p}_1 + \boldsymbol{p}_2 - \boldsymbol{p}_3 - \boldsymbol{p}_4\right) = \delta^3\left(\boldsymbol{P} - \boldsymbol{P}'\right)$ ensures that the center of mass momentum is conserved. The energy conserving delta function $\delta\left(p_1^2 + p_2^2 - p_3^2 - p_4^2\right) = \frac{1}{2}\,\delta\left(q^2 - q'^2\right)$ where we have used the fact that $\boldsymbol{P} = \boldsymbol{P}'$. Upon making these substitutions we find that

$$\begin{aligned} h(\epsilon_1\,\epsilon_2\,\epsilon_3\,\epsilon_4) \;&=\; \frac{1}{2}\int\limits_{U\le\epsilon_{\min}} d^3r \int d^3P\, d^3q\, d^3q'\, \delta\left(q^2 - q'^2\right)\,\Theta\left(P_{\max} - P\right)\,\Theta\left(P - P_{\min}\right) \\ &\quad\times \prod_{i=1}^{4}\,\delta\left(\epsilon_i - U(\boldsymbol{r}) - \frac{p_i^2}{2\,M}\right), \end{aligned} \tag{6.16}$$

where we have integrated over the center-of-mass momentum conserving δ-function. The fact that energy and momentum are conserved in the collision restricts the range of integration over P to values between $P_{\min}$ and $P_{\max}$ as indicated by the unit step functions Θ. Assuming that $\epsilon_{\min} = \epsilon_1$ and thus $p_1 = \min(p_1, p_2, p_3, p_4)$ one can show using energy and momentum conservation that the maximum possible value of P is given by $P_{\max} = p_1 + p_2$ and the minimum possible value of P is given by $P_{\min} = p_2 - p_1$. Due to the symmetry of (6.15) with respect to p_1, p_2, p_3 and p_4, the assumption that $p_1 = \min(p_1, p_2, p_3, p_4)$ is completely general.

To evaluate the momentum integrals in (6.16), the single particle momenta can be expressed in terms of the center of mass and relative momenta as $p_{1,2}^2 = P^2/4 + q^2 \pm P\,q\,u$ and $p_{3,4}^2 = P^2/4 + q^2 \pm P\,q\,u'$ where $u(u')$ is the cosine of the angle between $\boldsymbol{P}$ and $\boldsymbol{q}(\boldsymbol{q}')$ and we have used the fact that $P = P'$ and $q = q'$. Since the angular dependence only arises through the dependence on u and u' we may integrate over

the remaining azimuthal dependence to give

$$h(\epsilon_1\,\epsilon_2\,\epsilon_3\,\epsilon_4) = 4\pi^3 \int\limits_{U\leq\,\epsilon_{\rm min}} d^3r \int_{P_{\rm min}}^{P_{\rm max}} dP\,P^2 \int dq\,q^3\,du\,du' \prod_{i=1}^{4} \delta\left(U(\boldsymbol{r}) + \frac{p_i^2}{2M} - \epsilon_i\right). \tag{6.17}$$

where we have also integrated over the energy conserving δ-function. The integrations over u and u' may be performed to give

$$\begin{aligned} h(\epsilon_1\,\epsilon_2\,\epsilon_3\,\epsilon_4) &= 2\,(2\pi)^3\,M^2 \int\limits_{U\leq\,\epsilon_{\rm min}} d^3r \int_{P_{\rm min}}^{P_{\rm max}} dP \int dq\,q\,\delta\left(\epsilon_1+\epsilon_2 - \frac{P^2}{4M} - \frac{q^2}{M} - 2U\right) \\ &\quad \times \delta\left(\epsilon_3+\epsilon_4 - \frac{P^2}{4M} - \frac{q^2}{M} - 2U\right) \end{aligned} \tag{6.18}$$

Finally, integration over q gives

$$h(\epsilon_1\,\epsilon_2\,\epsilon_3\,\epsilon_4) = (2\pi)^3 M^3\,\delta(\epsilon_1+\epsilon_2-\epsilon_3-\epsilon_4) \int\limits_{U\leq\,\epsilon_{\rm min}} d^3r \int_{P_{\rm min}(\boldsymbol{r})}^{P_{\rm max}(\boldsymbol{r})} dP. \tag{6.19}$$

Again, without loss of generality, we may assume $\epsilon_1 = \epsilon_{\rm min}$ in which case $p_1 = p_{min} = \sqrt{2\,M\,(\epsilon_{min} - U(\boldsymbol{r}))}$ and $p_2 = \sqrt{2\,M\,(\epsilon - \epsilon_{min} - U(\boldsymbol{r}))}$. As mentioned above $P_{min} = p_2 - p_1$ and $P_{max} = p_1 + p_2$. The integral over P gives $P_{max} - P_{min} = 2\,p_1 = 2\,\sqrt{2\,M\,(\epsilon_{min} - U(\boldsymbol{r}))}$. The remaining integral over $\boldsymbol{r}$ can be expressed as

$$\begin{aligned} \int\limits_{U\leq\,\epsilon_{\rm min}} d^3r \int_{P_{\rm min}(\boldsymbol{r})}^{P_{\rm max}(\boldsymbol{r})} dP &= \frac{(2\,\pi\,\hbar)^3}{2\,\pi\,M} \left[\frac{2\,\pi\,(2\,M)^{3/2}}{(2\,\pi\,\hbar)^3} \int\limits_{U\leq\,\epsilon_{min}} d^3r\,\sqrt{\epsilon_{\rm min} - U(\boldsymbol{r})}\right] \\ &= \frac{(2\,\pi\,\hbar)^3}{2\,\pi\,M}\,\mathcal{D}(\epsilon_{min}), \end{aligned} \tag{6.20}$$

where, upon comparison with (6.29) below, the term appearing inside the square

brackets is identified as $\mathcal{D}(\epsilon_{\min})$. Inserting this result into (6.19) gives

$$h(\epsilon_1\,\epsilon_2\,\epsilon_3\,\epsilon_4) = (2\pi)^2\,M^2\,(2\pi\,\hbar)^3\,\delta(\epsilon_1+\epsilon_2-\epsilon_3-\epsilon_4)\,\mathcal{D}(\epsilon_{\min}). \tag{6.21}$$

Finally, Eq. (6.14) and Eq. (6.15) can be combined to yield the Boltzmann equation in the ergodic approximation

$$\begin{aligned}\mathcal{D}(\epsilon_4)\,\frac{\partial f(\epsilon_4)}{\partial t} &= \frac{M\,\sigma}{\pi^2\,\hbar^3}\int d\epsilon_1\,d\epsilon_2\,d\epsilon_3\,\delta(\epsilon_1+\epsilon_2-\epsilon_3-\epsilon_4)\,\mathcal{D}(\epsilon_{min}) \\ &\quad\times[f(\epsilon_1)\,f(\epsilon_2)-f(\epsilon_3)\,f(\epsilon_4)]\end{aligned} \tag{6.22}$$

which is the primary result of this section.

6.1.3 Coupled Boltzmann Equation for a Two-Component Fermi Gas

In order to observe evaporative cooling in an ultracold Fermi gas, fermions in at least two different spin states must be confined in the trap so that s-wave collisions can occur. A two-component Fermi gas must be described by two different phase space distribution functions $f_1(\epsilon)$ and $f_2(\epsilon)$ defined such that

$$N_1 = \int \frac{d^3r\,d^3p}{(2\pi\,\hbar)^3}\,f_1(\boldsymbol{r},\boldsymbol{p}) \tag{6.23}$$

$$N_2 = \int \frac{d^3r\,d^3p}{(2\pi\,\hbar)^3}\,f_2(\boldsymbol{r},\boldsymbol{p}) \tag{6.24}$$

where N_1 and N_2 are the total number of trapped atoms in state 1 and 2 respectively. Each of these phase space distribution functions evolve according to a separate Boltzmann equation. However, since only collisions between atoms in different

states can occur, the collision integral in the two Boltzmann equations cause the equations to be coupled. In a derivation identical to that given in the previous section, the coupled Boltzmann equation under the assumption of sufficient ergodicity are

$$\begin{aligned}
\mathcal{D}(\epsilon_4)\,\frac{\partial f_1(\epsilon_4)}{\partial t} &= \frac{M\,\sigma}{\pi^2\,\hbar^3}\int d\epsilon_1\,d\epsilon_2\,d\epsilon_3\,\delta(\epsilon_1+\epsilon_2-\epsilon_3-\epsilon_4)\,\mathcal{D}(\epsilon_{min}) \\
&\quad\times\left[f_1(\epsilon_1)\,f_2(\epsilon_2)-f_2(\epsilon_3)\,f_1(\epsilon_4)\right] \qquad (6.25)\\
\mathcal{D}(\epsilon_4)\,\frac{\partial f_2(\epsilon_4)}{\partial t} &= \frac{M\,\sigma}{\pi^2\,\hbar^3}\int d\epsilon_1\,d\epsilon_2\,d\epsilon_3\,\delta(\epsilon_1+\epsilon_2-\epsilon_3-\epsilon_4)\,\mathcal{D}(\epsilon_{min}) \\
&\quad\times\left[f_1(\epsilon_1)\,f_2(\epsilon_2)-f_1(\epsilon_3)\,f_2(\epsilon_4)\right], \qquad (6.26)
\end{aligned}$$

where $N_1 = \int_0^{U_0} d\epsilon\,\mathcal{D}(\epsilon)\,f_1(\epsilon)$ and $N_2 = \int_0^{U_0} d\epsilon\,\mathcal{D}(\epsilon)\,f_2(\epsilon)$. For a collision between an atom in spin state 1 and an atom in spin state 2, the antisymmetric spin state required for s-wave scattering occurs with a probability of 1/2. Thus, the effective cross section used in (6.25) and (6.26) is $\sigma = 4\pi a^2$ which is reduced by a factor of 2 from the total cross section for atoms in a symmetric spatial state.

If a 50/50 population exists in states 1 and 2, the coupled equations (6.25) and (6.26) are perfectly symmetric. In this case, we expect the phase space distribution functions $f_1(\epsilon)$ and $f_2(\epsilon)$ to be identical. Thus, we may replace $f_1(\epsilon)$ and $f_2(\epsilon)$ with $f(\epsilon) \equiv f_1(\epsilon) = f_2(\epsilon)$ in Eqs. (6.25) and (6.26). With this replacement these equations are made identical to one another and to (6.22). Thus, we conclude that to model the evaporation of a 50/50 mixture of fermions in states 1 and 2, the evolution of the phase space distribution corresponding to each state is governed by (6.22) where $\sigma = 4\pi a^2$ is the effective cross section and $N = \int d\epsilon\,\mathcal{D}(\epsilon)\,f(\epsilon)$ is the number of atoms per state.

6.1.4 Optical Trapping Potential

In this chapter we consider the evaporation of atoms from an optical trap. In Section 3.1, we found that the potential for a focused gaussian laser beam is given by the product of a gaussian potential in the radial direction with a lorentzian dependence in the axial direction. In order to make the calculations tractable in this chapter, we will approximate the lorentzian axial dependence on z with a gaussian. Thus we will consider a potential of the form

$$U(\boldsymbol{r}) = U_0 \left(1 - \exp\left[-\frac{x^2}{a^2} - \frac{y^2}{b^2} - \frac{z^2}{c^2}\right]\right) \tag{6.27}$$

where U_0 is the potential well depth and a, b and c are the $1/e$ radii of the laser intensity distribution in the $x-$, $y-$ and $z-$directions respectively. Note that we have defined the potential here so that the zero of energy is reference to the bottom of the well.

The well depth U_0 is proportional to the peak laser intensity I_0. Thus, by lowering the laser power, the well depth U_0 of the potential can be reduced. In Section 6.3, a time-dependent potential will be considered for which the well depth $U_0(t)$ is a function of time.

Atoms with an energy $\epsilon << U_0$ are confined near the bottom of the gaussian potential where the potential is nearly harmonic. For $x << a$, $y << b$ and $z << c$, the potential is approximately given by $U(\boldsymbol{r}) \simeq U_{ho}(\boldsymbol{r}) = \frac{1}{2} M(\omega_x^2 x^2 + \omega_y^2 y^2 + \omega_z^2 z^2)$ where M is the mass of the atom and $\omega_x = \sqrt{2\,U_0/(M\,a^2)}$, $\omega_y = \sqrt{2\,U_0/(M\,b^2)}$ and $\omega_z = \sqrt{2\,U_0/(M\,c^2)}$.

For the parameters considered in this dissertation the temperature $T >> \hbar\omega_{x,y,z}$. In this case, it is useful to consider the discrete states of the gaussian potential as

a continuum of states with a density of states $\mathcal{D}(\epsilon)$ where $\mathcal{D}(\epsilon)\,d\epsilon$ is the number of states with energy between ϵ and $\epsilon + d\epsilon$. The density of states is thus given by

$$\mathcal{D}(\epsilon)\,d\epsilon = \frac{d\epsilon}{(2\,\pi\,\hbar)^3}\int d^3r\,d^3p\,\delta\left(\epsilon - \frac{p^2}{2\,M} - U(\boldsymbol{r})\right). \tag{6.28}$$

Evaluation of the momentum integral gives

$$\mathcal{D}(\epsilon) = \frac{2\,\pi\,(2\,M)^{3/2}}{(2\,\pi\,\hbar)^3}\int\limits_{U\leq\,\epsilon} d^3r\,\sqrt{\epsilon - U(\boldsymbol{r})}, \tag{6.29}$$

where the spatial integral is evaluated over those values of $\boldsymbol{r}$ for which $U(\boldsymbol{r}) \leq \epsilon$. For the gaussian potential (6.27) the spatial integral can be evaluated to give the density of states for the gaussian potential

$$\mathcal{D}(\epsilon) = \mathcal{D}_{ho}(\epsilon)\,g_1(\epsilon), \tag{6.30}$$

where $\mathcal{D}_{ho}(\epsilon) = \epsilon^2/(2\,\hbar\omega_x\,\hbar\omega_y\,\hbar\omega_z)$ is the density of states for the harmonic oscillator potential $U_{ho}(\boldsymbol{r})$ and

$$g_1(\epsilon) = \frac{\alpha^{3/2}\,(1-\beta)^{1/2}}{\beta^2}\,\frac{16}{\pi}\int_0^1 du\,u^2\,\sqrt{e^{\alpha\,(1-u^2)} - 1}. \tag{6.31}$$

Here, we have defined $\beta \equiv \frac{\epsilon}{U_0}$ and $\alpha \equiv -\ln(1-\beta)$. The density of states for the gaussian potential will be required when we evaluate the s-wave Boltzmann equation in the following sections.

6.1.5 Numerical Solution of Kinetic Equation

In order to model evaporative cooling of atoms from an optical potential of fixed depth, we must numerically integrate the Boltzmann equation (6.22) using the density of states for a gaussian potential obtained in Section 6.1.4. To numerically integrate (6.22), we discretize the energy scale between zero and U_0 into n equally sized bins. The energy of the ith bin ($i = 1, \ldots, n$) is given by $\epsilon_i = (i - 1/2)\Delta\epsilon$ where $\Delta\epsilon = U_0/n$. Using the notation $\mathcal{D}(\epsilon_i) = \mathcal{D}_i$ and $f(\epsilon_i) = f_i$, the discretized Boltzmann equation is

$$\mathcal{D}_i \, \dot{f}_i = \frac{M \, \sigma}{\pi^2 \, \hbar^3} \, (\Delta\epsilon)^2 \sum_{k,l} \mathcal{D}_h \left[f_k \, f_l - f_i \, f_j \right], \tag{6.32}$$

where $j = k + l - i$ due to the energy conserving δ-function and $h = \min(i, j, k, l)$. Eq. (6.32) can be numerically integrated forward in time either using an Euler method or using a fourth order Runge-Kutta routine with adaptive step-size control [111].

In order to model the evaporation of energetic atoms, we assume that atoms with an energy $\epsilon > U_0$ escape the trap. Thus, we assume that $f_i = 0$ for $i > n$ in numerically integrating (6.32). However, note that the sum over k and l extend to $2n$ since a collision between two atoms for which $i = n$ and $j = n$ can yield an atom at energy $k = 2n$ or $l = 2n$.

Figure 6.1 shows the phase space distribution $f(\epsilon)$ at several times during numerical integration of (6.32). Each curve is labeled at the right by the total number of collisions per atom. Initially, the function $f(\epsilon) = f_0$. This represents a distribution at infinite temperature relative to the well depth since all of the energy states are filled with equal probability. As $f(\epsilon)$ evolves forward in time,

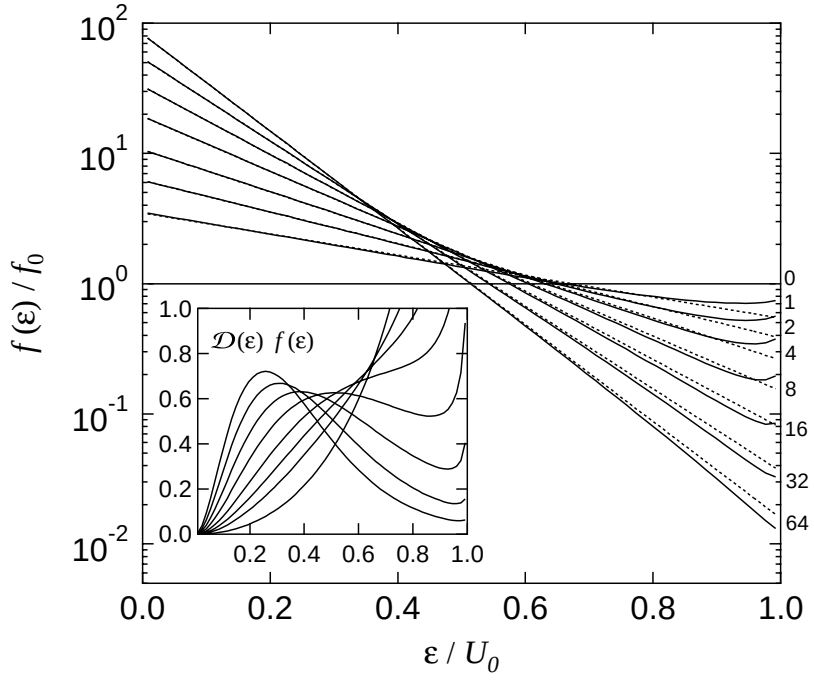

Figure 6.1: Evolution of the phase space distribution function $f(\epsilon)$ in a gaussian well of fixed depth. The main figure plots $f(\epsilon)$ at different times starting from a distribution at infinite temperature. Each curve is labeled at the right by the total number of collisions per atom which have occurred. The inset shows the corresponding plots of the number distribution function $n(\epsilon) = \mathcal{D}(\epsilon)\, f(\epsilon)$.

the distribution is well approximated at each time by a Boltzmann distribution $\exp(-\epsilon/k_B T)$. Both the calculated distribution (solid) and the best-fit Boltzmann distribution (dashed) are shown in Figure 6.1. As time evolves, the best-fit value for T decreases. The inset of Figure 6.1 shows $\mathcal{D}(\epsilon)\, f(\epsilon)$ corresponding to each $f(\epsilon)$ distribution shown in the main figure. $\mathcal{D}(\epsilon)\, f(\epsilon)\, d\epsilon$ gives the number of atoms between ϵ and $\epsilon + d\epsilon$. The distributions shown in Figure 6.1 were obtained using $n = 64$.

Figure 6.2 shows the temperature and number of trapped atoms as a function of time. The temperature T of the trapped atoms is given relative to the well depth U_0 and the number of atoms N is normalized by the initial number of trapped atoms N_0. The time scale is given in units of t_0 which is nominally the inverse of the initial collision rate for atoms of energy U_0, i.e. $1/t_0 \equiv (N_0/V_{\mathrm{FORT}})\sqrt{2\,U_0/M}\,\sigma$ where $V_{\mathrm{FORT}} = \pi^{3/2}\, a\, b\, c$ is the volume of the optical trap. Note that the temperature and number rapidly fall until the temperature reaches a value of approximately 1/10 of the trap depth at which point the evaporation process stagnates. As we will see in the following section, the evaporation rate stagnates due to an exponential suppression in the probability that an atom with energy $\epsilon > U_0$ is produced in an elastic collision. For evaporation from a well of fixed depth, the evaporation rate will eventually become so small that residual heating and loss rates will dominate. In order to increase the phase space density further, the well depth U_0 must be lowered as a function of time. In Section 6.3, we will study the Boltzmann equation for a time-dependent potential.

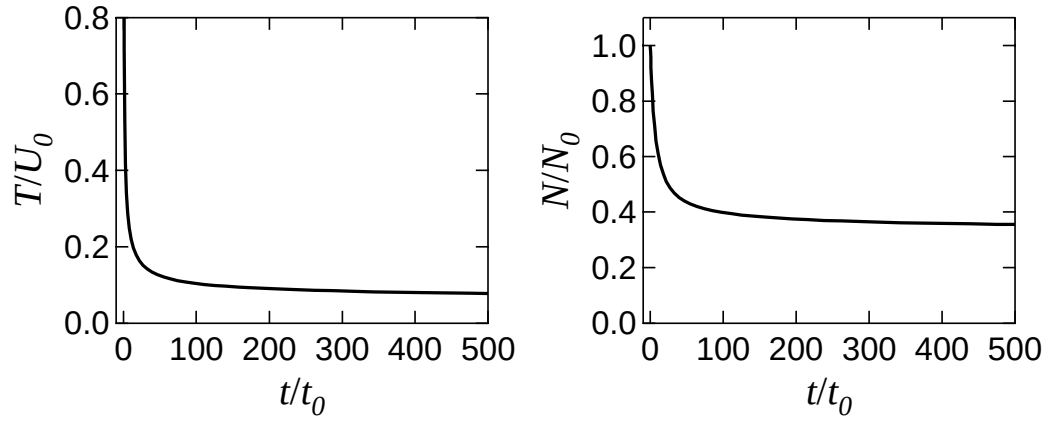

Figure 6.2: Evolution of the temperature T and number N in an optical potential as a function of time t.

6.1.6 Equations of Motion for Temperature and Number

In the previous section, we found that the phase space distribution function $f(\epsilon)$ is well approximated by a Boltzmann distribution function truncated at the well depth. If we make the assumption that $f(\epsilon) \propto \exp(-\epsilon/k_B T)$, we can find simple expressions for quantities of interest such as the loss rate of atoms and energy from the gas. Using this assumption we can also find first order differential equations of motion for the variables T and N which parameterize the state of the gas. Numerical integration of these simple equations of motion yield results in good agreement with integration of the Boltzmann equation.

In this section we will assume that $f(\epsilon)$ takes the form

$$f(\epsilon) = \rho_0 \, e^{\epsilon/k_B T} \, \Theta(U_0 - \epsilon), \tag{6.33}$$

where $\Theta(x)$ is the Heaviside step function and ρ_0 is the occupation number of the ground state of the potential (i.e. the peak phase space density). ρ_0 can be written

as $\rho_0 = n_0 \lambda_{dB}^3$ where n_0 is the peak spatial density in the limit $U_0 >> k_B T$ and $\lambda_{dB} = \sqrt{2\pi \hbar^2 / M k_B T}$ is the thermal de Broglie wavelength. Thus, as the gas approaches the degenerate regime, the occupation number of the ground state will approach unity and the average interparticle spacing at the center of the trap will be comparable to the thermal de Broglie wavelength. Note that, strictly speaking, T cannot be interpreted as the thermodynamic temperature of the system since the truncated Boltzmann distribution is an essentially nonequilibrium distribution. The equilibrium state of the system has zero atoms in the trap since, given an infinite amount of time, all of the atoms will evaporate out of the trap. However, the temperature T and the number of atoms N given by $N = \int_0^{U_0} d\epsilon \, \mathcal{D}(\epsilon) \, f(\epsilon)$ parameterize the distribution function $f(\epsilon)$ and $\rho_0 = n_0 \lambda_{dB}^3$ is a proper measure of the occupation number of the ground state.

Since the total number of atoms is conserved, the loss rate of atoms from the trap due to evaporation is given by

$$\dot{N}_{\rm ev} = - \int_{U_0}^{\infty} d\epsilon_4 \, \mathcal{D}(\epsilon_4) \, \dot{f}(\epsilon_4), \tag{6.34}$$

which gives the rate at which atoms are scattered into states with energy $\epsilon_4 > U_0$. The quantity $\mathcal{D}(\epsilon_4) \, \dot{f}(\epsilon_4)$ is obtained from the Boltzmann equation (Eq. (6.22)) which yields

$$\dot{N}_{\rm ev} = - \frac{M \sigma}{\pi^2 \hbar^3} \int d\epsilon_1 \, d\epsilon_2 \, d\epsilon_3 \, \mathcal{D}(\epsilon_3) \, f(\epsilon_1) \, f(\epsilon_2) \, \Theta(\epsilon_1 + \epsilon_2 - \epsilon_3 - U_0), \tag{6.35}$$

where we have used the fact that ϵ_3 must be the minimum energy since $\epsilon_4 > U_0$ and we have integrated over the energy conserving δ-function. The term containing $f(\epsilon_4)$ in the Boltzmann equation does not appear due to the presence of the Heaviside

step function in (6.33) and the fact that we are integrating over values of $\epsilon_4 > U_0$. Using (6.33) for $f(\epsilon_1)$ and $f(\epsilon_2)$ the integrals are easily performed to yield

$$\dot{N}_{\rm ev} = -n_0^2\,\sigma\,\bar{v}\,e^{-\eta}\,V_{\rm ev}, \tag{6.36}$$

where $\eta \equiv U_0/k_BT$, $\bar{v} = \sqrt{8k_BT/\pi M}$ and

$$V_{\rm ev} \equiv \frac{\lambda_{dB}^3}{k_BT}\int_0^{U_0} d\epsilon\,\mathcal{D}(\epsilon)\,\left[(U_0-\epsilon-k_BT)e^{-\epsilon/k_BT}+k_BT\,e^{-\eta}\right]. \tag{6.37}$$

The factor $\exp(-\eta)$ appearing in (6.36) indicates that the evaporation rate becomes exponentially suppressed as $\eta = U_0/k_BT$ becomes large. Thus, as the atoms cool the evaporation process eventually stagnates.

The evaporated atoms carry away an energy $\epsilon_4 > U_0$ from the trap which causes the average energy of the atoms that remain in the trap to decrease. The energy loss rate is given by

$$\dot{E}_{\rm ev} = -\int_{U_0}^{\infty} d\epsilon_4\,\epsilon_4\,\mathcal{D}(\epsilon_4)\,\dot{f}(\epsilon_4). \tag{6.38}$$

Using the Boltzmann equation (6.22) to give $\mathcal{D}(\epsilon_4)\,\dot{f}(\epsilon_4)$ and the assumption that $f(\epsilon)$ is given by a truncated Boltzmann distribution (6.33) we find that

$$\dot{E}_{\rm ev} = \dot{N}_{\rm ev}\,\left\{U_0 + \frac{W_{\rm ev}}{V_{\rm ev}}\,k_BT\right\} \tag{6.39}$$

where $W_{\rm ev} = V_{\rm ev} - X_{\rm ev}$ and

$$X_{\rm ev} = \frac{\lambda_{dB}^3}{k_BT}\int_0^{U_0} d\epsilon\,\mathcal{D}(\epsilon)\,\left[k_BTe^{\epsilon/k_BT}-(U_0-\epsilon+k_BT)e^{-\eta}\right]. \tag{6.40}$$

Evaluation of $W_{\rm ev}/V_{\rm ev}$ for a gaussian potential by numerical integration shows that $W_{\rm ev}/V_{\rm ev} < 1$. Thus, the average energy carried away by an evaporating atom is between U_0 and $U_0 + k_B T$.

Given the loss rates for the energy and the number of atoms, we can find differential equations which describe the evolution of the parameters T and N which parameterize the distribution function $f(\epsilon)$. The rate of change of the internal energy of the gas can be expressed as

$$\begin{aligned} \dot{E} &= \left(\frac{\partial E}{\partial T}\right)_N \dot{T} + \left(\frac{\partial E}{\partial N}\right)_T \dot{N} \\ &= C\,\dot{T} + \mu\,\dot{N} \end{aligned} \tag{6.41}$$

where C is the heat capacity of the gas and μ is the chemical potential. C and μ can be easily calculated from the energy of the gas $E = \int_0^{U_0} d\epsilon\,\epsilon\,\mathcal{D}(\epsilon)\,f(\epsilon)$ assuming $f(\epsilon)$ is a truncated Boltzmann distribution. Assuming that the number and energy loss rates are solely due to evaporation $\dot{E} = \dot{E}_{\rm ev}$ and $\dot{N} = \dot{N}_{\rm ev}$, we are led to the differential equations describing the evolution of T and N

$$\dot{N} = \dot{N}_{\rm ev} \tag{6.42}$$

$$\dot{T} = \frac{\dot{E}_{\rm ev} - \mu\,\dot{N}_{\rm ev}}{C} \tag{6.43}$$

where $\dot{N}_{\rm ev}$ is given by (6.36) and $\dot{E}_{\rm ev}$ is given by (6.39).

Figure 6.3 shows the evolution of T and N obtained by numerical integration of Eqs. (6.42) and (6.43) (solid curves). Also shown in Figure 6.3 are the evolution of T (triangles) and N (squares) obtained by numerical integration of the Boltzmann equation. The agreement between the two models obtained for the evolution of N is excellent. The agreement for the evolution of T is not quite as good for

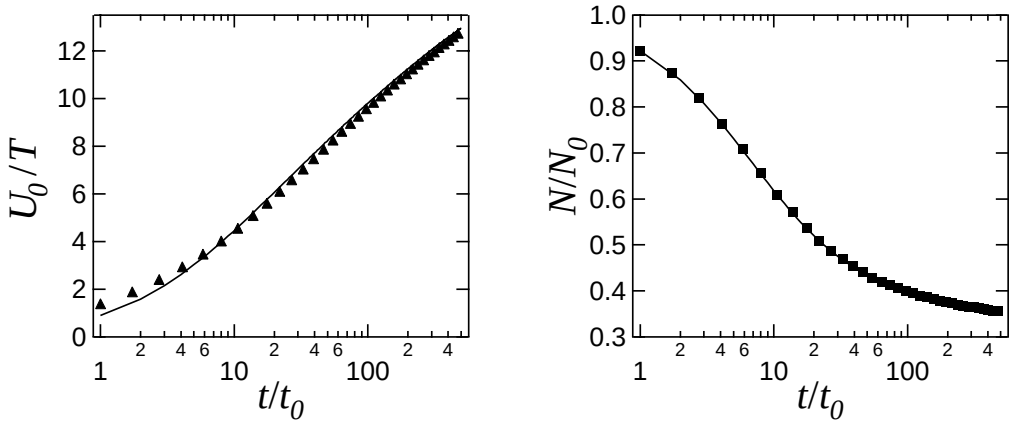

Figure 6.3: Evolution of thermodynamic variables T and N. The solid curve is generated by integrating the equations of motion for the thermodynamic variables forward in time. The solid triangles and solid squares are generated by numerically integrating the discretized kinetic Boltzmann equation forward in time.

early time. However, for later times, when the distribution function $f(\epsilon)$ is better approximated by a Boltzmann distribution as shown in Figure 6.1, the models are in better agreement.

The evolution of T and N shown in Figures 6.1 and 6.3 for the evaporation of atoms from a gaussian potential are universal functions of the reduced time t/t_0. As discussed above, the unit of time t_0 is nominally the inverse of the collision rate for atoms at energy U_0. To be specific

$$t_0 = \frac{2\,\pi^{3/2}\,U_0}{N_0\,M\,\sigma\,\omega^3}. \tag{6.44}$$

Assuming that the trap parameters ω and U_0 can be independently determined and the initial number of trapped atoms N_0 is known from calibrated fluorescence or absorption measurements, the only remaining unknown in equation (6.44) is σ. By measuring the number of atoms as a function of time during evaporation, the

value of σ can be determined by fitting the data to the universal function shown in Figures 6.1 and 6.3. Thus, by measuring the evaporation rate of ^{6}Li atoms from an optical trap, one might hope to extract the value of σ and thereby verify the theoretical prediction for the scattering length discussed in Chapter 2. However, the scattering length for ultracold ^{6}Li collisions are so large that the cross section is energy dependent even for the ultracold temperatures being considered. Thus, we must consider the Boltzmann equation assuming binary s-wave collisions with an energy dependent cross section.

6.2 S-Wave Boltzmann Equation with an Energy Dependent Cross Section

In Section 2.5 we found that the s-wave cross section for ultracold ^{6}Li collisions exhibits an energy dependent cross section

$$\sigma(q) = \frac{\sigma_0}{1 + q^2\, a_s^2/\hbar^2} \tag{6.45}$$

where q is the relative momentum of the colliding particles and a_s is the s-wave scattering length. The cross section is only constant for $q\,|a_s|/\hbar << 1$. Note that $q\,|a_s|/\hbar = 1$ corresponds to a relative kinetic energy of $\epsilon = \hbar^2/(2\,\mu\,a_s^2)$ where $\mu = M/2$ is the reduced mass. For $a_s = 1000\,a_0$, $\epsilon = 28\,\mu$K. Thus, given that ultracold ^{6}Li collisions can exhibit very large scattering lengths it is essential to consider the energy dependence of the cross section when considering evaporative cooling.

In Section 6.1.2 we assumed the s-wave cross section to be energy independent

in deriving the Boltzmann equation in the ergodic approximation. The majority of the derivation given in Section 6.1.2 is unchanged for an energy dependent cross section. However, since the cross section is a function of the relative momentum q the integral over q given in (6.18) must contain the q dependence of σ. For an energy dependent cross section we make the replacement

$$\begin{aligned}\sigma\, h(\epsilon_1\,\epsilon_2\,\epsilon_3\,\epsilon_4) \;\;\rightarrow\;\; & 2\,(2\pi)^3\,M^2 \int\limits_{U\leq\,\epsilon_{\min}} d^3r \int_{P_{\min}}^{P_{\max}} dP \int dq\, q\, \sigma(q) \\ & \times\,\delta\left(\epsilon_1+\epsilon_2-\frac{P^2}{4M}-\frac{q^2}{M}-2U(\boldsymbol{r})\right) \\ & \times\,\delta\left(\epsilon_3+\epsilon_4-\frac{P^2}{4M}-\frac{q^2}{M}-2U(\boldsymbol{r})\right). \end{aligned} \tag{6.46}$$

Integration over q then yields

$$\begin{aligned}\sigma\, h(\epsilon_1\,\epsilon_2\,\epsilon_3\,\epsilon_4) \;\;\rightarrow\;\; & (2\pi)^3\,M^3 \int\limits_{U\leq\,\epsilon_{\min}} d^3r \int_{P_{\min}}^{P_{\max}} dP\,\sigma\left(q=\sqrt{M(\epsilon-2U(\boldsymbol{r})-P^2/2M)}\right) \\ & \times\,\delta(\epsilon_1+\epsilon_2-\epsilon_3-\epsilon_4). \end{aligned} \tag{6.47}$$

Comparison with (6.21) shows that the Boltzmann equation with an energy dependent s-wave scattering cross section is given by the replacement

$$\mathcal{D}(\epsilon_{\min})\,\sigma \rightarrow \frac{2\pi\,M}{(2\pi\,\hbar)^3} \int\limits_{U\leq\,\epsilon_{\min}} d^3r \int_{P_{\min}(\boldsymbol{r})}^{P_{\max}(\boldsymbol{r})} dP\,\sigma\left(\sqrt{M(\epsilon-2U-P^2/4M)}\right) \tag{6.48}$$

in Eq. (6.22), where $\epsilon=\epsilon_1+\epsilon_2$.

The P integral in (6.48) is easily performed for the specific case of a cross section with a lorentzian dependence on q (see Eq. (6.45)) where the atoms are confined in a gaussian potential as described in Section 6.1.4. To perform the integral over P we can express q as $q=\sqrt{M(\epsilon-2U-P^2/4M)}=\sqrt{P_{\max}^2+P_{\min}^2-P^2}/2$. Once the

integral over P is performed we can substitute in the $\boldsymbol{r}$ dependence of $P_{\max}(\boldsymbol{r})$ and $P_{\min}(\boldsymbol{r})$. For the case of a gaussian potential, a change of spatial variables makes the spatial integral independent of orientation. After performing the integral over $\boldsymbol{P}$ and the orientation of $\boldsymbol{r}$ the resulting integral is given by

$$\frac{2\pi\, M}{(2\pi\,\hbar)^3} \int\limits_{U \leq \epsilon_{\min}} d^3r \int_{P_{\min}}^{P_{\max}} dP\, \sigma(q) = \sigma_0\, \mathcal{D}_{ho}(\epsilon_{min})\, F(\epsilon, \epsilon_{\min}), \tag{6.49}$$

where

$$F(\epsilon, \epsilon_{\min}) = \frac{4}{\pi} \frac{[-\ln(1-x_{\min})]^{3/2}}{x_{\min}^2\, \eta_s} \int_0^1 du\, \frac{u^2}{h_0}\, \ln \left| \frac{[h_0 + \eta_s\, h_+]}{[h_0 - \eta_s\, h_+]} \frac{[h_0 - \eta_s\, h_-]}{[h_0 + \eta_s\, h_-]} \right|, \tag{6.50}$$

$\epsilon_s \equiv 2\hbar^2/(M\, a_s^2)$, $\eta_s \equiv \sqrt{U_0/\epsilon_s}$ and

$$h_0(x, x_{\min}, u) = \sqrt{1 + \eta_s^2\, (h_+^2(x, x_{\min}, u) + h_-^2(x, x_{\min}, u))} \tag{6.51}$$

$$h_\pm(x, x_{\min}, u) = \sqrt{x - x_{\min} - 1 + (1 - x_{\min})^{u^2}} \pm \sqrt{x_{\min} - 1 + (1 - x_{\min})^{u^2}} \tag{6.52}$$

Here, $x \equiv \epsilon/U_0$ and $x_{\min} \equiv \epsilon_{\min}/U_0$. The integral in (6.50) has not been solved analytically, however it may be computed numerically.

Thus, the Boltzmann equation with an energy dependent cross section for a gaussian potential is obtained by the replacement $\sigma\, \mathcal{D}(\epsilon_{\min}) \rightarrow \sigma_0\, \mathcal{D}_{ho}(\epsilon_{\min})\, F(\epsilon, \epsilon_{\min})$ in (6.22) which yields

$$\begin{aligned} \mathcal{D}(\epsilon_4)\, \frac{\partial f(\epsilon_4)}{\partial t} &= \frac{M\, \sigma_0}{\pi^2\, \hbar^3} \int d\epsilon_1\, d\epsilon_2\, d\epsilon_3\, \delta(\epsilon_1 + \epsilon_2 - \epsilon_3 - \epsilon_4)\, \mathcal{D}_{ho}(\epsilon_{\min})\, F(\epsilon, \epsilon_{\min}) \\ &\quad \times [f(\epsilon_1)\, f(\epsilon_2) - f(\epsilon_3)\, f(\epsilon_4)]. \end{aligned} \tag{6.53}$$

For $U_0 << \epsilon_s$, $F(\epsilon, \epsilon_{\min}) \rightarrow g_1(\epsilon_{\min})$ of (6.31) and (6.53) reproduces (6.22). Thus,

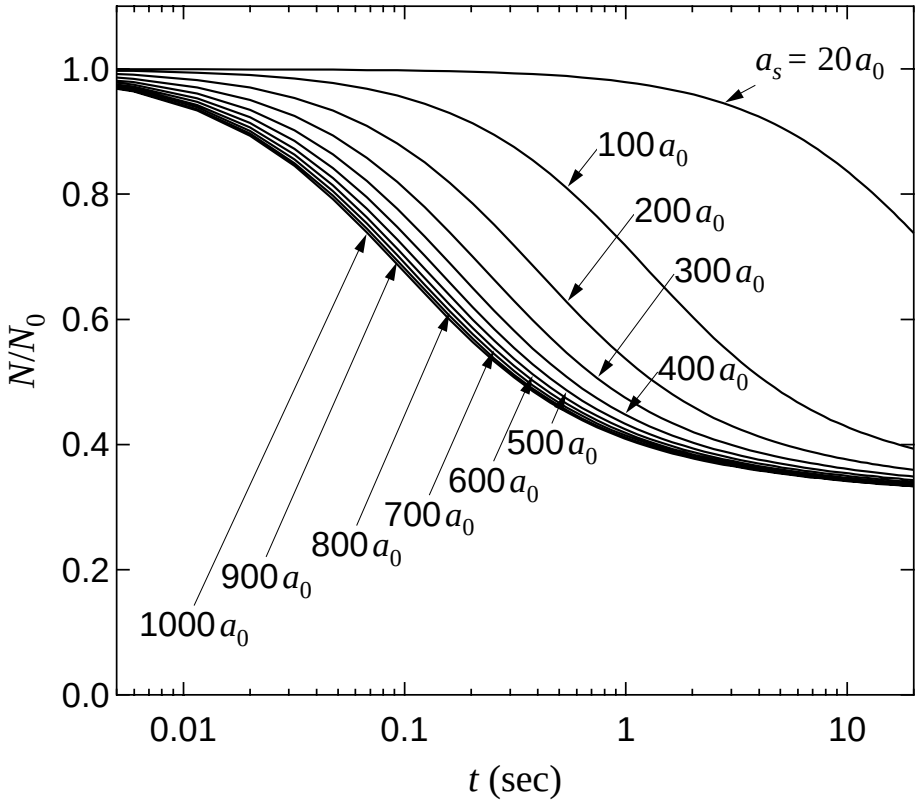

Figure 6.4: Evaporation of ^{6}Li atoms from a Gaussian potential with a depth of $500\,\mu$K. Each curve is labeled by the particular scattering length a_s assumed in the model. Note that for large values of a_s the evaporation curves become independent of the scattering length.

the cross section can be considered to be energy independent for $U_0 << \epsilon_s$.

Eq. (6.53) can be numerically integrated in a manner identical to that used to integrate (6.22). The energy scale is discretized to produce an equation similar to (6.32). The only difference is that the discretized equation corresponding to (6.53) contains the matrix $F_{k+l,h} \equiv F(\epsilon_k + \epsilon_l, \epsilon_h)$ and the harmonic oscillator density of states on the right hand side. Note that the maximum possible value of $\epsilon_k + \epsilon_l = 2\,U_0$.

Figure 6.4 shows the evaporation of ^{6}Li atoms from an optical trap for several different values of scattering length. In generating these plots the following param-

eters are assumed: $U_0 = 500\,\mu$K, $(\nu_x\,\nu_y\,\nu_z)^{1/3} = 1750\,$Hz, $N_0 = 100,000$ atoms (per state), and $T_0 = \infty$. For $U_0 = 500\,\mu$K, $\epsilon_s = U_0$ for a scattering length of $338\,a_0$. Thus, for scattering lengths much less than $\simeq 300\,a_0$ the cross section is essentially a constant function of energy for the parameters considered in generating Figure 6.4. The curves for $a_s = 20\,a_0$ and $a_s = 100\,a_0$ are in excellent agreement with evaporation models which assume a constant cross section. However, as the scattering length approaches $a_s = 300\,a_0$, the energy dependence of the s-wave cross section becomes important. For values of a_s exceeding $300\,a_0$, the energy dependence of the cross section is dominated by the unitarity limit $\sigma = 8\pi/k^2$ and the evaporation curves become independent of a_s as can be seen in Figure 6.4. Thus, in order to accurately determine a very large scattering length by measuring the evaporation rate from an optical trap, shallow well depths must be used in order to avoid the cross section becoming unitarity limited and therefore independent of the scattering length. In Chapter 7, we measure a very large scattering length for ultracold ^{6}Li collisions by monitoring the evaporation of ^{6}Li atoms from a $100\,\mu$K deep optical potential. Eq. (6.53) is used to fit the evaporation data and thereby extract the scattering length.

6.3 Evaporative Cooling in a Time-Dependent Potential

In Section 6.1.6 we found that the evaporative cooling process eventually stagnates in a well of fixed depth since the probability for an atom to escape the trapping potential is exponentially suppressed by a factor $\exp(-\epsilon_t/k_BT)$ where T is the temperature and ϵ_t is the threshold energy for escape. In order to sustain the

evaporative cooling process so that the trapped atoms can be cooled to ever lower temperatures, the threshold energy ϵ_t must be lowered as a function of time. In this section we consider the modification to the Boltzmann equation in the event that the confining potential is time dependent. Evaporative cooling of atoms from a time dependent potential has also been treated by Berg-Sørensen [117]. Berg-Sørensen examines the evaporation of atoms from a truncated harmonic potential in which the truncation energy is time-dependent. However, the modification of the kinetic Boltzmann equation due to the time-dependent potential is found to have negligible effect on the evaporative cooling process in this case [118]. In this section, we examine evaporation from a time-dependent gaussian potential in which the well depth U_0 is lowered as a function of time. Since, the spring constant for the trap is proportional to U_0, the time-dependent potential in this case gives rise to terms in the kinetic Boltzmann equation which have a significant effect on the evaporation process.

6.3.1 Collisionless Evolution in a Time-Dependent Potential

Let us first consider the Boltzmann equation in the absence of collisions:

$$\frac{\partial f(\boldsymbol{r},\boldsymbol{p})}{\partial t} + \frac{\boldsymbol{p}}{M}\cdot\nabla_{\boldsymbol{r}} f(\boldsymbol{r},\boldsymbol{p}) - \nabla_{\boldsymbol{r}} U(\boldsymbol{r},t)\cdot\nabla_{\boldsymbol{p}} f(\boldsymbol{r},\boldsymbol{p}) = 0 \tag{6.54}$$

where the confining potential $U(\boldsymbol{r},t)$ may be time dependent. Again, the Boltzmann equation is drastically simplified by making the assumption of sufficient ergodicity in which case the phase space distribution function $f(\boldsymbol{r},\boldsymbol{p})$ is only a function of the

single particle energy. This allows us to express $f(\boldsymbol{r},\boldsymbol{p})$ as

$$\begin{aligned} f(\boldsymbol{r},\boldsymbol{p}) &= \int d\epsilon\, \delta\left(\epsilon - \mathcal{H}(\boldsymbol{r},\boldsymbol{p},t)\right)\, f(\epsilon,t) \\ &= f(\mathcal{H}(\boldsymbol{r},\boldsymbol{p},t)), \end{aligned} \tag{6.55}$$

where $\mathcal{H}(\boldsymbol{r},\boldsymbol{p},t) = U(\boldsymbol{r},t) + p^2/2M$ is the single particle Hamiltonian. Applying the operation $(2\pi\,\hbar)^{-3}\int d^3r\, d^3p\, \delta\left(\epsilon - \mathcal{H}(\boldsymbol{r},\boldsymbol{p},t)\right)$ to Eq. (6.54) yields the ergodic Boltzmann equation. The gradient terms vanish since

$$\begin{aligned} \frac{\boldsymbol{p}}{M}\cdot\nabla_{\boldsymbol{r}} f\left(\mathcal{H},t\right) - \nabla_{\boldsymbol{r}} U\cdot\nabla_{\boldsymbol{p}} f(\mathcal{H},t) &= \left[\frac{\boldsymbol{p}}{M}\cdot\nabla_{\boldsymbol{r}}\mathcal{H} - \nabla_{\boldsymbol{r}} U\cdot\nabla_{\boldsymbol{p}}\mathcal{H}\right](\partial f/\partial\mathcal{H}) \\ &= 0, \end{aligned} \tag{6.56}$$

where the bracketed term sums to zero. The only remaining term is the time derivative. Under the integral the time derivative of f may be written as

$$\begin{aligned} \frac{\partial f(\boldsymbol{r},\boldsymbol{p})}{\partial t} = \frac{\partial f(\mathcal{H})}{\partial t} &= \frac{\partial f}{\partial\mathcal{H}}\frac{\partial\mathcal{H}}{\partial t} + \frac{\partial f}{\partial t} \\ &= \frac{\partial f}{\partial\epsilon}\dot{U} + \frac{\partial f}{\partial t}. \end{aligned} \tag{6.57}$$

Thus, the collisionless Boltzmann equation under the assumption of sufficient ergodicity is

$$\mathcal{D}(\epsilon)\left\{\frac{\partial f}{\partial t} + \frac{\partial f}{\partial\epsilon}\langle\dot{U}(\boldsymbol{r},t)\rangle_\epsilon\right\} = 0 \tag{6.58}$$

where $\langle\dot{U}(\boldsymbol{r},t)\rangle_\epsilon$ is the ergodic average of $\dot{U}$ defined as

$$\mathcal{D}(\epsilon)\,\langle\dot{U}(\boldsymbol{r},t)\rangle_\epsilon \equiv \int\frac{d^3r\, d^3p}{(2\pi\,\hbar)^3}\,\delta\left(\epsilon - \mathcal{H}(\boldsymbol{r},\boldsymbol{p})\right)\dot{U}(\boldsymbol{r},t). \tag{6.59}$$

For collisionless motion $(\partial f/\partial t) = -\langle \dot{U} \rangle_\epsilon \, (\partial f/\partial \epsilon)$. This equation of motion for $f(\epsilon, t)$ has a simple physical interpretation. According to this equation of motion, we may write

$$\begin{aligned} f(\epsilon, t + \Delta t) &= f(\epsilon, t) + \frac{\partial f}{\partial t} \Delta t \\ &= f(\epsilon, t) - \frac{\partial f}{\partial \epsilon} \langle \dot{U} \rangle_\epsilon \Delta t \\ &= f(\epsilon - \langle \dot{U} \rangle_\epsilon \Delta t, t) \\ &= f(\epsilon - \langle \dot{\mathcal{H}} \rangle_\epsilon \Delta t, t). \end{aligned} \tag{6.60}$$

where we have used the fact that $\langle \dot{U} \rangle_\epsilon = \langle \dot{\mathcal{H}} \rangle_\epsilon$. Eq. (6.60) simply reflects the fact that, for an adiabatic change in the confining potential, the occupation number $f(\epsilon, t)$ evolves such that the occupation of an energy eigenstate is constant in time. The time dependence of $f(\epsilon, t)$ simply arises from the fact that as the potential changes the energies of the eigenstates are time dependent. The collisionless evolution is depicted in Figure 6.5 where the grey circles denote the occupation of each eigenstate of the potentetial.

6.3.2 $\langle \dot{U} \rangle_\epsilon$ for a Gaussian Potential

In this section, we consider the ergodic average $\langle \dot{U} \rangle_\epsilon$ of a time-dependent gaussian potential which, as discussed in Section 6.1.4, is appropriate for the potential due to a focused gaussian laser beam. We consider the potential

$$U(\boldsymbol{r}, t) = U_0(t) \left(1 - \exp\left(-\frac{x^2}{a^2} - \frac{y^2}{b^2} - \frac{z^2}{c^2} \right) \right) \tag{6.61}$$

$$\dot{U}(\boldsymbol{r}, t) = \dot{U}_0(t) \left(1 - \exp\left(-\frac{x^2}{a^2} - \frac{y^2}{b^2} - \frac{z^2}{c^2} \right) \right) \tag{6.62}$$

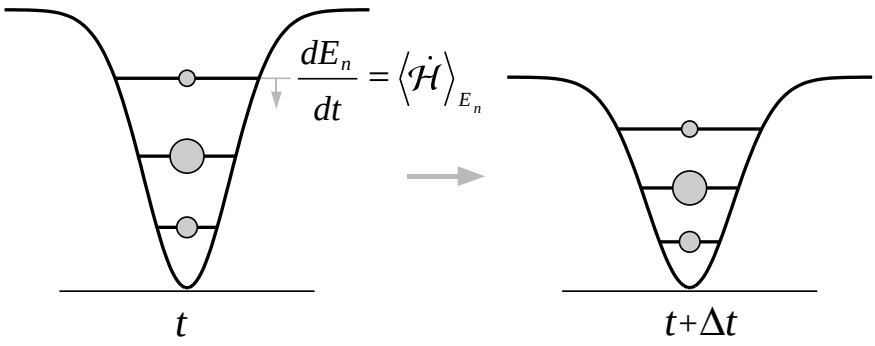

Figure 6.5: Collisionless evolution of the occupation number as the well depth is adiabatically reduced. The occupation number of each eigenstate remains constant as the well depth is adiabatically reduced. The time dependence of $f(\epsilon, t)$ arises from the fact that the energy of the eigenstates evolves in time.

where the well depth $U_0(t)$ is proportional to the laser intensity and may be time-dependent. By lowering the laser intensity during evaporative cooling the threshold energy ϵ_t required for an atom to escape the potential is lowered as a function of time in order to avoid stagnation of the evaporative cooling process.

For the time-dependent potential given in (6.61) and (6.62), we need to calculate the quantity

$$\mathcal{D}(\epsilon)\,\langle \dot{U} \rangle_\epsilon = \int \frac{d^3r\, d^3p}{(2\pi\,\hbar)^3}\,\dot{U}(\boldsymbol{r}, t)\,\delta\left(\epsilon - \frac{p^2}{2M} - U(\boldsymbol{r}, t)\right). \tag{6.63}$$

The integration over $\boldsymbol{p}$ gives a result identical to that of (6.29). After a change of spatial coordinates $d^3r \to a\,b\,c\,d^3r'$, the spatial integral becomes isotropic and the integral over the orientation of $\boldsymbol{r}'$ is easily performed to yield

$$\mathcal{D}(\epsilon)\,\langle \dot{U} \rangle_\epsilon = \frac{\epsilon^2\,\dot{U}_0}{2\,(\hbar\,\omega)^3}\,\beta\left[g_1(\beta) - \frac{1}{2}\,g_2(\beta)\right] \tag{6.64}$$

where $\omega^3 = \omega_x\,\omega_y\,\omega_z = [2U_0/(M\,a^2\,b^2\,c^2)]^{3/2}$, $\beta \equiv \epsilon/U_0$, the function $g_1(\beta)$ is defined

in (6.30) and

$$g_2(\beta) \equiv \frac{\alpha^{3/2}\,(1-\beta)^{3/2}}{\beta^{3/2}}\,\frac{32}{\pi}\,\int_0^1 du\,u^2\,\left(e^{\alpha\,(1-u^2)}-1\right)^{3/2}. \tag{6.65}$$

Here, $\alpha \equiv -\ln(1-\beta)$. Since $\mathcal{D}_{ho}(\epsilon) = \epsilon^2/(2\,(\hbar\,\omega)^3)$ and $\mathcal{D}(\epsilon) = \mathcal{D}_{ho}(\epsilon)\,g_1(\epsilon)$ we may write the ergodic average as

$$\langle \dot{U} \rangle_\epsilon = \dot{U}_0\,\beta\,\left[1 - \frac{1}{2}\,\frac{g_2(\beta)}{g_1(\beta)}\right]. \tag{6.66}$$

It is interesting to consider the form of $\langle \dot{U} \rangle_\epsilon$ in the limit of low energy $\beta \to 0$. In this limit, the potential is approximately harmonic. For $\beta \to 0$ the functions $g_1(\beta) \to 1$ and $g_2(\beta) \to 1$ to $\mathcal{O}(\beta^0)$. Thus, in the limit of low energy $\langle \dot{U} \rangle_\epsilon \simeq \dot{U}_0\ (\beta/2) = \frac{1}{2}\,(\dot{U}_0/U_0)\epsilon$ to $\mathcal{O}(\beta^1)$. The equation of motion for $f(\epsilon, t)$ for energies ϵ in the harmonic limit is then

$$\left(\frac{\partial f}{\partial t}\right) = -\frac{\epsilon}{2}\,\frac{\dot{U}_0}{U_0}\,\left(\frac{\partial f}{\partial \epsilon}\right). \tag{6.67}$$

It is easy to show that $f(\epsilon, t) = f\left(\epsilon\,\sqrt{\frac{U_0(0)}{U_0(t)}}, 0\right)$ is a solution to this equation of motion. This makes sense since we expect that as the potential is adiabatically changed, the number of atoms in a given harmonic oscillator eigenstate should remain constant. Since the energy of the harmonic eigenstates are given by $E[n_x, n_y, n_z, t] = (n_x + 1/2)\hbar\,\omega_x + (n_y + 1/2)\hbar\,\omega_y + (n_z + 1/2)\hbar\,\omega_z \propto \sqrt{U_0(t)}$ we find, as expected, that the phase space distribution $f\,(E[n_x, n_y, n_z, t], t) = f\left(E[n_x, n_y, n_z, t]\,\sqrt{\frac{U_0(0)}{U_0(t)}}, 0\right)$ to be a constant function of time.

Consider a gaussian potential containing a thermal distribution of atoms $f(\epsilon) = \rho_0\,\exp(-\epsilon/k_B T)$ whose temperature $T << U_0$. In this case, the majority of the

atoms experience a harmonic potential. If the potential depth U_0 is adiabatically lowered but the atoms do not experience collisions, the distribution will evolve according to $f(\epsilon, t) = f(\epsilon \sqrt{U_0(0)/U_0(t)}, t = 0)$. Therefore, at time t,

$$\begin{aligned} f(\epsilon, t) &= \rho_0 \exp\left(-\frac{\epsilon}{k_B T}\sqrt{\frac{U_0(0)}{U_0(t)}}\right) \\ &= \rho_0 \exp\left(-\frac{\epsilon}{k_B T'(t)}\right) \end{aligned} \tag{6.68}$$

where $T'(t) = T\sqrt{U_0(t)/U_0(0)}$. Thus, as the well depth U_0 is adiabatically lowered, the fractional change in the temperature of the atoms will decrease as the square root of the fractional change in the well depth in the absence of interatomic collisions.

6.3.3 Numerical Integration of Collisionless Boltzmann Equation with a Time-Dependent Potential

In this section we discuss the issues involved in the numerical integration of the collisionless Boltzmann equation (6.58) for a time-dependent gaussian potential. In order to numerically integrate (6.58), we discretize the energy scale into n equally spaced bins of width $\Delta\epsilon = \frac{U_0}{n}$. The energy of the i^{th} bin is $\epsilon_i = (i - 1/2)\Delta\epsilon$. The evolution of the i^{th} bin of the distribution function due to the collisionless Boltzmann equation is given by

$$\left(\frac{\partial f_i}{\partial t}\right)_{\text{boltz}} = -\frac{\partial f_i}{\partial \epsilon}\langle \dot{U} \rangle_{\epsilon_i}. \tag{6.69}$$

However, in addition to this evolution we must also consider the fact that the energies $\epsilon_i = (i - 1/2)\Delta\epsilon$ shift as a function of time as the well depth U_0 changes since the energy bin width $\Delta\epsilon = U_0/n$ changes. Thus, the i^{th} bin of the distribution

function f_i, must evolve due to the fact that ϵ_i is time dependent. For a change in time Δt the change in f_i is given by

$$\begin{aligned}\Delta f_i &= \frac{\partial f_i}{\partial \epsilon}\left[\epsilon_i(t+\Delta t)-\epsilon_i(t)\right] \\ &= \frac{\partial f_i}{\partial \epsilon}\,(i-1/2)\,[\frac{U_0(t+\Delta t)}{n}-\frac{U_0(t)}{n}] \\ &= \frac{\partial f_i}{\partial \epsilon}\,\frac{i-1/2}{n}\,\dot{U}_0\,\Delta t. \end{aligned} \tag{6.70}$$

Thus, the evolution of f_i arising from the shift in ϵ_i is given by

$$\left(\frac{\partial f_i}{\partial t}\right)_{\text{shift}} = \frac{\partial f_i}{\partial \epsilon}\,\frac{i-1/2}{n}\,\dot{U}_0. \tag{6.71}$$

Combining (6.69) and (6.71) gives the evolution of f_i due to both the collisionless Boltzmann equation and the shift in the energy bins due to the change in the potential well depth

$$\frac{\partial f_i}{\partial t} = -\frac{\partial f}{\partial \epsilon}\,\langle \dot{U}\rangle_{\epsilon_i} + \frac{\partial f_i}{\partial \epsilon}\,\frac{i-1/2}{n}\dot{U}_0. \tag{6.72}$$

Numerical integration of (6.72) is accomplished by replacing the partial derivatives of f_i with respect to ϵ with discretized approximations to the derivative. $\langle \dot{U}\rangle_{\epsilon_i}$ is given by (6.66) and (6.72) is integrated forward in time using an adaptive step-size fourth-order Runga Kutta routine. In practice, we find that the integration of (6.72) is stable if $\partial f/\partial \epsilon$ in the first term of (6.72) is given by

$$\frac{\partial f_i}{\partial \epsilon} = \frac{f_{i+1}-f_i}{\Delta \epsilon} \tag{6.73}$$

which gives the value of the derivative correct to $\mathcal{O}(\Delta\epsilon)$. The derivative $\partial f_i/\partial \epsilon$ in

the second term of (6.72) is replaced by

$$\frac{\partial f_i}{\partial \epsilon} = \frac{f_{i+1} - f_{i-1}}{2\Delta\epsilon} \tag{6.74}$$

which gives the value of the derivative correct to $\mathcal{O}(\Delta\epsilon^2)$. These replacements give the best results for numerical integration of (6.72) with respect to conservation of number.

Conservation of number can be verified by using an initial distribution function $f(\epsilon) = \rho_0 \exp(-\epsilon/k_B T_0)$ where $T_0 << U_0$ and integrating (6.72) forward in time as the well depth of the gaussian potential U_0 is lowered as a function of time. The number of trapped atoms initially remains constant as the well is lowered since none of the atoms "spill" out of the potential as the atoms are initially confined at the bottom of the potential well. For $U_0/T_0 \simeq 10$, conservation of number at the percent level requires the discretization of the energy scale into several hundred bins.

6.3.4 *S*-Wave Boltzmann Equation with a Time-Dependent Potential

In Section 6.3.1, we derived the ergodic Boltzmann equation for a time-dependent potential in the absence of collisions. If interatomic collisions exist in the trapped gas, the collision integral $\mathcal{I}(\boldsymbol{r}, \boldsymbol{p})$ given by (6.10) appears on the right hand side of (6.54). The Boltzmann equation under the assumption of sufficient ergodicity is given by

$$\begin{aligned} \mathcal{D}(\epsilon_4) \left\{ \frac{\partial f}{\partial t} + \frac{\partial f}{\partial \epsilon_4} \langle \dot{U}(\boldsymbol{r}, t) \rangle_{\epsilon_4} \right\} &= \frac{M\,\sigma}{\pi^2\,\hbar^3} \int d\epsilon_1\, d\epsilon_2\, d\epsilon_3\, \delta(\epsilon_1 + \epsilon_2 - \epsilon_3 - \epsilon_4) \\ &\quad \times \mathcal{D}(\epsilon_{\min}) \left[f(\epsilon_1)\, f(\epsilon_2) - f(\epsilon_3)\, f(\epsilon_4) \right] \end{aligned} \tag{6.75}$$

assuming s-wave collisions with a constant cross section. Here we have used the right hand side of (6.22) which gives the collision integral under the assumption of sufficient ergodicity. For s-wave collisions with an energy dependent cross section of the form given by Eq. (6.45), the ergodic Boltzmann equation is given by (6.75) with the replacement $\sigma\,\mathcal{D}(\epsilon_{\min}) \rightarrow \sigma_0\,\mathcal{D}_{ho}(\epsilon_{\min})\,F(\epsilon,\epsilon_{\min})$ as discussed in Section 6.2.

Eq. (6.75) can be numerically integrated by discretizing the energy scale and evaluating the collision integral on the right hand side of (6.75) as in Section 6.1.5 and Section 6.2. The terms arising from the time dependence of the potential are treated in a manner identical to that given in Section 6.3.2. As in Section 6.1.5 Section 6.2, we assume atoms with an energy greater than U_0 will cleanly escape the trap without experiencing a collision. Thus, we assume the distribution $f(\epsilon)$ is zero for $\epsilon > U_0$ during the integration of (6.75).

6.4 Evaporative Cooling in a Time-Dependent Optical Trap

In this section we investigate the possibility of increasing the phase space density of an atomic vapor by adiabatically lowering the well depth of an optical trap. We integrate (6.75) using parameters comparable to those obtainable for ^{6}Li atoms confined in the CO_2 laser trap discussed in Chapters 4 and 5. The model assumes a gaussian CO_2 laser beam focused to a waist with a $1/e$ intensity radius $a = 39\,\mu$m. The initial well depth $U_0 = 300\,\mu$K. These parameters correspond to a trap where the geometric mean of the trap oscillation frequencies is $\nu = (\nu_x\,\nu_y\,\nu_z)^{1/3} = 1300$ Hz.

We have also added the effect of background gas atoms in the vacuum system

which eject atoms from the trap at a rate $\dot{N} = -\Gamma N$. This loss is modeled by the addition of a term $-\Gamma \mathcal{D}(\epsilon_4) f(\epsilon_4)$ to the right hand side of (6.75). In the model $\Gamma = 0.003$, comparable to the loss rate observed in the current experimental system. The inclusion of a background loss rate is of importance in evaluating the potential for evaporative cooling since, in the absence of loss, one could merely wait an infinite amount of time for the atoms to cool. Given an infinite amount of time, the atoms will essentially cool to absolute zero. With this in mind, it is obvious that a large elastic collision rate is desirable since it permits the largest number of "good" collisions (elastic collisions) per "bad" collision (background gas collision). Fortunately, ultracold ^{6}Li elastic collisions can exhibit very large cross sections suitable for efficient evaporative cooling.

In Section 6.3.2 we found that conservation of number at the percent level requires the discretization of the energy scale into several hundred bins. This makes integration of (6.75) with an energy dependent cross section computationally time consuming since, as discussed in Section 6.2, this requires computation of a $2n \times n$ matrix $F_{k+l,h}$ for each time step. Therefore, we have chosen to model the evaporation of ^{6}Li atoms with a scattering length $|a_s| = 200\, a_0$. This choice provides a rather large effective collision cross section $\sigma = 4\pi a_s^2$ suitable for efficient evaporative cooling. However, the scattering length $|a_s| = 200\, a_0$ is small enough that the cross section can be treated as a constant for evaporation from an optical trap with $U_0 \leq 300\, \mu$K enabling integration of (6.75) in a reasonable amount of time. As discussed in Section 2.10, a scattering length $|a_s| = 200\, a_0$ can be realized in ^{6}Li for certain two-state mixtures with an appropriate bias magnetic field.

In the model, the well depth U_0 of the gaussian potential is exponentially lowered, i.e. $U_0 = \exp(-t/\tau)$. The time constant τ was coarsely adjusted to give the

largest number of atoms for a given phase space density at the end of evaporative cooling. This occurs for $\tau = 10$ sec. However, the chosen time dependence for U_0 is not necessarily an optimized evaporative cooling trajectory. It is by no means obvious that an exponential dependence of U_0 on time gives the largest number of atoms for a given phase space density. The model presented here should be considered a proof-of-principle that the phase space density of an atomic vapor can be substantially increased by evaporative cooling from an optical trap. The optimization of evaporative cooling from a truncated harmonic potential is given in Ref. [119]; a similar analysis would be an important extension to the model given here.

The model assumes that the initial temperature of the atoms satisfies $k_B T_0/U_0 = 1/10$, *i.e.* $T_0 = 30\,\mu$K. This initial temperature is appropriate for atoms that have been evaporatively cooled in the well at fixed depth until the evaporative cooling process stagnates yielding a temperature of 1/10 of the well depth. The initial conditions for the model assume 500,000 atoms per state are confined in the CO_2 laser trap. As discussed in Chapter 5, this is a feasible number of atoms to be captured from the magneto-optical trap (even considering that as many as 1/2 of the atoms are lost during evaporation from the well of fixed depth).

Figure 6.6 shows the peak phase space density given by $f(\epsilon = 0)$ versus the number of atoms N per state for the model with the parameters described above. The arrow shows the direction of time. The evaporative cooling curve shown corresponds to 40 seconds of evolution. Phase space densities exceeding 0.5 are not shown since Fermi statistics begin to play a role as the occupation number of the states approaches unity. The effect of Fermi statistics will be discussed in the following section. Note that approximately two orders of magnitude in phase space

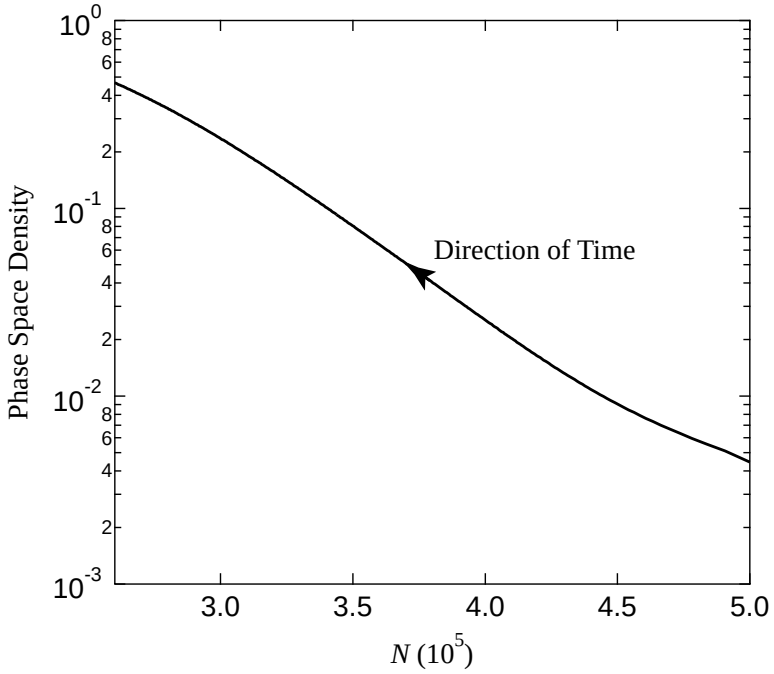

Figure 6.6: Phase Space Density versus Number

density are gained while the number of atoms per state only decreases by a factor of two. Figure 6.7 shows the phase space density versus well depth U_0. 40 seconds of the evaporative cooling trajectory is shown over which the well depth is lowered by a factor of $\exp(-4) \sim 10^{-2}$. Figure 6.8 shows the temperature of the gas as a function of time. The final temperature $T_f = 534$ nK, which is approximately 1/10 the well depth at that time. Over the course of the evaporative cooling process, the temperature remains at approximately 1/10 of the well depth. The ratio $k_B T/U_0$ is shown in Figure 6.9 as a function of time.

The model described above assumes that an atom with energy $\epsilon > U_0$ will cleanly escape the trap without experiencing another collision with a trapped atom. For this assumption to be valid the mean free path for an atom should exceed the size of the trapped atomic gas. Figure 6.10 shows the mean free path for a trapped

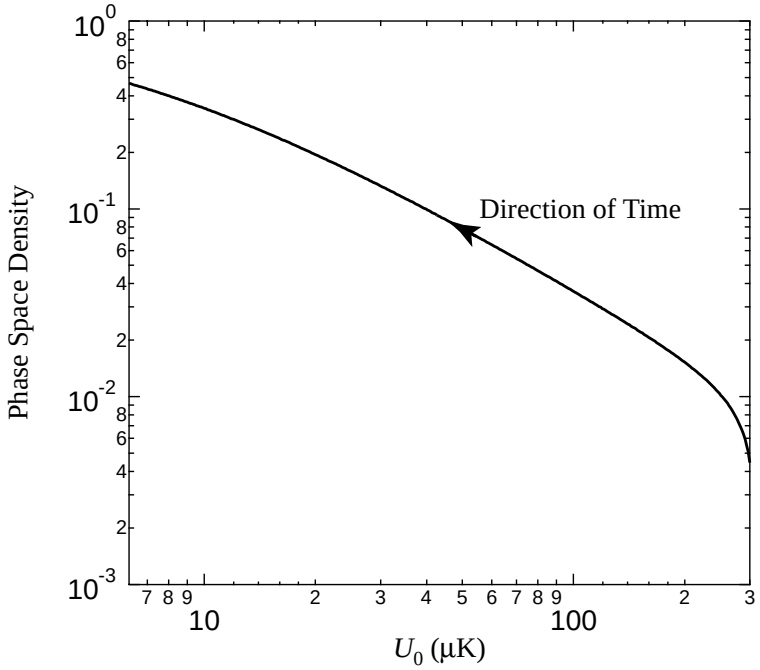

Figure 6.7: Phase Space Density versus U_0

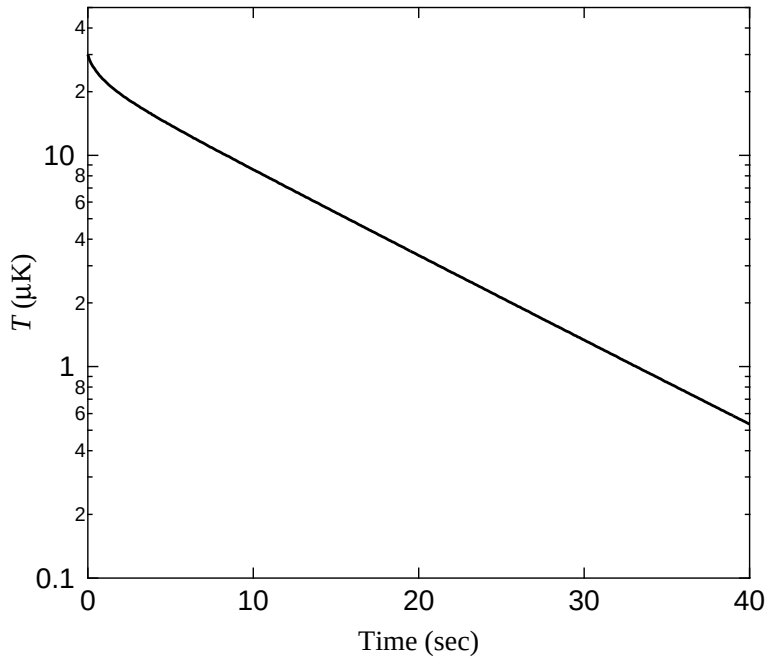

Figure 6.8: Temperature versus Time

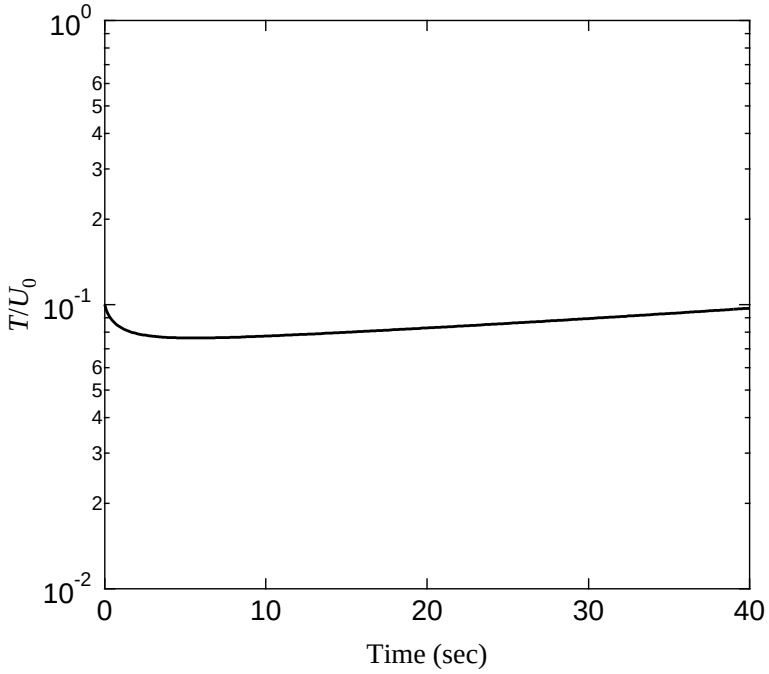

Figure 6.9: T/U_0 During Evaporation

atom as a function of time. Since the temperature $T << U_0$, the mean free path is approximately given by

$$l_{mfp} \simeq \frac{1}{n_0\,\sigma} = \frac{\lambda_{dB}^3}{f(0)\,\sigma} \tag{6.76}$$

where n_0 is to a good approximation the peak density and $\sigma = 4\pi a_s^2$. For $T << U_0$, the density distribution of the atomic gas is gaussian with a $1/e$ radius given by $\sigma_x = \sqrt{k_B T/U_0}\,a_x$ where a_x is the $1/e$ intensity radius of the focused gaussian laser beam. For the model described above the $1/e$ intensity radius is given by $a = 39\ \mu$m in the radial direction and $c = 900\ \mu$m in the axial direction. Figure 6.10 also shows the $1/e$ radius of the density distribution σ_ρ (σ_z) of the cloud as a function of time in the radial (axial) direction. The mean free path exceeds the radial $1/e$ radius of

the density distribution by over an order of magnitude throughout the evaporative cooling process. The mean free path is comparable to the axial $1/e$ radius of the density distribution at the beginning of evaporation. As the well depth is lowered the spring constant of the trap is lowered and the peak density decreases. Thus, the mean free path of an atom increases as a function of time and the assumption that energetic atoms cleanly escape the trap becomes a better and better approximation. However, even at the start of the evaporation trajectory when the mean free path is comparable to the $1/e$ radius of the density distribution in the axial direction, this assumption is still believed to be valid. Due to the cigar shape of the cloud, the solid angle for an energetic atom to escape in the radial direction greatly exceeds that for escape along the axis. Thus, while the mean free path is smaller than the characteristic size in the axial direction, the atom is expected to escape in the radial direction without experiencing a collision.

In order to verify that the numerical integration routine conserves number we have calculated the instantaneous loss rate as a function of time. If the number of particles is conserved, the sum of the integrated loss rate and the number of atoms remaining in the trap should be constant in time. The instantaneous loss rate is given by

$$\begin{aligned}
\dot{N} &= -\frac{d}{dt}\left(\int_{U_0}^{\infty} d\epsilon\, \mathcal{D}(\epsilon)\, f(\epsilon)\right) - \Gamma\, N \\
&= \dot{U}_0\, \mathcal{D}(U_0)\, f(U_0) - \int_{U_0}^{\infty} d\epsilon\, \dot{\mathcal{D}}(\epsilon)\, f(\epsilon) - \int_{U_0}^{\infty} d\epsilon\, \mathcal{D}(\epsilon)\, \dot{f}(\epsilon) - \Gamma\, N \\
&= \dot{U}_0\, \mathcal{D}(U_0)\, f(U_0) - \int_{U_0}^{\infty} d\epsilon\, \mathcal{D}(\epsilon)\, \dot{f}(\epsilon) - \Gamma\, N. \qquad (6.77)
\end{aligned}$$

The second term on the second line is zero since $f(\epsilon) = 0$ for $\epsilon > U_0$. The second term on the last line can be computed using the kinetic Boltzmann equation (6.75).

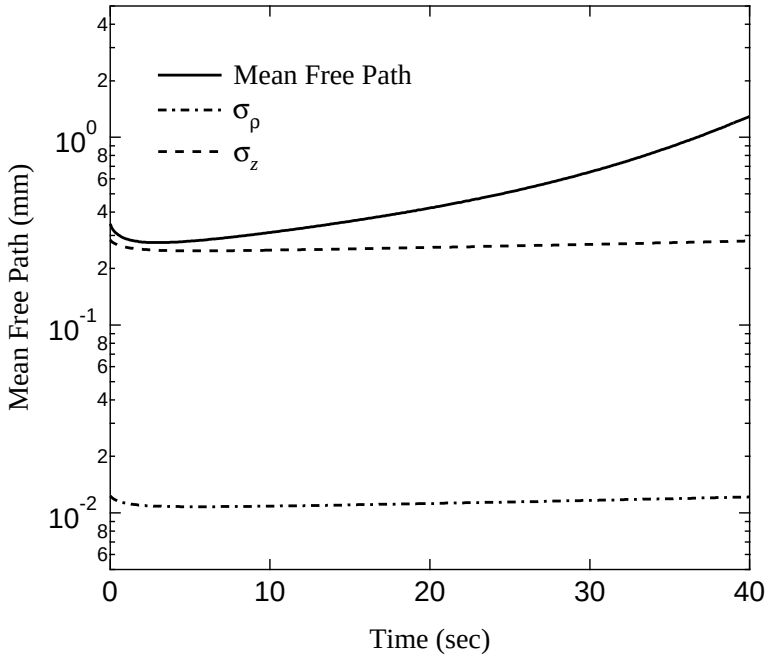

Figure 6.10: The solid curve gives the mean free path of an atom confined in the optical potential as a function of time during evaporation. Note that the mean free path exceeds the $1/e$ radius of the atomic cloud in the axial and radial directions shown as the dashed and dot-dashed curves respectively.
size of the

During the evaporation the distribution function $f(\epsilon)$ closely approximates a Boltzmann distribution $f(\epsilon) = \rho_0 \exp(-\epsilon/k_B T)$ truncated at the well depth U_0. Assuming $f(\epsilon)$ takes this form, the integral in (6.77) can be evaluated for a given temperature T and number N. By calculating the instantaneous collision rate for the model and integrating the instantaneous collision rate over time we find that the sum of the number of trapped atoms and the number of atoms lost is constant to less than 1% over the course of the 40 seconds of evolution studied. To achieve this accuracy, the numerical integration of (6.75) uses an energy scale discretized into 380 energy bins of equal width. Numerical integration of (6.75) to generate the 40 seconds of evolution shown takes several days of computation time on the department's public workstations.

6.5 Evaporative Cooling Scaling Laws

In this section we develop simple scaling laws which give good agreement with the more rigorous model of evaporative cooling discussed in the previous section. These simple scaling laws provide physical insight into general features of evaporative cooling in an optical trap.

Integration of the Boltzmann equation in the previous section demonstrated that the temperature of the trapped atoms is approximately 1/10 the well depth during evaporation (see Figure 6.9). We will assume in this section that the elastic collision rate in the trap is large enough to maintain $k_B T/U_0 \leq 1/10$. Since $T << U_0$ we will use the harmonic oscillator limit of the gaussian potential for a number of quantities.

The time rate of change of the internal energy of the gas can be written as

$$\begin{aligned} \dot{E} &= \frac{\partial E}{\partial T}\dot{T} + \frac{\partial E}{\partial N}\dot{N} \\ &= 3Nk_B\dot{T} + 3k_BT\dot{N} \end{aligned} \tag{6.78}$$

where we have used the harmonic oscillator approximation to evaluate $\partial E/\partial T = 3Nk_B$ and $\partial E/\partial N = 3k_BT$. The change in internal energy arises from the energy carried away by evaporated atoms and the work performed on the atoms by the potential. In Section 6.1.6 we found that the rate of loss of internal energy due to evaporated atoms is given by $\dot{E}_{ev} = \dot{N}(U_0 + (W_{ev}/V_{ev})k_BT)$ where $0 < W_{ev}/V_{ev} \leq 1$ (see Eq. (6.39)). Since $T << U_0$ we will assume $\dot{E}_{ev} = \dot{N}U_0$. The change in internal energy due to the change in the potential is given by $\langle\dot{\mathcal{H}}\rangle_\epsilon = (\epsilon/2)\,\dot{U}_0/U_0 = (3Nk_BT/2)\,\dot{U}_0/U_0$ in the harmonic oscillator limit. Therefore, we have

$$U_0\,\dot{N} + \frac{1}{2}\,\frac{\dot{U}_0}{U_0}\,3Nk_BT = 3Nk_B\dot{T} + 3k_BT\dot{N}. \tag{6.79}$$

If we assume that the temperature is locked to a fraction of the well depth $U_0 = \xi k_BT$, Eq. (6.79) can be rearranged to give

$$\frac{\dot{N}}{N} = \frac{1}{2}\,\frac{3}{\xi - 3}\,\frac{\dot{U}_0}{U_0}. \tag{6.80}$$

Thus, we arrive at the scaling law

$$\frac{N_i}{N_f} = \left(\frac{U_i}{U_f}\right)^{\frac{1}{2}\,\frac{3}{\xi-3}}. \tag{6.81}$$

In the harmonic limit the phase space density is given by

$$\rho = N \left(\frac{h\,\nu}{k_B\,T} \right)^3 . \tag{6.82}$$

Since the trap oscillation frequency $\nu \propto \sqrt{U_0}$ and we are assuming $U_0 = \xi k_B T$ we can use the scaling law (6.81) to give the scaling law for the phase space density

$$\frac{\rho_f}{\rho_i} = \left(\frac{U_i}{U_f} \right)^{\frac{3}{2}\frac{\xi-4}{\xi-3}} . \tag{6.83}$$

Alternatively, using (6.81), we may write

$$\frac{\rho_f}{\rho_i} = \left(\frac{N_i}{N_f} \right)^{\xi-4} . \tag{6.84}$$

Figure 6.11 shows the phase space density ρ_0 versus well depth U_0 for the Boltzmann equation model (solid curve) as well as a fit to the scaling law (6.83) assuming $\xi = 10$ (dashed curve). Figure 6.12 shows the ρ_0 versus the number of atoms per state N for the Boltzmann equation model (solid curve) and a fit to the scaling law (6.84) for $\xi = 10$ (dashed curve).

The collision rate $\gamma \simeq n_0\,\bar{v}\,\sigma$, where $n_0 \simeq \rho/\lambda_{dB}^3$ is the peak density and $\bar{v} = \sqrt{8k_BT/\pi M}$ is the average velocity. Using (6.84) we find that γ scales as

$$\frac{\gamma_f}{\gamma_i} = \left(\frac{U_f}{U_i} \right)^{\frac{1}{2}\frac{\xi}{\xi-3}} . \tag{6.85}$$

Figure 6.13 shows the collision rate γ for the Boltzmann equation model (solid curve) as well as a fit to the scaling law (6.85) for $\xi = 10$ (dashed curve).

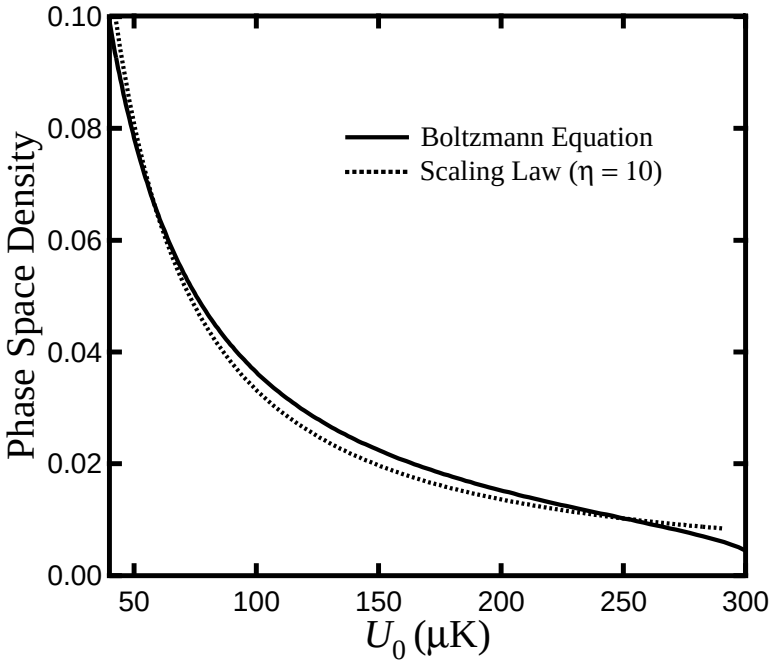

Figure 6.11: ρ_0 versus U_0 Scaling

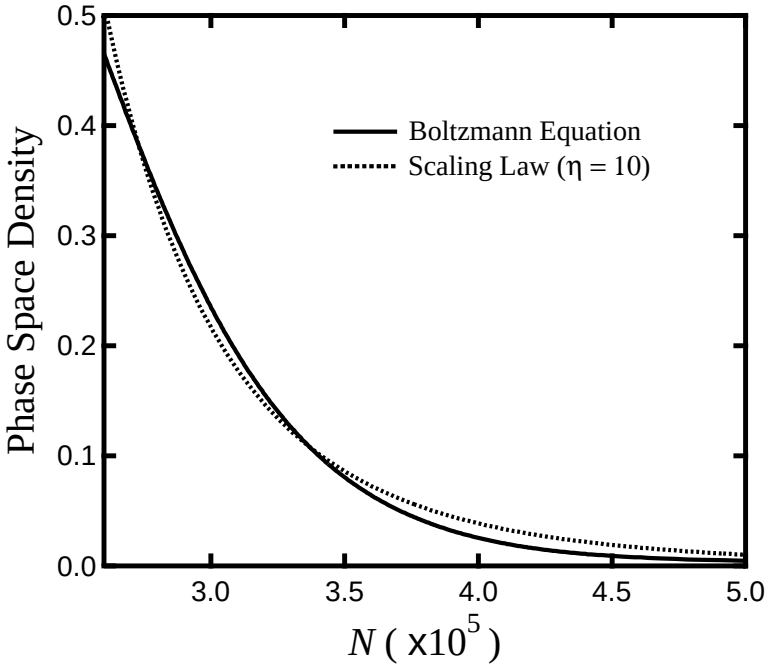

Figure 6.12: ρ_0 versus N Scaling

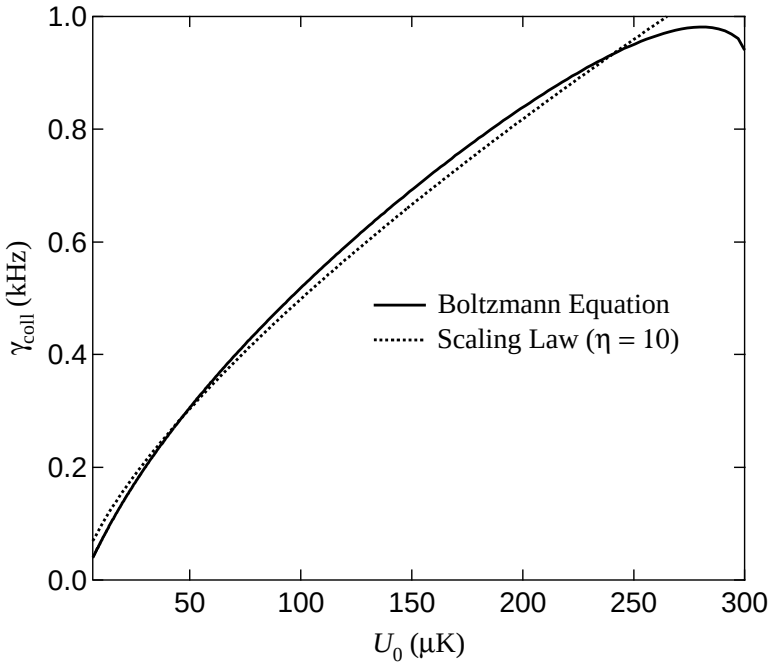

Figure 6.13: $\gamma_{\rm cl}$ Scaling

6.6 Evaporative Cooling of Fermionic Atoms to $T/T_F < 1$

In this section we include the effect of Fermi statistics in our model of evaporative cooling. Due to the Pauli exclusion principle no two fermions can occupy the same eigenstate of a system. In evaporative cooling, this suppresses the elastic collision rate as the atoms are cooled below $T/T_F = 1$ due to an effect known as Pauli blocking. For temperatures $T/T_F << 1$ the occupation number for states below the Fermi energy approach unity forming a filled Fermi sea. Fermions cannot scatter into these filled states. Thus, the collision rate is suppressed since the filled Fermi sea limits the energy phase space available to particles recoiling from an elastic collision. The recoiling atoms can only scatter into unfilled states.

Since Pauli blocking suppresses the collision rate for a Fermi gas cooled below $T/T_F = 1$, the evaporative cooling of fermions to temperatures well below T/T_F is widely believed to become challenging. Therefore, it is important to include the effect of Fermi statistics in the kinetic theory model when investigating evaporation trajectories which produce temperatures $T/T_F < 1$. In this section we will include the effect of Fermi statistics in the kinetic theory model and demonstrate that temperatures $T/T_F \simeq 0.1$ should be achievable given the initial conditions assumed above. In addition, we argue that the detrimental effect of Pauli blocking on evaporative cooling may not be as pronounced as originally anticipated.

6.6.1 Boltzmann Equation with Fermi Statistics

In order to include the effect of Fermi statistics in the kinetic Boltzmann equation, the collision integral appearing on the right hand side of (6.75) is replaced by [120]

$$\begin{aligned}\frac{M\,\sigma}{\pi^2\hbar^3}\int d\epsilon_1\,d\epsilon_2\,d\epsilon_3\,\delta(\epsilon_1+\epsilon_2-\epsilon_3-\epsilon_4)\mathcal{D}(\epsilon_{\min})\\ \times\left\{f(\epsilon_1)\,f(\epsilon_2)\,[1-f(\epsilon_3)]\,[1-f(\epsilon_4)]\right.\\ \left.-f(\epsilon_3)\,f(\epsilon_4)\,[1-f(\epsilon_1)]\,[1-f(\epsilon_2)]\right\}.\end{aligned} \tag{6.86}$$

This equation includes factors of $[1-f(\epsilon)]$ which take into account the fact that as the occupation number for a given energy state approaches unity the probability that a fermion can scatter into that state vanishes. The effect of Fermi statistics on the evaporative cooling of fermions from a truncated harmonic oscillator has also been treated recently in a similar manner [121, 122].

We have integrated (6.75) using the collision integral given by (6.86) for the same initial conditions used in Section 6.3.4. Figure 6.14 shows the time dependence of

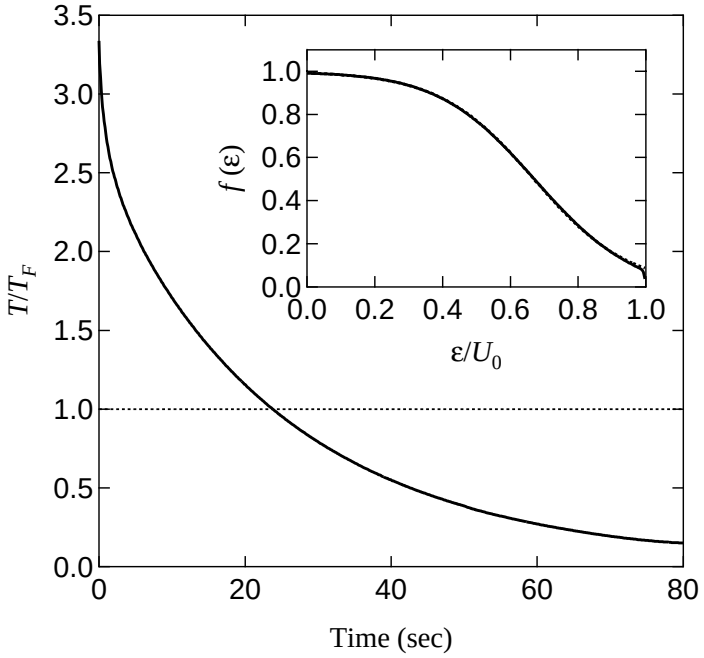

Figure 6.14: Evaporative cooling to $T/T_F < 1$. The main figure shows the temperature of a gas of fermions confined in an optical trap as a function of time as the well depth is adiabatically reduced. The inset shows the occupation number distribution function $f(\epsilon)$ after 80 seconds of evaporation demonstrating that $f(\epsilon)$ evolves into a Fermi distribution.

T/T_F over 80 seconds of evaporative cooling. At 80 seconds, the final temperature of the trapped atoms is $T = 15$ nK corresponding to $T/T_F = 0.15$. The inset to Figure 6.14 shows the occupation number distribution function $f(\epsilon)$ at the end of evaporation trajectory shown. As can be seen in the inset, occupation numbers approaching unity are present at the end of evaporation. The inset also shows a fit to the Fermi distribution function $1/(\exp[(\epsilon - \mu)/k_B T] + 1)$ as a dashed line. The temperatures over the entire evaporation trajectory are determined from fits to the Fermi distribution function. The Fermi temperature is calculated from $k_B T_F = \hbar\omega(6N)^{1/3}$ which is the harmonic oscillator result derived in Section 1.2.3.

Figure 6.15 shows T/T_F versus the number of atoms per state N. A factor of

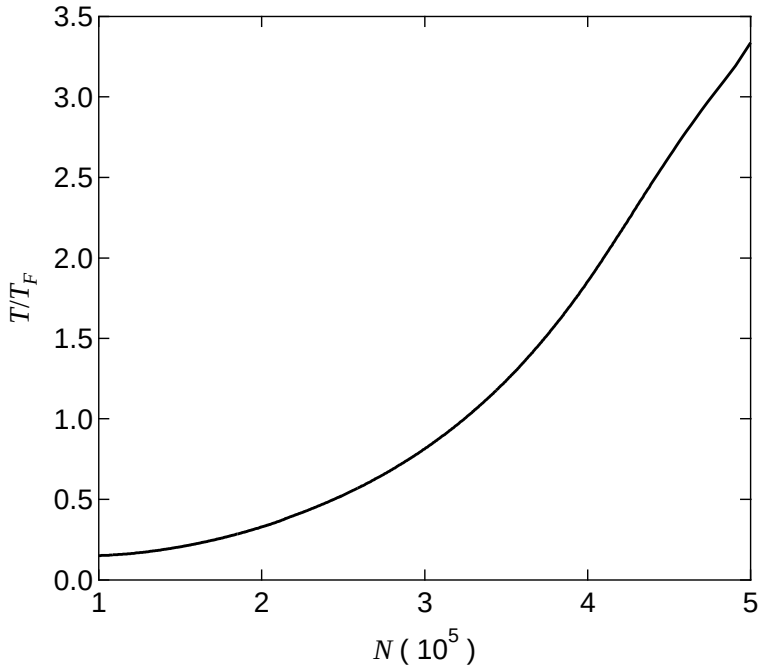

Figure 6.15: T/T_F versus N

five in the number of atoms per state is lost in decreasing the temperature from $T/T_F = 3.3$ (which corresponds to a phase space density $\rho = 0.0045$) to $T/T_F = 0.15$.

In the evaporation trajectories shown, the well depth U_0 is lowered expoentially with a time constant of 10 seconds. Beyond 80 seconds the well depth continues to lower exponentially and the ratio T/T_F begins to rise. This is due to the fact that as the well depth is lowered further, the well depth begins to cut into the Fermi sea causing a loss of atoms which lowers the Fermi temperature T_F and raises the ratio T/T_F. The time dependence for the well depth used in this model, namely $U_0 = U_i \exp(-t/\tau)$, is definitely not an optimized evaporative cooling trajectory for cooling fermions since the Fermi distribution at zero temperature corresponds to atoms filled up to a nonzero Fermi energy. Thus, any trajectory that lowers the

well depth to exactly zero is not optimum. Therefore, it is not obvious that much lower values for T/T_F cannot be achieved by evaporative cooling in an optical trap using an optimized trajectory. Exploration of different evaporation trajectories is an important future extension to this work.

Finally, we conclude this section by noting that the effect of Pauli blocking on the process of evaporative cooling of a two-state Fermi mixture to temperatures well below $T/T_F = 1$ may not be as severe as some authors have suggested. The collision rate in a two-state Fermi mixture is certainly suppressed at low temperature due to the effect of Pauli blocking. One can show that the collision rate in the trap scales as $(T/T_F)^2$ for $T << T_F$ [12]. However, the evaporation rate N_{ev} is determined by the rate at which an atom can escape from the trap in an elastic collision. Since the energy states above the well depth are unoccupied, only the atom that remains left behind in the trap suffers the effects of Pauli blocking. One can show that the evaporation rate scales as T/T_F for $T << T_F$. Thus, the energy loss rate due to evaporation $\dot{E}_{ev} = \dot{N}_{ev} U$ is suppressed as $T \to 0$. However, for a Fermi gas confined in a harmonic potential, the heat capacity $C \propto T$ for $T/T_F << 1$. Therefore, the suppression in the energy loss rate should be counterbalanced by the fact that the heat capacity of the gas also approaches zero as $T \to 0$. Evaporative cooling of a two-state Fermi mixture thus may yield temperatures well below $T/T_F = 1$.

6.7 Summary

In this chapter we have explored evaporative cooling of a two-state mixture of fermionic atoms confined in an optical trap. In the first part of the chapter, evaporative cooling from a well of fixed depth was considered. We extended the work of Ref. [115] by using kinetic theory to model the evaporation of atoms from

a gaussian potential which is appropriate for an optical trap. An s-wave Boltzmann equation which assumes an energy-independent cross section is used to determine the phase space distribution function $f(\epsilon)$ which under the assumption of sufficient ergodicity, only depends on the energy ϵ. The phase space distribution is found to be well described during the evolution by a Boltzmann distribution $f(\epsilon) = \rho \exp[-\epsilon/k_B T]\, \Theta(U_0 - \epsilon)$ truncated at the well depth U_0. Starting from a distribution for which $T >> U_0$ the temperature initially decreases rapidly to approximately 1/10 the well depth. The evaporation rate is exponentially suppressed by a factor $\exp(-U_0/k_B T)$. Once the temperature has reached approximately 1/10 the well depth, the evaporation rate stagnates due to the exponential suppression.

In Chapter 2 we found that certain two-state mixtures of ^{6}Li can exhibit very large values for the s-wave scattering length a_s. The effective s-wave cross section $\sigma = 4\pi a_s^2/(1 + k^2 a_s^2)$ exhibits a lorentzian dependence on the relative momentum wavenumber k. In the limit $ka_s << 1$ the cross section $\sigma = 4\pi a_s^2$ is energy-independent. However, for large values of a_s, the cross section exhibits an energy dependence even at the ultracold temperatures being considered in this dissertation. Therefore, we have extended the work of Ref. [115] to derive an s-wave Boltzmann equation assuming the cross section exhibits a lorentzian dependence on k. The resulting kinetic equation will be used for comparison to the experimental observation of evaporative cooling of optically confined ^{6}Li atoms in Chapter 7. Since the evaporation rate depends on the collision cross section, the energy-dependent s-wave Boltzmann equation can be used to extract the magnitude of the ^{6}Li scattering length in these experiments. However, we find that in order to measure a scattering length with a very large magnitude, the well depth U_0 must be chosen to be shallow so that the evaporation rate is not dominated by the unitarity limit of

the collision cross section $\sigma = 4\pi/k^2$ which is independent of a_s

Although measuring the rate of evaporation provides a practical means for measuring the large scattering lengths predicted to exist for ^{6}Li collisions, our primary interest in evaporative cooling is to increase the phase space density of the Fermi gas into the degenerate regime. Evaporation from a gaussian potential of fixed well depth causes the temperature to decrease and the phase space density of the gas to increase. Starting from a temperature $T >> U_0$ the phase space density can increase by $\sim 10^3$ in the fixed well before the evaporation rate stagnates. Since the evaporation rate is exponentially suppressed by a factor $\exp(-U_0/k_BT)$ as the gas cools, the well depth U_0 must be lowered as a function of time in order to sustain the evaporative cooling process. Therefore, we have also applied kinetic theory to study the evaporative cooling of atoms from a time dependent gaussian potential in which the well depth is lowered as a function of time. We find that for a large collision cross section, the temperature of the atoms remains at approximately 1/10 the well depth as U_0 is adiabatically lowered. The well depth, number of atoms and phase space density are found to be related by simple scaling laws to a good approximation. Assuming the collision cross section is high enough to maintain a ratio $k_BT/U_0 \leq 1/10$, the phase space density is found to vary approximately as $U_0^{-9/7}$ as the well depth is lowered. Thus, an increase in the phase space density by two orders of magnitude requires that the well depth be lowered by approximately two orders of magnitude. The number of atoms scales as the $\frac{1}{6}^{\text{th}}$ power of the phase space density for $k_BT/U_0 = 1/10$. Thus, a decrease in the number of atoms by only a factor of two is required to increase the phase space density by two orders of magnitude.

One can envision a feasible approach to attaining degeneracy in an optically

confined gas of ^{6}Li fermions. Based upon the conclusions drawn from Chapter 5, it is conceivable that the CO_2 laser trap can be loaded with 10^6 atoms per state by either increasing the well depth or lower the temperature of the atoms in the MOT. The atoms will undergo evaporation from the well while it remains at fixed depth. The temperature will be reduced to $\simeq 1/10$ of the well depth and in doing so may cost as many as $1/2$ of the initial population of atoms. For a $300\,\mu$K well depth with a trap oscillation frequency $\nu = (\nu_x\nu_y\nu_z)^{1/3} = 1300Hz$, $N = 5\times10^5$ atoms per state at a temperature of $30\,\mu$K have a phase space density $\simeq 5\times10^{-3}$. If the well is then adiabatically lowered by a factor of 200, the phase space density of the atoms will increase by more than a factor of 200 assuming the collision cross section is large enough for the atoms to maintain a the ratio $U_0/k_BT \geq 10$ due to evaporation. As the well depth is lowered the phase space density increases, approaching unity while the number of atoms is reduced by another factor of 2. At the end of evaporation, the $1.5\,\mu$K deep well will contain $\simeq 2.5\times10^5$ atoms per state at a temperature of $\simeq 150$ nK whith a phase space density of order unity.

Finally, we have explored the effect of Pauli blocking on the evaporative cooling process. By integrating the Boltzmann equation for a time-dependent gaussian potential which includes factors in the collision integral which describe the effect of Pauli blocking temperatures $T/T_F = 0.15$ can be achieved. With an optimized evaporative cooling trajectory, even lower temperatures may be possible. The predicted success of evaporative cooling of a two-state mixture of fermions to temperatures $T/T_F << 1$ may physically arise from the fact that the heat capacity of the harmonically confined Fermi gas goes to zero in proportion to T. The reduction in the heat capacity of the gas may counterbalance the fact that the evaporation rate also decreases in proportion to T due to the effect of Pauli blocking.

Chapter 7

Evaporative Cooling of Lithium Fermions

The development of a stable optical trap for neutral atoms has permitted the first study of evaporative cooling and interactions in a two-state mixture of lithium fermions. In this chapter, we review our initial studies of evaporative cooling performed in this system. The two primary results of this chapter are the observation of a large interaction strength between lithium fermions in agreement with the predictions of Chapter 2 and the use of evaporative cooling to increase the phase space density of the Fermi vapor by two orders of magnitude over that obtained in the MOT. These results pave the way for future experiments where optically trapped fermions are cooled to degeneracy and hopefully to a superfluid state.

In Chapter 2 we found that certain two-state mixtures exhibit a very large and widely tunable interaction strength. In this chapter, we study a two-state mixture of lithium fermions that is predicted to exhibit a very large and attractive scattering length at low magnetic field. We begin the chapter by describing how this interacting two-state mixture is generated from a noninteracting two-state mixture initially confined in the CO_2 laser trap. Immediately following the creation of this two-state mixture, the atoms are observed to undergo evaporative cooling from the optical trap. Evaporative cooling is distinguished by a loss of atoms with a corresponding reduction in the temperature of the gas. We measure the temperature

of the gas using a technique known as release and recapture [123] in which the velocity distribution of atoms is extracted by measuring the loss of atoms when the confining potential is removed for a variable amount of time. We find that the evaporation stagnates when the temperature of the gas is $\simeq 1/10$ of the well depth in agreement with the predictions of Chapter 6. By measuring the rate of evaporation from the trap, we determine the effective elastic scattering cross section $4\pi a^2$ to show that the magnitude of the scattering length $|a|$ is very large, in agreement with the predictions of Chapter 2. This result confirms for the first time that very large scattering lengths exist in ^{6}Li mixtures as required for the potential observation of a superfluid phase transition. Finally, forced evaporative cooling is accomplished by adiabatically lowering the CO_2 laser power which lowers the well depth as a function of time. Through forced evaporative cooling we achieve temperatures as low as $2.4\,\mu$K which corresponds to $T/T_F \simeq 5$ and a phase space density of 1.6×10^{-3}. By employing evaporative cooling in an optical trap we have achieved an increase in the phase space density by two orders-of-magnitude over that achieved in the MOT.

7.1 The $|3\rangle - |1\rangle$ Mixture

Theoretical treatments of an interacting Fermi gas have focused extensively on ^{6}Li [11, 12, 17–19, 39, 41, 42, 124]. Certain two-state ^{6}Li mixtures are predicted to be strongly attractive, i.e., they have anomalously large and negative scattering lengths [55] arising from a near-zero energy resonance in the triplet state [16] (see Chapter 2). It has been predicted that these strongly attractive mixtures can undergo a transition to a superfluid state at a relatively high transition temperature [17, 18, 39]. Furthermore, the two-state effective interaction potential is

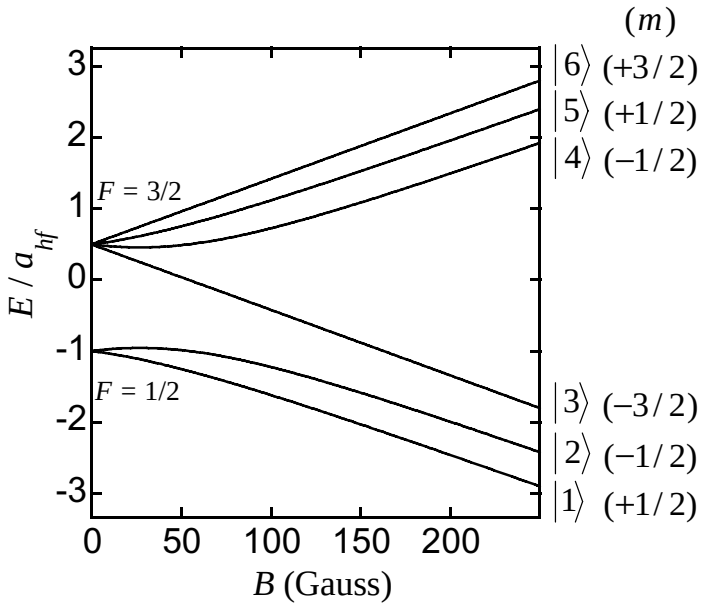

Figure 7.1: The ^{6}Li hyperfine states labeled $|1\rangle$-$|6\rangle$ in order of increasing energy in a magnetic field. At low field, the states $|1\rangle$ and $|2\rangle$ correspond to the $|F = 1/2, m\rangle$ states, while states $|3\rangle$ through $|6\rangle$ correspond to states $|F = 3/2, m\rangle$. At nonzero magnetic field, only the magnetic quantum number m, shown on the right, is conserved. The hyperfine constant $a_{hf} = 152.1$ MHz.

widely tunable in a magnetic field, permitting systematic studies of fundamental phenomena, such as collective oscillations for both the normal and superfluid phases [11, 12, 124], as well as new tests of superconductivity theory [18]. In addition, the large scattering length attainable with ^{6}Li yields a large elastic collision rate which may allow for efficient evaporative cooling.

As discussed in Chapter 2, magnetically trappable mixtures in ^{6}Li with large s-wave scattering lengths are not stable, since there are correspondingly large spin-exchange and dipolar decay rates [17, 19, 39, 55]. For this reason, we developed an ultrastable CO_2 laser trap to confine a stable mixture of the two lowest ^{6}Li hyperfine states (states $|1\rangle$ and $|2\rangle$ as defined in Appendix A and shown in Figure 7.1) . However, attaining a large and negative scattering length in this $|2\rangle$-$|1\rangle$ mixture

requires high magnetic fields $B \geq 800$ G to exploit either a Feshbach resonance or the triplet scattering length [19, 55] (also see Chapter 2). Unfortunately, generating a uniform magnetic field $B \geq 800$ G at the focus of the CO_2 laser trap is quite challenging when trying to satisfy the competing requirements for good optical access to the trapped atoms and ultra-high vacuum compatibility. At low field the scattering length for the $|2\rangle$ - $|1\rangle$ mixture is predicted to be small, going to zero at $B = 0$ [55].

In section Section 2.10, we showed that there exists another stable hyperfine state mixture in ^{6}Li (consisting of atoms in $|1\rangle$ and $|3\rangle$ shown in Figure 7.1) which has the following unique properties. First, we found that the scattering length a is large, negative, and widely tunable at *low* magnetic field B. The predicted scattering length is $-490\,a_0$ at $B = 8$ G and is expected to increase to $-1615\,a_0$ as $B \to 0$. Second, we found that this system is stable against spin exchange collisions provided that $B \neq 0$. In addition, the dipolar decay rate is predicted to be very small. Finally, as described below, a Raman π-pulse can be used to abruptly create this interacting mixture from the noninteracting $|2\rangle$-$|1\rangle$ mixture, a desirable feature for studies of many-body quantum dynamics. In this chapter, we describe experiments in which we study the evaporative cooling of a $|3\rangle$-$|1\rangle$ mixture of ^{6}Li atoms confined in the CO_2 laser trap.

Figure 7.2 shows the scattering length a_{31} for the $|3\rangle - |1\rangle$ mixture as a function of magnetic bias field B. We estimate $a_{31}(B)$ by using the asymptotic boundary condition (ABC) approximation [55] as described in Chapter 2. The scattering length varies from $-1620\,a_0$ ($\simeq 3a_T/4$ as $B \to 0$) to $-480\,a_0$ at $B = 10$ G. The scattering length can be tuned by a small applied field due to the fact that when $\mu_b B \sim \hbar^2/Ma_T^2$ the scattering length can change substantially as discussed in Sec-

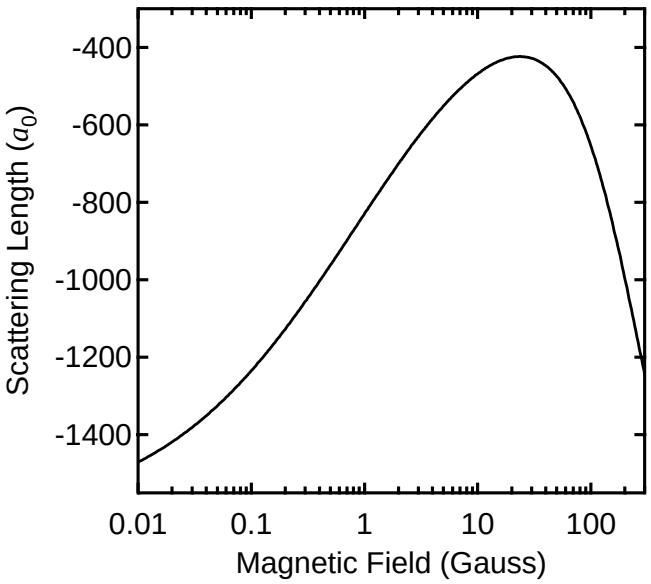

Figure 7.2: Field Dependence of a_{31}

tion 2.10. Since $a_T = -2160\,a_0$ this only requires $B \sim \frac{1}{10}$ G in order for a_{31} to be dramatically changed as is observed in Figure 7.2. The results of our approximate calculation for $B = 0$ to $B = 200$ G are confirmed within 10% by van Abeelen and Verhaar using a coupled channel calculation which includes the uncertainties in the potentials. At higher fields, near 800 G, we believe the scattering length exhibits a Feshbach resonance (not shown). Above this resonance, the scattering length approaches the triplet scattering length of $-2160\,a_0$.

The $|3\rangle - |1\rangle$ mixture is stable against spin-exchange collisions provided that a small bias magnetic field is applied. Spin-exchange inelastic collisions conserve the two-particle total magnetic quantum number M_T, where $M_T = -1$ for the $|\{3,1\}\rangle$ state. Note that $\{,\}$ denotes the antisymmetric two-particle spin state, as required for s-wave scattering which dominates at low temperatures. There are no lower-lying antisymmetric states with $M_T = -1$. Hence, exothermic collisions are

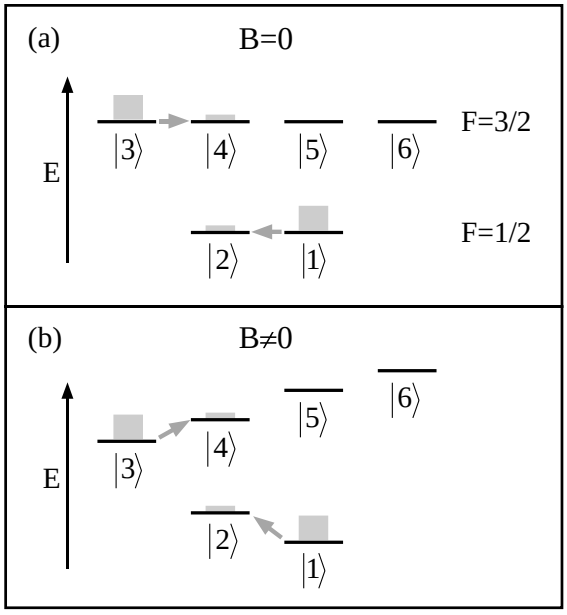

Figure 7.3: Spin-Exchange Collisions for $|\{3,1\}_-\rangle$. Since spin-exchange collisions conserve the two-particle total magnetic quantum number M_T, a collision can cause a transition to state $|\{4,2\}_-\rangle$ since $M_T = -1$ for both $|\{3,1\}_-\rangle$ and $|\{4,2\}_-\rangle$. However, application of a small bias magnetic field B causes the levels to Zeeman split, raising the energy of $|\{4,2\}_-\rangle$ above that of $|\{3,1\}_-\rangle$. If the energy of the two-particle states differ by more than the relative kinetic energy available, this spin-exchange collision will be energetically forbidden.

precluded. The only other states with $M_T = -1$ are $|\{4,2\}\rangle$ and $|\{5,3\}\rangle$. Without an adequate bias magnetic field, the energy of state $|\{4,2\}\rangle$ is nearly degenerate with state $|\{3,1\}\rangle$ and a transition to state $|\{4,2\}\rangle$ can occur during a collision. Transitions to this state lead to population in level $|4\rangle$ as shown in Figure 2.16. Then, exothermic $|\{3,4\}\rangle \rightarrow |\{3,2\}\rangle$ and $|\{4,1\}\rangle \rightarrow |\{1,2\}\rangle$ collisions can take place. However, with an adequate bias magnetic field, the energy of states $|\{4,2\}\rangle$ can be increased relative to that of state $|\{3,1\}\rangle$ by more than the maximum relative kinetic energy, i.e., twice the well depth during evaporative cooling. By energy conservation, spin-exchange transfer is then suppressed. In this case, the inelastic rate is limited to magnetic dipole-dipole (dipolar) interactions which contain a rank 2 relative coordinate operator of even parity (see Section 2.11). Since parity is conserved, and $\mathrm{p-wave} \rightarrow \mathrm{p-wave}$ scattering is frozen out at low temperature, the dominant dipolar process is a small $\mathrm{s} \rightarrow \mathrm{d}$ rate in which $|\{3,1\}\rangle \rightarrow |\{1,2\}\rangle$.

As described below, the evaporative cooling experiments employ an acousto-optic (A/O) modulator for the CO_2 laser which allows the CO_2 laser power reaching the trapping region to be adjusted. However, by using the A/O modulator the maximum power that reaches the trapping region is reduced from that described in Chapters 4 and 5. The maximum well depth that can be achieved in this case is $330\,\mu$K. A bias magnetic field of 8 G splits the two-particle energy states $|\{3,1\}_-\rangle$ and $|\{4,2\}_-\rangle$ by $\simeq 16$ MHz. This is over twice the maximum attainable energy at the largest well depth of $330\,\mu\mathrm{K} = 6.6$ MHz. Thus, application of an 8 Gauss field ensures that spin-exchange collisions are suppressed in this system.

7.2 Preparing the $|3\rangle - |1\rangle$ Mixture

In Chapters 3 and 5, we described the confinement of a $|2\rangle$-$|1\rangle$ mixture of ^{6}Li atoms in the CO_2 laser trap. This mixture is obtained by optically pumping the atoms out of the upper hyperfine $F = 3/2$ state during the final stage of transferring the atoms from the MOT into the CO_2 laser trap. Following the cooling phase described in Section 5.2.1 the MOT repumping beams are extinguished and the trapping beams which excite the $|F = 3/2\rangle \rightarrow |F' = 5/2\rangle$ transition are shifted in frequency to be on resonance and the intensity is adjusted such that the peak intensity $I \simeq I_{sat}$ for each of the six beams. These beams remain on for 100 μs. Without adjusting the intensity of the beams, a residual population remains in the $F = 3/2$ state as described in Section 4.3.2. However, when the intensity of each of the six beams is adjusted such that $I \simeq I_{sat}$, the atoms are optically pumped with essentially 100% efficiency into the lower $F = 1/2$ state. This is verified by observing that the fluorescence during the optical pumping phase decays to zero. We expect that the atoms in the MOT are unpolarized since the polarization of the optical beams changes over the dimension of an optical wavelength [125]. Thus, we expect that after the optical pumping phase, the atomic vapor will contain an equal population of atoms in the states $|1\rangle = \left|F = \frac{1}{2}, M_F = \frac{1}{2}\right\rangle$ and $|2\rangle = \left|F = \frac{1}{2}, M_F = -\frac{1}{2}\right\rangle$. This is verified experimentally as described toward the end of this section.

As described above, the $|2\rangle$-$|1\rangle$ mixture is noninteracting in a small magnetic field. In order to study interactions and evaporative cooling in a two-state mixture of lithium fermions we wish to create a mixture of atoms in the states $|3\rangle$ and $|1\rangle$. Starting from a 50/50 mixture of atoms in state $|2\rangle$ and $|1\rangle$, a $|3\rangle$-$|1\rangle$ mixture can be created by transferring the entire population of atoms in state $|2\rangle$ into state $|3\rangle$ as depicted in Figure 7.4. We have chosen to bring about this transference by using

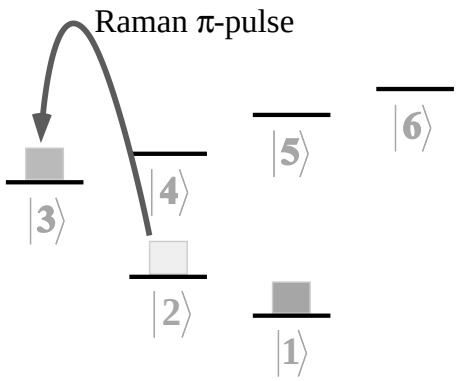

Figure 7.4: Creating the $|3\rangle$-$|1\rangle$ Mixture from the $|2\rangle$-$|1\rangle$ Mixture

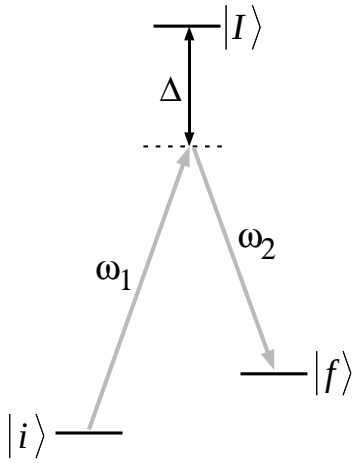

Figure 7.5: A Two-Photon Raman Transition

a two-photon Raman transition.

In a two-photon Raman transition, two optical beams of frequency ω_1 and ω_2 illuminate the atoms and cause a transition between an initial state $|i\rangle$ and a final state $|f\rangle$ as depicted in Figure 7.5. The electric field which impinges on the atoms is described by

$$\boldsymbol{E} = \frac{\boldsymbol{E}_1}{2} e^{-i\omega_1 t} + \text{c.c.} + \frac{\boldsymbol{E}_2}{2} e^{-i\omega_2 t} + \text{c.c.} \tag{7.1}$$

The difference frequency $\omega_{12} \equiv \omega_1 - \omega_2$ between the two optical fields is chosen such that $\omega_{12} = \omega_{fi} \equiv \omega_f - \omega_i$ where $\hbar\omega_i$ and $\hbar\omega_f$ are the energies of states $|i\rangle$ and $|f\rangle$ respectively. In the simplest case, the two photon transition proceeds through a single intermediate state $|I\rangle$ where $|i\rangle$ and $|f\rangle$ are only coupled to $|I\rangle$ through $\boldsymbol{E}_1$ and $\boldsymbol{E}_2$ respectively. Note that the optical fields are detuned from the single-photon resonance by $\Delta >> \Gamma_{\text{spont}}$ in order to avoid single-photon transitions into the excited state $|I\rangle$. As shown in [98, 104], if the detuning $\Delta >> \Gamma$, where Γ is the linewidth of the intermediate state $|I\rangle$, the intermediate state $|I\rangle$ may be adiabatically eliminated and the atomic wavefunction $|\psi(t)\rangle$ may be expressed as

$$|\psi(t)\rangle = A_i(t)\, e^{-i\omega_i t}\ |i\rangle + A_f(t)\, e^{-i\omega_f t}\ |f\rangle \tag{7.2}$$

where the amplitudes A_i and A_f obey the equations of motion

$$\dot{A}_i(t) = \frac{i\,\beta}{2}\, A_f(t) \tag{7.3a}$$

$$\dot{A}_f(t) = \frac{i\,\beta^*}{2}\, A_i(t). \tag{7.3b}$$

Here, β is the Raman Rabi frequency defined as

$$\beta = -\frac{\Omega_1^*\,\Omega_2^*}{2\,\Delta} \tag{7.4}$$

where $\Omega_1 \equiv \langle I|\boldsymbol{\mu}\cdot\boldsymbol{E}_1|i\rangle/\hbar$ and $\Omega_2 \equiv \langle I|\boldsymbol{\mu}\cdot\boldsymbol{E}_2|f\rangle/\hbar$ are the Rabi frequencies for the single-photon optical transitions driven by $\boldsymbol{E}_1$ and $\boldsymbol{E}_2$ respectively. $\boldsymbol{\mu}$ is the electric dipole moment operator.

If at $t = 0$ the atom is in the initial state $|i\rangle$, $A_i = 1$ and $A_f = 0$. If the atom is illuminated by the two optical fields for a time τ, (7.3b) may be solved to give

the amplitude A_f following the pulse as a function of the pulse duration τ. We find that $A_f = i\,\sin(|\beta|\,\tau/2)$. The probability P_f that an atom is found in the final state $|f\rangle$ following the pulse is given by $P_f = |A_f|^2 = \sin^2(|\beta|\,\tau/2)$. The quantity $|\beta|\,\tau$ is known as the pulse area. For $|\beta|\,\tau = \pi$, $P_f = 1$ signifying that the entire population of $|i\rangle$ is transferred into state $|f\rangle$. Thus, by applying a two-photon Raman π-pulse in ^{6}Li we can transfer the entire population from state $|2\rangle$ to state $|3\rangle$.

If the difference frequency ω_{12} is detuned from the Raman transition frequency ω_{fi} by an amount $\delta = \omega_{12} - \omega_{fi}$ one can show that the probability for finding an atom in the final state following a square pulse of duration τ is approximately given by

$$P_f \simeq \sin^2\left(\frac{|\beta|\,\tau}{2}\right)\,\mathrm{sinc}^2\left(\frac{\delta\,\tau}{2}\right) \tag{7.5}$$

if the pulse area $|\beta|\,\tau < 4\,\pi$ [98, 104]. Here $\mathrm{sinc}(x) = \sin(x)/x$. Thus, the spectral linewidth for a square pulse of duration τ is given in Hz by $\Delta\nu \simeq 1/\tau$ which corresponds to the FWHM of the sinc^2 function.

The level structure of ^{6}Li is more complicated than a simple three level system. Figure 7.6 shows how the two-photon Raman transition used to transfer population in state $|2\rangle$ to $|3\rangle$ in ^{6}Li is implemented. Two optical fields of frequency ω_1 and ω_2 illuminate the atoms. Both fields are linearly polarized. The optical beam of frequency ω_1 is $\hat{\boldsymbol{z}}$ polarized with its electric field vector oscillating along the quantization axis which is defined by an external uniform magnetic field B. The optical beam of frequency ω_2 is $\hat{\boldsymbol{x}}$ polarized. This beam copropagates with the field oscillating at ω_1. The $\hat{\boldsymbol{x}}$ polarized light is composed of equal portions of σ^+ and σ^- polarized light which are shown in Figure 7.6. The external uniform field B Zeeman splits the hyperfine state energies. If the energy levels are split such

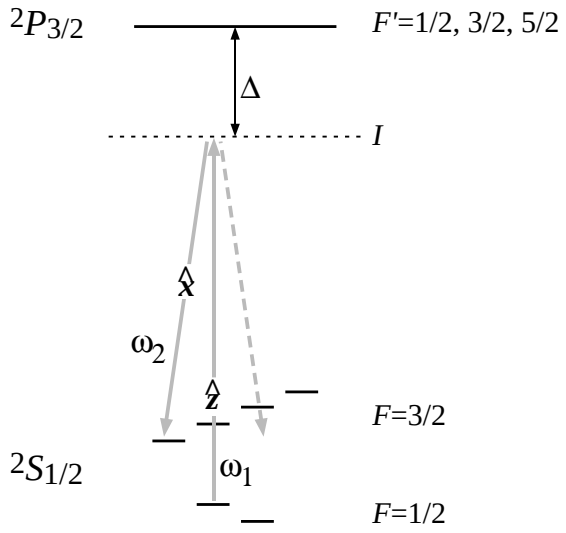

Figure 7.6: Raman Transition Used to Create the $|3\rangle$-$|1\rangle$ Mixture

that the difference frequency between any two levels is separated by more than the Raman transition linewidth, only one transition is resonant at any particular Raman difference frequency. Thus, the presence of the B field allows us to resolve the lower levels and we may treat the $|2\rangle$ to $|3\rangle$ transition as if they are the only ground state levels. Note that only the σ^- component of the $\hat{\boldsymbol{x}}$-polarized light contributes to the Raman transition since the σ^+ component (shown as a dashed line in Figure 7.6) is off resonance.

The intermediate state $|I\rangle$ used in the Raman transition is the first excited $^2P_{3/2}$ state in ^{6}Li. The $^2P_{3/2}$ state has hyperfine structure and contains three F'-levels, $F' = 1/2, 3/2$ and $5/2$. For a multi-level intermediate state $|I\rangle$, one must sum the Raman transition strength over the possible paths through all of the intermediate states. In this case the Raman Rabi frequency becomes

$$\beta = -\sum_I \frac{\langle f|\boldsymbol{\mu}\cdot\boldsymbol{E}_2|I\rangle\langle I|\boldsymbol{\mu}\cdot\boldsymbol{E}_1|i\rangle}{2\,\hbar^2\,\Delta_I}, \tag{7.6}$$

where Δ_I is the detuning from $|I\rangle$. In the experiments the detuning is much greater than the splitting between the hyperfine states F'. Thus, we may assume $\Delta_I = \Delta$ is independent of the particular intermediate state $|I\rangle$. For the Raman transition shown in Figure 7.6, only two intermediate states $|I\rangle$ contribute to the Raman transition and the sum (7.6) becomes

$$\begin{aligned}\beta &= -\frac{1}{2\,\hbar^2\,\Delta}\,[\langle F=1/2, M_F=-1/2|\boldsymbol{\mu}\cdot\boldsymbol{E}_1|F'=3/2, M_{F'}=-1/2\rangle \\ &\quad\times\langle F'=3/2, M_{F'}=-1/2|\boldsymbol{\mu}\cdot\boldsymbol{E}_2|F=3/2, M_F=-3/2\rangle \\ &\quad+\langle F=1/2, M_F=-1/2|\boldsymbol{\mu}\cdot\boldsymbol{E}_1|F'=1/2, M_{F'}=-1/2\rangle \\ &\quad\times\langle F'=1/2, M_{F'}=-1/2|\boldsymbol{\mu}\cdot\boldsymbol{E}_2|F=3/2, M_F=-3/2\rangle]. \qquad (7.7)\end{aligned}$$

The matrix elements required to evaluate (7.7) have been calculated previously by Tom Savard [98]. These matrix elements are given in Appendix C in terms of the dipole moment μ_0 for the $|F=3/2, M_F=3/2\rangle \rightarrow |F'=5/2, M'_F=5/2\rangle$ cycling transition. Since this is a closed transition, the dipole moment μ_0 can be calculated from its the relationship to the excited state lifetime $\Gamma = 4k^3\mu_0^2/3\hbar$, where Γ^{-1} is the excited state lifetime and $k = 2\pi/\lambda$ is the wavenumber for the atomic transition. Using the matrix elements found in Appendix C, we find that (7.7) is given by

$$\beta = -\frac{\mu_0^2\,E_2\,E_1}{2\,\hbar^2\,\Delta}\,\frac{1}{3}\,\sqrt{\frac{2}{3}} \qquad (7.8)$$

where we have taken into account the fact that only the σ^- component of the $\hat{\boldsymbol{x}}$ polarized beam takes part in the Raman transition.

The observed lifetime $\Gamma^{-1} = 27.2$ ns from which we find that $\mu_0 = 5.9$ Debye (1

Debye = 10^{-18} esu·cm). We can reexpress (7.8) as

$$\beta = -\frac{\Omega_0^2(I_1)}{\Delta}\sqrt{\frac{I_2}{I_1}}\frac{1}{3\sqrt{6}} \tag{7.9}$$

where I_1 and I_2 are the intensities of the Raman beams and $\Omega_0(I_1) \equiv \mu_0 E_1/\hbar = 1.6\times10^8\sqrt{I_1[\mathrm{mW/mm^2}]}$. Here Ω_0 is expressed in rad/s and I_1 is given in mW/mm^2.

In the experiment, the Raman beams are detuned from the $^2P_{3/2}$ state by an amount $\Delta = 2\pi \times 710$ MHz in order to avoid optical pumping due to single-photon excitation into the excited state. The Raman beams have been spatially mode matched by coupling them both into a single mode optical fiber before they propagate to the trapping region. The ratio of intensities $I_2/I_1 = 2$. Typically, the intensity of the light at frequency ω_1 is $I_1 = 1.56\,\mathrm{mW/mm^2}$. To generate a Raman π-pulse to transfer the population of atoms in state $|2\rangle$ to $|3\rangle$, we require that the pulse area $|\beta|\tau = \pi$. For $I_1 = 1.56\,\mathrm{mW/mm^2}$, $I_2/I_1 = 2$ and $\Delta = 2\pi\times710$ MHz, we find from Eq. (7.9) that $|\beta| = 1.7\times10^6$ rad/s. Thus, in order to generate a π-pulse, the Raman beams must be pulsed on for a time $\tau = \pi/|\beta| = 1.8\,\mu$s. Experimentally, we find that the maximum number of atoms is transferred into state $|3\rangle$ for a pulse length of $2\,\mu$s, in good agreement with prediction.

The spectral resolution for this pulse duration is $\simeq 1/\tau = 0.5$ MHz. We typically apply a uniform 8 Gauss magnetic field which, as described in Section 7.1, is chosen to suppress spin-exchange collisions once the $|3\rangle$-$|1\rangle$ mixture has been created. In an 8 G field the $|2\rangle$-$|3\rangle$ Raman transition frequency $\simeq$ 213.5 MHz. The nearest lying Raman transitions which can be driven by these fields are the $|2\rangle \rightarrow |5\rangle$ and $|1\rangle \rightarrow |4\rangle$ transitions which are both resonant at $\simeq$ 229 MHz and are thus far detuned from resonance with the $|2\rangle \rightarrow |3\rangle$ transition.

Note that the Raman Rabi frequency is proportional to the intensity of the

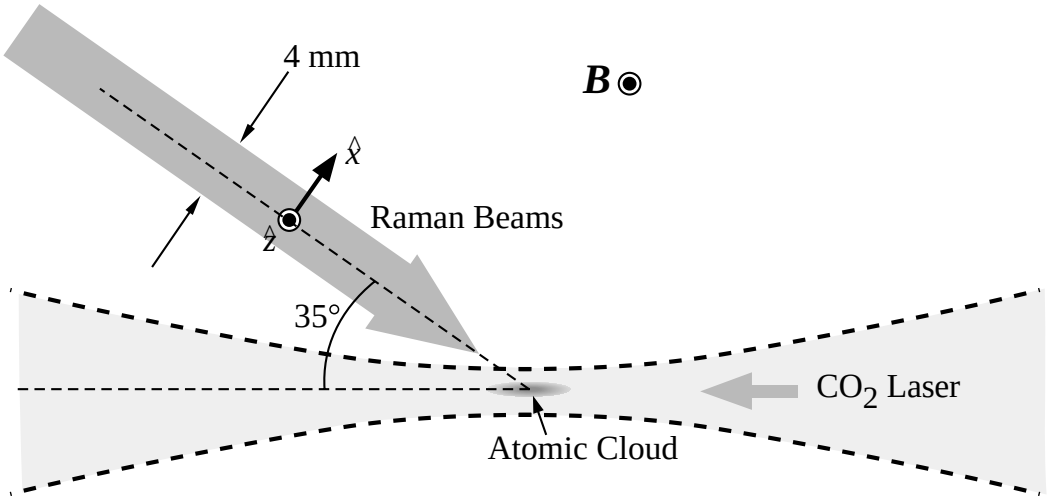

Figure 7.7: Orientation of the Raman Beams

Raman beams. Therefore, it is important for the intensity profile of the Raman beams to be approximately constant over the spatial dimension of the trapped atomic vapor so that all of the atoms see approximately the same pulse area. In addition, the Raman beams also cause an intensity dependent light shift of the transition frequency. For $I_1 = 1.56\,\mathrm{mW/mm^2}$, $I_2/I_1 = 2$ and $\Delta = 2\pi \times 710$ MHz, the light shift caused by the Raman beams shift the Raman transition frequency by approximately 0.23 MHz. Since this frequency shift is proportional to the intensity, it is again important to keep the intensity constant across the sample.

The configuration for the Raman beams used in the experiment is shown in Figure 7.7. The Raman beams have an elliptical gaussian profile with $1/e$ diameter of 4.0 mm and 1.6 mm in the $\hat{\boldsymbol{x}}$- and $\hat{\boldsymbol{z}}$- dimensions respectively as shown in Figure 7.7. The Raman beam of frequency ω_1 is $\hat{\boldsymbol{z}}$-polarized while the Raman beam of frequency ω_2 is $\hat{\boldsymbol{x}}$-polarized. The $\hat{\boldsymbol{z}}$-axis is defined by the uniform magnetic field $\boldsymbol{B}$ which is directed out of the page in Figure 7.7. For reference, the $\hat{\boldsymbol{z}}$-axis is parallel to the axis of the slower described in Chapter 4. The $\hat{\boldsymbol{x}}$-axis is perpendicular to the

$\hat{\boldsymbol{z}}$-axis and perpendicular to the direction of propagation of the Raman beams. The Raman beams propagate at an angle of 35° with respect to horizontal. Thus, the spatial intensity profile of the Raman beam projected along the axis of the CO_2 laser trap has a $1/e$ diameter of $4\,\mathrm{mm}/\sin 35^\circ \simeq 7\,\mathrm{mm}$. The dimensions of the trapped atomic cloud are $\simeq 1.6\,\mathrm{mm}$ along the CO_2 laser axis (horizontal) and $\simeq 0.1\,\mathrm{mm}$ in the $\hat{\boldsymbol{z}}$-dimension (where $\hat{\boldsymbol{z}}$ is the quantization axis). The $1/e$ intensity diameter of the Raman beams are approximately 4.4 and 16 times the dimension of the atomic cloud along the axis and in the radial direction of the CO_2 laser beam respectively. This ensures that the intensity profile of the Raman beams across the atomic cloud is approximately constant. The total power contained in the Raman beams during a Raman pulse is typically 3.75 mW and 7.5 mW in the $\hat{\boldsymbol{x}}$- and $\hat{\boldsymbol{z}}$-polarized beams respectively.

The Raman beams need to be spatially overlapped with the trapped atomic cloud. To initially align the beam, a beam containing frequencies resonant with the single-photon ${}^2S_{1/2} \rightarrow {}^2P_{3/2}$ transitions is made to copropagate with the Raman beam. The change in the position of the MOT due to the radiation pressure from this beam is easily observed by eye. Once this initial alignment is accomplished, the alignment of the Raman beams with the atoms confined in the CO_2 laser trap is peaked up. This is accomplished by measuring the number of atoms stored in the CO_2 laser trap following a several millisecond long Raman beam pulse. During this long pulse, the Raman beams can optically pump a signficant number of atoms into the upper $F = 3/2$ hyperfine levels. Inelastic collisions between atoms in the $F = 3/2$ levels cause the number of atoms stored in the CO_2 laser trap to decay. Thus, to align the Raman beams, the number of atoms which remain in the CO_2 laser trap following the Raman pulse is minimized by adjusting the position of the

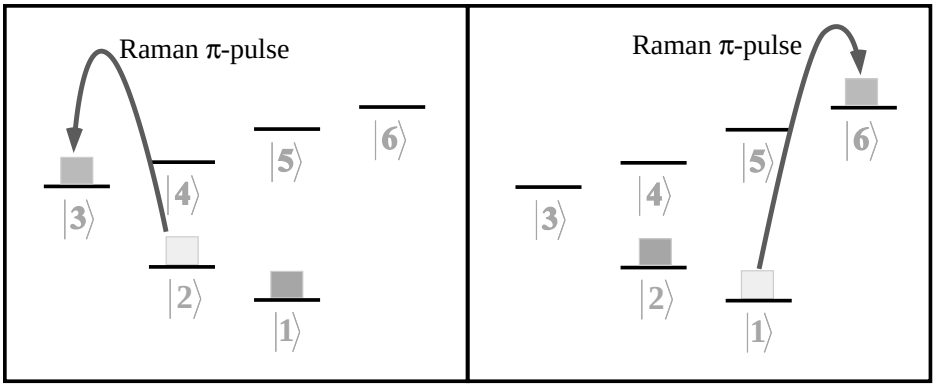

Figure 7.8: Preparing a $|6\rangle$-$|2\rangle$ Mixture

Raman beams.

As discussed at the beginning of this section, attaining a 50/50 mixture of atoms in states $|3\rangle$ and $|1\rangle$ requires that prior to the Raman π-pulse a 50/50 mixture of atoms populates states $|1\rangle$ and $|2\rangle$. We believe that after the atoms are optically pumped into the $F = 1/2$ state during the final stage of loading from the MOT the atoms are unpolarized and have an equal probability of being in either of the $|F = 1/2, M_F = \pm 1/2\rangle$ states. We wish to verify that this assumption is correct.

In order to measure the population of states $|1\rangle$ and $|2\rangle$ in the atomic vapor following the optical pumping phase, we use a Raman π-pulses to selectively excite either the $|2\rangle \rightarrow |3\rangle$ transition or the $|1\rangle \rightarrow |6\rangle$ transition as shown in Figure 7.8. The $|2\rangle \rightarrow |3\rangle$ and $|1\rangle \rightarrow |6\rangle$ transitions occur at Raman transition frequencies of $\simeq 213.5$ MHz and $\simeq 243.5$ MHz respectively in an 8 G magnetic field and are easily resolvable. Following the Raman π-pulse, the number of atoms in the $|F = 3/2\rangle$ state is measured by exciting the atoms with a probe beam resonant with the $\left|^2S_{1/2}, F = 3/2\right\rangle \rightarrow \left|^2P_{3/2}, F' = 5/2\right\rangle$ transition. Note that this probe beam does *not* contain a repumping beam resonant with the $\left|^2S_{1/2}, F = 1/2\right\rangle \rightarrow \left|^2P_{3/2}, F' = 3/2\right\rangle$ transition. Thus, atoms in the lower $|F = 1/2\rangle$ state do not fluoresce. While the

probe beam is on, the atoms are optically pumped into the lower $|F = 1/2\rangle$ state and thus the fluorescence signal quickly decays in a few absorption-emission cycles. Unfortunately, due to the geometry of the system, we cannot use a σ^+ polarized probe beam which could optically pump the atoms into the cycling transition. Thus, the size of the fluorescence signal is greatly reduced when the repumping beam is not used. Unfortunately, our system does not have enough signal to noise to measure the number of atoms in the CO_2 laser trap without the use of a repumping beam. However, we can measure the population balance between states $|1\rangle$ and $|2\rangle$ immediately after the atoms are released from the MOT. Following the optical pumping phase, the magnetic field gradient is turned off and a uniform 8 G field is applied. Within 3 ms, the Raman π-pulse which excites either the $|2\rangle \rightarrow |3\rangle$ or the $|1\rangle \rightarrow |6\rangle$ transition fires and the number of atoms transferred into the $|F = 3/2\rangle$ state is measured. We find, using this technique, that the population imbalance between the states $|1\rangle$ and $|2\rangle$ is less than 5%.

7.3 CO_2 Laser Optics

The evaporative cooling experiments described in this chapter employ an acousto-optic (A/O) modulator for the CO_2 laser which allows the CO_2 laser power reaching the trapping region to be adjusted. A number of the experiments described in this chapter require that the CO_2 laser power reaching the trapping region be adjusted. For example, in Section 7.6 we describe experiments in which we modulate the CO_2 laser power at various frequencies to locate parametric resonances in order to characterize the CO_2 laser potential. In Section 7.6 the temperature of atoms is measured by turning off the CO_2 laser for a variable amount of time and measuring the number of atoms which are recaptured when the potential is turned back

on. Finally, in Section 7.9, we explore forced evaporative cooling by adiabatically lowering the CO_2 laser power reaching the trapping region.

An acousto-optic (A/O) modulator, as described in Section 4.2.4, provides a convenient means for continuously adjusting the amount of laser power that is deflected toward a particularly section of the experiment. By adjusting the RF power that is transmitted to the acousto-optic crystal, the amount of light that is deflected into the first order reflection can be adjusted. However, in comparison to the A/O modulators used to deflect visible light, the A/O modulator used to deflect a 65 W CO_2 laser beam is a much more unwieldy piece of equipment. In order to deflect 65 W of CO_2 laser power, approximately 50 W of RF power is required. Since this power must be dissipated by an absorber at one end of the crystal, A/O modulators for CO_2 lasers require water cooling. The physical size of the crystal is also an order of magnitude larger than its visible counterpart. The acousto-optic crystal is made of Ge which has the unfortunate properties that it is opaque to visible light and it has a larger absorption coefficient than ZnSe for 10.6 μm radiation.

The CO_2 laser power which reaches the trapping region in the experiments described below is controlled by an A/O modulator and driver purchased from IntraAction Corporation. The modulator is a model AGM-4010BG1 which is driven at 40 MHz. The Bragg diffraction angle is 38.5 mrad. The acoustic-wave in this modulator has a usable height of 1 cm. The Ge crystal is $\simeq$ 1.5 cm tall and $\simeq$ 4.5 cm deep along the direction of propagation of the laser. The modulator is connected to a recirculating coolant system which is cooled by a Neslab model CFT-33D chiller. A mixture of Ethelyne-Glychol and water circulates through the closed loop system so that the modulator can be cooled to temperatures as low as

0° C. A gas feedthrough has been added to the housing of the A/O modulator so that dry nitrogen can be blown across the face of the crystal in order to prevent water vapor condensation when the modulator is cooled below 15° C. The crystal is cooled to these low temperatures in order to reduce the absorption coefficient of Ge at 10.6 μm which is strongly temperature dependent. At 15° C, the optical insertion loss is estimated to be 7%. However, the optical insertion loss is estimated to drop to 4.5% at 0°C. The modulator is driven by a model GE-4050 50 W RF driver. The driver produces a fixed frequency of 40 MHz which can be amplitude modulated.

The A/O modulator is placed directly after the first fold mirror following the output from the CO_2 laser. There are no focusing lenses used to focus the CO_2 laser through the A/O crystal. The $1/e$ diameter of the CO_2 laser at the output is approximately 6 mm and is small enough to achieve efficient diffraction into the first order reflection. We typically achieve $80-85\%$ diffraction efficiency into the first order diffraction reflection at full RF drive power. The overall efficiency into the first order reflection including absorption loss is between $73-78\%$. The deflected beam is directed toward the trapping region while the undeflected beam is absorbed by a water-cooled beam dump.

Unfortunately, we have observed that the acousto-optic modulator causes astigmatism in the CO_2 laser beam. The beam is focused as it propagates through the crystal with a different focal length in the vertical and horizontal directions. To the best of our knowledge the astigmatism is caused by thermal lensing in the Ge crystal. The source of the heat appears to arise from the 50 Watts of acoustic power which propagates through the crystal. The astigmatism disappears as the RF power supplied to the crystal is lowered. Cooling the crystal to 0° C does not correct the astigmatism. A solution to this problem remains outstanding.

Following the acousto-optic modulator, a diffractive beam splitter has been added to the CO_2 laser beam path. This diffractive beam splitter splits off $\simeq 1\%$ of the CO_2 laser beam power into two beams. One of the beams is absorbed by a beam dump while the other beam is monitored by the PD-3 fast infrared detector. This allows us to monitor the CO_2 laser beam power being used to form the trap.

Due to the thermal lensing caused by the A/O modulator, the CO_2 laser beam is expanded by a different telescope than that used in Chapter 4. The telescope is formed by a 3.8 cm focal length meniscus lens and a 28.6 cm focal length plano convex lens. The CO_2 laser trap is formed at the focus of a 19 cm focal length aspheric lens. This combination of lenses is found to give the largest number of trapped atoms loaded from the MOT.

7.4 Observation of Evaporation

Figure 7.9 shows the salient features of the timing diagram used in the evaporative cooling experiments. The atoms are loaded from the Zeeman slower into the MOT for 3 seconds during the MOT loading phase. The frequency and intensity of the MOT laser beams are adjusted to cool the atoms to near the Doppler cooling limit as described in Chapter 5. The cooling phase lasts for 4 ms. The repumping beam is then shut off and the intensity and frequency of the MOT beams are adjusted to optically pump the atoms into the $|F = 1/2\rangle$ ground state with nearly 100% efficiency. The optical cooling beams are extinguished after 100 μs of optical pumping and the quadrupole magnetic field is shut off. With a CO_2 laser trap depth of 330 μK, up to 4×10^5 atoms are confined in the lowest-lying hyperfine states at an initial temperature between 100 and 200 μK. Immediately after the quadrupole magnetic field is shut off, the uniform 8 G magnetic field is applied and after a 0.5

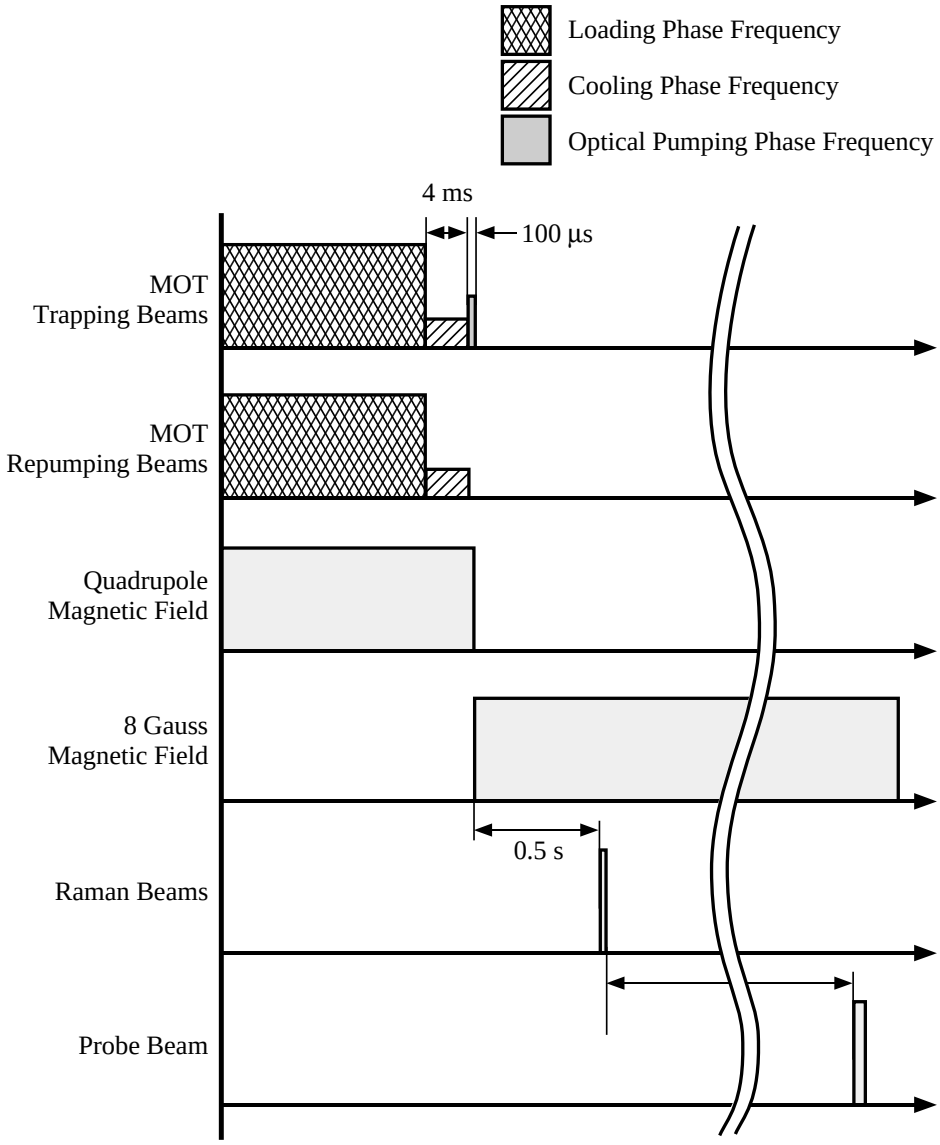

Figure 7.9: Timing Diagram for Evaporative Cooling Experiments

second delay the Raman π-pulse fires to create the interacting $|3\rangle$ - $|1\rangle$ mixture. Once this mixture is created, the two-state mixture of lithium fermions is expected to interact via s-wave collisions with a scattering length of $-490\,a_0$. A variable delay time after the $|3\rangle$ - $|1\rangle$ mixture is created, we measure the number of atoms confined in the trap by monitoring the fluorescence induced by pulsed, retroreflected, $\sigma^{\pm}$ probe and repumper beams which are strongly saturating ($I/I_{sat} = 26$ for the strongest transition).

Since the temperature of the atoms is comparable to the well depth when the atoms are loaded from the MOT, we expect that the atoms will undergo evaporative cooling. Evaporation is characterized by a loss of atoms with a corresponding reduction in the temperature of the atoms that remain confined in the trap. We expect that the evaporation process eventually stagnates when the temperature of the atoms is approximately 1/10 of the well depth.

Figure 7.10 shows the number of atoms confined in the CO_2 laser trap as a function of time following the Raman π-pulse. The data are shown as filled circles. Each data point is the mean obtained from ten separate measurement sequences through the complete decay curve. The error bars shown indicate the standard deviation of the mean. The number of atoms indicated is the total number of atoms contained in the CO_2 laser trap (i.e. twice the number of atoms per state). The number of atoms is observed to undergo an initial rapid decay followed by a much slower decay and resembles the evaporation curves shown in Section 6.2 for evaporation from a well of fixed depth. As determined in Section 7.5, the well depth for the CO_2 laser trap in this case is $\simeq 300\,\mu$K. We expect that the loss of atoms is due to evaporation. In Section 7.6, we describe how the temperature of the atoms is measured and find that after 20 seconds of evaporation the atoms have reached

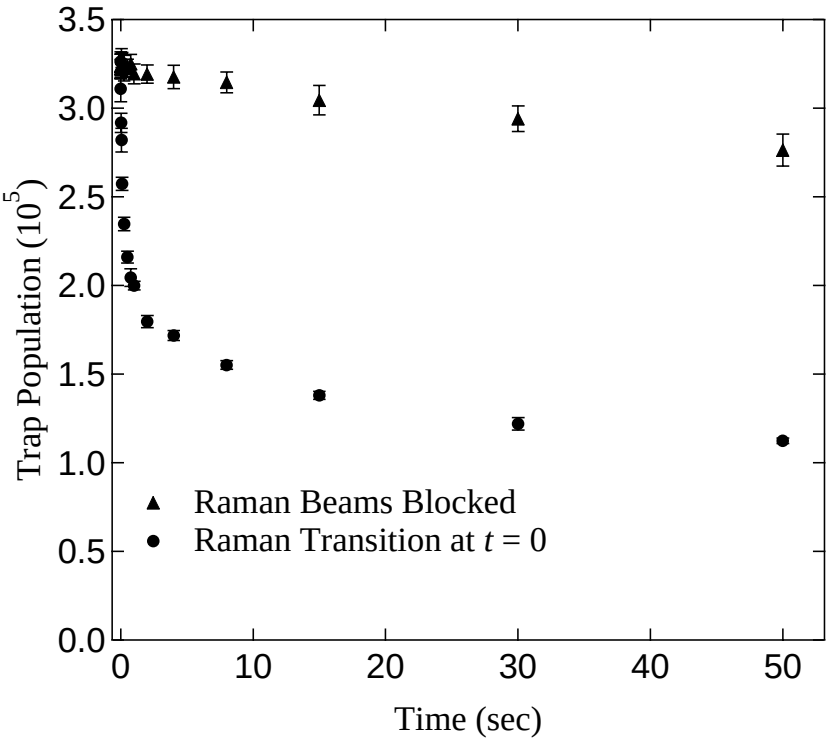

Figure 7.10: Observation of evaporation. The number of atoms N as a function of time t when the Raman transition occurs at $t = 0$ (circles) and when the Raman beams are blocked (triangles).

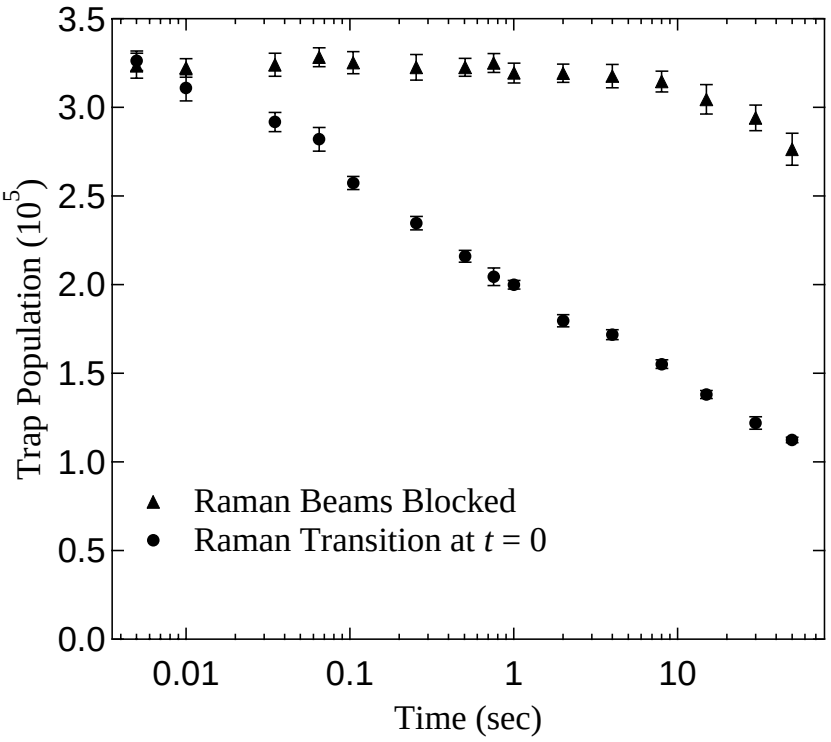

Figure 7.11: Observation of evaporation (logarithmic scale). The same data as in Figure 7.10 plotted on logarithmic time axis.

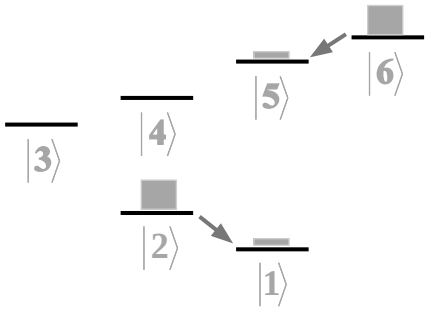

Figure 7.12: Spin-Exchange Collisions in a $|6\rangle$-$|2\rangle$ Mixture

a temperature of approximately 1/10 the well depth.

If the beams which induce the Raman π-pulse are physically blocked, the data points shown as filled triangles in Figure 7.10 are obtained. In this case, a 50/50 mixture remains in states $|1\rangle$ and $|2\rangle$. The slow decay is consistent with an exponential decay with a $\simeq 300$ s time constant. Beyond 50 seconds the number of atoms in the $|2\rangle$-$|1\rangle$ mixture continues to decay exponentially with a time constant $\simeq 300$ s. The $|3\rangle$ - $|1\rangle$ mixture, on the other hand, exhibits an exponential decay with a 370 second time constant for data points beyond 50 seconds. The difference in the time constant between the lifetime of the $|2\rangle - |1\rangle$ mixture and the $|3\rangle - |1\rangle$ mixture once evaporation has stagnated may be due to a small residual heating rate in the CO_2 laser trap or a finite scattering length for the $|2\rangle - |1\rangle$ mixture. If the temperature of the atoms is 1/2 the well depth when initially loaded into the $|2\rangle - |1\rangle$ mixture, the difference in time constants can be explained by a $\simeq 50$ nK/s heating rate assuming that the 370 s time constant is due to background collisions. Alternatively, the difference in the time constants could be explained by a $\simeq 5\,a_0$ scattering length for the $|2\rangle - |1\rangle$ mixture.

By adjusting the difference frequency between the Raman beams we can also choose to excite the $|1\rangle \rightarrow |6\rangle$ transition to create a $|6\rangle$ - $|2\rangle$ mixture of lithium

atoms in the optical trap. The $|6\rangle$ - $|2\rangle$ mixture is unstable with respect to spin-exchange collisions as shown in Figure 7.12. An exothermic spin-exchange collision may occur in which the state $|\{6,2\}_-\rangle$ makes a transition to the state $|\{5,1\}_-\rangle$. This collision is allowed since both the $|\{6,2\}_-\rangle$ and $|\{5,1\}_-\rangle$ two-particle states have total magnetic quantum number $M_T = 1$. In an 8 G field, the energy released in the collision is just large enough to eject both atoms involved in the collision from the trap. However, if the atom in state $|1\rangle$ is not ejected from the trap in this initial collision the atom will remain in the trap since state $|1\rangle$ is a stable state. On the other hand, if the atom in state $|5\rangle$ is not initially ejected, the atom will most likely suffer another spin-exchange collision in which either $|\{6,5\}_-\rangle \rightarrow |\{6,1\}_-\rangle$ or $|\{5,2\}_-\rangle \rightarrow |\{2,1\}_-\rangle$. In either case approximately 200 MHz of energy, which is over twenty times the well depth, is released in the collision.

Figure 7.13 shows the number of atoms as a function of time after the $|6\rangle$ - $|2\rangle$ mixture has been created. After an initial rapid drop in the number of atoms, the trap population decays slowly with approximately 1/8 of the initial population remaining in the trap. Presumably, the initial rapid decay is caused by the spin-exchange processes described above. The residual population of atoms that remains in the trap is most likely a stable mixture of atoms in either states $|1\rangle$ and $|6\rangle$ or states $|1\rangle$ and $|2\rangle$.

For small uniform magnetic fields, the Raman Rabi frequency for the $|1\rangle \rightarrow |6\rangle$ transition is identical to the Raman Rabi frequency for the $|2\rangle \rightarrow |3\rangle$ transition as can be seen from the symmetry of the states. Thus, the same pulse area which induces a $|1\rangle \rightarrow |6\rangle$ Raman π-pulse will also generate a π-pulse for the $|2\rangle \rightarrow |3\rangle$ transition albeit at a different Raman resonance frequency. We use this fact to peak up the π-pulse for the $|2\rangle \rightarrow |3\rangle$ transition from day to day. We use the observed

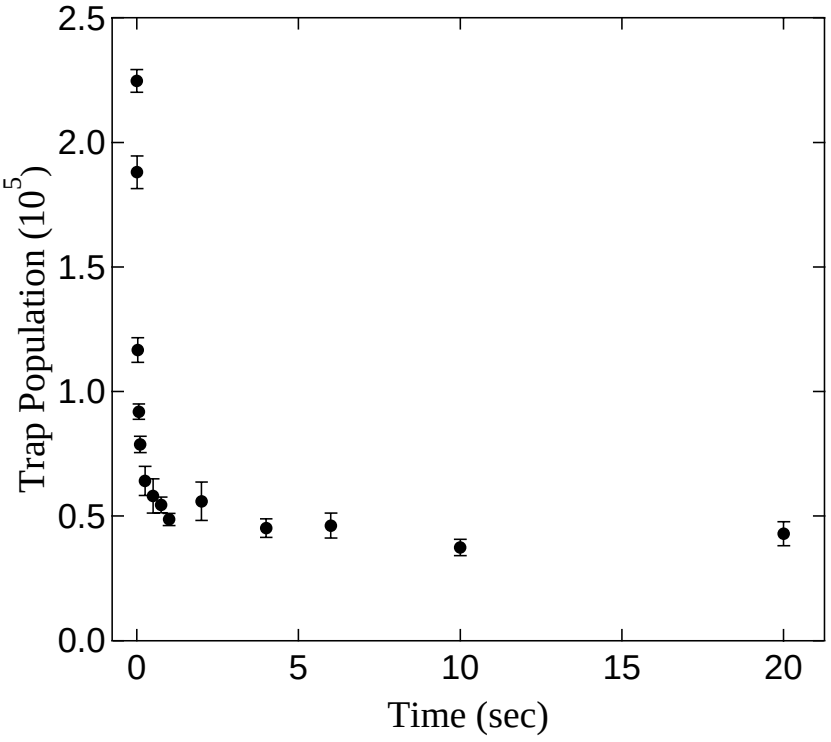

Figure 7.13: Decay of the $|6\rangle$-$|2\rangle$ mixture. The number of atoms as a function of time t following a Raman pulse at $t = 0$ which creates a $|6\rangle$-$|2\rangle$ mixture.

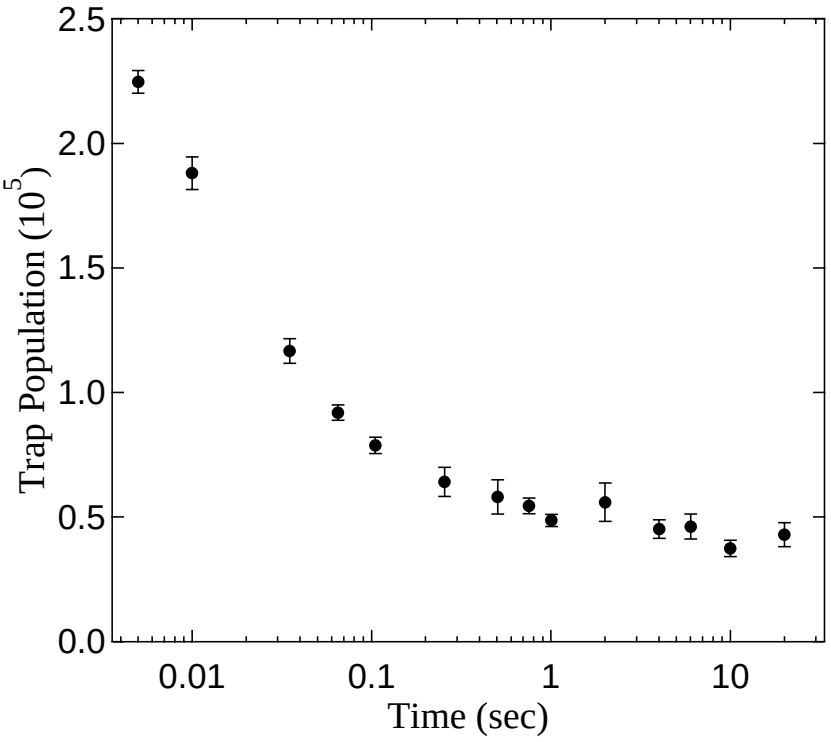

Figure 7.14: Decay of the $|6\rangle$-$|2\rangle$ mixture (logarithmic scale). The same data as in Figure 7.13 plotted on a logarithmic time scale.

loss in the $|6\rangle - |2\rangle$ mixture to peak up the π-pulse for the $|1\rangle \rightarrow |6\rangle$ transition. Since state $|2\rangle$ is stable against spin-exchange collisions, the number of atoms confined in the CO_2 laser trap after several seconds is minimized when the maximum number of atoms have been transferred via the Raman transition into the unstable state $|6\rangle$. Thus, we peak up the $|2\rangle \rightarrow |6\rangle$ π-pulse by minimizing the number of atoms detected in the CO_2 laser trap approximately 1 second after the mixture is generated. The same pulse duration can be used to induce a π-pulse in the $|1\rangle \rightarrow |3\rangle$ transition although the difference frequency of the Raman beams must be adjusted to drive this transition.

7.5 Parametric Resonance

In order to verify that we are observing evaporation and not just trap loss in Figure 7.10 we need a technique to measure the temperature of the atoms after the evaporation process has stagnated. In Section 7.6 we describe a technique known as release and recapture that can be used to determine the temperature of atoms confined in the trap. However, before we can measure the temperature, we must first characterize the CO_2 laser trap.

The CO_2 laser trap potential is parameterized by the $1/e$ intensity radii of the CO_2 laser beam and the well depth. These values can all be expressed in terms of the trap oscillation frequencies. A useful technique for measuring the trap oscillation frequencies is accomplished by exciting oscillation of the atoms through a parametric resonance [78]. In this technique, we modulate the trap spring constant at various frequencies and monitor whether the atoms have been heated. If the trap spring constant is modulated at twice the trap oscillation frequency we excite a parametric resonance and the average energy of the atoms increases exponentially

with time [126].

To excite the parametric resonances, the CO_2 laser power is modulated at various frequencies. As discussed in Chapter 3, for low energies in the trap the potential is approximately harmonic and the effective spring constant is proportional to the laser beam power. Thus, by modulating the CO_2 laser power we modulate the effective spring constant. By modulating the spring constant at twice the trap oscillation frequency the atoms are parametrically excited causing the average energy of the atoms to increase exponentially with time [126]. Eventually the atoms are heated out of the trap. Thus, one can locate the parametric resonances by monitoring the number of atoms remaining in the trap following the modulation as a function of modulation frequencies. The location of the parametric resonances will be indicated by a large loss of atoms at a particular modulation frequency [78].

Since the potential is harmonic only for atoms near the bottom of the well, we believe that the parametric resonances will be more accurately determied if we monitor the heating of atoms out of the lowest 1/10 of the well depth rather than the full well depth. If we allow the atoms to be heated out of the full gaussian potential we expect that the location of the parametric resonances will be broadened and/or shifted in frequency as the atoms are heated through a region of the potential which is not harmonic. In order to measure the heating of atoms out of the lower 1/10 of the well, we begin by modulating the CO_2 laser power for $\simeq 1$ s. At this point, we suddenly (nonadiabatically) lower the well depth to 1/10 of its original value and wait for 200 ms for the atoms released in this transition to fall under the force of gravity before we monitor the number of atoms remaining. By using this technique we are most sensitive to monitoring the heating of atoms which experience a nearly harmonic potential. However, in order to maintain a good signal to noise ratio

when using this technique, a large number of atoms need to have energies $\leq U_0/10$. Therefore, when performing these measurements we load the trap with a $|3\rangle$ - $|1\rangle$ mixture of atoms and allow the atoms time to cool by evaporation.

The CO_2 laser A/O modulator is used to modulate the CO_2 laser power in order to excite the parametric resonances. The sine wave is generated by a Hewlett Packard model 3325A synthesizer/function generator. A fixed duration of sinusoidal modulation is fed into the A/O driver through its analog voltage input. The rf power output by the driver is proportional to the analog voltage input. Unfortunately, the diffraction efficiency as a function of rf drive power is highly nonlinear when the diffraction efficiency is near its maximum value of $\simeq 82\%$. When the diffraction efficiency is at its maximum, the diffraction efficiency as a function of rf power is at a zero derivative point. Therefore, when the maximum amount of power is being deflected to form the trap, a sinusoidal modulation voltage applied to the A/O driver's analog input causes a modulation in the CO_2 laser power which contains frequency components not only at the modulation frequency but also at its harmonics due to the nonlinearity. However, if we reduce the rf power and thereby reduce the amount of CO_2 laser power used to form the trap, the diffraction efficiency more closely approximates a linear function of the applied rf power. A sinusoidal modulation applied to the input in this case causes the deflected CO_2 laser power to exhibit a sinusoidal modulation primarily at the desired modulation frequency. Figure 7.15 shows the one-sided fractional intensity noise power spectrum of the CO_2 laser beam power when a 14 kHz sinusoidal modulation is applied to the analog voltage input of the A/O driver. The rf power is reduced in this case such that the diffraction efficiency is $\sim 40\%$ in order to minimize the effect of nonlinearity in the system. The peak in the power spectrum at 14 kHz is clearly

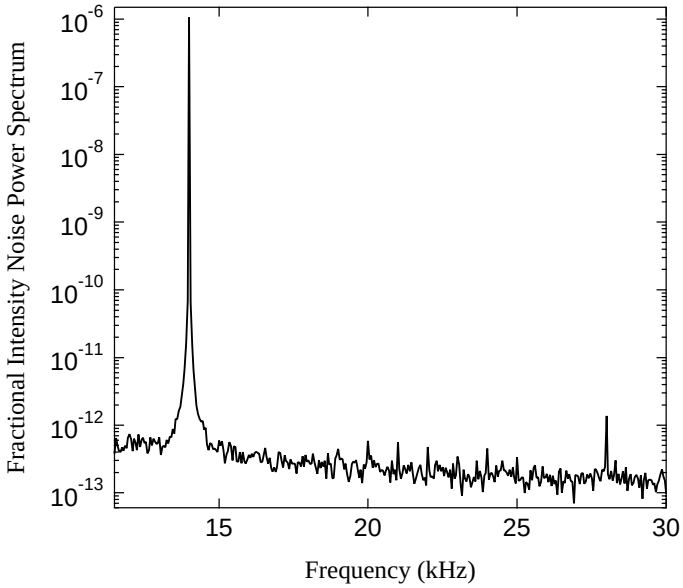

Figure 7.15: Fractional intensity noise power spectrum of the CO_2 laser beam following the A/O modulator when a sinusoidal modulation of 14 kHz is being applied to the analog voltage input of the A/O. The A/O is being supplied with reduced rf power such that it is operating at $\sim 40\%$ diffraction efficiency to minimize the effect of nonlinearity. The peak in the power spectrum at 14 kHz is clearly visible. A much smaller peak at 28 kHz occurs due to the residual nonlinearity in the system.

visible. Due to residual nonlinearity in the system, a small peak at 28 kHz is also observed. However, when the A/O is operated at this reduced diffraction efficiency, the vast majority of the power in the spectrum arises from the peak at the desired modulation frequency.

To observe the parametric resonances in our trap we proceed as follows. We begin by loading the CO_2 laser trap with the potential well at full depth in order to load the maximum number of atoms possible from the MOT. The $|3\rangle - |1\rangle$ mixture is created by application of a Raman π-pulse. The atoms are allowed to evaporatively cool in the full well depth for 5 seconds. At this point we adiabatically reduce the CO_2 laser power over 5 seconds to 1/3 of its original power by reducing the voltage

applied to the A/O driver's analog input. With the CO_2 laser power being deflected by the A/O modulator at 1/3 of its maximum value, we modulate the deflected CO_2 laser power for 0.9 s. The CO_2 laser power is then suddenly lowered (in $\simeq 5\,\mu$s) to 1/30 of its original depth (i.e. 1/10 of the reduced well depth). After a delay of 200 ms, which allows atoms released from the well to fall under the force of gravity, the number of atoms remaining in the shallow well is measured by monitoring the fluorescence induced by the probe beam. This process is repeated a number of times for various modulation frequencies. The number of atoms remaining in the trap in the reduced well depth is recorded as a function of modulation frequency. A LabView program written by Stephen Granade triggers the pulse sequence, adjusts the modulation frequency of the function generator via GPIB communication and records the number of atoms remaining in the trap as a function of modulation frequency.

Figure 7.16 shows the number of atoms remaining in the reduced well depth as a function of modulation frequency. The sinusoidal modulation is applied when the trap is at 1/3 of its full well depth which corresponds to a trap depth of $\simeq 100\,\mu$K. The CO_2 laser power used to form the trap in this case is measured to be 14 W. For modulation frequencies up to 1 kHz, the peak-to-peak amplitude of the applied sinusoidal modulation is 30% of the $100\,\mu$K well depth. For modulation frequencies above 1 kHz, the peak-to-peak amplitude of the sinusoidal modulation is 18% of the $100\,\mu$K well depth. The line through the data points is given to guide the eye. The peak trap loss appears to occur at frequencies of 190 Hz, 3.3 kHz and 4.5 kHz. We expect that the peak trap loss occurs at approximately twice the trap oscillation frequency and thus expect that the trap frequencies are near 95 Hz, 1.65 kHz and 2.25 kHz when the trap is operating at 1/3 of its full depth.

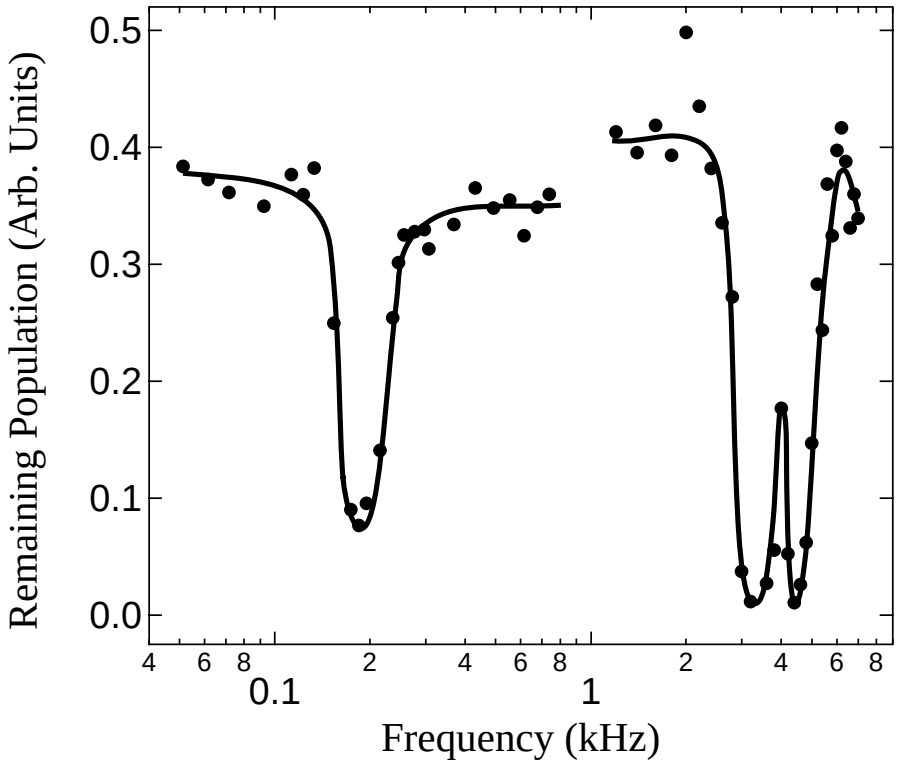

Figure 7.16: Parametric resonances for the 100 μK deep well. The number of atoms remaining in the reduced well depth following sinusoidal modulation of the laser intensity as a function of modulation frequency. Parametric resonances occur near 190 Hz, 3.3 kHz and 4.5 kHz resulting in a substantial loss of atoms when the laser power is modulated at these frequencies.

Michael Gehm has numerically modeled the parametric resonance experiment described above to determine whether this technique accurately reproduces the actual trap frequencies. Initially, the computer program generates a list of trapped atoms where each atom has a random position and velocity subject to the condition that the statistical distribution of positions and velocities exhibit a thermal Boltzmann distribution. The program assumes that the atoms are confined in a three-dimensional gaussian potential. The program also assumes that the trap initially contains a thermal distribution of atoms with a temperature equal to 1/10 the well depth. This initial condition is appropriate for atoms confined in the optical trap once evaporative cooling has stagnated. The motion of the atoms is evolved forward in time in accordance with Newton's laws of motion subject to the confining gaussian potential. The well depth of the gaussian potential is modulated with a peak-to-peak amplitude identical to that used in the experiment described above. The modulation of the well is terminated and the number of atoms that are confined when the well depth is suddenly lowered to 1/10 its original value is calculated. The modulation frequency and final number of atoms is then recorded. This procedure is repeated for a number of modulation frequencies. Also, for each modulation frequency, a number of different randomly chosen initial atomic spatial and velocity distributions are used and the results are averaged together. The resonance spectrum obtained from this program is similar to that shown in Figure 7.16. The position of the resonance peaks obtained in the simulation are compared with the exact harmonic oscillation frequencies which are calculated from the actual gaussian potential used in the model. The position of the resonant peak below 1 kHz is found to occur at a frequency 10% below the calculated harmonic oscillator frequency. The position of the resonant peaks above 1 kHz are found to occur at

frequencies 5% below the calculated harmonic oscillator frequencies. The difference in the shifts is most likely due to the difference in the modulation amplitudes used.

Based on this computer simulation we estimate that the trap oscillation frequencies for the trap formed from 14 W of CO_2 laser power are given by $\nu_x = 2.4$ kHz, $\nu_y = 1.8$ kHz and $\nu_z = 104$ Hz where the CO_2 laser beam propagates along the $\hat{\boldsymbol{z}}$-axis. Using the measured total power as a constraint, we find that the trap intensity $1/e^2$ radii are given by $w_x = 50\,\mu$m and $w_y = 67\,\mu$m, and the axial intensity $1/e^2$ length $z_f = 1.13$ mm, where z_f is consistent with the expected Rayleigh length within 15%. To determine the trap parameters for different CO_2 laser powers, we assume that the shape of the trap does not change substantially and simply scale the trap depth according to the measured amount of power being used to form the trap.

7.6 Temperature Measurement

To measure the temperature of the atoms confined in the trap we use a technique known as release and recapture [123]. In this technique the atoms are release from the confining potential by suddenly ($\leq 5\,\mu$s) turning off the CO_2 laser potential using the A/O modulator. Once released, the atoms ballistically expand and fall under the force of gravity. After a variable delay time, the CO_2 laser potential is suddenly turned on again. A fraction of the atoms initially confined in the trap are recaptured by the CO_2 laser potential. The number of atoms recaptured is measured by monitoring the fluorescence induced by a probe beam. By measuring the number of atoms recaptured as a function of delay time, the temperature of the atoms can be determined. Qualitatively, if the atoms are at a high temperature the atoms will quickly leave the trap region once released and the number of atoms

recaptured as a function of delay time will decay rapidly. Extremely cold atoms, on the other hand, will leave the trapping region on a much longer time scale. In this case, the number of atoms recaptured as a function of delay time will decay much more slowly in comparison to the high temperature distribution.

The residual trap power with the A/O off is measured to be 10^{-4} of the maximum, so the A/O rejection ratio is sufficient for the current experiments. The rejection ratio is measured by chopping the CO_2 laser beam and using lock-in detection of the of the CO_2 laser power with the A/O rf power on and off. The rejection ratio is limited by a small amount of rf leakage from the driver that is transmitted to the A/O crystal even though the analog voltage is being held at zero volts. If a better rejection ratio is required in future experiments, the driver can be modified to provide a better rejection ratio.

Figure 7.17 shows typical data obtained using the release and recapture technique. The data shown is obtained 20 seconds after the $|3\rangle - |1\rangle$ mixture is created by the Raman π-pulse. Once the mixture is created, the atoms undergo evaporative cooling in the well of fixed depth for 20 seconds. In this case, the well depth is determined from the measured CO_2 laser power to be 250 μK. The data points shown are the mean of 4 complete cycles through the entire timing sequence for each point in the curve. The error bars indicate the standard deviation in the mean.

To make a quantitative measurement of the temperature a computer simulation written by Michael Gehm is used to fit the data obtained experimentally. The simulation is related to that used to model the parametric resonance data described in Section 7.5. The program begins by generating a thermal distribution of atoms confined in a gaussian potential. The well depth and CO_2 laser $1/e$ intensity radii obtained in Section 7.5 are used to parameterize the gaussian potential. Each atom

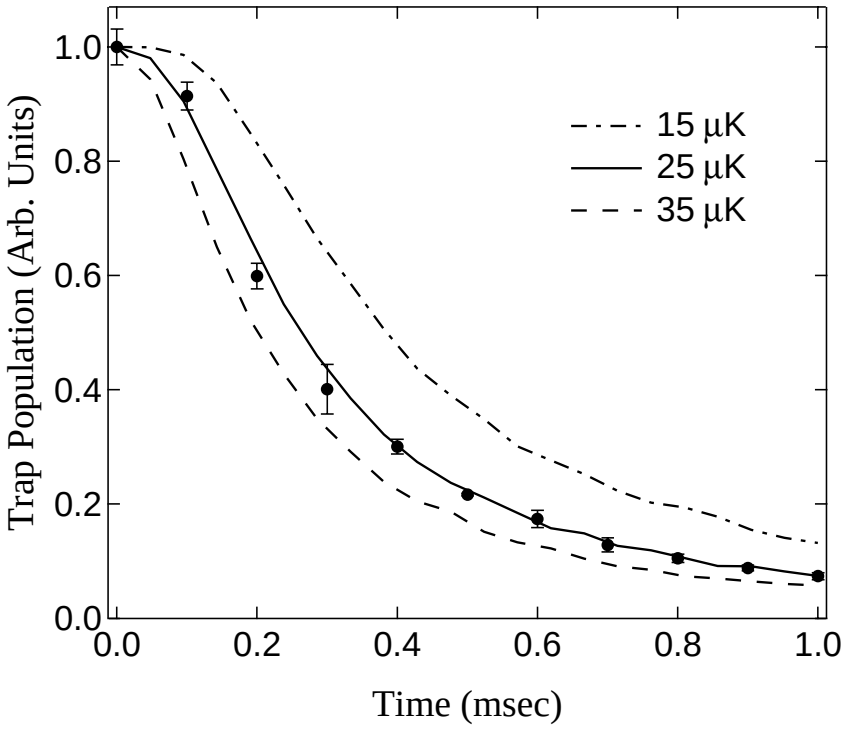

Figure 7.17: Temperature measurement via release and recapture. The number of atoms recaptured in the trap after a variable release time. The error bars indicate the standard deviation of the mean. The solid line shows the best fit to the data for $T = 25\,\mu$K. Also shown are fits for $T = 15\,\mu$K and $T = 35\,\mu$K.

used in the model is given an initial random position and momentum subject to the constraint that the statistical distribution of position and momenta of all the atoms obeys a thermal Boltzmann distribution. Once this initial distribution of atoms is generated, the model assumes that the confining potential is suddenly turned off so that the position and momenta of each atom remains unchanged. The motion of each atom is evolved forward in time according to Newton's equation of motion under the subject of gravity. The atoms expand ballistically and fall under the force of gravity. After a variable delay time the model assumes that the potential is suddenly reinstated (i.e. the position and momentum of the atoms remain unchanged while the potential is turned on). The energy of each atom in the potential can then be calculated. Those atoms with a negative total energy are assumed to be recaptured by the CO_2 laser trap. This sequence is repeated a number of times assuming that the atoms are released for a different amount of time. The number of atoms recaptured versus release time for a given initial temperature is thereby obtained. For each value of release time, several data points are averaged together to provide an ensemble average of the statistical distribution of data produced by the simulation.

This simulation is used to fit the data shown in Figure 7.17. The best fit to the data is obtained by minimizing χ^2. The best fit is given assuming a thermal distribution at temperature $T = 25\,\mu$K. For comparison, the predictions of the simulation for temperatures of $T = 15\,\mu$K and $T = 35\,\mu$K are also shown. Thus, we have shown that after 20 seconds of evaporation the temperature of the atoms has cooled to 1/10 the well depth. This is in agreement with the predictions of Chapter 6 where we found that the evaporation of atoms from a well of fixed depth would stagnate as the temperature of the atoms falls below 1/10 the well depth.

7.7 Measurement of $|a_{31}|$

In the previous sections, we determined that when the atoms are transferred into the interacting $|3\rangle - |1\rangle$ mixture, the two-state mixture undergoes evaporative cooling. In Chapter 6, we found that the time scale for evaporative cooling is determined by the s-wave elastic scattering cross section for collisions between atoms in state $|3\rangle$ and state $|1\rangle$. Therefore, by monitoring the rate of evaporation we can measure the effective cross section $\sigma = 4\pi a_{31}^2$ where a_{31} is the scattering length for the state $|\{3,1\}_-\rangle$. In this section, we describe an experiment in which we monitor the rate of evaporation from the CO_2 laser trap at a fixed well depth. By comparing this to the s-wave Boltzmann model developed in Section 6.2, we measure $|a_{31}| = 540^{+210}_{-100}\, a_0$ at $B = 8.3$ G. This result confirms for the first time that very large scattering lengths exist in ^{6}Li mixtures. The predicted scattering length at $B = 8.3$ G is $-490\, a_0$, consistent with our observations. The scattering length is expected to increase to $-1615\, a_0$ as $B \to 0$.

In Section 6.2 we found that the evaporation rate becomes independent of the scattering length if a large well depth is used due to the fact that at high energy the s-wave cross section becomes unitarity limited. The energy dependent cross section for atoms in the two-particle state $|\{3,1\}_-\rangle$ is given by

$$\sigma(k) = \frac{8\,\pi\, a_{31}^2}{1 + k^2\, a_{31}^2}, \tag{7.10}$$

where $\hbar k$ is the relative momentum. For $k|a_{31}| << 1$, the cross section is maximized. When $k|a_{31}| >> 1$, the cross section approaches the unitarity limit $8\pi/k^2$ which is independent of a_{31}. Note that $k|a_{31}| = 1$ corresponds to a relative kinetic energy of $\epsilon = \hbar^2/(2\mu\, a_{31}^2)$, where $\mu = M/2$ is the reduced mass. For $|a_{31}| = 500\, a_0$,

$\epsilon = 115\,\mu$K. Note that, the effective cross section is reduced by a factor of 2 from that given in (7.10) due to the fact that the antisymmetric combination between two colliding atoms occurs with a probability of 1/2.

The acousto-optic modulator in front of the CO_2 laser controls the laser intensity which is reduced to yield a shallow trap depth of $100\,\mu$K for the experiment. By using a shallow well, we avoid the problem that the elastic cross section becomes independent of the scattering length at high energy. In addition, the shallow well greatly reduces the number of loaded atoms and makes the sample optically thin, simplifying calibration of the number of trapped atoms.

The number of atoms in the trap $N(t)$ is estimated using a calibrated photomultiplier. The detection system monitors the fluorescence induced by pulsed, retroreflected, $\sigma^{\pm}$ probe and repumper beams which are strongly saturating ($I/I_{sat} = 26$ for the strongest transition). To simplify calibration, only the isotropic component of the fluorescence angular distribution is measured: The collecting lens is placed at the magic angle [67] of 55° ($P_2(\cos\theta) = 0$) with respect to the propagation direction of the probe beams. The net efficiency of the detection system is determined using laser light of known power. The primary uncertainty in the calibration arises from the excited state population fraction, which we estimate lies between 1/4 and 1/2.

Figure 7.18 shows the number of trapped atoms $N(t)$ measured for the $|3\rangle - |1\rangle$ mixture at a well depth $U_0 = 100\,\mu$K and a bias field of 8.3 G as a function of time between 5 ms and 20 seconds after evaporation is initiated. For times beyond 50 seconds (not shown), the evaporation stagnates, and we observe an exponential decay of the cooled $|3\rangle - |1\rangle$ mixture with a time constant of 370 seconds over a period of a few hundred seconds. The error bars are the standard deviation of the mean of ten complete runs through the entire time sequence.

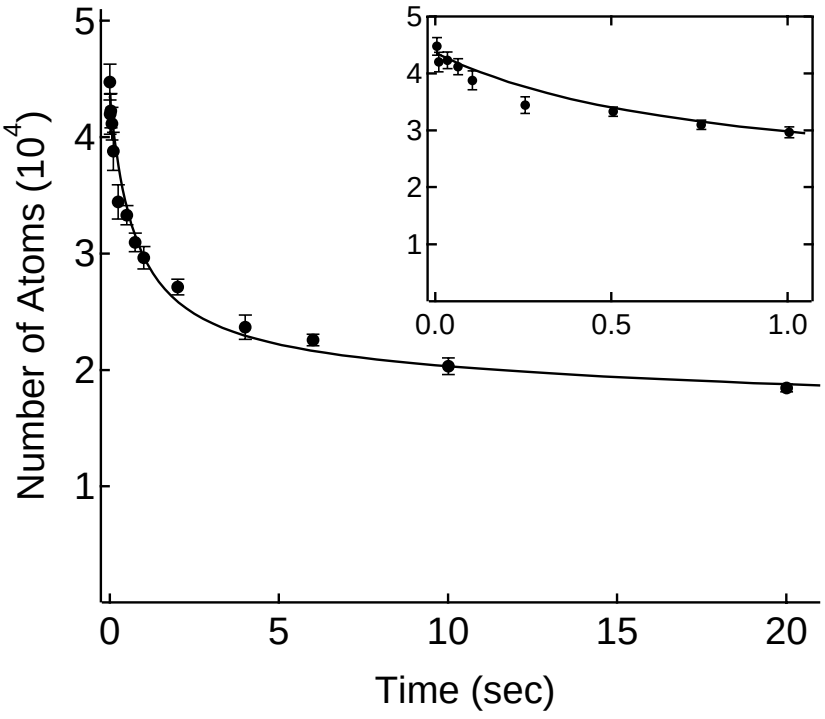

Figure 7.18: Number of trapped atoms versus time for evaporation of a $|3\rangle$-$|1\rangle$ mixture of ^{6}Li at a fixed well depth of $100\,\mu$K. The solid curve shows the s-wave Boltzmann equation fit for a scattering length of $|a_{31}| = 540\,a_0$. The inset shows the same data from 0 - 1 sec.

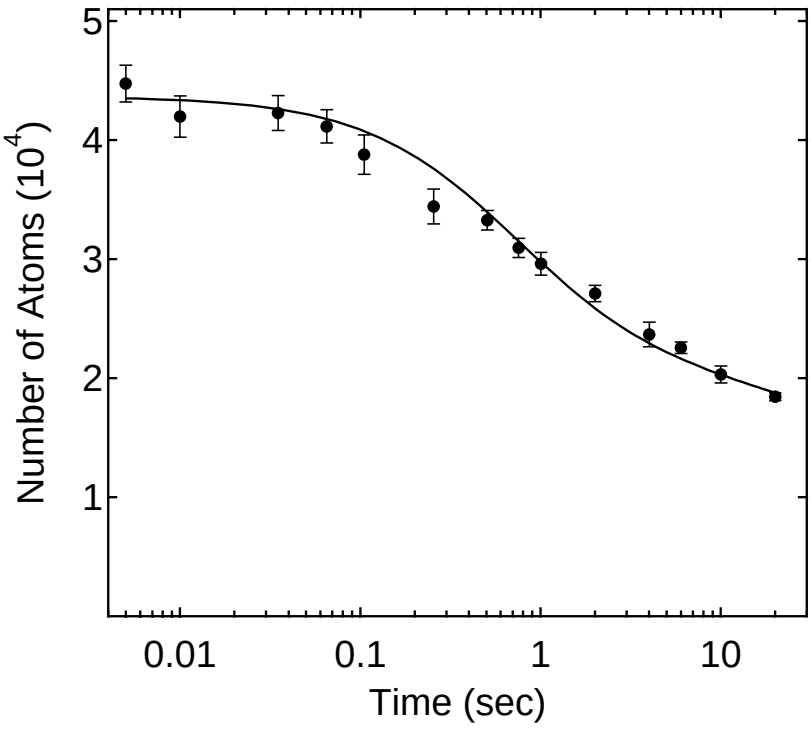

Figure 7.19: Measurement of a_{31} (logarithmic scale). The data shown is the same as that in Figure 7.18.

The s-wave Boltmann equation model developed in Section 6.2 is used to predict $N(t)$ for comparison to the experiment. Eq. (6.53) is integrated in order to fit the data. The density of states for a gaussian potential with the parameters determined in Section 7.5 is used in the integration of (6.53). A decay term $-\mathcal{D}(\epsilon_4)\, f(\epsilon_4)/\tau$ with $\tau = 370$ sec is added to the right hand side of (6.53) to account for the measured trap lifetime. The effective cross section $\sigma_0 = 4\pi\, a_{31}^2$.

The s-wave Boltzmann equation is numerically integrated to determine $N(t)$ using the well parameters as fixed inputs. From the calibrated photomultiplier signal, assuming that 1/3 of the atoms are in the excited state, we obtain an initial total number $N_0 = 44,000$. For this case, the initial collision rate in Hz is estimated to be $1/(2\pi\tau_c) \simeq 2N_0 M\sigma_0\nu^3/(k_B T)$, where $\nu^3 = \nu_x\nu_y\nu_z$, $\sigma_0 = 4\pi a_{31}^2$, and M is the ^{6}Li mass. Assuming $|a_{31}| = 500\, a_0$, $\tau_c = 30$ ms. Hence, for $t > 0.3$ seconds, when on average 10 collisions have occurred, the sample should be thermalized as assumed in the theory.

The best fit to the data starting with 22,000 atoms in each state is shown as the solid curve in Figure 7.18. The χ^2 per degree of freedom for this fit is 1.4 and is found to be very sensitive to the initial temperature T_0 of the atoms in the optical trap. From the fit, we find $T_0 = 46 \pm 2.5\,\mu$K, which is less than the well depth. We believe that this low temperature is a consequence of the MOT gradient magnet, which is turned off after the MOT laser beams. The effective well depth of the optical trap is therefore reduced until the gradient is fully off, allowing hotter atoms to escape before the Raman pulse is applied to create the $|3\rangle - |1\rangle$ mixture. The fit is most sensitive to data for $t > 0.5$ second, where the thermal approximation is expected to be valid. From the fit, we obtain the scattering length $|a_{31}| = 540 \pm 25\, a_0$, which is within 10% of the predictions of Figure 7.2. The

quoted statistical error of $\pm 25\,a_0$ corresponds to a change of 1 in the total χ^2 [127]. Since the χ^2 per degree of freedom for the fit is 1.4, the Boltzmann equation model appears to provide a good fit to the data.

We determine the systematic errors in a_{31} due to the uncertainties in the calibration and in the population imbalance as follows. The data is fit for an initial number of atoms N_0 of 58,000 and 29,000, corresponding to an excited state fraction of 1/4 and 1/2. This yields $|a_{31}| = 440 \pm 20\,a_0$ and $|a_{31}| = 750 \pm 42\,a_0$, respectively. Note that for the larger scattering lengths, the cross section given by Eq. (7.10) approaches the unitarity limit and the statistical error increases. We assume that the initial population imbalance for states $|3\rangle$ and $|1\rangle$ is comparable to that of states $|2\rangle$ and $|1\rangle$ in the optically pumped MOT which we observed to be $\leq 10\%$. Note that residual population in state $|2\rangle$ is expected to be stable and weakly interacting. We estimate $|a_{32}| < 30\,a_0$ for $0 \leq B \leq 50$ G using the ABC method, and $a_{12} \simeq 0$ [55]. Using the parameters for the fit shown in Figure 7.18, but changing the initial mixture from 50-50 to 60-40, we find a slight increase in the fitted scattering length from $540\,a_0$ to $563\,a_0$. Thus, the uncertainty in the calibration of the number of atoms produces the dominant uncertainty and $|a_{31}| = 540^{+210}_{-100}\,a_0$.

The theory also predicts that the final temperature after 20 s of evaporation is 8.7 μK. Hence, to further test the consistency of the evaporative cooling model, the final temperature is measured by abruptly turning off the CO_2 laser trap after 20 sec using the A/O modulator and then recapturing the atoms from 0-1 ms later to determine the velocity distribution. The results shown in Figure 7.20 determine the best fit final temperature to be 9.8 μK which is within 10% of the final temperature of 8.7 μK predicted by the Boltzmann equation model. For comparison, theoretical predictions for 7.8 μK and 11.8 μK are also shown. An excellent fit to the

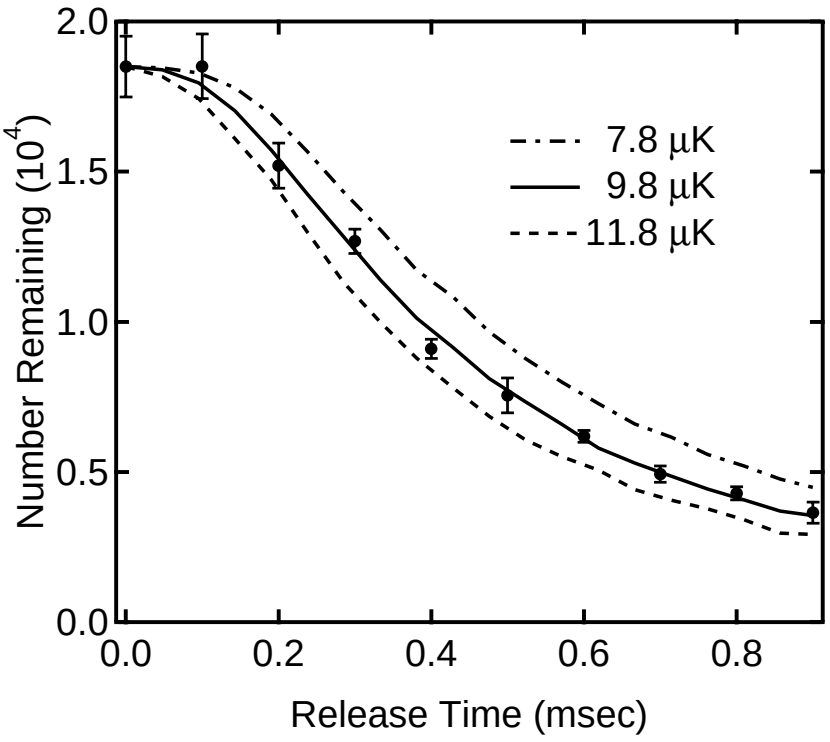

Figure 7.20: Determination of the final temperature by release and recapture. Error bars indicate the standard deviation of the mean. The solid line shows the best fit to the data for $T = 9.8\,\mu$K, which agrees with the s-wave Boltzmann equation result within 10%. Also shown are fits for $T = 7.8\,\mu$K and $11.8\,\mu$K.

data is obtained for the final temperature, which describes a thermal distribution. However, the initial temperature is not so readily measured, as it is nonthermal before evaporation is initiated, and is rapidly changing during evaporation, unlike the final temperature, which stagnates.

7.8 Estimate of $G_{31\to21}$

Good fits to the evaporation data are obtained in Section 7.7 neglecting inelastic collisions, suggesting that the dipolar rate for the $|3\rangle - |1\rangle$ mixture is small, in contrast to the scattering length. A limit on the dipolar loss rate for the $|3\rangle - |1\rangle$ mixture can be estimated from the $\tau = 370$ second lifetime of the mixture after evaporation stagnates. For equal populations in both states, dipolar decay results in an initial loss rate $\dot{n} = -Gn^2/4$, where G is the dipolar rate constant and n is the total density. To obtain a high density, the trap is loaded at a well depth of $330\,\mu$K and the temperature of the atoms is reduced by evaporation to $T \simeq 30\,\mu$K. The number of atoms remaining in each state after evaporation is estimated to be $N = 6.5 \pm 2.2 \times 10^4$, where the uncertainty is in the calibration of the number. We cannot rule out the possibility that one state is depleted on a long time scale, since we do not directly measure the individual state populations. However, we believe that a mixture exists after evaporation slows in the deep well, since further reducing the well depth yields final temperatures consistent with evaporative cooling as described in Section 7.9. Note that the mixture ratio is not critical: An 80-20 mixture yields an initial loss rate $\dot{n} = -0.16\,Gn^2$, $\simeq 2/3$ that of a 50-50 mixture. For a fixed $330\,\mu$K trap depth, $\nu^3 = 2.6 \pm 0.3\,\mathrm{kHz}^3$, and the phase space density for one state in the harmonic approximation is then $\rho = N/(k_B T/h\nu)^3 = 7\times10^{-4}$. This corresponds to a maximum total density of $n = 2\,\rho/\lambda_{dB}^3 = 6.4 \times 10^{11}/\mathrm{cm}^3$, where

$\lambda_B \equiv h/\sqrt{2\pi M k_B T}$. Since the exponential decay time of the $|3\rangle - |1\rangle$ mixture is similar to that obtained in the noninteracting $|1\rangle - |2\rangle$ mixture, we assume the loss is dominated by background gas collisions. Thus, we must have $Gn/4 << 1/\tau$, which yields $G << 2 \times 10^{-14}\text{cm}^3/\text{sec}$. This result is consistent with the value $G \simeq 2 \times 10^{-15}\,\text{cm}^3/\text{sec}$ predicted for the dipolar rate constant at $30\,\mu$K by van Abeelen and Verhaar.

7.9 Forced Evaporative Cooling

As the temperature of a confined atomic vapor decreases, the evaporation rate from a well of fixed depth is exponentially suppressed by a factor $\exp(-U_0/k_B T)$. As we have seen in the previous sections, this eventually causes the evaporation process to stagnate. In order to further cool the atoms and increase the phase space density by evaporative cooling, the ratio $U_0/k_B T$ must be lowered. In an optical trap this can be accomplished by adiabatically lowering the trap intensity as a function of time. In Section 6.3.4, we investigated theoretically evaporative cooling in a time-dependent optical potential. We found that the phase space density of the atomic vapor can be substantially increased by evaporative cooling if the well depth of the trap is lowered. In Section 6.5 we found that if the collision rate in the trap is large enough to maintain a ratio $U_0/k_B T \simeq 10$ as the trap is adiabatically lowered, the phase space density of a gas in the classical regime should scale as

$$\frac{\rho_f}{\rho_i} = \left(\frac{U_i}{U_f}\right)^{\frac{3}{2}\frac{\xi-4}{\xi-3}} . \tag{7.11}$$

where $\xi = U_0/k_B T$. Thus for $\xi \simeq 10$ we expect that the phase space density will be increased by a factor of 79 if we adiabatically lower the well depth by a factor

of 30. The number of atoms in the trap is expected to scale as

$$\frac{N_i}{N_f} = \left(\frac{U_i}{U_f}\right)^{\frac{1}{2}\frac{3}{\xi-3}}. \tag{7.12}$$

Therefore, we expect to lose approximately half of the atoms as the well depth is lowered by a factor of 30 assuming again that $\xi \simeq 10$. In this section we describe our experimental attempts at increasing the phase space density of the trapped lithium fermions by adiabatically lowering the CO_2 laser power.

In the experiments, lithium atoms are loaded from the MOT into the CO_2 laser trap which is initially run at full power producing a well depth $\simeq 300\,\mu$K. The atoms are optically pumped into states $|1\rangle$ and $|2\rangle$. After a delay of 0.5 s, a Raman π-pulse transfers the population of atoms in state $|2\rangle$ into $|3\rangle$ creating a $|3\rangle - |1\rangle$ mixture of atoms. Once this mixture is created, the atoms undergo evaporative cooling from the $300\,\mu$K deep well for 5 s over which time the temperature of the atoms is reduced to $\simeq 30\,\mu$K. Approximately half of the atoms are lost during this initial stage of evaporation. At this point, the CO_2 laser power is exponentially lowered as a function of time for 40 seconds with a time constant $\simeq 11.5$ s eventually reducing the well depth to $\simeq 10\,\mu$K. The number and temperature of the atoms are measured at this point using the techniques described previously.

The atoms are initially loaded from the MOT which has a peak phase space density $n_0\,\lambda_{dB}^3 \simeq 10^{-5}$ where n_0 is the density of atoms at the center of the MOT and $\lambda_{dB} = \sqrt{2\pi\hbar^2/Mk_BT}$ is the thermal de Broglie wavelength of the atoms at temperature T. The CO_2 laser trap initially contains $\simeq 10^5$ atoms per state and the initial phase space density is comparable to that of the MOT. After the atoms undergo evaporative cooling from the well at fixed depth, the temperature of the atoms stagnates at 1/10 the well depth. At this temperature the atoms are confined

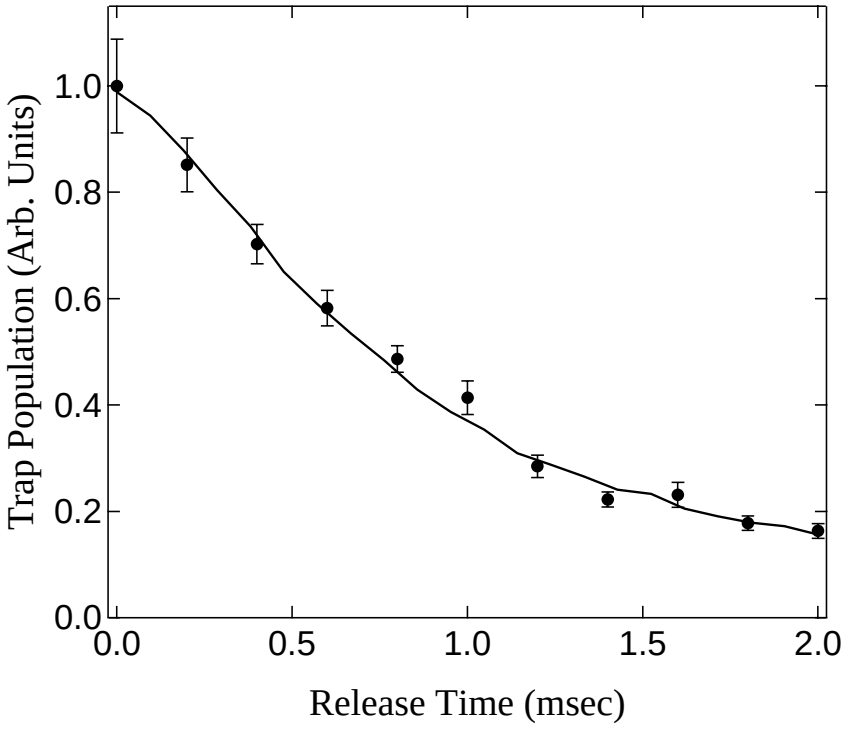

Figure 7.21: Temperature of the atoms following forced evaporative cooling. The error bars indicate the standard deviation of the mean. The solid line shows the best fit to the data for $T = 2.4\,\mu$K.

in an approximately harmonic potential. In the harmonic limit the phase space density is given by $\rho = N(h\nu/k_B T)^3$ where $\nu = (\nu_x \nu_y \nu_z)^{1/3}$ is the geometric mean of the trap oscillation frequencies and N is the number of atoms per state. At a well depth of $300\,\mu$K, $\nu \simeq 1.3$ kHz. The temperature in the full well depth stagnates at $30\,\mu$K and $N = 50,000$. Thus, the corresponding phase space density $\rho = 4 \times 10^{-4}$ at this point.

After the CO_2 laser power is adiabatically reduced over 40 s, the number and temperature of the remaining atoms are measured. The well depth has been reduced to $\simeq 10\,\mu$K and we estimate that $\nu \simeq 240$ Hz. Approximately 15,000 atoms per state are left in the trap. Figure 7.21 shows the measurement of the temperature.

The best fit to the data is given for $T = 2.4\,\mu$K. Thus, the phase space density is $\simeq 1.6 \times 10^{-3}$ and has increased by roughly a factor of 4 over that obtained from evaporation from the fixed well depth. To our knowledge, this is the highest phase space density ever achieved in a dilute gas of lithium fermions.

However, we had expected that the temperature at the end of evaporation would be $\leq 1\,\mu$K and the phase space density would have increased by a factor of ≥ 80 based on the scaling argument given in Section 6.5 assuming $U_0/k_BT \leq 10$ over the course of the experiment. Numerical integration of the time dependent Boltzmann equation (Eq. (6.75)) indicates that the collision rate should be large enough over the entirety of the evaporative cooling trajectory to maintain a temperature equal to 1/10 the well depth or less. Thus, we expect that the observed temperature and phase space density should be comparable to that predicted by the scaling argument. Unfortunately, in disagreement with the predictions, we have not observed phase space densities any higher than 1.6×10^{-3}.

There are a number of possible explanations for why the atoms did not reach a higher final phase space density. The high final temperature may be the result of a small residual source of heating. The expected heating rate based on the pointing noise measurements of the CO_2 laser beam (see Section 4.1.2) may be as high as 50 nK/s at certain trap oscillation frequencies. This could cause significant heating over the 40 seconds during which the CO_2 power is adiabatically lowered. In an attempt to directly measure the residual heating rate in the CO_2 laser trap, we measured the temperature of the atoms 20 s and 120 s following the creation of the $|3\rangle - |1\rangle$ mixture in the $100\,\mu$K deep well. The temperature of the atoms as measured using release and recapture was not observed to increase over this 100 s period. However, it is not obvious that this indicates that no residual heating rate

is present. The residual heating rate may simply be balanced by an equal amount of cooling due to evaporation of the atoms. In future experiments the heating rate should be measured when there is no possibility of a competing cooling mechanism. This can be accomplished by turning the interactions off after the cooled sample of atoms has been initially created.

Another possible explanation for the unexpectedly high final temperature is that by the end of evaporation a large imbalance existed in the $|3\rangle - |1\rangle$ mixture. The evaporation rate is largest if the trap contains a 50/50 mixture of atoms in states $|3\rangle$ and $|1\rangle$. If a large imbalance exists, the cooling rate due to evaporation is significantly reduced. We are certain that the trap still contains a mixture of atoms in state $|3\rangle$ and $|1\rangle$ when the evaporation process stagnates in the full well depth since we observe an increase in phase space density when the CO_2 laser power is adiabatically reduced from this point. The fact that the phase space density increases indicates that some amount of evaporative cooling took place while the trap is lowered. In the absence of collisions, the phase space density should remain constant as the trap is exponentially lowered. The reduction in temperature and increase in phase space density is consistent with a finite collision rate. In the absence of collisions we expect that the temperature should scale approximately as $\sqrt{U_0}$ as the well depth U_0 is lowered due solely to the adiabatic expansion of the well (see Section 6.3.1). Thus, we would expect that in the absence of collisions the final temperature would be $T_f = 30\,\mu\text{K}/\sqrt{30} \simeq 5.5\,\mu\text{K}$. This is clearly inconsistent with the final temperature measured by release and recapture. Thus, we are certain that the trap contained atoms in both $|3\rangle$ and $|1\rangle$ when the well is initially reduced. However, over the course of evaporation we are not certain that this mixture was maintained. We are not aware of any physical mechanism which would cause one

state to be evaporated more rapidly than the other. However, the initial imbalance may be significant after a large fraction of atoms are lost. In future experiments it is important to develop a diagnostic that can measure the population imbalance in the CO_2 laser trap over the course of evaporation.

The measurement of the final temperature using release and recapture is less than ideal. This technique requires that the entire timing sequence be repeated multiple times. To generate the data shown in Figure 7.21, the entire timing sequence needed to be repeated 44 times (the data shown is the mean of 4 measurements for each release time). Since, the timing sequence for each measurement requires about 50 s to complete, the experiment must be stable over the span of 1/2 hour. Also, lower temperatures and higher phase space densities may have been obtained for individual shots but unfortunately the release and recapture technique does not measure the temperature in a single shot. Using a low noise CCD camera, single shot temperature measurements can be made either by image the velocity distribution after the atoms are released from the trap or by directly imaging the distribution of atoms along axis of the trap. In future experiments, the use of a single shot temperature measurement technique will be a major improvement over the use of the release and recapture technique.

7.10 Summary

In conclusion, we have observed that an optically trapped $|3\rangle - |1\rangle$ mixture of ^{6}Li atoms exhibits a very large scattering length at low magnetic field, in agreement with predictions. This mixture is stable against spin-exchange collisions provided that a small bias magnetic field is applied. The evaporation curves measured for this mixture are in good agreement with a model based on an s-wave Boltzmann equation

which neglects inelastic processes or residual heating. By fitting the number of atoms in the trap as a function of time using the s-wave Boltzmann equation derived in Section 6.2, we measured the s-wave scattering length for this mixture and found $|a_{31}| = 540^{+210}_{-100}\, a_0$ for $B = 8.3$ G. The predicted scattering length $a_{31} = -490\, a_0$. This measurement confirms for the first time that certain two-state mixtures in ^{6}Li exhibit a large scattering length. We predict that the scattering length a_{31} is strongly attractive and widely tunable at low magnetic field. Hence, this system may be a suitable candidate for the observation of a superfluid phase transition. Further, since s-wave interactions can be turned on and off in a few microseconds, this system is well suited for studies of many-body quantum dynamics.

In our initial attempts at using evaporative cooling to increase the phase space density in this system, we have observed increases in the phase space density by over a factor of 100 beyond that which is obtained in the magneto- optical trap. By adiabatically lowering the CO_2 laser trap depth, we have achieved a peak phase space density of 1.6×10^{-3} corresponding to $T/T_F \simeq 4.8$. To our knowledge, this is the largest phase space ever achieved in a ^{6}Li vapor. However, there is a disagreement between the theoretical prediction for evaporative cooling and experimental observations in our initial experiments. There are a number of plausible reasons for the discrepency. Future experiments will focus at first on identifying and eliminating possible sources of heating or imbalance in the mixture. Temperatures below T/T_F should be obtainable in this system.

Chapter 8

Conclusion

In this dissertation we have described the development of the first stable optical trap for neutral atoms and its application to the study of interactions and evaporative cooling in a two-state mixture of fermionic lithium atoms. Optical traps have previously suffered from unexplained heating and loss rates which have limited their usefulness. We identified and investigated theoretically residual heating sources which may have plagued previous optical traps. Based on this, we concluded that a stable CO_2 laser was ideally suited for optically confining atoms. By employing an ultrastable CO_2 laser which confines atoms inside an ultra high vacuum environment which operates at a pressure $\leq 10^{-11}$ Torr, we demonstrated storage of lithium atoms for several hundred seconds, nearly two orders of magnitude longer than any previous optical trap. The development of a stable optical trap which exhibits a 370 second lifetime has far reaching implications due to the wide variety of applications for which optical traps are useful. These include uses ranging from precision measurements to quantum computing to the study of condensed matter physics in dilute, ultracold atomic vapors. Optical traps are particularly well suited for the study of an ultracold interacting Fermi gas since they provide a means of confining stable two-state mixtures which are required for s-wave interactions to occur.

Following the development of a stable optical trap, the first study of interactions

in a two-state mixture of lithium fermions was performed. Many of the exciting phenomena predicted to exist in a degenerate ^{6}Li gas, such as the possibility of observing a superfluid phase transition, are predicated on the existence of a large and attractive interaction strength predicted to exist for certain two-state ^{6}Li mixtures. The evaporative cooling experiments described in Chapter 7 provided the first verification that certain two-state mixtures of ^{6}Li fermions interact with a very large interaction strength in agreement with predictions.

We also have performed initial studies of evaporative cooling in this system as a means of increasing the phase space density of the vapor. In the experiments, evaporative cooling was used to increase the phase space density of the trapped Fermi gas by over two orders of magnitude beyond that achieved using the magneto-optical trap. The maximum phase space density obtained was $\simeq 1.6 \times 10^3$ which, to our knowledge, is the largest phase space density ever achieved in a ^{6}Li vapor. We have developed a theoretical model which describes the evaporative cooling of fermionic atoms from a time-dependent optical potential. The model indicates that much larger increases in the phase space density should be obtainable in this system via evaporative cooling. Even when Fermi statistics are included in the model, temperatures much lower than the Fermi temperature are expected to be attainable. Unfortunately, the first experimental attempts at obtaining a temperature $T \simeq T_F$ did not perform as well as expected. Resolving the discrepency between the theoretical and experimental results remains of utmost concern for future experiments. However, the development of a stable optical trap, the verification of ^{6}Li's extraordinary collisional properties and the initial theoretical and experimental studies of evaporative cooling presented in this dissertation will provide a foundation for future investigations of a dilute, degenerate Fermi gas.

8.1 Summary

The dissertation began by motivating ^{6}Li as an appealing candidate for the study of many-body quantum statistical effects in a dilute Fermi gas based on its extraordinary collisional properties. Certain two-state mixtures of ^{6}Li exhibit large and widely tunable interaction strengths which may permit the systematic study of remarkable many body quantum phenomena such as a superfluid transition via the formation of Cooper pairs. In Chapter 2 we gave an overview of ultracold ^{6}Li-^{6}Li scattering theory. We found that the remarkable properties of ultracold ^{6}Li collisions arise from two resonant scattering effects: (1) a zero-energy resonance in the triplet molecular interaction potential and (2) a Feshbach resonance in which a bound state of the singlet molecular potential can be made degenerate with the free two-particle energy state by application of a magnetic field. Each of these effects give rise to a scattering length which is widely tunable in a magnetic field. Very large attractive and repulsive interactions can be obtained for ultracold ^{6}Li-^{6}Li collisions. A large and attractive interaction is a prerequisite for the observation of a superfluid transition at an experimentally attainable critical temperature.

In Chapter 2, we also motivated the need for optical confinement of a two-state mixture of ^{6}Li atoms due to the prohibitively large inelastic spin-exchange collision rates which occur in magnetically trapable mixtures. At the end of Chapter 2, we reviewed two stable two-state ^{6}Li mixtures which can be optically confined and provide large and widely tunable interaction strengths. One of these mixtures, the $|3\rangle - |1\rangle$ mixtures had not been explored previously in the literature. This mixture provides a number of appealing features. It provides a large, attractive and widely tunable interaction strength in a small magnetic field. This is in contrast to the $|1\rangle - |2\rangle$ mixture which has been examined previously in the literature and requires

a magnetic field of $\simeq$ 1 kG or greater in order to obtain a large and attractive interaction strength. We showed that the inelastic collision rate in the $|3\rangle - |1\rangle$ mixture can be suppressed by application of a small bias magnetic field. In addition, by suddenly transferring the atomic population from the $|1\rangle - |2\rangle$ mixture which is noninteracting at low field to the $|3\rangle - |1\rangle$ mixture, interactions can be turned on and off on a fast time scale which may be useful for studies of many-body quantum dynamics. The ability to suppress spin-exchange collisions in the $|3\rangle - |1\rangle$ mixture may also be of interest for future experiments in which a three-state mixture of fermions is explored [40, 128]. A mixture of ^{6}Li atoms in states $|1\rangle$, $|2\rangle$ and $|3\rangle$ may be an appealing candidate for such investigations since inelastic loss rates can be suppressed in this system.

While magnetic traps can only confine two-state mixtures of ^{6}Li which are unstable with respect inelastic spin-exchange collisions, optical traps are ideally suited for studies of interacting two-state mixtures of fermions since inelastic collisions can be avoided by confining the lowest energy hyperfine states. In Chapter 3, we gave an overview of the operation of optical dipole traps. In reviewing the literature we found that a number of optical traps have suffered from unexplained heating and trap loss rates. For optical traps in which optical heating processes are negligible, residual heating and loss rates may arise from noise in the intensity and position of the trap laser beam. We presented a model which estimates the heating rates due to intensity and position noise based on measured trap laser noise spectra. The achievement of long storage times and low residual heating rates imposes stringent requirements on the trap laser noise spectra. We also estimated the heating and loss rates that arise from collisions of trapped atoms with background gas atoms in the vacuum system. We concluded that an ultrastable CO_2 laser trap operating in an

ultra-high vacuum environment is ideally suited for providing a confining potential with minimal residual heating. For the CO_2 laser trap, optical heating is negligible since photon scattering rates are measured in photons per hour for this system. The CO_2 laser also provides a stable source of optical power with intensity noise induced heating time constants measured in days and position noise induced heating rates measured in nK/s. Combined with an ultra-high vacuum environment operating at a pressure $\leq 10^{-11}$ Torr, the CO_2 laser trap provides a means of confining atoms for hundreds of seconds.

Chapter 4 described the first experimental demonstration of a stable optical trap based on an ultrastable CO_2 laser. The design, construction and measured laser noise power spectra for the CO_2 laser are initially presented. The design and construction of the vacuum system which provides a $\leq 10^{-11}$ Torr environment in which atoms can be stored for several hundred seconds is also described. An overview of the magneto-optical trap used to load the CO_2 laser trap is given and a description of the techniques used to overlap the CO_2 laser trap with the MOT are reviewed. Finally, the observation of optical confinement and demonstration of long term storage of ^{6}Li fermions is presented. The number of atoms in the trap is observed to decay exponentially with a time constant of $\simeq 300$ sec. This lifetime is consistent with loss due to collisions with background gas atoms at a pressure of 10^{-11} Torr.

The development of a stable optical trap will potentially impact a wide variety of applications some of which are reviewed in Chapter 1. The confinement of lithium fermions in a stable optical trap has enabled the first study of interactions and evaporative cooling in a two-state mixture of ^{6}Li described in the dissertation. The development of a stable optical trap may also be useful in the investigation of a

fermionic gas of ^{40}K atoms. Although a stable two-state mixture of ^{40}K atoms can be confined in a magnetic trap [10,44], this mixture only provides a repulsive interaction potential with only a limited range of tunability. Since the interaction is repulsive, a superfluid transition is not possible in this system. However, an optically confined two-state mixture of ^{40}K is expected to exhibit a widely tunable interaction strength which may include a large and attractive interaction strength [57]. Therefore, the development of a stable optical trap may also permit the observation of a superfluid transition in ultracold ^{40}K.

Chapter 5 described our experimental attempts at increasing the transfer efficiency of atoms from the magneto-optical trap (MOT) into the CO_2 laser trap. We found that by bringing the MOT beams closer to resonance and reducing their intensity for 4 ms following the MOT loading phase we could increase the number of atoms loaded into the CO_2 laser trap by a factor of 20 over that obtained in the original trap lifetime experiments described in Chapter 4. Approximately 7×10^5 ^{6}Li atoms have been transferred to the CO_2 laser trap by this method. Time-of-flight and imaging techniques used to measure the temperature and density of atoms in the MOT were also described. During the cooling phase, temperatures approaching the Doppler cooling limit of $T_D = 140\,\mu$K were achieved at peak densities of 5×10^{10} atoms/cm^3. This corresponds to a peak phase space density $\simeq 10^{-5}$, comparable to the best phase space densities ever achieved in a MOT. For comparison with the experimental observations, we presented a simple model describing the loading dynamics of the CO_2 laser trap. Although this model ignores several physical processes that may complicate the loading dynamics, it provides a basic physical picture of the mechanisms at work when the CO_2 laser trap is loaded from the MOT. The model predicts the number of atoms that should be loaded into the

CO_2 laser trap as a function of time for a given set of MOT and CO_2 laser trap parameters. We find good agreement between the theoretical predictions and the observed trap number. The model predicts that the number of atoms loaded from the MOT into the CO_2 laser trap increases exponentially with the ratio of the CO_2 laser trap well depth to the MOT temperature U_0/k_BT. While we believe that the model eventually breaks down for large values of U_0/k_BT we are hopeful that substantial improvements in the transfer efficiency can be obtained in future experiments. The value of U_0/k_BT can be increased in future experiments by reducing the temperature of atoms in the MOT using polarization gradient cooling or by doubling the well depth via retroreflection of the CO_2 laser beam through the trap focus.

Chapter 6 investigates theoretically the evaporation of a two-state mixture of fermions from an optical trap potential. In this chapter we have extended the work of previous authors by studying the kinetic theory of evaporative cooling from a gaussian potential assuming that the atoms interact via s-wave collisions with an energy dependent cross section. We found that during the evaporation, the phase space distribution of the trapped gas is described by a thermal Boltzmann distribution truncated at the well depth. The temperature of the atoms rapidly falls at first but eventually the evaporation process stagnates once the temperature of the atoms is reduced to $\simeq 1/10$ of the well depth. Since the evaporation rate depends on the s-wave elastic cross section $\sigma = 4\pi\, a_s^2$ where a_s is the scattering length, we conjectured that by monitoring the evaporation of atoms from an optical trap, the magnitude of the s-wave scattering length could be measured. However, in order for the evaporation rate to be sensitive to the s-wave scattering length, the well depth of the optical trap U_0 cannot be much larger than $\hbar^2/(M\, a_s^2)$ otherwise

the elastic collisions are dominated by the unitarity limited behavior of the s-wave cross section which is independent of the scattering length. Therefore, to measure a large scattering length, a shallow well depth must be used. The theoretical model developed here is used to fit the experimental data reported on in Chapter 7 in order to extract the ^{6}Li scattering length for the $|3\rangle - |1\rangle$ mixture.

Once the evaporation process stagnates in a well of fixed depth, residual trap heating and/or loss mechanisms will dominate over the evaporative cooling process. Thus, to decrease the temperature further the well depth of the optical trap must be lowered as a function of time. The second half of Chapter 6 was devoted to the theoretical investigation of evaporative cooling from a time-dependent potential where we have developed the first theory for the evaporative cooling of atoms from an optical trap. Since the trap spring constant is reduced as the well depth is lowered it is not obvious that substantial improvements in the phase space density can be obtained by this method. However, we find that if the initial collision rate is large, as is the case with ^{6}Li, the phase space density can be improved by over two orders of magnitude. We also include the effect of Fermi statistics in the model and find that starting from feasible initial conditions, temperatures much lower than the Fermi temperature can be obtained in our system, a prerequisite for obtaining superfluidity.

In Chapter 7 we present the initial experimental studies of interactions and evaporative cooling in a two-state mixture of ^{6}Li fermions. To obtain an interacting mixture of atoms we generate a $|3\rangle - |1\rangle$ mixture of ^{6}Li atoms in the CO_2 laser trap. This mixture is created from a noninteracting $|2\rangle - |1\rangle$ mixture by application of a two-photon Raman π-pulse which transfers the atomic population in state $|2\rangle$ to state $|3\rangle$ in $2\,\mu$s. This ability to turn interactions on and off quickly may be

useful for future studies of many body quantum dynamics. Although the $|3\rangle - |1\rangle$ mixture decays via inelastic spin-exchange collisions at zero field, application of an 8 G field suppresses spin-exchange collisions. At 8 G the scattering length for collisions in the $|3\rangle - |1\rangle$ mixture is predicted to be $a_{31} = -490\, a_0$. By measuring the number of atoms in the CO_2 laser trap as a function of time and fitting the data using the kinetic theory model developed in Chapter 6 we find that the magnitude of the scattering length $|a_{31}| = 540^{210}_{-100}\, a_0$ in agreement with predictions. The uncertainty is due primarily to our uncertainty in the calibration of the number of trapped atoms. This result confirms for the first time that large scattering lengths do indeed exist for certain two-state mixtures of ^{6}Li.

The evaporation of ^{6}Li atoms from the CO_2 laser trap lowers the temperature and also increases the phase space density. After the atoms are loaded into the CO_2 laser trap from the MOT which has a phase space density $\simeq 10^{-5}$, the atoms are transferred into the $|3\rangle - |1\rangle$ mixture and undergo evaporative cooling. The evaporation stagnates after the temperature of the atoms has fallen to $\simeq 1/10$ of the well depth. Approximately half of the atoms are lost due to evaporation in the process. We have observed phase space density increases by as large as a factor of 700 by evaporation from a well of fixed depth. Finally, in an attempt to increase the phase space density of the gas further, we adiabatically lowered the well depth of the CO_2 laser trap. Using this technique we have observed phase space density increases of a factor of 4. The peak phase space density observed was $\simeq 1.6 \times 10^{-3}$ which corresponds to $T/T_F = 4.8$. To our knowledge, this is the largest phase space density ever achieved in a dilute gas of ^{6}Li. However, much larger increases in the phase space density were expected based on the theoretical model developed in Chapter 6. A resolution of the discrepancy between the theoretical prediction

and the experimental observation remains an open question.

8.2 Improvements to the Experiment

In the near future, we hope to substantially increase the number of atoms initially loaded into the CO_2 laser trap and decrease the ratio T/T_F obtained by evaporative cooling. We are hopeful that substantial increases in the initial number of loaded atoms can be achieved either by retroreflecting the CO_2 laser beam, which will approximately double the well depth, or by decreasing the temperature of atoms obtained in the MOT by employing polarization gradient cooling techniques. Obtaining a large number of atoms at low temperature will provide improved initial conditions for evaporative cooling.

It is of utmost importance to identify the source of disagreement between our theoretical predictions and our experimental observations of evaporative cooling. Based on our theoretical model of evaporative cooling, we expect that starting from reasonable initial conditions (5×10^5 atoms per state in a $300\,\mu$K deep well at a temperature of $30\,\mu$K) we should be able to obtain temperatures $T/T_F << 1$ by adiabatically reducing the depth of the optical trap. Unfortunately, in our initial experiments we did not observe good agreement between our theoretical expectations and the experimental results when we adiabatically lowered the CO_2 laser power. In order to better diagnose the evaporative cooling process several changes to the experiment can be made.

For the initial experiments, we can use a mixture of ^{6}Li atoms in the states $|1\rangle$ and $|2\rangle$ to obtain a moderately large scattering length $a_{21} = -150\,a_0$ by applying a uniform field of 150 G. A field of this size is easily obtained in the current system. Although this cross section is reduced from that obtained in the $|3\rangle - |1\rangle$ mixture

($a_{31} = -490\,a_0$ at 8 G), using the $|2\rangle - |1\rangle$ mixture reduces the complexity of the experiment since Raman beams are not required to produce an interacting mixture. Using the Raman beams to create the $|3\rangle - |1\rangle$ mixture was at times experimentally cumbersome since the pulse area would drift over time as the dye laser power slowly changed. This would eventually cause an imbalance in the mixture ratio. The drift in the pulse area over time made diagnostic measurements such as determination of the heating rate by measuring the temperature change over 100 seconds rather difficult. Using the $|2\rangle - |1\rangle$ mixture for diagnostics may also provide increased flexibility since the interatomic interactions can be turned on and off by simply adjusting the applied magnetic field. This will enable us to make reliable measurements of the heating rate. To measure the heating rate, the atoms can be initially cooled to $\simeq 1/10$ of the well depth by applying the 150 G field. The interactions can then be turned off by extinguishing the 150 G field. A measurement of the temperature change over 100 seconds with the collisions turned off will give a reliable estimate of the residual heating rate since we are assured that the heating rate is not being offset by evaporative cooling. Of course, once we feel that we understand the source of the discrepancy between the evaporative cooling theory and experiment we can return to using the $|3\rangle$-$|1\rangle$ mixture to obtain large scattering lengths at low field.

The experiment can be greatly improved by developing the technology to image the trapped atoms in the CO_2 laser trap. Since the number of atoms in the CO_2 laser trap is much smaller than the number of atoms in the MOT this will require use of a low-noise CCD camera. Once we have developed this technology, a number of new diagnostic tools will be available. Using either time-of-flight images of the expansion of the vapor following its release or direct imaging of the axial distribution of atoms in the trap, we should be able to simultaneously extract the temperature

and number of trapped atoms in a single shot. This would greatly increase both the reliability and efficiency of our ability to characterize the evaporation process. In the time it takes us to take a single measurement of the temperature distribution at the end of evaporation by release and recapture, this technology would allow us to measure the number and temperature of the trapped atoms at several times during the evaporation process. This will allow us to determine where the experimental results begin to disagree with the theoretical predictions. The ability to image the atoms will also allow us to measure the population imbalance in the two-state mixture. For example, one can release the atoms from the trap in a magnetic field gradient and after a short delay image the resulting spatial distribution. Since the atoms which are in different spin states have different magnetic moments, the two populations will separate in space in the field gradient and the population imbalance can be determined by measuring the number of atoms in each cloud. We can then determine if a severe imbalance is causing the evaporative cooling process to cease. Such diagnostic tools will allow us to identify and eliminate any experimental artifacts which impede our ability to attain temperatures below the Fermi temperature.

8.3 Future Outlook

An ultracold gas of ^{6}Li fermions confined in a stable optical trap provides the foundation for a wide range of future investigations. Even before degeneracy is attained, this system already provides a basis for the study of many remarkable physical phenomena.

Currently, there is interest in using ultracold, fermionic atoms to improve upon the accuracy of precision measurements. A number of precision measurements such

as atomic time and frequency standards or the measurement of the electric dipole moment (EDM) of an atom depend on monitoring the relative frequency between two hyperfine ground states of an atom. The relevant figure of merit for an EDM measurement is proportional to the product of the number of atoms observed and the coherence lifetime [58]. The coherence lifetime determines the spectral linewidth in atomic clock applications. Collisions between the atoms limit the sensitivity of both EDM measurements [58] and atomic clock standards [129, 130] since collisions cause systematic shifts in frequency and reduce the coherence lifetime. It has been suggested that ultracold, fermionic vapors may improve these measurements [58, 131]. If a collection of ultracold fermionic atoms are all placed in the same superposition state, s-wave collisions between these atoms are prohibited by the exclusion principle. Thus, the unwanted effects of collisions are expected to be avoided. It is therefore of current interest to study the properties of an ultracold gas of fermionic atoms where the atoms are placed in a coherent superposition state. Our system is ideally suited for such studies since the potential provided by the CO_2 laser trap is state independent allowing the coherent superposition state to exhibit a long lifetime. Coherence lifetimes beyond 100 seconds should be obtainable in this system.

The development of a stable optical trap for fermionic atoms may also provide the foundation for future fundamental investigations of the properties of a Fermi gas confined in a periodic potential. By retroreflecting the CO_2 laser beam through the focus of the trap with the same polarization a one-dimensional optical lattice potential is formed. By using multiple intersecting beams, more complicated two- and three-dimensional lattices can be formed. Currently a number of groups are investigating bosonic atoms confined in optical lattices. The properties of a Fermi

gas confined in a periodic lattice would provide complimentary experiments. This system would provide a unique environment for the systematic study of the Hubbard Hamiltonian which has recieved a great deal of theoretical attention as a model for high-T_C superconductors (see for example Ref. [132] and references therein).

If a degenerate gas of ^{6}Li fermions can be obtained, a number of interesting phenomena should be observable. For temperatures $T < T_F$ the light scattering properties of the gas are expected to be altered [10, 13, 14]. This is due to the fact that the presence of the filled Fermi sea inhibits spontaneous emission. When a ^{6}Li atom below the Fermi level absorbs a photon, the atom receives a momentum kick in the direction of propagation of the light and is promoted to an unoccupied momentum state above the Fermi level. However, when the atom subsequently emits a photon, the number of available momentum states that the atom can occupy following emission is reduced due to the presence of the filled Fermi sea.

The collective oscillations of a degenerate Fermi gas should also be of interest to study. These oscillations can be excited by shaking the CO_2 laser trap or modulating its intensity. There have been a number of theoretical predictions which explore the expected collective excitation spectrum for a degenerate gas of fermions [11, 12, 38]. Due to the large and widely tunable scattering lengths obtainable with certain two-state mixtures in ^{6}Li, the collective oscillation spectrum for the gas in both the collisionless (zero sound) and hydrodynamic (first sound) regime should be observable [11]. It is interesting to note that as the temperature T is lowered far below T_F, a gas which exhibits hydrodynamic oscillation will eventually exhibit a collisionless excitation spectrum as the gas is cooled due to the suppression of collisions by Pauli blocking. For a two-state mixture of ^{6}Li atoms, a spin-dipole mode of oscillation in which the spins oscillate 180° out of phase with one another

can be excited. This spin-dipole mode of oscillation is related to the giant dipole resonance explored in nuclear physics [12]. It should prove interesting to study these collective oscillation modes in a system in which the temperature, density and interaction strength can be independently controlled.

Since the CO_2 laser trap can confine both neutral atoms and molecules, this system is ideally suited for a novel form of nonlinear matter wave optics recently suggested in which atoms in a Fermi gas can be converted to bosonic diatomic molecules via a two-photon Raman transition [133]. If the gas is degenerate the dynamics of the system become extremely interesting as it causes the interconversion between a degenerate Fermi gas of atoms and a Bose-Einstein condensate of molecules. It is interesting to note that the description of this system is related to the Friedberg-Lee quantum field theory model of high-T_C superconductivity [134].

One of the most exciting possibilities for future research is the observation of a superfluid transition as the atoms are cooled below a critical temperature T_C [17–19, 39–42]. Due to the very large and negative scattering length exhibited by certain two-state mixtures of ^{6}Li, the superfluid transition is expected to occur at temperatures and densities comparable to those achieved in Bose-Einstein condensation experiments with alkali atom vapors. As mentioned previously, only optically confined two-state mixtures of either ^{40}K or ^{6}Li are predicted to make a superfluid transition. Thus, the development of a stable optical trap for fermionic atoms may enable the observation of a superfluid transition in a dilute Fermi gas in which the temperature, density and interaction strength can be independently controlled. This would permit the systematic study of the properties of the gas for comparison with BCS theory.

There have been a number of theoretical papers which investigate the collective

excitation spectrum of a Fermi gas in the superfluid phase [11, 12, 124, 135]. It is interesting to note that the gap energy due to the formation of Cooper pairs may be observable as a shift in the mechanical resonance frequency spectrum [124]. Other methods have been proposed for observing the superfluid transition. The presence of Cooper pairs may cause a change in the light scattering properties of the gas [43]. Another method for detecting the energy gap requires the ability to suddenly transfer atoms from an interacting to a noninteracting state [136]. The transition from the interacting $|3\rangle - |1\rangle$ mixture to the noninteracting $|2\rangle - |1\rangle$ proposed and demonstrated in this dissertation may be useful in detecting the energy gap by this method.

In addition to comparison with BCS theory, regions of parameter space that cannot be described in the context of mean field theory can also be studied. The effect of density fluctuations on the critical temperature have been explored theoretically [18, 137]. In addition, since the ^{6}Li interaction strength is widely tunable, we may be able to investigate experimentally the crossover between weakly coupled Cooper pairs to the Bose-Einstein condensation of molecules [138]. Many of these experiments may have relevance to current theories of high-T_C superconductivity.

Appendix A

Internal Structure of ^{6}Li

The ^{6}Li atom is composed of three protons, three neutrons and three electrons. A ^{6}Li atom in its ground state contains 2 electrons in the $1s$ orbital and a single valance electron in the $2s$ orbital. The ^{6}Li nucleus has a spin $i = 1$ which couples via the hyperfine interaction to the valance electron spin $s = 1/2$ giving rise to six possible hyperfine states in the $2s\ ^2S_{1/2}$ electronic ground state. The internal state Hamiltonian for ^{6}Li in its $2s$ ground state is given by

$$H^{int}(\mathbf{B}) = \frac{a_{hf}}{\hbar^2}\,\mathbf{s}\cdot\mathbf{i} + \left(\frac{2\mu_e}{\hbar}\,\mathbf{s} - \frac{\mu_n}{\hbar}\,\mathbf{i}\right)\cdot\mathbf{B}, \tag{A.1}$$

where a_{hf} is the hyperfine constant, μ_e is the Bohr magneton, μ_n is the nuclear magnetic moment, and $\mathbf{B}$ is an external magnetic field. The hyperfine coupling term $a_{hf}\mathbf{s}\cdot\mathbf{i}/\hbar^2$ couples the product basis states $|m_s\, m_i\rangle$ where m_s and m_i are the projections of $\mathbf{s}$ and $\mathbf{i}$ respectively onto the quantization axis.

For $\mathbf{B} = 0$, this Hamiltonian is diagonal in the $|f\, m_f\rangle$ basis where $\mathbf{f} = \mathbf{s} + \mathbf{i}$ and m_f is the projection of $\mathbf{f}$ onto the quantization axis. The eigenstates of $H^{int}(\mathbf{B} = 0)$

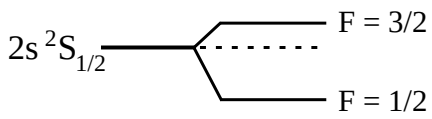

Figure A.1: Hyperfine Ground State of ^{6}Li

are $|f = 3/2,\, m_f = \pm 3/2, \pm 1/2\rangle$ with energy $E = a_{hf}/2$ and $|f = 1/2,\, m_f = \pm 1/2\rangle$ with energy $E = -a_{hf}$. Thus, at zero field there exists a hyperfine ground state splitting $E_{hf} = 3a_{hf}/2$. From the measured zero-field hyperfine splitting of $E_{hf}/h =$ 228.2 MHz, we find that $a_{hf}/h = 152.1$ MHz. Figure A.1 summarizes these results.

For an arbitrary **B** field, the internal state Hamiltonian can be diagonalized by six eigenstates $|1\rangle$-$|6\rangle$ which we can express in terms of superpositions of the product states $|m_s\, m_i\rangle$. The diagonalization procedure is simplified by the fact that $H^{int}(\mathbf{B})$ is block diagonal in the product basis since it conserves the quantity $m_f = m_s + m_i$. Thus, only states with the same total spin projection m_f are coupled and only 2×2 matrices need to be diagonalized. The resulting eigenstates written in terms of the product states $|m_s\, m_i\rangle$ are

$$\begin{aligned}
|1\rangle &= \sin\theta_+ \,|1/2\ 0\rangle - \cos\theta_+ \,|-1/2\ 1\rangle \\
|2\rangle &= \sin\theta_- \,|1/2\ -1\rangle - \cos\theta_- \,|-1/2\ 0\rangle \\
|3\rangle &= |-1/2\ -1\rangle \\
|4\rangle &= \cos\theta_- \,|1/2\ -1\rangle + \sin\theta_- \,|-1/2\ 0\rangle \\
|5\rangle &= \cos\theta_+ \,|1/2\ 0\rangle + \sin\theta_+ \,|-1/2\ 1\rangle \\
|6\rangle &= |1/2\ 1\rangle\,, \qquad\qquad (A.2)
\end{aligned}$$

where $\sin\theta_\pm = 1/\sqrt{1 + (Z^\pm + R^\pm)^2/2}$, $Z^\pm = (\mu_n + 2\mu_e)B/a_{hf} \pm 1/2$, and $R^\pm = \sqrt{(Z^\pm)^2 + 2}$. These states are labeled 1 through 6 in order of increasing energy in an external **B** field. Figure A.2 shows the corresponding energies as a function of applied B field.

Note that for large magnetic fields ($\mu_e B >> a_{hf}$) the product states $|m_s\, m_i\rangle$ become good approximations to the true eigenstates of the Hamiltonian. The high-

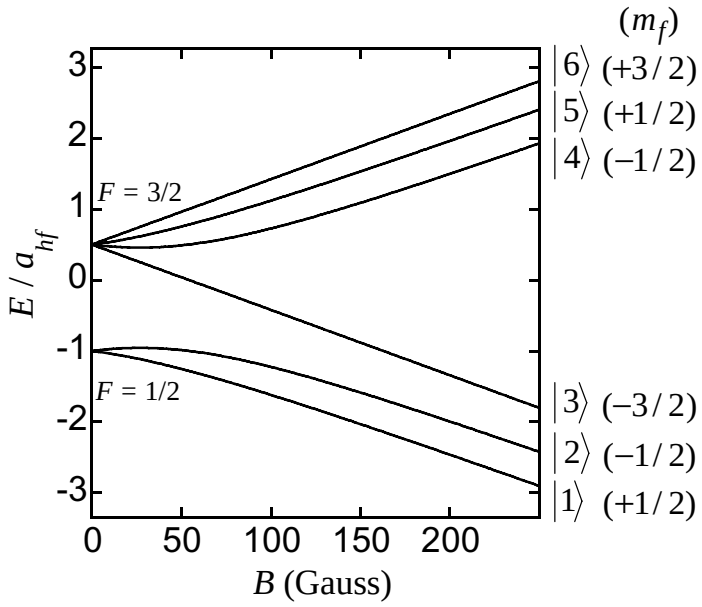

Figure A.2: Hyperfine State Energies in an External B-Field

field eigenstates are $|m_s = 1/2\, m_i = 0, \pm 1\rangle$ and $|m_s = -1/2\, m_i = 0, \pm 1\rangle$ with energy $E \cong \mu_e B$ and $E \cong -\mu_e B$ respectively since $\mu_e >> \mu_n$.

Appendix B

Magnetic Trap for ^{6}Li

Alkali atoms can be confined in a magnetic field through the interaction between the permanent magnetic dipole moment of the atom $\boldsymbol{\mu}$ and a magnetic field $\boldsymbol{B}$. The interaction is given by $U(\boldsymbol{r}) = -\boldsymbol{\mu} \cdot \boldsymbol{B}(\boldsymbol{r})$. The atoms are confined if $U(\boldsymbol{r})$ has a local minimum.

As long as the direction of the $\boldsymbol{B}$-field due to the motion of the atoms in the trap does not change more rapidly than the Larmor precession frequency (i.e. $\boldsymbol{v} \cdot \nabla \hat{\boldsymbol{B}} < \mu|\boldsymbol{B}|/\hbar$ where $\boldsymbol{v}$ is the velocity of an atom) than the magnetic dipole moment of the atom will adiabatically follow the direction of the $\boldsymbol{B}$ field and the interaction potential is simply

$$U(\boldsymbol{r}) = -\mu \cdot |\boldsymbol{B}|. \tag{B.1}$$

Thus, the potential is proportional to the local magnetic field magnitude and is given by the interaction energy between the atom and the local magnetic field.

In Appendix A we calculated the interaction energy for the hyperfine ground states of ^{6}Li in a magnetic field. From Figure A.2 and (B.1) we see that the states labeled $|1\rangle - |3\rangle$ will be attracted to regions of high magnetic field in a magnetic trap. These are referred to as the "high-field-seeking" states. Conversely, the states $|4\rangle - |6\rangle$ will be attracted to a region of small magnetic field in a magnetic trap. These are referred to as the "low-field-seeking" states.

Only the low-field-seeking states can be confined in a magnetic field. Maxwell's equations do not allow for a local maximum in $|\boldsymbol{B}|$ in free space as shown below. Thus, only a magnetic trap with a local minimum in $|\boldsymbol{B}|$ can be constructed which can be used to confine the low-field-seeking states. Unfortunately, the low-field-seeking state all contain stored energy. Therefore, an inelastic collision can occur in which an atom in a confined low-field-seeking state can make a transition to a high-field-seeking state which will be expelled from the trap. In Chapter 2 we show that, for two-state mixtures of ^{6}Li which can be confined in a magnetic trap, the inelastic collision rate is prohibitively high. Thus, magnetic traps are not well suited for confining two-state mixtures of ^{6}Li.

To show that Maxwell's equations do not allow for a magnetic field maximum in free space, we begin by considering the quantity $\nabla^2(\boldsymbol{B}\cdot\boldsymbol{B})$, where $\boldsymbol{B}$ is the magnetic field. The quantity can be written as

$$\begin{aligned}\nabla^2(\boldsymbol{B}\cdot\boldsymbol{B}) &= \partial_{ii}(B_j\,B_j)\\ &= \partial_i(2\,B_j\,\partial_i B_j)\\ &= 2B_j\,\partial_{ii}B_j + 2(\partial_i B_j)^2 \qquad \text{(B.2)}\end{aligned}$$

where we are using the notation $\partial_i = \partial/\partial x_i$, $\partial_{ii} = \partial^2/\partial x_i^2$ and we assume that all repeated indices are summed over. In free space $\nabla\times\boldsymbol{B} = 0$ and $\nabla\cdot\boldsymbol{B} = 0$. This implies that $\nabla^2\boldsymbol{B} = \boldsymbol{0}$, i.e. each component of $\boldsymbol{B}$ satisfies Laplace's equation. Thus, the first term in the last line of (B.2), $2\,B_j\,\partial_{ii}B_j = 0$ since $\partial_{ii}B_j = 0$. Thus, we have

$$\nabla^2(\boldsymbol{B}\cdot\boldsymbol{B}) = 2(\partial_i B_j)^2 \geq 0, \qquad \text{(B.3)}$$

implying that a local field maximum in $|\boldsymbol{B}|$ is forbidden.

Appendix C

The Transition Dipole Moments in ^{6}Li

In order to compute the Raman Rabi frequency required in Section 7.2, the dipole moment matrix elements for the $^2S_{1/2} \rightarrow^2 P_{3/2}$ transitions in ^{6}Li need to be calculated. The relevant matrix elements have been computed previously by Tom Savard [98].

The results of these calculations are given in Figure C.1. Each matrix element is expressed in units of $\mu_0 = 5.9$ Debye (1 Debye $= 10^{-18}\,\mathrm{esu}\cdot\mathrm{cm}$). Here, μ_0 is the dipole transition matrix element for the $\left|^2S_{1/2}, F = 3/2\, M_F = 3/2\right\rangle \rightarrow \left|^2P_{3/2}, F' = 5/2\, M_{F'} = 5/2\right\rangle$ cycling transition. Since this is a closed transition, the dipole moment μ_0 can be calculated from the observed excited state lifetime $\Gamma^{-1} = 27.2$ ns using the relationship $\mu_0 = \sqrt{3\,\hbar\,\Gamma/4\,k^3}$ where $k = 2\pi/\lambda$ is the wavenumber for the optical transition. Due to symmetry, only half of the matrix elements are shown. The other half are related by a factor r, which is either 1 or -1, depending on the particular levels involved as shown in Figure C.1.

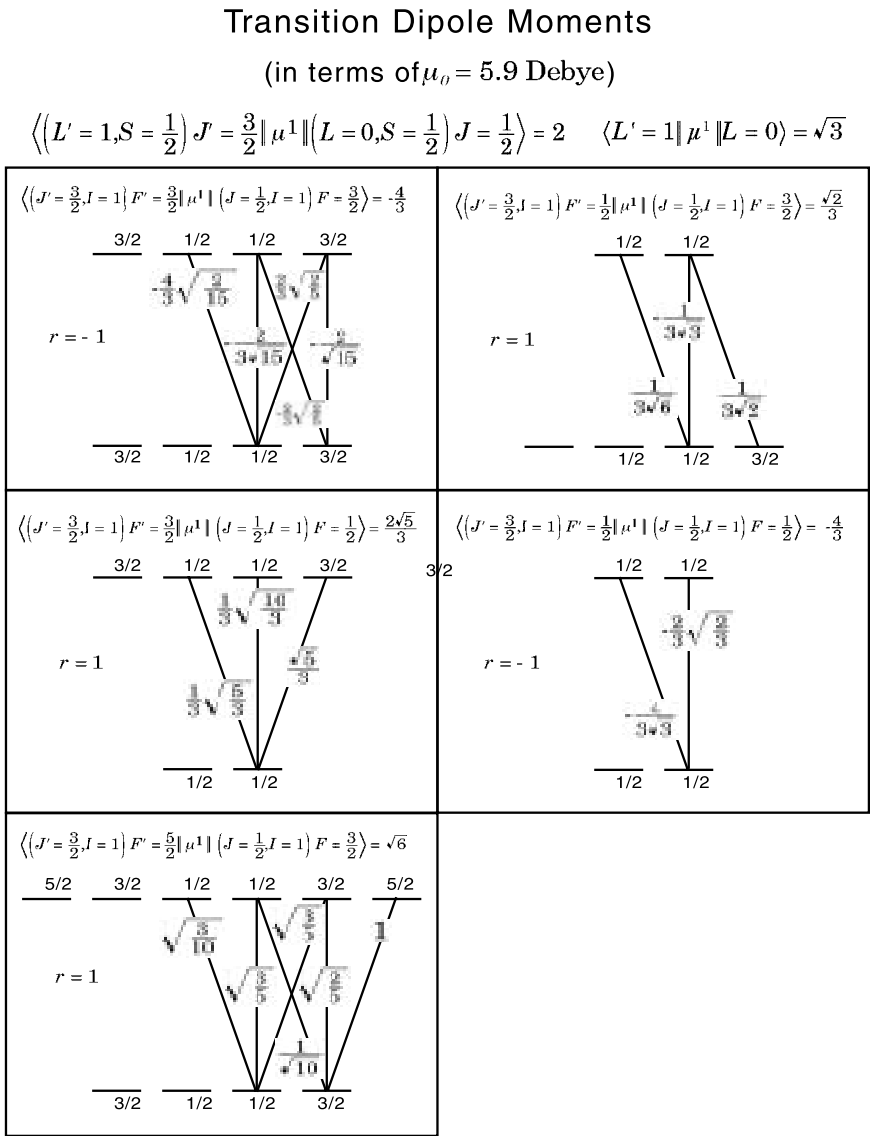

Figure C.1: Transition dipole moments of the $^2S_{1/2} \rightarrow ^2 P_{3/2}$ line in ^{6}Li.

Bibliography

[1] M. H. Anderson, J. R. Ensher, M. R. Matthews, C. E. Wieman, and E. A. Cornell. Observation of Bose-Einstein condensation in a dilute atomic vapor. *Science*, 269(0):198, July 1995.

[2] C. C. Bradley, C. A. Sackett, J. J. Tollett, and R. G. Hulet. Evidence of Bose-Einstein condensation in an atomic gas with attractive interactions. *Phys. Rev. Lett.*, 75(9):1687, August 1995. *ibid.* **79**, 1170 (1997).

[3] K. B. Davis, M.-O. Mewes, M. R. Andrews, N. J. van Druten, D. S. Durfee, D. M. Kurn, and W. Ketterle. Bose-Einstein condensation in a gas of sodium atoms. *Phys. Rev. Lett.*, 75(22):3969, November 1995.

[4] M.-O. Mewes, M. R. Andrews, D. M. Kurn, D. S. Durfee, C. G. Townsend, and W. Ketterle. Output coupler for Bose-Einstein condensed atoms. *Phys. Rev. Lett.*, 78(4):582, January 1997.

[5] E. W. Hagley, L. Deng, M. Kozuma, J. Wen, K. Helmerson, S. L. Rolston, and W. D. Phillips. A well-collimated quasi-continuous atom laser. *Science*, 283:1706, March 1999.

[6] Immanuel Bloch, Theodor W. Hänsch, and Tilman Esslinger. Atom laser with a cw output coupler. *Phys. Rev. Lett.*, 82(15):3008, April 1999.

[7] D. A. Butts and D. S. Rokhsar. Trapped Fermi gases. *Phys. Rev. A*, 55(6):4346, June 1997.

[8] J. Schneider and H. Wallis. Mesoscopic Fermi gas in a harmonic trap. *Phys. Rev. A*, 57(2):1253, February 1998.

[9] G. M. Bruun and K. Burnett. Interacting Fermi gas in a harmonic trap. *Phys. Rev. A*, 58(3):2427, September 1998.

[10] B. DeMarco and D. S. Jin. Exploring a quantum degenerate gas of fermionic atoms. *Phys. Rev. A*, 58(6):R4267, December 1998.

[11] G. M. Bruun and C. W. Clark. Hydrodynamic excitations of trapped Fermi gases. *Phys. Rev. Lett.*, 83(26):5415, December 1999.

[12] L. Vichi and S. Stringari. Collective oscillations of an interacting trapped Fermi gas. *Phys. Rev. A*, 60(6):4734, December 1999.

[13] Janne Ruostekoski and Juha Javanainen. Optical linewidth of a low density Fermi-Dirac gas. *Phys. Rev. Lett.*, 82(24):4741, June 1999.

[14] T. Busch, J. R. Anglin, J. I. Cirac, and P. Zoller. Inhibition of spontaneous emission in Fermi gases. *Europhys. Lett.*, 44(1):1, 1998.

[15] A.J. Leggett. Cooper pairing in spin-polarized fermi systems. *Journal de Physique Colloque*, 41(C-7):19, 1980.

[16] E. R. I. Abraham, W. I. McAlexander, J. M. Gerton, R. G. Hulet, R. Côté, and A. Dalgarno. Triplet s-wave resonance in ^{6}Li collisions and scattering lengths of ^{6}Li and ^{7}Li. *Phys. Rev. A*, 55(5):R3299, May 1997.

[17] H. T. C. Stoof, M. Houbiers, C. A. Sackett, and R. G. Hulet. Superfluidity of spin-polarized ^{6}Li. *Phys. Rev. Lett.*, 76(1):10, January 1996.

[18] R. Combescot. Trapped ^{6}Li: a high T_c superfluid? *Phys. Rev. Lett.*, 83(19):3766, November 1999.

[19] M. Houbiers and H. T. C. Stoof. Cooper-pair formation in trapped atomic Fermi gases. *Phys. Rev. A*, 59(2):1556, February 1999.

[20] K. M. O'Hara, S. R. Granade, M. E. Gehm, T. A. Savard, S. Bali, C. Freed, and J. E. Thomas. Ultrastable CO_2 laser trapping of lithium fermions. *Phys. Rev. Lett.*, 82(21):4204, May 1999.

[21] K. M. O'Hara, M. E. Gehm, S. R. Granade, S. Bali, and J. E. Thomas. Stable, strongly attractive, two-state mixture of lithium fermions in an optical trap. *Phys. Rev. Lett.*, 85(10):2092, September 2000.

[22] Mark Edwards, P. A. Ruprecht, K. Burnett, R. J. Dodd, and Charles W. Clark. Collective excitations of atomic Bose-Einstein condensates. *Phys. Rev. Lett.*, 77(9):1671, August 1996.

[23] D. S. Jin, J. R. Ensher, M. R. Matthews, C. E. Wieman, and E. A. Cornell. Collective excitations of a Bose-Einstein condensate in a dilute gas. *Phys. Rev. Lett.*, 77(3):420, July 1996.

[24] M.-O. Mewes, M. R. Andrews, N. J. van Druten, D. M. Kurn, D. S. Durfee, C. G. Townsend, and W. Ketterle. Collective excitations of a Bose-Einstein condensate in a magnetic trap. *Phys. Rev. Lett.*, 77(6):988, August 1996.

[25] D. S. Jin, M. R. Matthews, J. R. Ensher, C. E. Wieman, and E. A. Cornell. Temperature-dependent damping and frequency shifts in collective excitations of a dilute Bose-Einstein condensate. *Phys. Rev. Lett.*, 78(5):764, February 1997.

[26] M. R. Andrews, C. G. Townsend, H.-J. Miesner, D. S. Durfee, D. M. Kurn, and W. Ketterle. Observation of interference between two Bose-Einstein condensates. *Science*, 275(0):637, January 1997.

[27] M.-O. Mewes, M. R. Andrews, N. J. van Druten, D. M. Kurn, D. S. Durfee, and W. Ketterle. Bose-Einstein condensation in a tightly confining dc magnetic trap. *Phys. Rev. Lett.*, 77(3):416, July 1996.

[28] M. J. Holland, D. S. Jin, M. L. Chiofalo, and J. Cooper. Emergence of interaction effects in Bose-Einstein condensation. *Phys. Rev. Lett.*, 78(20):3801, May 1997.

[29] Wolfgang Ketterle and Hans-Joachim Miesner. Coherence properties of Bose-Einstein condensates and atom lasers. *Phys. Rev. A*, 56(4):3291, October 1997.

[30] E. A. Burt, R. W. Ghrist, C. J. Myatt, M. J. Holland, E. A. Cornell, and C. E. Wieman. Coherence, correlations, and collisions: What one learns about Bose-Einstein condensates from their decay. *Phys. Rev. Lett.*, 79(3):337, July 1997.

[31] S. Inouye, M. R. Andrews, J. Stenger, H.-J. Miesner, D. M. Stamper-Kurn, and W. Ketterle. Observation of Feshbach resonances in a Bose-Einstein condensate. *Nature*, 392(0):151, March 1998.

[32] J. L. Roberts, N. R. Claussen, James P. Burke, Jr., Chris H. Greene, E. A. Cornell, and C. E. Wieman. Resonant magnetic field control of elastic scattering of cold ^{85}Rb. *Phys. Rev. Lett.*, 81(23):5109, December 1998.

[33] M. R. Matthews, D. S. Hall, D. S. Jin, J. R. Ensher, C. E. Wieman, E. A. Cornell, F. Dalfovo, C. Minniti, and S. Stringari. Dynamical response of a Bose-Einstein condensate to a discontinuous change in internal state. *Phys. Rev. Lett.*, 81(2):243, July 1998.

[34] C. Raman, M. Köhl, R. Onofrio, D. S. Durfee, C. E. Kuklewicz, Z. Hadzibabic, and W. Ketterle. Evidence for a critical velocity in a Bose-Einstein condensed gas. *Phys. Rev. Lett.*, 83(13):2502, September 1999.

[35] H.-J. Miesner, D. M. Stamper-Kurn, M. R. Andrews, D. S. Durfee, S. Inouye, and W. Ketterle. Bosonic stimulation in the formation of a Bose-Einstein condensate. *Science*, 279(0):1005, February 1998.

[36] L. Deng, E. W. Hagley, J. Wen, M. Trippenbach, Y. Band, P. S. Julienne, J. E. Simsarian, K. Helmerson, S. L. Rolston, and W. D. Phillips. Four-wave mixing with matter waves. *Nature*, 398(6724):218, March 1999.

[37] J. Denschlag, , J. E. Simsarian, D. L. Feder, C. W. Clark, L. A. Collins, J. Cubizolles, L. Deng, E. W. Hagley, K. Helmerson, W. P. Reinhardt, S. L. Rolston, B. I. Schneider, and W. D. Phillips. Generating solitons by phase engineering of a Bose-Einstein condensate. *Science*, 287(5450):97, January 2000.

[38] S.-K. Yip and Tin-Lun Ho. Zero sound modes of dilute Fermi gases with arbitrary spin. *Phys. Rev. A*, 59(6):4653, June 1999.

[39] M. Houbiers, R. Ferwerda, H. T. C. Stoof, W. I. McAlexander, C. A. Sackett, and R. G. Hulet. Superfluid state of atomic ^{6}Li in a magnetic trap. *Phys. Rev. A*, 56(6):4864, December 1997.

[40] M. A. Baranov and D. S. Petrov. Critical temperature and Ginzburg-Landau equation for a trapped Fermi gas. *Phys. Rev. A*, 58(2):R801, August 1998.

[41] H. T. C. Stoof and M. Houbiers. Condensed matter physics with trapped atomic Fermi gases. In M. Inguscio, S. Stringari, and C. E. Wieman, editors, *Proceedings of the International School of Physics - Enrico Fermi*, page 537. IOS Press, 1999.

[42] G. Bruun, Y. Castin, R. Dum, and K. Burnett. BCS theory for trapped ultracold fermions. *Euro. Phys. J. D*, 7(3):433, November 1999.

[43] Weiping Zhang, C. A. Sackett, and R. G. Hulet. Optical detection of a Bardeen-Cooper-Schrieffer phase transition in a trapped gas of fermionic atoms. *Phys. Rev. A*, 60(1):504, July 1999.

[44] B. DeMarco and D. S. Jin. Onset of Fermi degenereracy in a trapped atomic gas. *Science*, 285(5434):1703, September 1999.

[45] T. A. Savard, K. M. O'Hara, and J. E. Thomas. Laser-noise-induced heating in far-off resonance optical traps. *Phys. Rev. A*, 56(2):R1095, August 1997.

[46] M. E. Gehm, K. M. O'Hara, T. A. Savard, and J. E. Thomas. Dynamics of noise-induced heating in atom traps. *Phys. Rev. A*, 58(5):3914, November 1998.

[47] D. M. Stamper-Kurn, M. R. Andrews, A. P. Chikkatur, S. Inouye, H.-J. Miesner, J. Stenger, and W. Ketterle. Optical confinement of a Bose-Einstein consensate. *Phys. Rev. Lett.*, 80(10):2027, 1998.

[48] J. Stenger, S. Inouye, D. M. Stamper-Kurn, H.-J. Miesner, A. P. Chikkatur, and W. Ketterle. Spin domains in ground-state Bose-Einstein condensates. *Nature*, 396:345, November 1998.

[49] H.-J. Miesner, D. M. Stamper-Kurn, J. Stenger, S. Inouye, A. P. Chikkatur, and W. Ketterle. Observation of metastable states in spinor Bose-Einstein condensates. *Phys. Rev. Lett.*, 82(11):2228, March 1999.

[50] M. Kasevich and S. Chu. Laser cooling below a photon recoil with three-level atoms. *Phys. Rev. Lett.*, 69(12):1741, September 1992.

[51] H. J. Lee, C. S. Adams, N. Davidson, B. Young, M. Weitz, M. Kasevich, and Steven Chu. Dipole trapping, cooling in traps, and long coherence times. *At. Phys.*, 14(323):258, 1995.

[52] V. Vuletić, C. Chin, J. Kerman, and S. Chu. Degenerate raman sideband cooling of trapped cesium atoms at very high atomic densities. *Phys. Rev. Lett.*, 81(26):5768, December 1998.

[53] M. R. Andrews, D. M. Kurn, H.-J. Miesner, D. S. Durfee, C. G. Townsend, S. Inouye, and W. Ketterle. Propagation of sound in a Bose-Einstein condensate. *Phys. Rev. Lett.*, 79(4):553, July 1997. *ibid.* **80**, 2967 (1998).

[54] M. R. Matthews, B. P. Anderson, P. C. Haljan, D. S. Hall, C. E. Wieman, and E. A. Cornell. Vortices in a Bose-Einstein condensate. *Phys. Rev. Lett.*, 83(13):2498, September 1999.

[55] M. Houbiers, H. T. C. Stoof, W. I. McAlexander, and R. G. Hulet. Elastic and inelastic collisions of Li-6 atoms in magnetic and optical traps. *Phys. Rev. A*, 57(3):R1497, March 1998.

[56] B. DeMarco, J. L. Bohn, J. P. Burke, Jr., M. Holland, and D. S. Jin. Measurement of p-wave threshold law using evaporatively cooled fermionic atoms. *Phys. Rev. Lett.*, 82(21):4208, May 1999.

[57] J. L. Bohn. Cooper pairing in ultracold ^{40}k using feshbach resonances. *Phys. Rev. A*, 61(5):053409/1–4, 2000.

[58] M. V. Romalis and E. N. Fortson. Zeeman frequency shifts in an optical dipole trap used to search for an electric-dipole moment. *Phys. Rev. A*, 59(59):4547, June 1999.

[59] C. J. Joachain. *Quantum Collision Theory.* North-Holland Publishing Company, 1983.

[60] R. Côté, A. Dalgarno, and M. J. Jamieson. Elastic scattering of two ^{7}Li atoms. *Phys. Rev. A*, 50(1):399, July 1994.

[61] B. Barakat, R. Bacis, F. Carrot, S. Churassy, P. Crozet, F. Martin, and J. Verges. Extensive analysis of the X $^1\Sigma_g^+$ ground state of $^7Li_2$ by laser-induced fluorescence fourier transform spectrometry. *Chemical Physics*, 102:215, 1986.

[62] D. D. Konowalow and M. L. Olson. The electronic structure and spectra of the X $^1\Sigma_g^+$ and A $^1\Sigma_u^+$ states of Li_2. *J. Chem. Phys.*, 71(1):450, July 1979.

[63] I. Schmidt-Mink, W. Müller, and W. Meyer. Ground- and excited-state properties of Li_2 and Li_2^+ from *ab initio* calculations with effective core polarization potentials. *Chemical Physics*, 92:263, 1985.

[64] Z.-C. Yan, J. F. Babb, A. Dalgarno, and G. W. F. Drake. Variational calculations of dispersion coefficients for interacctions among H, He, and Li atoms. *Phys. Rev. A*, 54(4):2824, October 1996.

[65] W. T. Zemke and W. C. Stwalley. Analysis of long-range dispersion and exchange interactions of two lithium atoms. *J. Phys. Chem.*, 97(10):2053, 1993.

[66] D. D. Konowalow, R. M. Regan, and M. E. Rosenkrantz. The "most likely" potential energy curve for the lowest $^3\Sigma_u^+$ state of Li_2. *J. Chem. Phys.*, 81(10):4534, November 1984.

[67] G. W. F. Drake, editor. *Atomic, Molecular, and Optical Physics Handbook.* American Instutute of Physics, 1996.

[68] N. F. Mott and H. S. W. Massey. *The Theory of Atomic Collisions.* Clarendon Press, Oxford, 1965.

[69] M. S. Child. *Molecular Collision Theory.* Academic Press, London and New York, 1974.

[70] F. A. van Abeelen, B. J. Verhaar, and A. Moerdijk. Sympathetic cooling of ^{6}Li atoms. *Phys. Rev. A*, 55(6):4377, June 1997.

[71] H. Feshbach. *Theoretical Nuclear Physics- Nuclear Reactions.* John Wiley & Sons, New York, 1992.

[72] C. Cohen-Tannoudji, B. Diu, and F. Laloe. *Quantum Mechanics.* John Wiley and Sons, New York, 1977.

[73] A. Ashkin. Trapping of atoms by resonance radiation pressure. *Phys. Rev. Lett.*, 40(12):729, March 1978.

[74] Steven Chu, J. E. Bjorkholm, A. Ashkin, and A. Cable. Experimental observation of optically trapped atoms. *Phys. Rev. Lett.*, 57(3):314, July 1986.

[75] C. Cohen-Tannoudji. *Atom Photon Interactions: basic processes and applications*. J. Wiley, New York, 1992.

[76] J. D. Miller, R. A. Cline, and D. J. Heinzen. Far-off-resonance optical trapping of atoms. *Phys. Rev. A*, 47(6):R4567, June 1993.

[77] T. Takekoshi and R. J. Knize. CO_2 laser trap for cesium atoms. *Opt. Lett.*, 21(1):77, January 1996.

[78] S. Friebel, C. D'Andrea, J. Walz, M. Weitz, and T. W. Hänsch. CO_2-laser optical lattice with cold rubidium atoms. *Phys. Rev. A.*, 57(1):R20, January 1998.

[79] M. Weidemüller, H. Engler, M. Nill, T. Weber, and R. Grimm. Lithium and cesium in a quasi-electrostatic CO_2-laser trap. *Laser Spectroscopy. 14th International Conference. ICOLS99*, page 336, 1999.

[80] T. Takekoshi, J. R. Yeh, and R. J. Knize. Quasi-electrostatic trap for neutral atoms. *Opt. Comm.*, 114:421, February 1995.

[81] Charles S. Adams, Heun Lee, Nir Davidson, Mark Kasevich, and Steven Chu. Evaporative cooling in a crossed dipole trap. *Phys. Rev. Lett.*, 74(18):3577, May 1995.

[82] Nir Davidson, Heun Jin Lee, Charles S. Adams, Mark Kasevich, and Steven Chu. Long atomic coherence times in an optical dipole trap. *Phys. Rev. Lett.*, 74(8):1311, February 1995.

[83] H. J. Lee, C. S. Adams, M. Kasevich, and S. Chu. Raman cooling of atoms in an optical dipole trap. *Phys. Rev. Lett.*, 76(15):2658, April 1996.

[84] C. S. Adams and E. Riis. Laser cooling and trapping of neutral atoms. *Prog. Quant. Electr.*, 21(1):1, 1997.

[85] M. Zielonkowski, I. Manek, U Moslener, P. Rosenbusch, and R. Grimm. Manipulation of spin-polarized atoms in an optical dipole-force trap. *Europhys. Lett.*, 44(6):700, December 1998.

[86] J. E. Bjorkholm. Collision-limited lifetimes of atom traps. *Phys. Rev. A*, 38(3):1599, August 1988.

[87] S. Bali, K. M. O'Hara, M. E. Gehm, S. R. Granade, and J. E. Thomas. Quantum-diffractive background gas collisions in atom-trap heating and loss. *Phys. Rev. A*, 60(1):R29, July 1999.

[88] H. C. W. Beijerinck. Rigorous calculation of heating in alkali-metal traps by bckground gas collisions. *Phys. Rev. A*, 61(3):033606/1–6, March 2000.

[89] C. Freed. Ultrastable CO_2 lasers. *The Lincoln Laboratory Journal*, 3(3):479, 1990.

[90] J. E. Thomas, M. J. Kelly, J.-P. Monchalin, N. A. Kurnit, and A. Javan. Stable CO_2 and N_2O laser design. *Rev. Sci. Instrum.*, 51(2):240, February 1980.

[91] L. Windholz. Precise stark-effect investigations of the lithium D_1 and D_2 lines. *Phys. Rev. A*, 46(9):5812, November 1992.

[92] Theodore S. Fahlen. CO_2 laser design procedure. *Appl. Opt.*, 12(10):2381, October 1973.

[93] T. M. Hard. Laser wavelength selection and output coupling by a grating. *Appl. Opt.*, 9(8):1825, August 1970.

[94] E. L. Raab, M. Prentiss, Alex Cable, Steven Chu, and D. E. Pritchard. Trapping of neutral sodium atoms with radiation pressure. *Phys. Rev. Lett.*, 59(23):2631, December 1987.

[95] Alan L. Migdall, John V. Prodan, William D. Phillips, Thomas H. Bergeman, and Harold J. Metcalf. First observation of magnetically trapped neutral atoms. *Phys. Rev. Lett.*, 54(24):2596, June 1985.

[96] W. D. Philips and H. Metcalf. Laser deceleration of an atomic beam. *Phys. Rev. Lett.*, 8(9):596, March 1982.

[97] John V. Prodan, William D. Phillips, and Harold J. Metcalf. Laser production of a very slow monoenergetic atomic beam. *Phys. Rev. Lett.*, 49(16):1149, October 1982.

[98] Thomas Alan Savard. *Raman Induced Resonance Imaging of Trapped Atoms.* PhD thesis, Duke University, 1998.

[99] C. A. Baird. Design and characterization of a multi-coil zeeman slower. Master's thesis, Duke University, 1996.

[100] P. D. Lett, W. D. Phillips, S. L. Rolston, C. E. Tanner, R. N. Watts, and C. I. Westbrook. Optical molasses. *J. Opt. Soc. Am. B*, 6(11):2084, November 1989.

[101] Paul D. Lett, Richard N. Watts, Christoph I. Westbrook, William D. Phillips, Phillip L. Gould, and Harold J. Metcalf. Observation of atoms laser cooled below the Doppler limit. *Phys. Rev. Lett.*, 61(2):169, July 1988.

[102] J. Dalibard and C. Cohen-Tannoudji. Laser cooling below the Doppler limit by polarization gradients: simple theoretical-models. *J. Opt. Soc. Am. B*, 6(11):2023, November 1989.

[103] D. W. Sesko, T. G. Walker, and C. E. Wieman. Behavior of neutral atoms in a spontaneous force trap. *J. Opt. Soc. Am. B*, 8(5):946, May 1991.

[104] M. L. Marable. *Adaptive Resonance Imaging and All-Optical Interferometry.* PhD thesis, Duke University, 1995.

[105] J. R. Gardner. *Ultra-High Resolution Atom Imaging in a Light-Shift Gradient.* PhD thesis, Duke University, 1995.

[106] W. L. Wiese, M. W. Smith, and B. M. Glennon, editors. *Atomic Transition Probabilities.* Washington, U. S. Dept. of Commerce, National Bureau of Standards, 1966.

[107] Charlotte Emma Moore. *Atomic energy levels as derived from the analyses of optical spectra.* Washington, U. S. Dept. of Commerce, National Bureau of Standards, 1971.

[108] H. Margenau and N. R. Kestner. *Theory of Intermolecular Forces.* Pergamon, New York, 1971.

[109] F. Reif. *Fundamentals of Statistical and Thermal Physics.* McGraw-Hill, New York, 1965.

[110] V. Gomer, B. Ueberholz, S. Knappe, F. Strauch, D. Frese, and D. Meschede. Decoding the dynamics of a single trapped atom from photon correlations. *Appl. Phys. B*, 67(6):689, December 1998.

[111] William H. Press, Brian P. Flannery, Saul A. Teukolsky, and William T. Vetterling. *Numerical Recipes in C: The Art of Scientific Computing.* Cambridge University Press, Cambridge, 1989.

[112] K. L. Corwin, S. J. M. Kuppens, D. Cho, and C. E. Wieman. Spin-polarized atoms in a circularly polarized optical dipole trap. *Phys. Rev. Lett.*, 83(7):1311, August 1999.

[113] K. L. Corwin, T. E. Chupp, K. W. Miller, and C. E. Wieman. Investigations of far-off resonance trap loading and loss mechanisms. *Bull. Am. Phys. Soc.*, 43:1292, 1998.

[114] C. Salomon, J. Dalibard, W. D. Phillips, A. Clairon, and S. Guellati. Laser cooling of cesium atoms below 3 μk. *Europhys. Lett.*, 12(8):683, August 1990.

[115] O. J. Luiten, M. W. Reynolds, and J. T. M. Walraven. Kinetic theory of the evaporative cooling of a trapped gas. *Phys. Rev. A*, 53(1):381, January 1996.

[116] K. Huang, editor. *Statistical Mechanics*. Wiley, New York, 1987.

[117] Kirstine Berg-Sørensen. Kinetics for evaporative cooling of a trapped gas. *Phys. Rev. A*, 55(2):1281, February 1997.

[118] Kirstine Berg-Sorensen. Erratum: Kinetics for evaporative cooling of a trapped gas. *Phys. Rev. A*, 56(4):3308, 1997.

[119] C. A. Sackett, C. C. Bradley, and R. G. Hulet. Optimization of evaporative cooling. *Phys. Rev. A*, 55(5):3797, May 1997.

[120] Edward G. Harris. *A Pedestrian Approach to Quantum Field Theory*. John Wiley & Sons, Inc., 1972.

[121] M. J. Holland, B. DeMarco, and D. S. Jin. Evaporative cooling of a two-component degenerate Fermi gas. *Phys. Rev. A*, 61:053610, April 2000.

[122] W. Geist, A. Idrizbegovic, M. Marinescu, T. A. B. Kennedy, and L. You. Evaporative cooling of trapped fermionic atoms. *Phys. Rev. A*, 61(1):013406/1–7, January 2000.

[123] Steven Chu, L. Hollberg, J. E. Bjorkholm, Alex Cable, and A. Ashkin. Three-dimensional viscous confinement and cooling of atoms by resonance radiation pressure. *Phys. Rev. Lett.*, 55(1):48, July 1985.

[124] G. M. Bruun and C. W. Clark. Detection of the BCS transition of a trapped Fermi gas. see cond-mat/9906392.

[125] T. Walker, P. Feng, D. Hoffmann, and III R. S. Williamson. Spin-polarized spontaneous-force atom trap. *Phys. Rev. Lett.*, 69(15):2168, October 1992.

[126] L. D. Landau and E. M. Lifshitz. *Mechanik*. Akademie-Verlag, Berlin, 1964.

[127] P. R. Bevington and D. K. Robinson. *Data reduction and error analysis for the physical sciences.* McGraw-Hill, New York, 1992.

[128] A. G. W. Modawi and A. J. Leggett. Some properties of a spin-1 Fermi superfluid: application to spin-polarized ^{6}Li. *J. of Low Temp. Phys.*, 109(3):625, 1997.

[129] E. Tiesinga, B. J. Verhaar, H. T. C. Stoof, and D. van Bragt. Spin-exchange frequency shift in a cesium atomic fountain. *Phys. Rev. A*, 45(5):R2671, March 1992.

[130] K. Gibble and S. Chu. Laser-cooled Cs frequency standard and a measurement of the frequency shift due to ultracold collisions. *Phys. Rev. Lett.*, 70(12):1771, March 1993.

[131] K. Gibble and B. J. Verhaar. Eliminating cold-collision frequency shifts. *Phys. Rev. A*, 52(4):3370, October 1995.

[132] E. Dagotto. Correlated electrons in high-temperature superconductors. *Rev. Mod. Phys.*, 66(3):763, July 1994.

[133] D. J. Heinzen, Roahn Wynar, P. D. Drummond, and K. V. Kheruntsyan. Superchemistry: Dynamics of coupled atomic and molecular Bose-Einstein condensates. *Phys. Rev. Lett.*, 84(22):5029, 2000.

[134] R. Friedberg and T. D. Lee. Gap energy and long-range order in the boson-fermion model of superconductivity. *Phys. Rev. B*, 40(10):6745, 1989.

[135] M. A. Baranov and D. S. Petrov. Low-energy collective excitations in a superfluid trapped Fermi gas. *Phys. Rev. A.*, 62:041601/1–4, 2000.

[136] P. Törmä and P. Zoller. Laser probing of atomic cooper pairs. *Phys. Rev. Lett.*, 85(3):487, 2000.

[137] H. Heiselberg, C. J. Pethick, H Smith, and L. Viverit. Influence of induced interactions on the superfluid transition in dilute Fermi gases. *Phys. Rev. Lett.*, 85(12):2418, 2000.

[138] M. Randeria. Crossover from BCS theory to Bose-Einstein condensation. In A. Griffin, D. W. Snoke, and S. Stringari, editors, *Bose-Einstein Condensation*, pages 355–392. Cambridge Univ. Press, 1995.

Biography

Ken O'Hara was born in Columbus, Ohio on April 28, 1972. He grew up in Columbus and graduated from Northland High School in 1990. He majored in physics at the University of Notre Dame in South Bend, Indiana. In 1994, he graduated *Magna Cum Laude* and was inducted into the *Phi Beta Kappa* Society. In the fall of 1994, he enrolled in the graduate physics program at Duke University. While at Duke, he received the Fritz London Fellowship for his work in ultracold Fermi gases under the direction of Professor John E. Thomas. His research at Duke University focused on developing a stable optical trap for studies of interactions in an ultracold Fermi gas. On May 27, 2000, he married Jessica Shoup, whom he had met while attending Notre Dame. He received his A.M. in 1997 and a Ph.D. in 2000, both in Physics.

Publications

K. M. O'Hara, M. E. Gehm, S. R. Granade, S. Bali and J. E. Thomas. Stable, strongly attractive, two-state mixture of lithium fermions in an optical trap. *Physical Review Letters*, 85(10):2092-2095, 2000.

K. M. O'Hara, S. R. Granade, M. E. Gehm, S. Bali and J. E. Thomas. Spatial loading dynamics of CO_2 laser traps. In preparation.

K. M. O'Hara, M. E. Gehm, S. R. Granade, S. Bali and J. E. Thomas. Evaporative Cooling of Lithium Fermions in an Ultrastable Optical Trap, 2000 Annual Meeting of the Division of Atomic, Molecular, and Optical Physics (DAMOP) (June 2000)

S. R. Granade, K. M. O'Hara, M. E. Gehm, S. Bali and J. E. Thomas. Spatial

Loading Dynamics of CO_2 Laser Traps, 2000 Annual Meeting of the Division of Atomic, Molecular, and Optical Physics (DAMOP) (June 2000)

T. A. Savard, K. M. O'Hara, S. R. Granade, M. E. Gehm, and J. E. Thomas. Raman-Induced Magnetic Resonance Imaging of Atoms in a Magneto-Optical Trap. *Physical Review A*, 60(6):4788-4795, 1999.

K. M. O'Hara, S. R. Granade, M. E. Gehm, S. Bali and J. E. Thomas. Evaporative Cooling of Lithium Fermions in a Stable Optical Trap, 1999 Meeting of the Southeastern Section of the American Physical Society (November 1999)

S. Bali, K. M. O'Hara, M. E. Gehm, S. R. Granade, and J. E. Thomas. Quantum-diffractive background gas collisions in atom-trap heating and loss. *Physical Review A*, 60(1):R29-R32, 1999.

K. M. O'Hara, S. R. Granade, M. E. Gehm, T. A. Savard, S. Bali, C. Freed, and J. E. Thomas. Ultrastable CO_2 laser trapping of lithium fermions. *Physical Review Letters*, 82(21):4204-4207, 1999.). Highlighted in *Physical Review Focus*, on the web page of *Science* magazine, in *Physics World* and *Physics Today*, and in *Scientific American*.

K. M. O'Hara, M. E. Gehm, S. R. Granade, S. Bali and J. E. Thomas. Ultrastable CO_2 Laser Trapping of Lithium Fermions, OPTICS Conference (April 1999)

K. M. O'Hara, S. R. Granade, M. E. Gehm, S. Bali and J. E. Thomas. Ultrastable CO_2 Laser Trapping of Lithium Fermions, Centennial Meeting of the American Physical Society (March 1999)

M. E. Gehm, K. M. O'Hara, T. A. Savard and J. E. Thomas. Dynamics of Noise-Induced Heating in Atom Traps, Centennial Meeting of the American Physical Society (March 1999)

M. E. Gehm, K. M. O'Hara, T. A. Savard, and J. E. Thomas. Dynamics of noise-induced heating in atom traps. *Physical Review A*, 58(5):3914-3921, 1998.

T. A. Savard, S. R. Granade, K. M. O'Hara, M. E. Gehm, J. E. Thomas. Raman Induced Magnetic Resonance Imaging of Trapped Atoms in a MOT, 1998 Annual Meeting of the Division of Atomic, Molecular, and Optical Physics (DAMOP) (May 1998)

T.A. Savard, K.M. O'Hara, and J.E. Thomas. Laser-noise-induced heating in far-off resonance optical traps. *Physical Review A*, 56(2):R1095–8, 1997.

T. A. Savard, K. M. O'Hara, and J. E. Thomas. Laser Noise Induced Heating in Far Off Resonance Optical Traps, conference on Quantum Electronics and Laser Science QELS ' 97 (May 1997)

T. A. Savard, C. A. Baird, K. M. O'Hara and J. E. Thomas. A Multi-coil Zeeman Slower, conference on Quantum Electronics and Laser Science QELS ' 97 (May 1997)